Technical Report Documentation Page

1. Report No.	2. Government Accession No.	3. Recipient's Catalog No.
CA14-2240		

4. Title and Subtitle	5. Report Date
Required Embedment Length of Column Reinforcement Extended into Type II Shafts	9/27/2013
	6. Performing Organization Code

7. Author(s)	8. Performing Organization Report No.
Juan Murcia-Delso, P. Benson Shing, Andreas Stavridis, and Yujia Liu	UCSD/SSRP-13/05

9. Performing Organization Name and Address	10. Work Unit No. (TRAIS)
Department of Structural Engineering University of California, San Diego 9500 Gilman Drive, Mail Code 0085 La Jolla, California 92093-0085	11. Contract or Grant No. 59A0710

12. Sponsoring Agency Name and Address	13. Type of Report and Period Covered
California Department of Transportation Division of Engineering Services 1801 30th St., MS #9-2/5I Sacramento, California 95816	Final Report
	14. Sponsoring Agency Code

15. Supplementary Notes

Prepared in cooperation with the State of California Department of Transportation.

16. Abstract

Cast-in-drilled hole (CIDH) shafts are frequently used to support reinforced concrete bridge columns because they have smaller footprints as compared to spread footings. The use of enlarged (Type II) pile shafts has additional advantages in that they provide more tolerance in pile positioning and also prevent the formation of below-surface plastic hinges in the piles in the event of a severe earthquake. The latter will lead to easier post-earthquake damage inspection. According to the specifications of the California Department of Transportation (Caltrans), the diameter of a Type II shaft shall be at least 610 mm (2 ft) larger than the cross-section dimension of the column. Hence, the column reinforcement extended into a pile shaft forms a non-contact splice with the shaft reinforcement. Because of the lack of information on the performance of these splices, the seismic design specifications of Caltrans on the embedment length of column reinforcement terminating in a Type II shaft are very conservative, especially for large-diameter columns. This complicates the construction work and increases construction costs.

This report presents an experimental and analytical investigation to determine the minimum embedment length required for column longitudinal reinforcement extended into a Type II shaft and the transverse reinforcement required in the bar anchorage regions of these shafts. Experiments were carried out to investigate the bond strength and cyclic bond deterioration of large-diameter bars (No. 11, 14, and 18 bars), which are frequently used in large-diameter bridge columns and piles, and to evaluate the adequacy of the development length requirements in the AASHTO LRFD Bridge Design Specifications for these bars when they are subjected to severe cyclic tensile and compressive loads. Such data were not available in the literature and are crucial to acquiring a good understanding of the anchorage performance of large-diameter bridge columns when they are subjected to a severe earthquake event. The experimental results have been used to develop, calibrate, and validate a semi-empirical bond-slip model for bars embedded in well-confined concrete. The model can successfully reproduce bond deterioration caused by cyclic bar-slip reversals and the tensile yielding of the bar. It has been implemented in an interface element in a finite element program.

While the development length tests have indicated that the AASHTO requirements are adequate to develop the expected yield and tensile strengths of a large-diameter bar, further numerical studies using finite element models and Monte Carlo simulations have indicated that they do not have sufficient reliability to develop the full tensile capacity of a bar when uncertainties in material properties and construction quality are considered.

In addition, large-scale tests were conducted on four column-pile shaft assemblies. Based on these tests, additional finite element analyses, and the aforementioned reliability analysis, new design recommendations on the minimum embedment length for column reinforcement extended into enlarge shafts have been proposed. Recommendations on the transverse reinforcement required in the bar anchorage region of a shaft are also provided. While the amount of transverse reinforcement recommended is higher than that required by the current design specifications of Caltrans and AASHTO, the required embedment length is reduced by 40 to 50%. Furthermore, it has also been shown in the tests that engineered steel casing is effective in providing the necessary confinement to control tensile splitting cracks induced by bar slip in a Type II shaft, which can minimize the need for post-earthquake damage repair on these shafts.

17. Key Words	18. Distribution Statement
Type II shafts, RC columns, embedment length, development length, bond-slip behavior, seismic performance, bond-slip law, large-diameter bars, finite element analysis	No restrictions. This document is available to the public through the National Technical Information Service, Springfield, Virginia 22161.

19. Security Classification (of this report)	20. Security Classification (of this page)	21. No. of Pages	22. Price
Unclassified	Unclassified	367	

Form DOT F 1700.7 (8-72)

DISCLAIMER

This document is disseminated in the interest of information exchange. The contents of this report reflect the views of the authors who are responsible for the facts and accuracy of the data presented herein. The contents do not necessarily reflect the official views or policies of the State of California or the Federal Highway Administration. This publication does not constitute a standard, specification or regulation. This report does not constitute an endorsement by the California Department of Transportation of any product described herein.

For individuals with sensory disabilities, this document is available in Braille, large print, audiocassette, or compact disk. To obtain a copy of this document in one of these alternate formats, please contact: the Division of Research and Innovation, MS-83, California Department of Transportation, P.O. Box 942873, Sacramento, CA 94273-0001.

STRUCTURAL SYSTEMS

RESEARCH PROJECT

Report No.
SSRP–13/05

REQUIRED EMBEDMENT LENGTH OF COLUMN REINFORCEMENT EXTENDED INTO TYPE II SHAFTS

by

JUAN MURCIA-DELSO
P. BENSON SHING
ANDREAS STAVRIDIS
YUJIA LIU

Final Report Submitted to the California Department of Transportation under Contract No. 59A0710

September 2013

Department of Structural Engineering
University of California, San Diego
La Jolla, California 92093-0085

University of California, San Diego
Department of Structural Engineering
Structural Systems Research Project
Report No. SSRP–13/05

Required Embedment Length of Column Reinforcement Extended into Type II Shafts

by

Juan Murcia-Delso
Postdoctoral Scholar

P. Benson Shing
Professor of Structural Engineering

Andreas Stavridis
Assistant Professor, University at Buffalo
(Formerly Postdoctoral Scholar at UCSD)

Yujia Liu
Graduate Student Researcher

Final Report Submitted to the California Department of Transportation under Contract No. 59A0710

Department of Structural Engineering
University of California, San Diego
La Jolla, California 92093-0085
September 2013

ACKNOWLEDGMENTS

Funding for the investigation presented in this report was provided by the California Department of Transportation (Caltrans) under Contract No. 59A0710. The authors are most grateful to Caltrans engineers, and in particular, the General Earthquake Committee, for their continuous technical input and advice throughout this study. Dr. Charles Sikorsky of Caltrans was the project manager, who provided unfailing support and guidance to assure the successful completion of this project.

The research presented in this report was part of the doctoral dissertation work of Dr. Juan Murcia-Delso carried out under the supervision of Professor Benson Shing. The contents of this report constituted a large portion of his doctoral dissertation titled “Bond-slip behavior and development of column longitudinal reinforcing bars in enlarged pile shafts.” Professor Andreas Stavridis participated in this research as a postdoctoral scholar at UCSD. He contributed to the experimental work on the basic bond-slip tests presented in Chapter 3, and the development length tests presented in Chapter 5. Ms. Yujia Liu participated in the design and preparation of the first two column-shaft assembly tests presented in Chapters 6 and 7 of this report. She also analyzed the behavior of the columns in these two tests for her master’s thesis.

The experiments presented in this report were conducted in the Charles Lee Powell Structural Engineering Laboratories at UCSD. The authors would like to express their gratitude to the laboratory staff, especially Dr. Christopher Latham, for their professionalism and high-quality technical support.

The authors would also like to thank Mr. Charles Cummings, an undergraduate student, for his assistance in the preparation of the column-pile shaft assembly tests, and Mr. Vassilis Papadopoulos, a graduate student researcher, for his contributions in the evaluation and calibration of the constitutive model for concrete that has been used in the numerical studies presented in this report.

ABSTRACT

Cast-in-drilled hole (CIDH) shafts are frequently used to support reinforced concrete bridge columns because they have smaller footprints as compared to spread footings. The use of enlarged (Type II) pile shafts has additional advantages in that they provide more tolerance in pile positioning and also prevent the formation of below-surface plastic hinges in the piles in the event of a severe earthquake. The latter will lead to easier post-earthquake damage inspection. According to the specifications of the California Department of Transportation (Caltrans), the diameter of a Type II shaft shall be at least 610 mm (2 ft) larger than the cross-section dimension of the column. Hence, the column reinforcement extended into a pile shaft forms a non-contact splice with the shaft reinforcement. Because of the lack of information on the performance of these splices, the seismic design specifications of Caltrans on the embedment length of column reinforcement terminating in a Type II shaft are very conservative, especially for large-diameter columns. This complicates the construction work and increases construction costs.

This report presents an experimental and analytical investigation to determine the minimum embedment length required for column longitudinal reinforcement extended into a Type II shaft and the transverse reinforcement required in the bar anchorage regions of these shafts. Experiments were carried out to investigate the bond strength and cyclic bond deterioration of large-diameter bars (No. 11, 14, and 18 bars), which are frequently used in large-diameter bridge columns and piles, and to evaluate the adequacy of the development length requirements in the AASHTO LRFD Bridge Design Specifications for these bars when they are subjected to severe cyclic tensile and compressive loads. Such data were not available in the literature and are crucial to acquiring a good understanding of the anchorage performance of large-diameter bridge columns when they are subjected to a severe earthquake event. The experimental results have been used to develop, calibrate, and validate a semi-empirical bond-slip model for bars embedded in well-confined concrete. The model can successfully reproduce bond

deterioration caused by cyclic bar-slip reversals and the tensile yielding of the bar. It has been implemented in an interface element in a finite element program.

While the development length tests have indicated that the AASHTO requirements are adequate to develop the expected yield and tensile strengths of a large-diameter bar, further numerical studies using finite element models and Monte Carlo simulations have indicated that they do not have sufficient reliability to develop the full tensile capacity of a bar when uncertainties in material properties and construction quality are considered.

In addition, large-scale tests were conducted on four column-pile shaft assemblies. Based on these tests, additional finite element analyses, and the aforementioned reliability analysis, new design recommendations on the minimum embedment length for column reinforcement extended into enlarge shafts have been proposed. Recommendations on the transverse reinforcement required in the bar anchorage region of a shaft are also provided. While the amount of transverse reinforcement recommended is higher than that required by the current design specifications of Caltrans and AASHTO, the required embedment length is reduced by 40 to 50%. Furthermore, it has also been shown in the tests that engineered steel casing is effective in providing the necessary confinement to control tensile splitting cracks induced by bar slip in a Type II shaft, which can minimize the need for post-earthquake damage repair on these shafts.

TABLE OF CONTENTS

LIST OF FIGURES

LIST OF TABLES

CHAPTER 1

INTRODUCTION

The performance of reinforced concrete (RC) structures depends on the composite action of the concrete and reinforcing steel, which relies on the bond between the two materials. When RC structures are subjected to earthquake loads, they may experience severe bond stress demands in regions where the reinforcement is anchored, e.g., in the foundation of a bridge column. Inadequate embedment lengths in these regions can lead to anchorage failures, and, thereby, structural collapse. Figure 1.1 shows the collapse of large bridge columns during the 1971 San Fernando earthquake due to anchorage failures. After this earthquake, the embedment length for large-diameter bars in bridge foundations was increased and more confinement steel was provided in bridge footings and columns (Yashinsky 2001).

Large-diameter bars are frequency used in bridge columns and pile shafts. In spite of the fact that extensive research has been carried out over the last few decades on the bond strength and bond-slip behavior of reinforcing bars, there were little such data available on large-diameter (No.11 [36-mm] and larger) bars. The development length specifications in ACI 318-08 (ACI 2008) and the AASHTO LRFD Bridge Design Specifications (AASHTO 2010) are largely based on experimental data obtained from No. 11 and smaller bars, and they do not allow lap-splicing of bars larger than No. 11. Moreover, no data were available on the cyclic bond-slip behavior for large-diameter bars. Most of the experimental data on the cyclic bond-slip behavior of reinforcing bars were obtained from No. 8 (25-mm) bars by Eligehausen et al. (1983). Therefore, experimental data on the bond strength, cyclic bond deterioration, and development of

large-diameter bars are needed to validate current code provisions and improve them if necessary.

While the bond-slip behavior of reinforcing bars can have a strong influence on the strength and stiffness of reinforced concrete structures, this aspect has been frequently neglected in the finite element analysis of RC structures. Reliable bond-slip models are essential to properly capture crack spacing, and the stiffness and deformation capability of RC members. Such models are also needed for fundamental studies to determine the development and lap-splice lengths required for reinforcing bars in RC members of different designs when experimental data are not available, and for the interpretation of experimental results. For seismic performance assessments, accurate and efficient models that can capture the cyclic bond-slip behavior of reinforcing bars in large and complex structures are needed.

1.1 Embedment length of column reinforcement extending into Type II shafts

Cast-in-drilled hole (CIDH) piles are used frequently as foundations for RC bridge columns because they have smaller footprints as compared to spread footings. Two types of pile shafts are used in California: pile shafts that have the same diameter as the column (Type I), and pile shafts with diameters at least 0.61 m (2 ft) larger than that of the column (Type II), as shown in Figure 1.2. For columns supported on Type I shafts, plastic hinges will develop in the shafts underneath the ground surface when the bridge is subjected to severe seismic loads (e.g., see Budek et al. 2000, Chai 2002, Chai and Hutchinson 2002). Type II shafts are capacity protected elements forcing plastic hinges to form at the column base. This leads to easier damage inspection after an earthquake. Besides the structural benefits, Type II shafts have more tolerance in positioning without affecting the alignment of bridge columns. However, because the column and shaft diameters are different, it is not possible to have a continuous reinforcing cage for both elements, and the column longitudinal reinforcement extended into the shaft is terminated at a certain distance forming a non-contact lap splice with the longitudinal reinforcement for the shaft.

The Seismic Design Criteria of Caltrans (Caltrans 2010) contains the minimum design requirements for *Ordinary* bridges in California to meet the performance goals. Section 8.2.4 of the Seismic Design Criteria requires that column longitudinal reinforcement extended into a Type II shaft be terminated in a staggered manner with minimum embedment lengths of $D_{c,\max} + l_d$ and $D_{c,\max} + 2l_d$, respectively, where $D_{c,\max}$ is the larger cross-sectional dimension of the column and l_d is the development length required for a straight bar in tension. This requirement was found to be conservative for large-diameter columns in an analytical study conducted by Chang and Dameron (2009) using finite element models. However, there were no experimental data on the cyclic bond-slip behavior of large diameter bars to calibrate the finite element models used in that study, and as a result, no definitive conclusions could be drawn on the minimum required embedment length.

1.2 Research objectives and scope

The main objective of this investigation was to determine the minimum embedment length required for column reinforcement extended into Type II shafts and develop improved design recommendations on the embedment length and the transverse reinforcement required for the bar anchorage zone of a pile shaft. To this end, basic experimental data on the cyclic bond-slip behavior of large-diameter (No. 11 [36-mm], 14 [43-mm], and 18 [57-mm]) reinforcing bars were obtained from 22 bond-slip tests, and 3 development length tests were conducted on No. 14 and 18 bars to evaluate the adequacy of the current requirements in the AASHTO LRFD Bridge Design Specifications (AASHTO 2010). In all these tests, bars were embedded in well-confined cylindrical concrete specimens with a confinement level comparable to that required for a Type II shaft. A bond-slip law that accounts for the cyclic bond deterioration and the radial stress introduced by bond-slip in a semi-empirical fashion has been developed and implemented in the finite element analysis program ABAQUS (Simulia 2010). As part of this study, the reliability of the development length requirements in the AASHTO LRFD Specifications in developing the expected yield and tensile strengths of large-diameter

bars in a well-confined situation has been evaluated. With the aforementioned test data and detailed finite element analyses of column-shaft assemblies accounting for the bond-slip phenomenon, the minimum embedment length required for column reinforcement extended into an enlarge shaft was determined. This was validated with large-scale tests conducted on four column-shaft assemblies. A simplified analytical model has been developed to determine the amount of transverse reinforcement required for the bar anchorage zone of a shaft to counteract the splitting forces developed by bar slip and ensure the development of adequate bond strength. Design recommendations have been developed based on results of the numerical, analytical, and experimental studies.

1.3 Outline of the report

Chapter 2 presents the fundamental aspects of the bond between a reinforcing bar and the surrounding concrete, and a literature review of notable experimental and analytical studies in this area.

Chapter 3 presents an experimental study carried out in this project to investigate the bond-slip behavior of large-diameter bars embedded in well-confined concrete. A total of 22 monotonic pull-out and cyclic pull-pull tests were conducted on No. 11, 14, and 18 bars to study their bond strength and bond stress-vs.-slip relations. The tests examined the influence of the load history and loading direction applied to a bar, and the concrete strength on the bond strength and bond-slip behavior. The specimen design, test setup, and experimental results are presented in detail. Based on these results and studies carried out by others, the effects of the bar diameter, concrete strength, pull direction and loading history on the bond strength are discussed.

Chapter 4 presents a newly developed bond-slip model that can be used in finite element analysis to capture the bar slip behavior in RC structures. The model adopts a semi-empirical law that can accurately reproduce the bond stress-vs.-bar slip behavior under monotonic and cyclic load conditions. The bond-slip law has been calibrated with the experimental data presented in Chapter 3, and implemented in an interface element in the finite element analysis program ABAQUS. The accuracy of the model has been validated with finite element analyses using data obtained from bond-slip tests,

development length tests, and an RC column test. Even though the model accounts for the radial stress introduced by bar slip and the degradation of bond strength due to splitting cracks, it is intended for bars embedded in well-confined concrete.

Chapter 5 presents results of experimental and computational studies on the development of large-diameter bars in well-confined concrete. These studies included three pull-push tests conducted to evaluate the development length requirements in the AASHTO LRFD Bridge Design Specifications (AASHTO 2010) for large-diameter bars in tension under a well-confined situation. Finite element analyses have been conducted on the test specimens using the bond-slip model presented in Chapter 4. The accuracy of the models has been validated by the test results. The models have been used to understand the distribution of bond stress during different stages of loading. A parametric study has been carried out with finite element models. Based on the numerical results, an analytical equation has been derived to relate the tensile capacity of a bar with a straight anchorage to the bar diameter, the embedment length, the compressive strength of the concrete, and the yield strength of the steel. With this equation, a Monte Carlo simulation has been conducted to assess the reliability of the AASHTO development length specifications in developing the yield and tensile strengths of a bar in a well-confined condition with different uncertainties.

Chapter 6 presents the specimen design, test setup, instrumentation, and loading protocol for four large-scale, quasi-static, cyclic, load tests conducted on RC column-enlarged pile shaft assemblies. This test program was to determine the minimum embedment length required for column reinforcement extended into an enlarged shaft and the transverse reinforcement required in the bar anchorage region of a shaft, and to validate nonlinear finite element models used for a subsequent parametric study. The rationale for the design of the test specimens and the embedment lengths used is explained. An analytical model is presented to determine the minimum transverse reinforcement required in the bar anchorage region of a shaft.

Chapter 7 presents the results of the tests conducted on the four large-scale column–enlarged pile shaft assemblies.

Chapter 8 presents a numerical study conducted to investigate the bond-slip behavior in column-pile shaft assemblies using nonlinear finite element analysis. Finite element models developed for the column-pile shaft specimens discussed in Chapters 6 and 7 are described. These models were used for pre-test predictive analyses, and have been refined and validated with the test results. The correlations between the numerical and experimental results are presented and the bond-stress variations along the anchorage zone of a bar at different stages of loading are obtained numerically to assess the reserve anchorage capacities in the test specimens. A parametric study has been conducted with finite element models to evaluate the adequacy of the minimum embedment length requirements deduced from the assembly tests for column-shaft systems of various dimensions and with different sizes and quantities of longitudinal bars and different confinement conditions.

In Chapter 9, design recommendations are proposed for the minimum embedment length required for column reinforcement extended into an enlarged pile shaft, and the quantity of transverse steel required in the bar anchorage zone of a shaft. These recommendations are based on the experimental, numerical, and analytical studies presented in the previous chapters.

Chapter 10 presents a summary of the study and the major observations and conclusions. Recommendations for future research are also presented.

(a) Anchorage failure for a column supported on a pile shaft

(b) Anchorage failure in a bridge footing

Figure 1.1: Anchorage failures of bridge columns during the 1971 San Fernando earthquake (Yashinsky 2001)

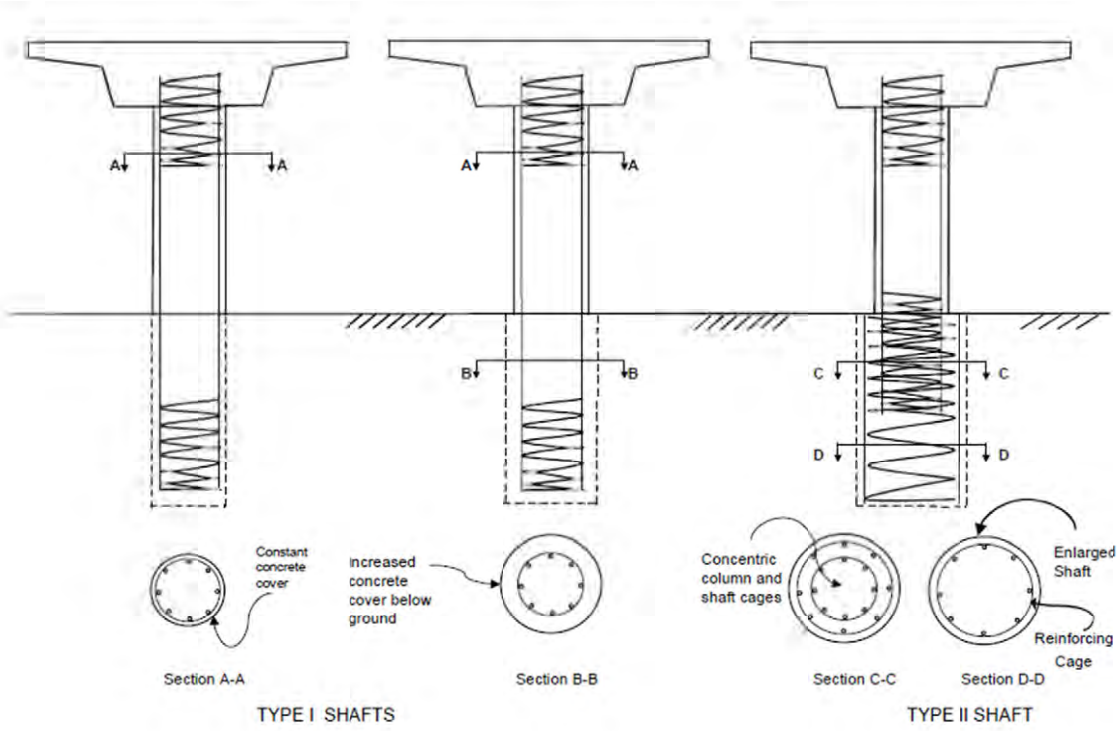

Figure 1.2: Type I and Type II shafts (Caltrans 2010)

CHAPTER 2

BOND OF REINFORCEMENT: A LITERATURE REVIEW

The stress transfer mechanism between concrete and a reinforcing bar is generally referred to as the bond of reinforcement. It is an essential mechanism that engages the composite action of concrete and steel in reinforced concrete (RC) structures. The study of bond between concrete and a reinforcing bar has attracted the attention of many researchers. According to Abrams (1913), tests to study the bond between concrete and iron bars were conducted as early as 1876 (only nine years after Joseph Monier had obtained his first patent on reinforced concrete) by Thaddeus Hyatt. Bond of deformed steel bars, used in modern RC construction, has been extensively studied over the last few decades, and comprehensive monographic reports have been published by the International Federation for Structural Concrete (fib 2000) and the American Concrete Institute (ACI 2003).

In this chapter, the fundamental mechanisms governing the bond behavior of deformed bars as reported in different studies are first discussed, and relevant experimental studies of the bond strength and bond-slip behavior of deformed bars are summarized. Special attention is given to studies focused on the cyclic deterioration of bond resistance and on the bond characteristics of large-diameter bars because they are especially relevant to the research presented in this report. Finally, different approaches that have been proposed to model the bond-slip behavior of deformed bars are summarized.

2.1 Bond of deformed bars

In deformed bars, the term bond refers not only to the chemical adhesion between the two materials, but also to the resistance provided by friction forces and the interlocking action introduced by the bar deformations (or ribs). The bond behavior of deformed bars has been well characterized by the work of a number of researchers, which has led to a certain agreement on its fundamental mechanisms, as documented in fib (2000) and ACI (2003). The description of the bond behavior presented here is based on the findings described in these two reports. This description is limited to deformed bars. No reference to plain bars, which correspond to older concrete construction practice, is made here.

2.1.1 Sources of bond resistance and bond-slip behavior

The bond force between a deformed bar and the surrounding concrete can be attributed to the resisting mechanisms shown in Figure 2.1: (a) chemical adhesion between the steel and the concrete, (b) friction forces acting at the interface, and (c) bearing forces of the bar ribs acting against the concrete. The nature and magnitude of the bond force depends on the relative displacement, or slip, between the concrete and the bar. Some could argue that there is no such phenomenon as bar slip based on the fact that most of the relative displacement of a bar is due to inelastic phenomena (cracking, crushing, and shearing) that take place in the concrete surrounding the bar, but not at the interface. However, in this report, as in most studies, slip is idealized as the sum of the relative displacement at the interface and that due to the above-mentioned inelastic deformations.

At low bond stress demands, bond is mostly due to chemical adhesion, and no slip occurs between the bar and the concrete. As the chemical adhesion is overcome by increased bond stress demand, the bar starts to slip with respect to the concrete, which mobilizes friction forces at the bar surface due to its roughness and bearing forces at the ribs against the concrete. The pressure that the ribs exert onto the concrete creates micro-cracks, commonly referred to as Goto cracks (Goto 1971), starting at the tip of the ribs and propagating transversely away from the bar, as shown in Figure 2.2. The opening of

these micro-cracks allows further slippage of the bar with respect to the concrete. As slip occurs, the wedging action of the ribs tends to introduce a radial expansion at the interface, which activates the passive confinement in the concrete. Radial expansion produces a hoop tension in the concrete, which causes splitting cracks to develop at the surface in contact with the bar and propagate radially, as shown in Figure 2.2. This hoop tension is balanced by the undamaged outer concrete ring as well as the confining reinforcement if any. For low confinement conditions, splitting cracks propagate radially through the concrete cover and the bond fails abruptly, as shown in Figure 2.3. This type of failure is referred to as splitting failure. Figure 2.4 shows a splitting failure obtained during a pull-out test by Choi et al. (2011).

With sufficient cover and confining reinforcement, the opening of splitting cracks is prohibited and large normal stresses can be developed at the contact surface between the concrete and the steel, which increase the bond resistance. In this case, further slip is achieved by crushing the concrete in front of the ribs. The accumulation of crushed particles in front of the ribs contributes to the expansion of the interface and increases the radial component of the bearing forces. At this stage, the increase of the hoop stresses can still result in a splitting failure if the cover and the confining reinforcement are not sufficient. When the concrete is well confined, splitting failure is precluded and higher bond strengths can be achieved, as shown in Figure 2.3. In this case, the bond fails due to loss of the interlocking action caused by the crushing and shearing of the concrete keys between the ribs. Finally, the bar is pulled out from the concrete, and only a residual frictional resistance remains. This type of failure is referred to as pull-out failure. Figure 2.5 shows a bar that was pulled out from the concrete during a test presented in Chapter 3, with crushed concrete particles visible between the ribs.

The bond-slip mechanism for bars with pull-out failures under cyclic loading has been theorized by Eligehausen et al. (1983). Figure 2.6 shows the damage mechanisms and bond-slip behavior under cyclic loading as presented by Eligehausen et al. (1983). In Figure 2.6a, it is assumed that the slip is reversed before horizontal shear cracks develop. After unloading (along path AF in the figure), the gap between the right side of the ribs and the adjacent concrete, caused by concrete crushing on the left side of the ribs,

remains open with a width equal to the residual slip at point F. Only a small fraction of the slip is recovered by the elastic unloading of the concrete. When the slip is reversed (along path GH), some frictional resistance is built up. At H, the ribs are in contact again with the concrete (but a gap has opened on the left side of the ribs). Because of a resumed contact with the concrete, a sharp increase in stiffness occurs (along path HI). With increasing load, the opened inclined cracks close, allowing the transfer of compressive stresses across them with no noticeable reduction in stiffness (with the monotonic loading curve recovered at this point). Inclined cracks perpendicular to the previously opened ones appear as the stress increases in this direction. At point I, a gap equal to the distance between points F and I has opened. When reversing the slip, the path IKL is similar to AFH, described previously. However, the bond resistance starts to increase again at L, when the ribs start to press broken pieces of concrete against the previous bearing face. With further bar slip, the transverse cracks previously closed are opened and the cracks previously opened are closed. At M, the ribs and the concrete are in full contact and the monotonic loading curve is recovered.

If the slip reversal takes place after horizontal shear cracks have initiated, a different behavior is obtained as shown in Figure 2.6b. When loading in the opposite direction (along path HI), the ribs press against the concrete in between, whose resistance has been lowered by the shear cracks. Therefore, the bond resistance is lowered compared to the monotonic curve. When reversing the slip again (along path IKLMN), the resistance is further lowered compared to that at point I because of the additional shearing damage in the concrete.

When a large slip is imposed during the first cycle, almost all the concrete between the ribs can be sheared off and the behavior will be like the one shown in Figure 2.6c. When moving the bar back (along path GH), the frictional resistance is higher than that for the above cases, in which the slip in the first cycle is smaller, because the concrete surface along the shear crack is rougher. When reloading in the opposite direction, the peak resistance (point I) is lowered. When reversing the slip again, the frictional resistance is lowered because the surface has been smoothened (path KL).

2.1.2 Factors affecting bond resistance

The bond between reinforcement and concrete depends on many factors that involve not only the characteristics of the contact surface but also the concrete properties, bar properties, and structural properties as discussed in ACI (2003). Concrete properties that have an important influence on the bond are the compressive and tensile strengths. Bar properties that influence the bond include, but are not limited to, the bar size, the rib geometry, and the yield strength of the bar. Among the structural properties, the most important ones are the cover and spacing of bars, the quantity and spacing of the transverse reinforcement, and the bar casting position. The influence of these factors is summarized in the following paragraphs. A more exhaustive list of factors and a detailed explanation of their effects are provided in ACI (2003).

Bond resistance is related to the compressive and tensile strengths of concrete because it depends on the bearing resistance of the concrete in front of the ribs, the shearing resistance of the concrete keys between the ribs, and the tensile strength of the concrete to resist splitting stresses (fib 2000). Experimental studies have shown a significant increase of the bond strength with the increase of the compressive strength of the concrete, f_c'. A number of studies, e.g., Eligehausen et al. (1983), have suggested that the bond strength can be assumed to be proportional to $f_c'^{1/2}$. This relation has been adopted in bond-strength equations (ACI 2003) and in development-length equations given in design codes such as ACI 318-08 (ACI 2008) and the AASHTO LRFD Bridge Design Specifications (AASHTO 2010). However, there are other studies that have indicated that the bond strength is proportional to f_c' (Rehm 1961) or $f_c'^{1/3}$ (Zsutty 1985). Based on a large number of lap-splice tests, Zuo and Darwin (2000) have concluded that for splices not confined by transverse reinforcement, the average bond strength is proportional to $f_c'^{1/4}$, and the additional bond strength attributed to the presence of transverse reinforcement is proportional to $f_c'^{3/4}$. Based on these observations, the relation between the compressive strength of concrete and the bond strength seems to depend on the level of the confinement, which could explain the

different conclusions obtained in different studies. ACI (2003) states that $f_c'^{1/2}$ may not accurately represent the effect of the concrete strength on the bond strength because the effect of other parameters has been generally overlooked. In conclusion, even though the resisting mechanisms of bond are known to be related to the concrete strength, a general theory to relate the compressive and tensile strengths of concrete with the bond strength is not available.

Regarding the effect of the bar size on the bond resistance, it is generally accepted that smaller bars have an advantage as compared to larger bars (ACI 2003). Several researchers, e.g., Eligehausen et al. (1983), have reported a reduction of the bond strength with increasing bar size. As a result, the ACI 318-08 (ACI 2008) and AASHTO LRFD (AASHTO 2010) provisions for the development length consider that the bond strength is larger for smaller bars. However, Ichinose et al. (2004) have provided experimental evidence that the influence of the bar size on the bond strength depends on the level of confinement. In their tests, the bond strength decreased with increasing bar size for specimens with low levels of confinement and splitting failures, but this effect was negligible for specimens with high levels of confinement and pull-out failures.

As explained earlier, the bond resistance of deformed bars depends to a large extent on the wedging action of the ribs. Therefore, the geometry of the ribs can be regarded as an important parameter affecting bond strength. Some studies have shown that the rib pattern has a strong influence on the bond strength, but others have shown that this influence is very small (ACI 2003). Current ASTM standards for reinforcing bars, e.g., ASTM A706 (ASTM 2009), have specifications on the height and spacing of the ribs, which are based on test results obtained by Clark (1946, 1950) for bars with different deformation patterns. Studies by Clark have shown that bond performance tends to improve as the relative rib area (R_r) increases. The relative rib area is defined as the ratio of the projected rib area normal to the bar axis (A_R) to the bar perimeter times the center-to-center rib spacing ($s_{R,C}$), i.e.,

$$R_r = \frac{A_R}{\pi d_b s_{R,C}} \tag{2.1}$$

in which d_b is the bar diameter. Typical values of R_r for bars used in the US are between 0.057 and 0.087 (Choi et al. 1990). Based on the results of an experimental investigation, Darwin and Graham (1993) have concluded that under conditions of relatively low confinement, in which bond is governed by the splitting of concrete, the bond strength is not influenced by the rib pattern, but the bond strength increases as the relative rib area increases (regardless of the rib height and rib spacing) when additional confinement is provided by transverse reinforcement or larger concrete covers.

Bond resistance is also affected by the strain in the reinforcing bar. This influence is small as long as the steel remains in the elastic range (fib 2000). Experimental studies by Viwathanatepa et al. (1979) and Shima et al. (1987b) have shown that bond resistance can be considerably reduced after a reinforcing bar yields in tension. In the pull-out tests carried out by Shima et al. (1987b), the bond stress-vs.-slip relations were estimated at different locations along the embedment length of a bar being pulled out from a concrete block. As shown in Figure 2.7, their results have indicated that the bond resistance dropped rapidly to 25% of the peak stress once a bar yielded regardless of the amount of bar slip.

The concrete cover and bar spacing are important parameters that affect the bond resistance and bond failure mode. With the increase of the cover and spacing, the failure mode changes from concrete splitting to bar pull-out resulting in an increased bond strength. Additional confinement can be provided by transverse reinforcement. The confining effect of concrete and transverse steel is accounted for in the development-length equations of most design codes. For example, the development length required in ACI 318-08 (ACI 2008) is inversely proportional to a confinement index defined as $\left(c_b + 40A_{tr} / s_{tr} n\right)/ d_b$, in which c_b is the smaller of the cover of the bar measured from its center and half of the center-to-center spacing of the bars, s_{tr} is the spacing of the transverse reinforcement, A_{tr} is the transverse reinforcement area within distance s_{tr}, and n is the number of bars being spliced or developed at the plane of splitting. According to ACI 318-08, when $\left(c_b + 40A_{tr} / sn\right)/ d_b$ is less than 2.5, a splitting failure is likely, and for values above 2.5, a pull-out failure is expected.

Finally, the position of the bar during concrete casting affects the bond performance. Horizontal bars located near the top face of a concrete member have lower bond strengths than horizontal bars lower in the member. This is because the higher the location of a horizontal bar is, the more is the paste settlement and the accumulation of bleed water underneath the bar (ACI 2003). This effect is taken into account in the ACI 318-08 provisions on the development length of bars. For bars that are vertical during casting, bond performance is better when the bars are loaded upward than when they are loaded downward because the qualities of the concrete above and below a rib are different for similar reasons (fib 2000).

2.2 Experimental characterization of bond of reinforcement

2.2.1 Basic bond-slip tests

Pull-out tests of bars with short embedment lengths (typically equal to or less than five times the bar diameter) are commonly used to study the bond strength and bond stress-vs.-slip relations. Test specimens and setups used in different studies are all very similar to those shown in Figure 2.8, which was proposed by Rehm (1961). With this type of setup, the concrete is placed in compression when the bar is pulled, which does not represent the actual stress state in concrete in real structures. However, this is adequate for the assessment of the local bond behavior of a bar. In these tests, the bonded area of the bar is located away from the surface on which the compressive force is applied to reduce the arching effect that may unrealistically increase the bond strength.

Many researchers have conducted pull-out tests to obtain the bond strength and bond stress-vs.-slip relations of bars subjected to monotonically increasing slip. However, few studies have focused on the cyclic bond-slip behavior of bars. The study by Eligehausen et al. (1983) has been the only major effort that has provided most of our understanding of the cyclic bond-slip behavior of reinforcing bars. Their experimental investigation focused on the bond deterioration of deformed bars under fully reversed cyclic loading with confinement conditions similar to those in beam-column joints. A typical specimen and the test setup are shown in Figure 2.9. A total of 125 pull-out tests

were carried out to study the influence of different parameters, such as the loading history, the level of confinement, and the bar size, on the bond-slip behavior. Most of the tests were carried out with 25-mm (1-in.) diameter bars, and some tests were done with 32-mm (1.25-in.) bars. The bond stress-vs.-slip relations obtained from some of these tests are shown in Figure 2.10.

2.2.2 Effect of confinement on bond strength and radial dilatation

A few researchers have investigated experimentally the interaction between the tangential (bond) stress-displacement (slip) relations and the normal (confining) stress/displacement (radial dilatation) along a bar-concrete interface. They carried out pull-out tests with short embedment lengths and employed special setups to control and/or monitor the confining stress and radial dilatation. These studies have provided very valuable data to understand the effect of confinement on the bond-slip behavior of bars.

Gambarova et al. (1989, 1996) carried out pull-out tests on bars in pre-splitted concrete specimens subjected to external confinement, as shown in Figure 2.11. Most of the specimens were tested by maintaining the crack opening constant during the test. The bond stress-vs.-slip and confining stress-vs.-slip relations were obtained for different values of crack opening. With increasing crack opening, both the bond strength and stiffness decreased, as shown in Figure 2.12. Gambarova et al. (1996) conducted a second set of tests on specimens that were subjected to a constant confining stress. Results of these tests show that the bond strength varied almost linearly with the confining stress.

Malvar (1992) carried out a set of pull-out tests on bars in pre-splitted concrete cylinders under a constant confining stress. Relations between the bond stress, the bar slip, and the radial displacement were obtained for different levels of confining stress, as shown in Figure 2.13. They showed that the bond strength increased significantly with increasing confining stress. As the bar slip continued to increase, the radial dilatation increased up to a value, which was dependent on the confining stress, and then decreased due to the smoothening of the interface. The higher the confinement is, the lower is the radial dilatation.

Lundgren (2000) carried out monotonic pull-out and cyclic pull-pull tests on bars embedded in concrete cylinders confined by a thin steel tube. Relations between the hoop strains in the tube, the applied load, and the slip were obtained, as shown in Figure 2.14.

2.2.3 Development length and lap splice tests

Beam specimens, like those presented in Figure 2.15, have been used to study the required development and lap-splice lengths for reinforcing bars. A database of results from this type of tests is maintained by the ACI 408 Committee (ACI 2003). Based on this database, several equations have been proposed to determine the required development and lap-splice lengths. The equations developed by Orangun et al. (1975, 1977) have been adopted by ACI 318-08 (ACI 2008). More recently, new design equations have been recommended by the ACI 408 Committee (ACI 2003) based on the work of Zuo and Darwin (2000).

2.2.4 Tests on large-diameter bars

In spite of the extensive experimental work on the bond of reinforcement, data on the bond strength and bond-slip behavior of large-diameter bars is scarce. As shown in Figure 2.16, there are very few test results available in the ACI 408 Committee database (ACI 2003) for bars larger than No. 11 (36 mm in diameter). For this reason, the development length requirements in ACI 318-08 (ACI 2008) and the AASHTO LRFD Bridge Design Specifications (AASHTO 2010) are largely based on experimental data obtained from No. 11 and smaller bars, and they do not allow lap-splicing of bars larger than No. 11.

Recently, pull-out and lap-splice tests were conducted on large-diameter bars (Ichinose et al. 2004, Plizzari and Mettelli 2009, and Steuck et al. 2009). Ichinose et al. (2004) carried out such tests on bars up to 52 mm (2 in.) in diameter. In their pull-out and lap-splice tests conducted on specimens with no stirrups, bond failures were governed by concrete splitting and the bond strength decreased significantly with the increase of the bar size. Even though lap splices in specimens confined by stirrups also failed by the

splitting of concrete, the effect of the bar size was not so significant. However, in the pull-out tests conducted on specimens confined by stirrups, bond failures were caused by the localized crushing of concrete in front of the bar ribs and the effect of the bar size on the bond strength was not noticeable. Plizzari and Mettelli (2009) carried out pull-out tests on 40-mm (1.6-in.) and 50-mm (2-in.) diameter bars under low confinement conditions. Bond failures in all these tests were caused by the splitting of concrete, and the resulting bond strengths were significantly lower than those obtained for smaller bars tested by the same researchers. Steuck et al. (2009) carried out pull-out tests on No.10 (32-mm), 14 (43-mm), and 18 (57-mm) bars embedded in well-confined high-strength grout. All specimens failed by the pull-out of the bars and no significant variation in the bond strengths was observed for the different bar sizes. All the tests on large-diameter bars mentioned in these studies were carried out under monotonically increasing slip. No data have been reported on the cyclic bond-slip behavior of large-diameter bars.

2.3 Modeling of bond-slip behavior

Modeling of the bond-slip behavior of reinforcement is needed to properly capture crack spacing, and the stiffness and deformation capability of RC members. It can also be used to study the anchorage capacity of bars, and determine the minimum development lengths required. Cox and Herrmann (1998) have classified bond-slip models into three categories depending on their scale: rib scale, bar scale, and member scale. In *rib-scale* models, the interaction between the deformed bar and the concrete is accounted for by explicitly modeling in a detailed manner the concrete and the steel bar including the ribs. In *bar-scale* models, the concrete-steel interaction is represented by a law that relates the stresses and relative displacements at their interface. In *member-scale* models, the effect of bond-slip is accounted for with rotational springs or special structural element formulations. The literature review presented in this section is organized based on this classification.

2.3.1 *Rib-scale* models

Several researchers, e.g., Reinhardt et al. (1984a), Maekawa et al. (2003), Daoud et al. (2012), have used *rib-scale* finite element models to study the interaction between a deformed bar and the surrounding concrete. In these models, both the concrete and the bar including the ribs were represented with continuum elements, e.g., see Figure 2.17. The explicit modeling of the ribs is what ultimately provides the interaction between the reinforcement and concrete. These models require a detailed definition of the bar geometry and the use of appropriate constitutive laws for steel and concrete. Some studies have included modeling features like the contact conditions (Reinhardt et al. 1984a, Maekawa et al. 2003), the steel-concrete transition zone (Maekawa et al. 2003), or the internal structure of concrete consisting of cement matrix and aggregate (Daoud et al. 2012).

Detailed models like these can be used to investigate the basic characteristics of the bond of reinforcement, but are not deemed suitable for the analysis of RC structures because they are computationally very demanding. Furthermore, they may not necessarily yield more reliable results because of the uncertainties related to the bar surface deformation, friction, and adhesion, and the various simplifying assumptions used in the constitutive models for concrete, which may not allow a precise simulation of the localized failure mechanism.

2.3.2 *Bar-scale* models

Bar-scale models express the force transfer between the reinforcement and the concrete in terms of the average stresses and relative displacements along an interface parallel to the longitudinal axis of the bar, as shown in Figure 2.18 and Figure 2.19. This modeling strategy is computationally more efficient than rib-scale models, and is appropriate for studying the effect of bond-slip on crack spacing in structural members or the required development and lap-splice lengths for reinforcing bars. The idealized interface has no ribs, and the relative displacements are assumed to occur between the bar surface and a layer of concrete not subjected to any of the inelastic phenomena induced by the local action of the ribs: crushing, shearing, and transverse cracking. The term bar

slip is usually considered as the relative tangential displacement defined under these terms. The bond forces acting between two consecutive ribs (due to the adhesion and friction forces at the steel surface, and bearing forces at the rib) are homogenized as a tangential (bond) stress and a normal stress at this idealized interface. Coupling between the tangential and normal components of stresses and displacements due to the wedging action of the ribs can also be considered in an approximate fashion.

When studying the interaction between the reinforcement and the concrete, most of the interest is focused on the bond stress and the slip of a bar. For this reason, a number of models have been proposed to relate the bond stress and the slip, but ignoring the interaction between the normal and tangential directions. The bond stress-vs.-slip relations provided by these models are only valid for specific levels of confinement and failure modes. More advanced models have been proposed to account for the coupling between the tangential and normal stresses and displacements by incorporating the shear dilatation of the interface. These models have the capability of predicting different failure modes and providing appropriate bond stress-vs.-slip relations for different levels of confinement. Examples of these two types of models are described below.

Bond stress-vs.-slip models

Most of the models proposed for the bond stress-vs.-slip relations are limited to relatively well-confined conditions for which bar pullout failure is expected. Typically, they are phenomenological models, in which the bond stress is defined as a nonlinear function of the monotonically increasing slip. The resulting function is scaled to the bond strength, which is related to the compressive strength of concrete empirically. The first model of this type was proposed by Rehm (1961), while the most widely used is that proposed by Eligehausen et al. (1983), which is shown in Figure 2.20, based on extensive experimental data obtained from No. 8 bars. Some models of this type have factors that modify the bond stress to account for the axial strain in the reinforcement (Shima et al. 1989a, Fernandez Ruiz et al. 2007, Lowes et al. 2004), or to account for the confining pressure (Lowes et al. 2004).

Some of these models can also predict the bond stress-slip relation under severe cyclic slip demands. In Eligehausen et al.’s model, the monotonic bond stress-slip

relation is reduced at each slip reversal using a damage parameter that depends on the energy dissipated by bond-slip. In addition, unloading and reloading rules are defined. Other models have been proposed based on similar concepts but with different improvements. The main variation in these models is the way the monotonic envelope is scaled to account for cyclic bond deterioration. The scaling factor proposed by Lowes et al. (2004) depends on the maximum slip and the number of cycles. Pochanart and Harmon (1989) and Yankelevski et al. (1992) have proposed to scale the bearing and friction contributions to the total bond resistance independently based on the maximum slip and the number of load cycles.

The local bond stress-vs.-slip relation can be viewed as a constitutive model for the bond behavior of reinforcing bars. Combining such a model with material models for steel and concrete, and applying the necessary equilibrium and kinematic conditions, one can derive a governing differential equation for the bond-slip behavior of a bar embedded in concrete. Closed-form solutions have been found for simple bond stress-vs.-slip relations (Raynor 2000), but, in general, numerical methods are required to solve such problems. Ciampi et al. (1982) have solved the differential equation based on the bond-slip law proposed by Eligehausen et al. (1983) using a finite difference scheme to study the behavior of an anchored bar that is being pulled and pushed at one of its ends (see Figure 2.21). Filippou et al. (1983) have proposed a weighted residual method to study the same problem using different shape functions to approximate the displacement and stress fields in the bar. Monti et al. (1997) have found it to be more advantageous to approximate the bond and bar stress fields, and have proposed a flexibility-based finite element formulation to solve this problem. Other researchers have opted to incorporate local bond-slip laws in interface elements to connect steel and concrete elements in general-purpose finite element programs. Lowes (2004) has formulated a four-node zero-thickness bond-slip element to be used for two-dimensional finite element modeling of reinforced concrete structures (see Figure 2.22). The model is defined by a normalized bond stress-vs.-slip relation and a relationship between the maximum bond strength and the concrete confining pressure, the concrete damage state, and the steel strain in the vicinity of the concrete-steel interface. A nonlocal modeling technique has been used to

relate the bond strength to the steel strain and concrete damage attained in the surrounding elements. Santos and Henriques (2012) have implemented the bond stress-vs.-slip law proposed in Model Code 2010 (fib 2012) in an orthotropic four-node plane stress element to model the steel-concrete interface using the commercial finite element program DIANA.

Dilatant interface formulations

In these models, the wedging action between the ribs of a bar and the concrete can be captured in terms of the shear dilatation of the interface. Dilatant interface formulations have been proposed to model the bond-slip behavior of deformed bars by Herrmann and Cox (1994), Cox and Herrmann (1998, 1999), Lundgren and Magnusson (2001), and Serpieri and Alfano (2011).

Herrmann and Cox (1994) and Cox and Herrmann (1998) have used an elasto-plastic formulation with a non-associative flow rule to control shear dilatation. The evolution of the yield surface and the flow rule is shown in Figure 2.23. It is based on the experimental data obtained by Malvar (1992). The model requires the calibration of a few physical properties and shows acceptable accuracy as compared to experimental results corresponding to different levels of confinement obtained from different studies. Tests with monotonically increasing slip and pull-out failures have been used to validate the model (Cox and Herrmann 1999). In Herrmann and Cox (1994), an extension of this model was proposed for cyclic loading using ad-hoc reloading rules.

A similar plasticity model has been proposed by Lundgren and Magnusson (2001) for monotonic loading. In this model, a Mohr-Coulomb yield criterion with a non-associated flow rule is used to represent the frictional behavior at the interface, and a second yield surface with associated plasticity is used as a cap for pull-out failure, as shown in Figure 2.24. Lundgren (2005) has extended the model to account for cyclic behavior using ad-hoc reloading rules. The model has been successful in reproducing experimental results from a limited number of monotonic and cyclic tests.

The formulation proposed by Serpieri and Alfano (2011) represents the periodic geometry of the steel-concrete interface by three planes with different inclinations, as shown in Figure 2.25. The interaction within each of these surfaces is governed by a

damage-friction interface formulation modeling adhesion and friction. The dilatation and wedging mechanism are obtained as a result of the prescribed surface geometry. The model is capable of qualitatively reproducing the bond stress-vs.-slip behaviors under monotonic and cyclic loading. However, the concrete crushing mechanism that dominates the pull-out failure of a bar is not simulated. The model has shown reasonably good agreement with results from a monotonic pull-out test. No attempt has been made to validate the model with experimental data from cyclic tests.

2.3.3 *Member-scale* models

Several researchers have proposed special beam-column elements or used simple macro-models that inherently account for the bond-slip behavior without the explicit definition of steel-concrete interfaces. This type of models is useful in the analysis of large structures.

Monti and Spacone (2000) have proposed a force-based fiber-section beam-column element that accounts for slip between the longitudinal reinforcement and the concrete. In this element, a bar model with bond-slip proposed by Monti et al. (1997) is introduced into the force-based fiber-section element developed by Spacone et al. (1996). The beam section is assumed to remain plane, but the steel fiber strains are computed as the sum of two contributions: the bar strain and anchorage slip. A similar model has been proposed by Ayoub (2006) based on a two-field mixed formulation with independent approximations of forces and displacements.

Simple macro models have been proposed to simulate the end rotation of RC beams and columns due to the slip of the reinforcement anchored in connected members. In these models, bars are assumed to be well-anchored and bar slip is entirely due to strain penetration in the anchorage zone. Sritharan et al. (2000) have proposed the use of a set of springs in finite element analysis to represent the opening of a joint due to bar slip. Tension springs are used to represent bar elongation due to strain penetration in the anchorage zone and compression springs are used to represent the contact between concrete surfaces. Based on experimental data, Zhao and Sritharan (2007) have proposed a law to relate the bar stress and bar slip at the end of the anchorage in a footing-column

or beam-column connection. This law has been used as a constitutive relation for the steel fibers in a zero-length fiber-section element to simulate the end rotation of an RC column represented by a fiber-section beam-column element, as shown in Figure 2.26. Berry and Eberhard (2007) have used the same modeling strategy, but they have obtained the bar stress-vs.-slip law analytically based on a simple bond stress-vs.-slip relation.

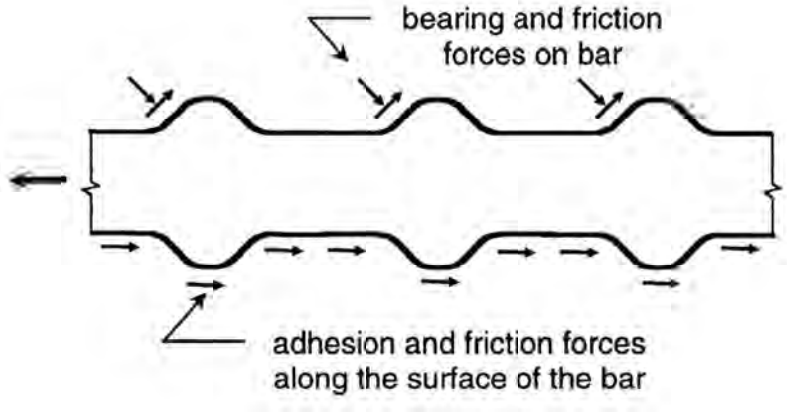

Figure 2.1: Mechanisms of bond resistance (ACI 2003)

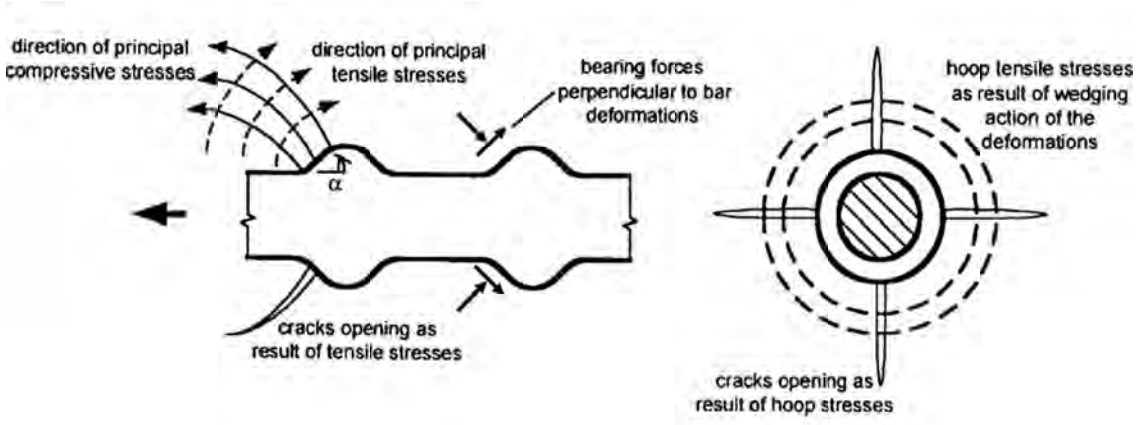

Figure 2.2: Cracks introduced by bond slip (ACI 2003)

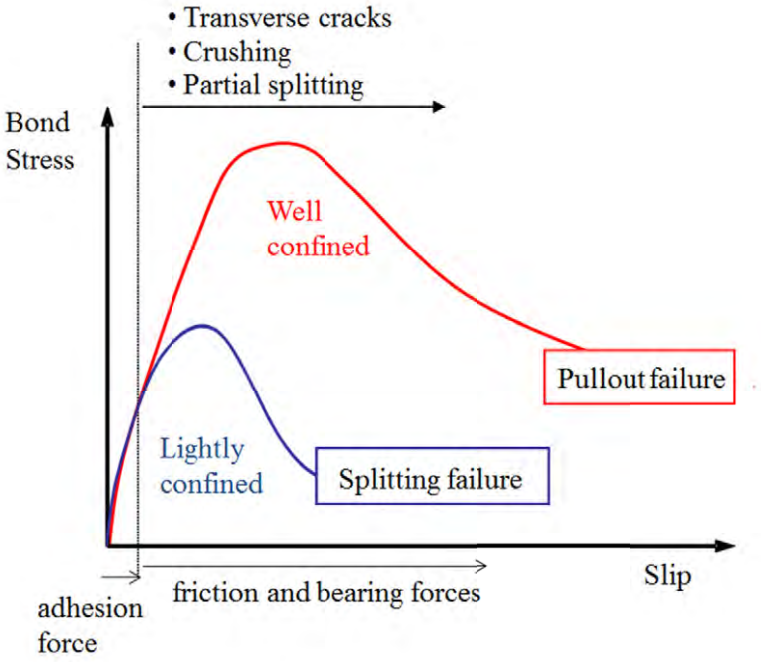

Figure 2.3: Bond stress vs. slip for different confinement conditions

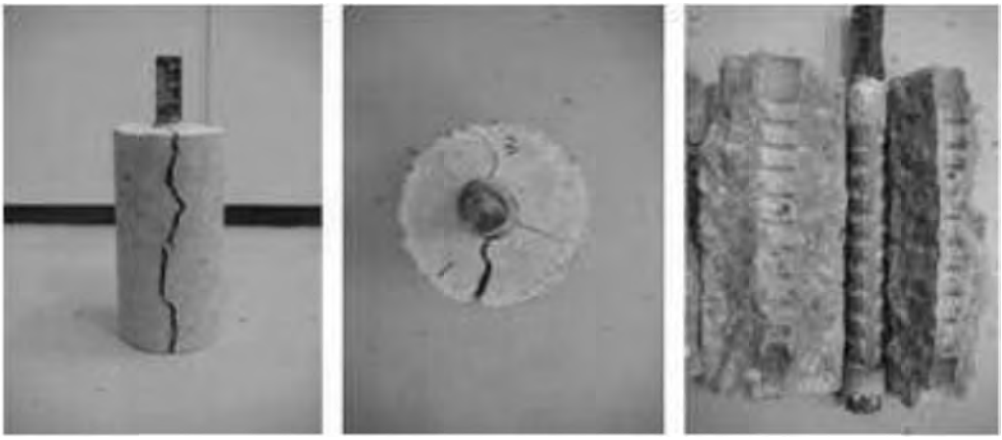

Figure 2.4: Bond failure by splitting of concrete (Choi et al. 2011)

Figure 2.5: Crushing and shearing of concrete between ribs in a bar pull-out failure

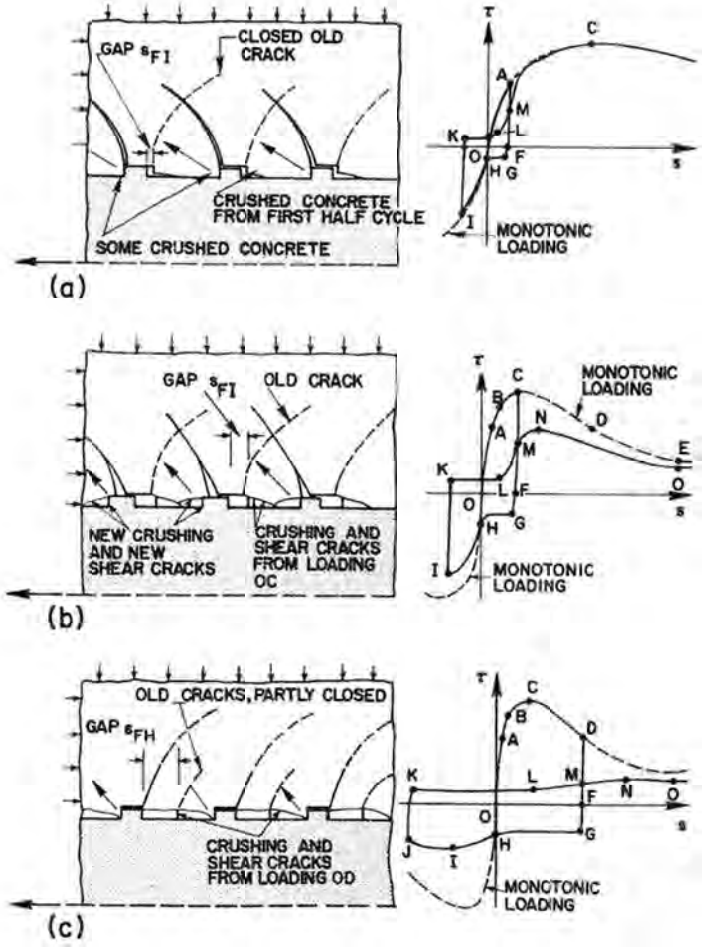

Figure 2.6: Cyclic bond-slip behavior in pull-out failures (Eligehausen et al. 1983)

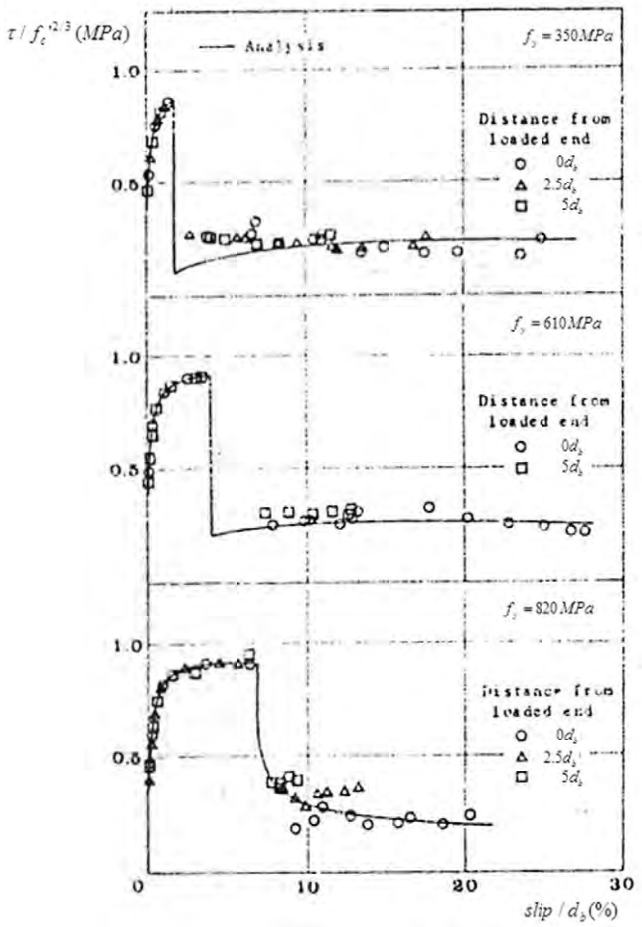

Figure 2.7: Bond-slip relations obtained by Shima et al. (1987b) for bars yielding in tension

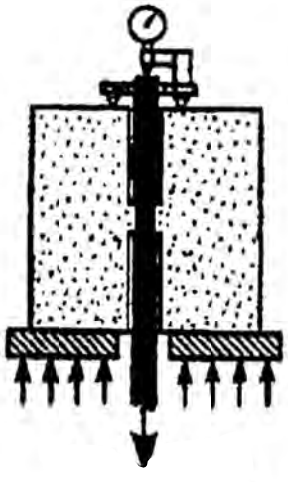

Figure 2.8: Bond-slip test specimen and setup used by Rehm (1961)

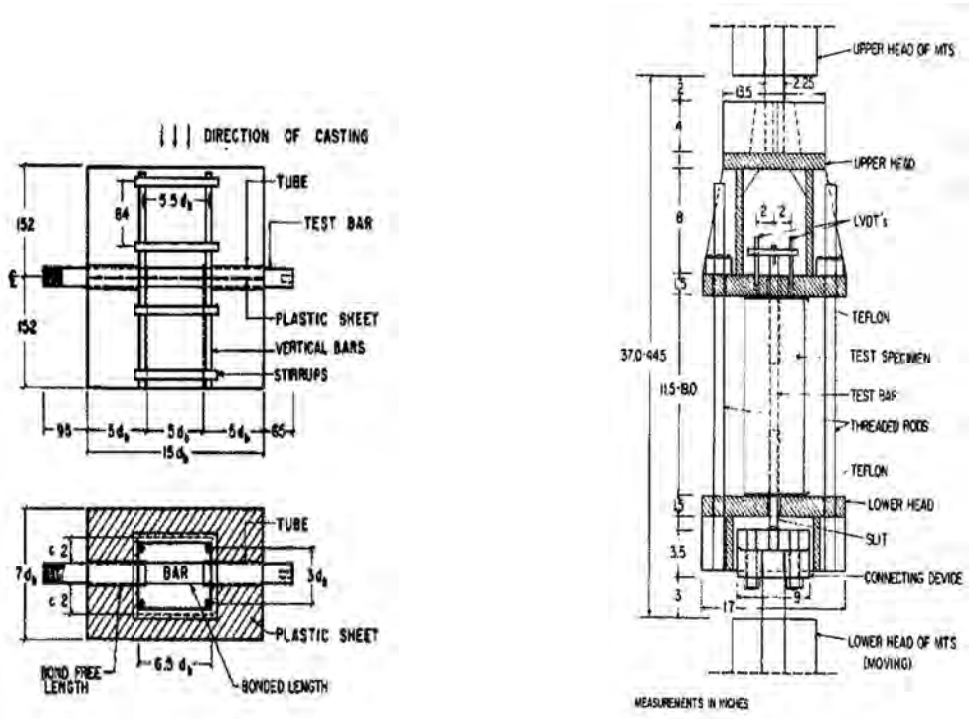

(a) Specimen (b) Setup

Figure 2.9: Bond-slip test specimen and setup used by Eligehausen et al. (1983)

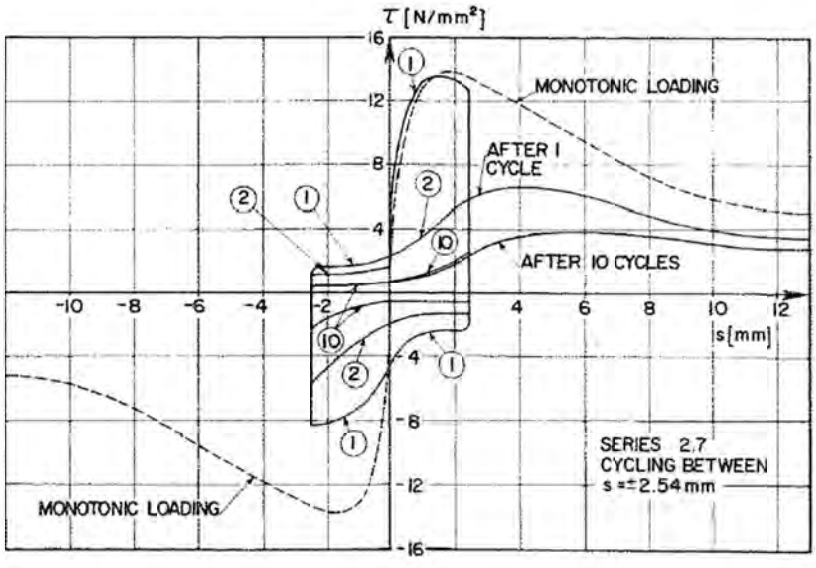

Figure 2.10: Cyclic bond stress-vs.-slip relations obtained by Eligehausen et al. (1983)

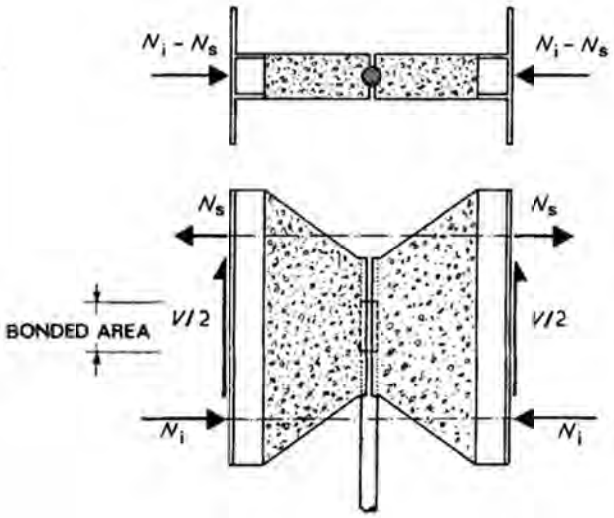

Figure 2.11: Bond-slip test specimen with different crack openings used by Gambarova et al. (1989)

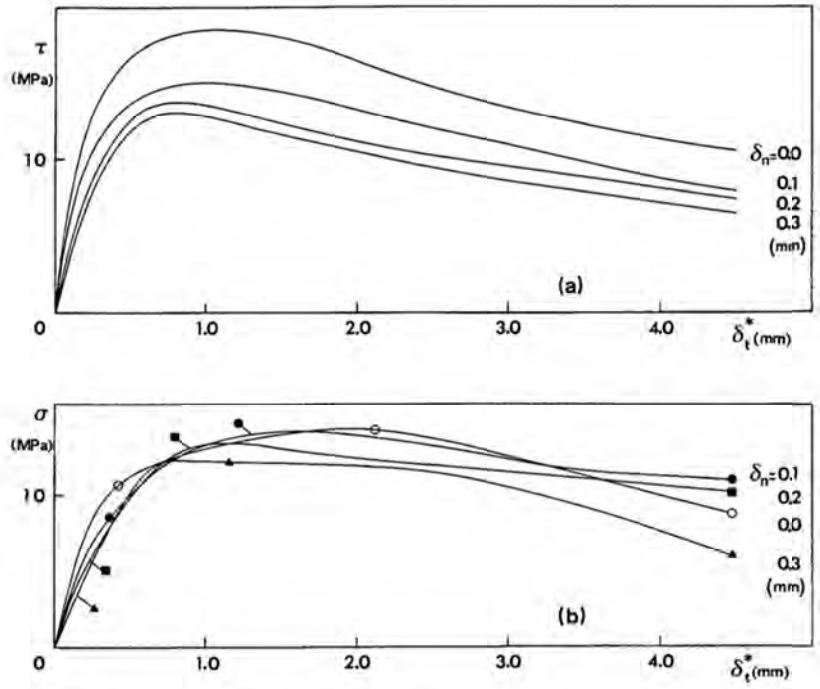

Figure 2.12: Bond stress-vs.-slip and confining stress-vs.-slip relations for different crack openings obtained by Gambarova et al. (1989)

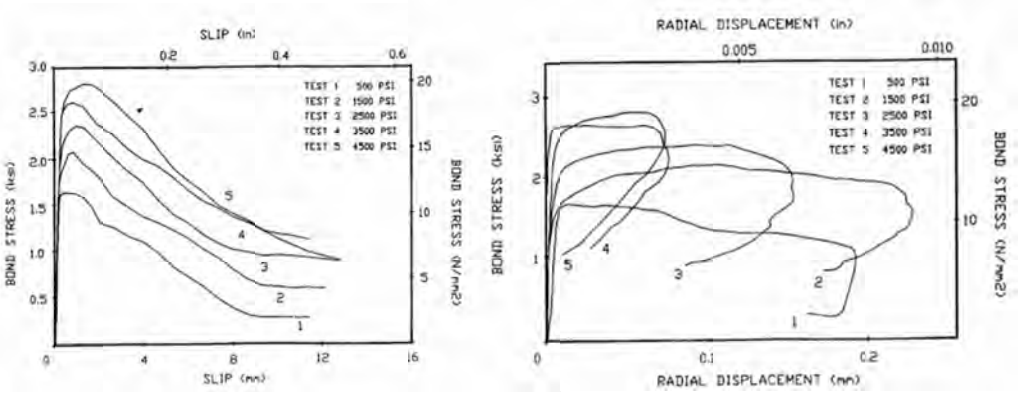

Figure 2.13: Bond stress-vs.-slip and bond stress-vs.-radial displacement relations obtained by Malvar (1992)

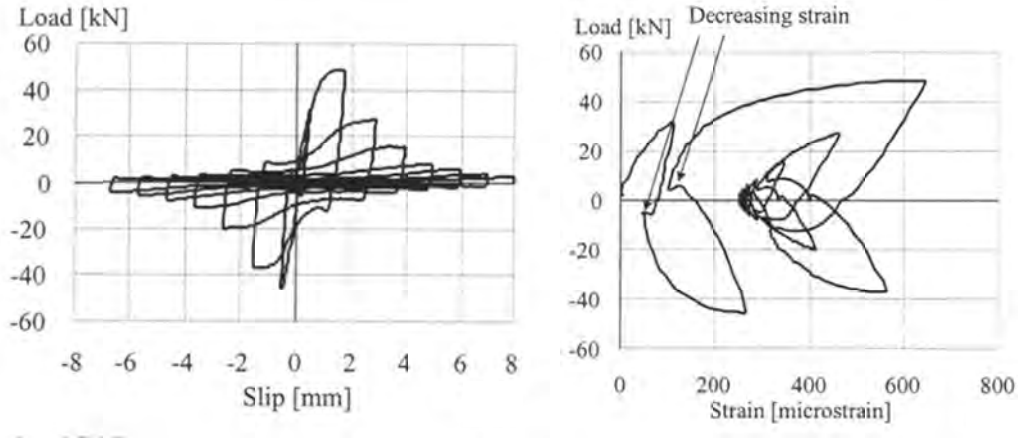

Figure 2.14: Load-vs.-slip and load-vs.- bar strain relations obtained by Lundgren (2000)

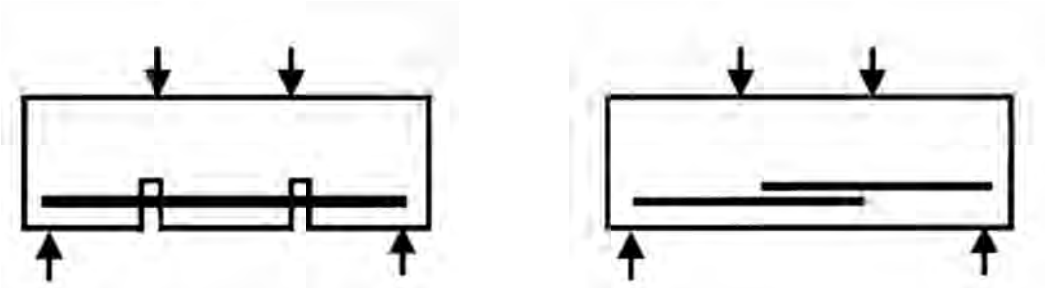

(a) Development tests (b) Lap splice tests

Figure 2.15: Sketch of typical development and lap-splice tests (ACI 2003)

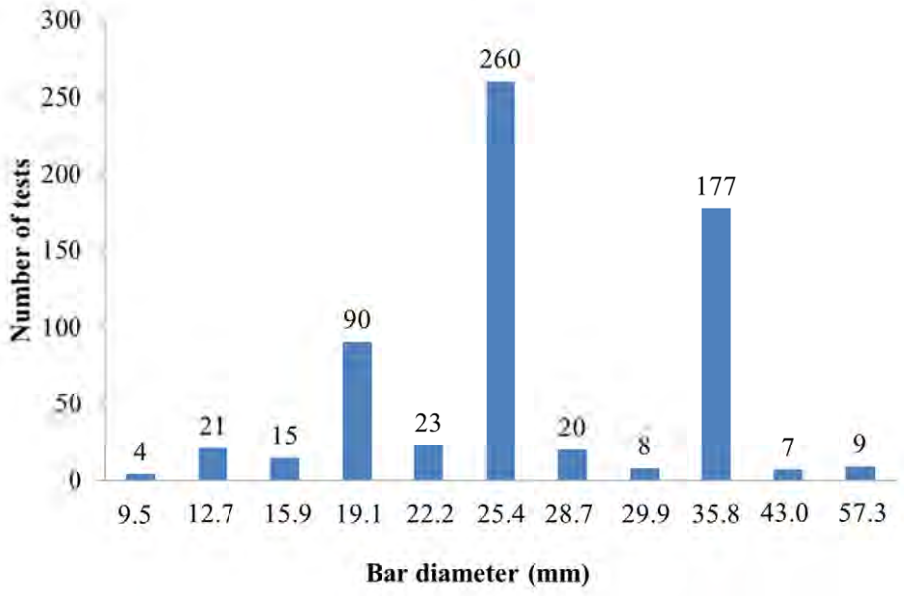

Figure 2.16: Experimental database of ACI 408 Committee

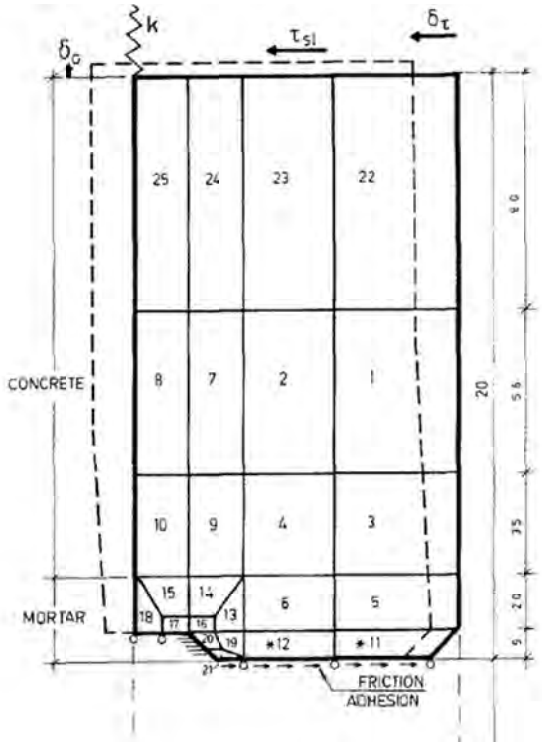

Figure 2.17: Finite element model used by Reinhardt et al. (1984a) to study the bond-slip behavior of bars

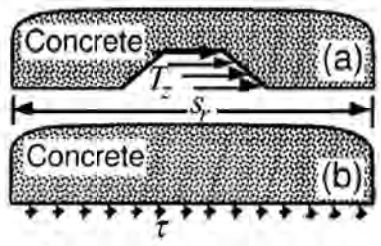

Figure 2.18: (a) Actual vs. (b) Idealized force transfer (Cox and Herrmann 1998)

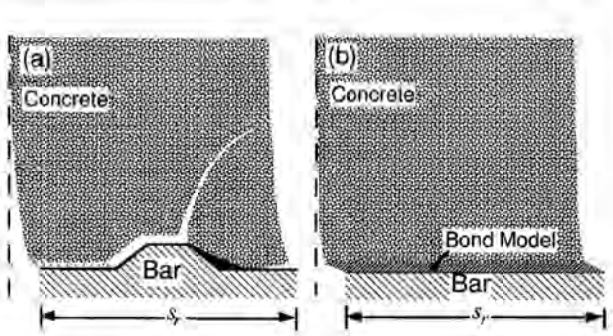

Figure 2.19: (a) Actual vs. (b) Idealized deformations in the contact zone (Cox and Herrmann 1998)

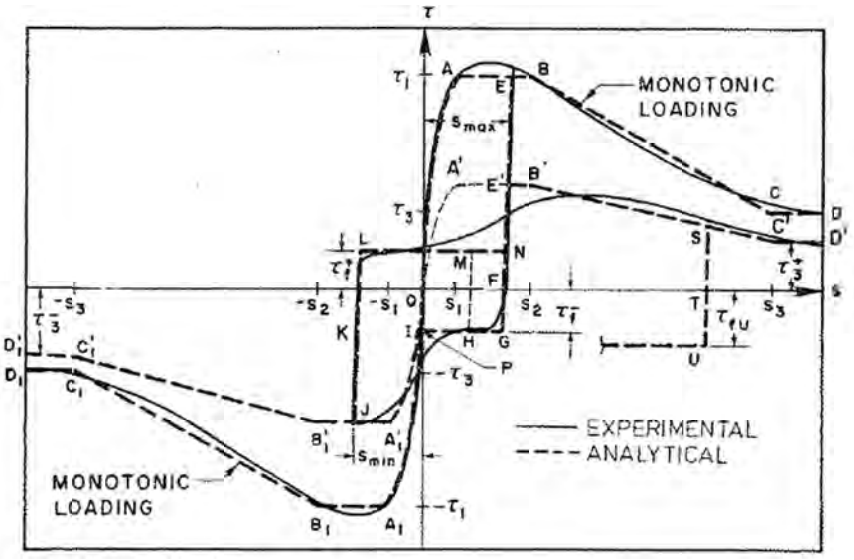

Figure 2.20: Analytical bond stress-vs.-slip model proposed by Eligehausen et al. (1983)

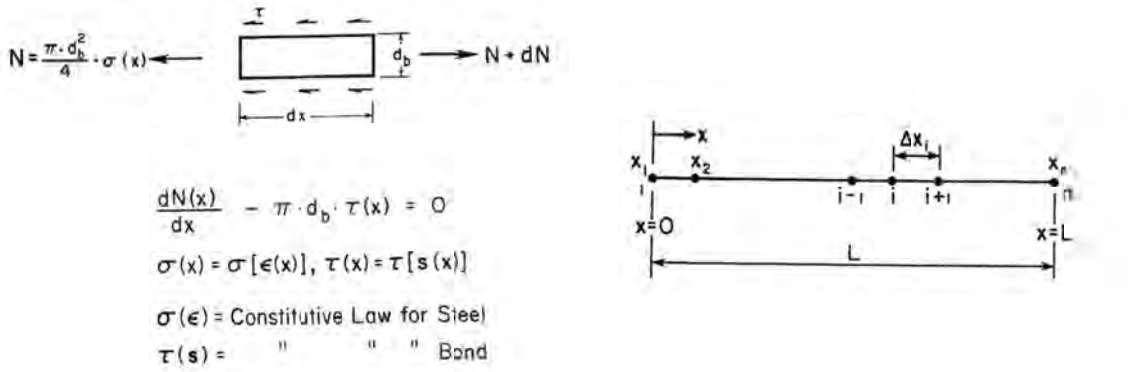

Figure 2.21: Differential equation describing bond slip and finite difference discretization of a bar (Ciampi et al. 1982)

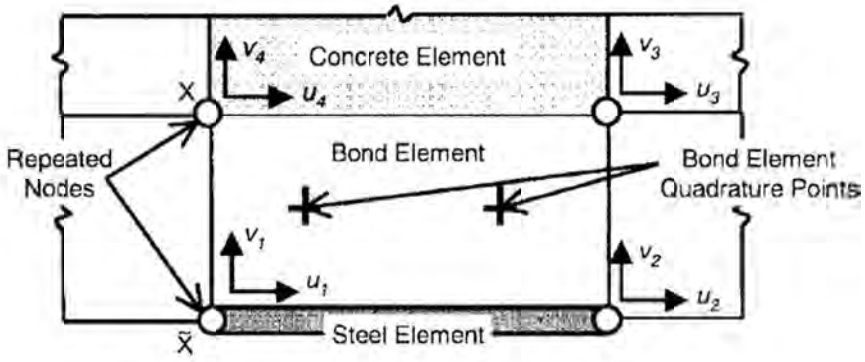

Figure 2.22: Bond-slip element by Lowes et al. (2004)

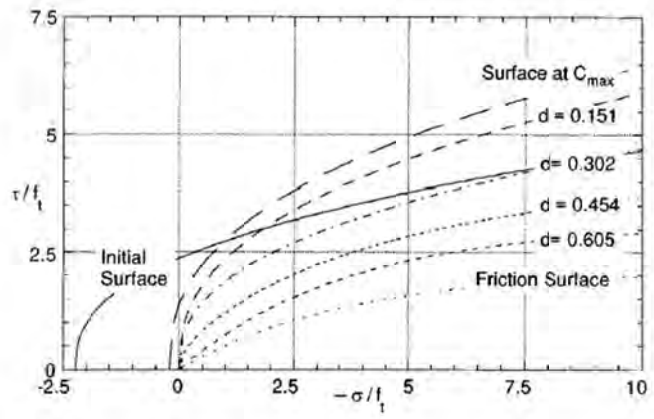

Figure 2.23: Yield surface evolution for the bond-slip model of Cox and Herrmann (1998)

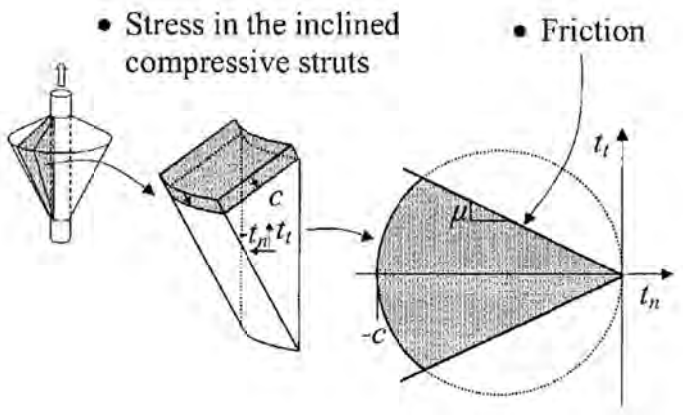

Figure 2.24: Yield surfaces for the bond-slip model of Lundgren and Magnusson (2001)

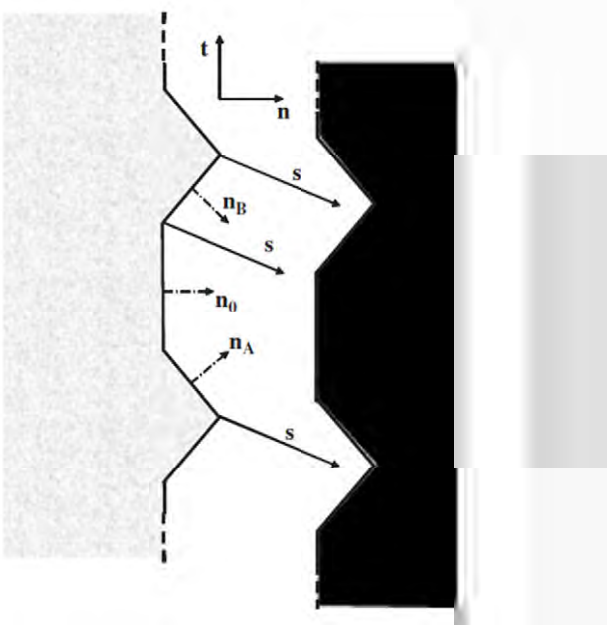

Figure 2.25: Surface geometry assumed in the interface element of Serpieri and Alfano (2011)

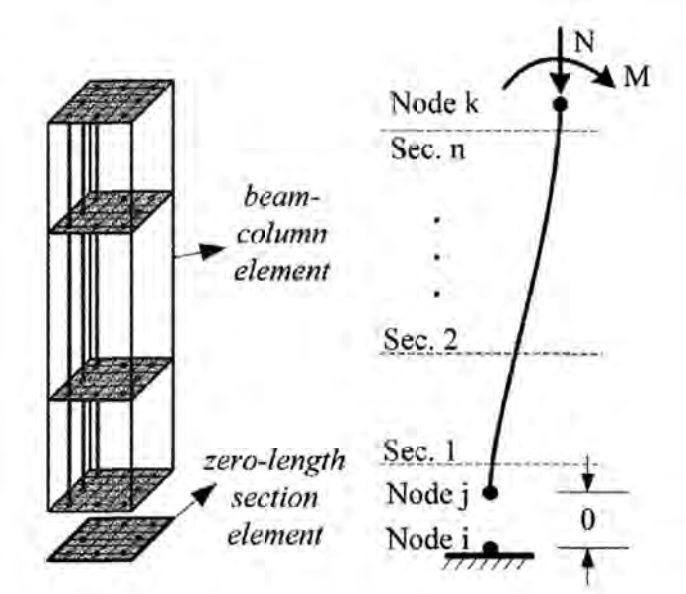

Figure 2.26: Zero-length element proposed by Zhao and Sritharan (2007)

CHAPTER 3

EXPERIMENTAL STUDY ON THE BOND-SLIP BEHAVIOR OF LARGE-DIAMETER BARS IN WELL-CONFINED CONCRETE

This chapter presents an experimental study on the bond strength and cyclic bond deterioration of large-diameter reinforcing bars embedded in well-confined concrete. For large RC components, such as large bridge columns and piles, the use of reinforcing bars with diameters greater than 25 mm (No. 8) is common. However, data on the bond strength and bond-slip behavior of large-diameter bars is scarce. Because of the lack of experimental data, the development length requirements in ACI 318-08 (ACI 2008) and the AASHTO LRFD Bridge Design Specifications (AASHTO 2010) are largely based on experimental data obtained from No. 11 (36-mm) and smaller bars, and these codes do not allow lap-splicing of bars larger than No. 11.

Recently, pull-out and lap-splice tests were conducted on large-diameter bars by Ichinose et al. (2004), Plizzari and Mettelli (2009), and Steuck et al. (2009), as discussed in Chapter 2. However, all these tests were conducted by subjecting bars to monotonically increasing slip. No tests were reported on the cyclic bond-slip behavior of large-diameter bars. It was not certain that data on the cyclic bond-slip behavior of No. 8 bars obtained by Eligehausen et al. (1983) would be applicable to larger bars.

This chapter presents the monotonic pull-out and cyclic pull-pull tests that were conducted on No. 11, 14, and 18 (36, 43, and 57-mm diameter) bars to obtain the bond strengths and cyclic bond stress-slip relations of these bars. The confinement level

considered in the tests is representative of that used in Type II shafts designed according to the Caltrans Bridge Design Specifications (Caltrans 2008) and Seismic Design Criteria (Caltrans 2010). Based on these tests and on studies carried out by others, the effects of the bar diameter, concrete strength, pull direction (for a vertically cast bar), and loading history on the bond strength are determined.

3.1 Test program, specimen design, test setup, and instrumentation

Four series of pull-out tests were conducted on large-diameter reinforcing bars embedded in well-confined concrete. Three of them were conducted to study the bond-slip behavior of No. 11, 14, and 18 bars under different loading histories, and the fourth was conducted to study the influence of the compressive strength of concrete on the bond strength. A total of 22 specimens were tested, of which 8 were subjected to a monotonically increasing slip and 14 to cyclic loading. The specimen properties, type of loading, and the bond strengths obtained are summarized in Table 3.1. These tests were conducted to identify the fundamental bond stress-vs.-slip relation of a bar. In all the tests, bond failure was governed by the pull-out of the bars from the concrete rather than concrete splitting.

The design of a typical specimen and the test setup are shown in Figure 3.1. Each specimen consisted of a reinforcing bar embedded in a 914-mm (3-ft) diameter concrete cylinder that had a height 15 times the nominal bar diameter, d_b. The bar was bonded only in the mid-height region of the concrete cylinder over a length of $5d_b$, and PVC tubes were used to create unbonded regions of $5d_b$ in length on each end of the bonded zone to minimize any local disturbance to the bond stress that could be caused by the load application. This short embedment length was intended to provide a fairly uniform bond stress distribution and to prevent the yielding of the steel so that the fundamental bond stress-vs.-slip relation could be obtained.

Bars with a specified yield strength of 414 MPa (60 ksi) were used. The No. 11, 14, and 18 bars had relative rib areas (ratio of the projected rib area normal to the bar axis to the bar surface area between the ribs) ranging from 0.068 to 0.095. The geometric

properties of the bars are summarized in Table 3.2. Each end of a bar had a T-headed anchor, which provided a reaction for the application of the pulling force during a test.

The diameter of the cylinder and the quantity of the spiral reinforcement were selected to mimic the concrete cover and confinement level for the vertical reinforcing bars extending from a bridge column into an enlarged pile shaft designed according to the Caltrans Bridge Design Specifications (Caltrans 2008) and the AASHTO LRFD Bridge Design Specifications (AASHTO 2010). The concrete cylinder was confined with No. 4 (13-mm) spiral reinforcement having a pitch of 61 mm (2.4 in.) on center and an outer diameter of 813 mm (32 in.). This resulted in a confinement volumetric ratio of 1%.

Two concrete mixes with different compressive strengths were used. Series 1 through 3 tests had a concrete with a targeted compressive strength of 34.5MPa (5 ksi), maximum aggregate size of 9.5 mm (3/8 in.), water-to-cement ratio of 0.45, and specified slump of 178 mm (7 in.). Series 4 had a concrete with a targeted compressive strength of 55 MPa (8 ksi), maximum aggregate size of 12.7 mm (0.5 in.), water-to-cement ratio of 0.32, and slump of 203 mm (8 in.). The aggregate size and high slump used in these two mixes represent what is typically used for CIDH (Cast-In-Drilled-Hole) piles. All specimens in each series were fabricated with the construction sequence shown in Figure 3.2. They were cast together in an upright position. The test numbering in Table 3.1 reflects the order in which the specimens were tested. The tests started on a day when the concrete strength was close to the targeted value. Setting up a test, testing, and dismantling took one to two days per specimen. The compressive and tensile splitting strengths of the concrete on the first and last days of testing for each test series are shown in Table 3.1.

The test setup is shown in Figure 3.1b. This setup was designed to allow the bar to be pulled upward or downward using center-hole hydraulic jacks that were positioned one at each end of the bar. The bar was pulled out from the concrete cylinder when one of the hydraulic jacks pushed against the adjacent anchor head while the other jack was de-pressurized to allow the opposite end of the bar to move freely. To reverse the pull direction, the jack initially pushing against the anchor head was de-pressurized before the other jack started to push against the anchor head at the opposite end. This was a self-

reacting system; thus, the concrete was subjected to compression when the bar was being pulled out.

3.2 Instrumentation and loading protocol

A load cell was placed between a hydraulic jack and the adjacent bearing head to measure the pull-out force during the test. Two strain gages were attached on the opposite sides of the bar right outside the bonded region at each end to measure the bar deformation, as shown in Figure 3.1a. In Series 3, four strain gages were attached on the opposite sides of the spiral with two at each elevation to monitor the strain that could be introduced by the dilatation of the concrete during bar slip. Bar slip was measured with two linear potentiometers mounted at each end on the opposite sides of the bar, as shown in Figure 3.1b. Each pair of potentiometers measured the displacement of the attachment point on the bar with respect to the bearing head. A picture of one of the specimens and the test setup is shown in Figure 3.3.

For all but one specimens that were tested with a monotonically increasing slip, the bar was pulled upward. Several load histories were used for the cyclic tests, with variables including the increment size of the slip amplitude in each loading cycle, the number of cycles per amplitude, and the type of cyclic reversals. Two types of cyclic reversals were considered: (a) full cycles with the same slip amplitudes in both directions for each cycle; and (b) half cycles with slips mainly in one direction and slightly passing the origin in the other. In most of the tests, only a single cycle was applied for each slip amplitude. However, in two tests, each amplitude had two cycles. The type of loading protocol used for each specimen is given in Table 3.1.

3.3 Monotonic test results

The local bond stress (τ) - slip (s) relations have been obtained as the average bond stress vs. the average of the slips at the two ends of the bonded zone. The average bond stress was calculated by dividing the pull-out force, F, by the nominal contact area between the bar and the concrete as shown in the following equation.

$$\tau = \frac{F}{\pi d_b l_e} \tag{3.1}$$

in which l_e is the bonded length of the bar.

The slip at each end was calculated as the average of the slips measured by the pair of linear potentiometers. At the loaded end, the bar elongation between the attachment point of the linear potentiometers and the end of the bonded zone was subtracted from the potentiometer reading to get the actual slip. The bar elongation was calculated from strain gage readings. Figure 3.4 shows the pull force vs. the slips at the loaded and unloaded ends, and the average slip for one of the monotonic tests. Based on the small differences in bar slips observed at the two ends, the average values provide a good approximation of the local bond stress-slip relations.

The bond stress-slip relations obtained from monotonic pull-out tests in Series 1 to 3, which had concrete strengths around 34.5 MPa (5 ksi), are plotted in Figure 3.5. For comparison, the curve obtained by Eligehausen et al. (1983) for a No. 8 (25-mm) bar and 30-MPa (4.35-ksi) concrete is also included in Figure 3.5. All the bond stress-slip curves show similar patterns. The slip at the peak strength was around 1.8 mm (0.07 in.) for the No. 8 bar, and around 3.0 mm (0.12 in.) for the No. 11, 14, and 18 bars. With increasing slip, the bond resistance dropped and tended to stabilize at a residual value that was approximately 20-30% of the peak resistance. Eligehausen et al. (1983) pointed out that a practically constant residual resistance was achieved when the value of the slip was approximately equal to the clear rib spacing of the bar, s_R. This can be explained by the total damage of the concrete between the ribs. Beyond this point, the resistance to slip was provided solely by friction. Figure 3.5 and the s_R values given in Table 3.2 confirm this observation for the large-diameter bars. However, the transition between the peak and the residual resistance seems to be more gradual for large-diameter bars as compared to the No. 8 bars tested by Eligehausen et al. (1983).

The bond strengths, τ_u, obtained from the tests are summarized in Table 3.1. Results from Test Series 1 through 3 show that τ_u increases slightly with the increase of the bar diameter. It is15.2 MPa (2.2 ksi) for No. 11 bars and has an average value of 17.6

MPa (2.55 ksi) for No. 18 bars. The tests conducted by Eligehausen et al. (1983) on No. 8 bars showed an average bond strength of 13.8 MPa (2.0 ksi). However, a direct comparison cannot be made for the two test programs because Eligehausen et al.'s tests had a lower concrete compressive strength and a lower level of confinement. Furthermore, as Figure 3.5 shows, the bond strength obtained for a No. 11 bar that was pulled downward (Test 2 in Series 1) was 20% lower than that for a bar that was pulled upward (Test 1 in Series 1). For the bar that was pulled downward, the initial stiffness was also reduced and the peak strength was reached at a slightly higher slip of 4.6 mm (0.18 in.).

Results from Series 4 tests on No. 14 bars with 55-MPa (8-ksi) concrete have shown a 45% increase of the average bond strength as compared to that obtained from Series 2, which had the same bar size but 34.5-MPa (5-ksi) concrete. Owing to the high bond strengths developed in Series 4, the bars subjected to a monotonically increasing load (Tests 1 and 2) yielded at the pulled end. As shown in Figure 3.6, the difference in slips at the loaded and unloaded ends of the bonded region was very large once the bar yielded at the loaded end, which implies that yielding penetrated to some extent into the bonded region. As a result, the slip and the bond stress distribution cannot be assumed uniform and meaningful bond stress-slip curves cannot be obtained from the test data. As mentioned in Chapter 2, studies have shown that bond resistance could be reduced in regions where a bar yielded. Hence, the bond strength for the bars would have been higher than the average strength calculated from the results of this test series if the bars had not yielded. However, this influence does not appear to be significant because the ratio of the average bond strength obtained from these two tests to that obtained from the cyclic tests (Test 3 and 4 of Series 4), in which the bars did not yield, is comparable to the strength ratios obtained for the other test series.

The strain gages placed in the confining spirals registered small tensile strains (with the maximum being $2 \cdot 10^{-5}$), as shown in Figure 3.7. The tension in the spirals indicates that the concrete expanded slightly in the lateral direction as the bar was being pulled out. This can be explained in part by the dilatation caused by the wedging action of the bar ribs when the bar slipped. Another cause is the Poisson effect induced by the

vertical compressive force exerted on the concrete cylinder as the bar was pulled. Figure 3.7 also shows the estimated strain due to the Poisson effect. The small strain readings indicate that the lateral dilatation of the concrete cylinder induced by bar slip is negligible. This is because a very good confinement was provided by the large concrete cover.

3.4 Cyclic test results

The bond stress-slip relations obtained from the cyclic tests are presented and compared to the monotonic test results in Figure 3.8 through Figure 3.14. The hysteresis curves from the tests show a consistent trend. Upon the reversal of the slip direction, a small resistance immediately developed in the other direction. This resistance started to increase when the slip approached the previously attained maximum slip. After this point, the resistance followed a curve similar in shape to the monotonic bond stress-slip curve. However, the stress level attained by this new curve is lower than that by the monotonic bond stress-slip curve due to bond deterioration induced by cyclic slip reversals. In addition, the absolute value of the slip at which the peak stress developed in each cycle increased as the cumulative slip increased.

The maximum bond resistance obtained from a cyclic test is between 75% and 95% of that obtained from a monotonic load test, as shown in Table 3.1. The residual bond resistance diminishes to almost zero after severe cyclic slip reversals, as shown in Figure 3.8 through Figure 3.14. Moreover, the results presented in Figure 3.9 and Figure 3.10 indicate that full cycles induced a more severe deterioration of the bond resistance than half cycles. Likewise, Figure 3.11 and Figure 3.14 show that a second cycle of the same slip amplitude produced an additional reduction of the bond stress. Overall, the observed hysteretic bond stress-slip relation for large diameter bars is similar to that obtained by Eligehausen et al. (1983) for No. 8 bars.

Figure 3.15 shows the tensile strain registered in the confining spirals during one of the cyclic tests, and the estimated contribution of the Poisson effect to this strain. The magnitude of the strain is small and is comparable to that obtained from the monotonic tests.

3.5 Discussion on factors affecting bond strength

The tests presented here have provided useful information on the influence of the compressive strength of concrete, bar size, pull direction (for a vertically cast bar), and slip history on the bond strength. A review of previous findings in the literature related to these effects has been presented in Chapter 2. The observations made here and by others are compared, and these effects are analyzed and quantified based on the test results and the additional data available in the literature.

3.5.1 Effect of compressive strength of concrete

The tests presented in this chapter have shown that the compressive strength of concrete, f_c' , has an important effect on the bond strength. These tests have shown that the bond strength was increased by about 45% when 55-MPa (8-ksi) concrete was used instead of 34.5-MPa (5-ksi) concrete. This implies that the bond strength is more or less proportional to $f_c'^{3/4}$, although it is possible that this effect could be slightly under-estimated here because, as mentioned in Section 3.3, the bond strength calculated for the 8-ksi (55-MPa) concrete could be influenced by the yielding of the bars. In any case, this effect is stronger than what has been reported by Eligehausen et al. (1983) and what is assumed in most codes, which suggest that the bond strength is proportional to $f_c'^{1/2}$.

As mentioned in Chapter 2, the relation between the compressive strength of concrete and the bond strength can be influenced by the level of the confinement, as indicated by empirical equations proposed by Zuo and Darwin (2000) to calculate the strength of lap splices. The level of confinement in the tests presented here is higher than that used by Eligehausen et al. (1983). Therefore, it can be expected that the influence of the compressive strength of concrete on the bond strength should be higher here. This difference can be explained by the failure mechanisms associated with different levels of confinement. For low levels of confinement, bond failure is caused by the splitting of the concrete surrounding the bar, and the bond strength is, thereby, governed by the tensile strength of the concrete, which tends to be proportional to $f_c'^{1/2}$ (ACI 2003). For high

levels of confinement, bond failure is caused by the pull-out of the bar associated with the crushing of the concrete in front of the ribs, and, therefore, the bond strength tends to be proportional to f_c' .

3.5.2 Effect of bar size

The test results show a slight increase of the bond strength with increasing bar size. The bond strength for No. 14 bars is approximately 7% higher than that for No. 11 bars, and that for No. 18 is about 8% higher than that for No. 14. However, the ACI 318-08 (2008) and AASHTO LRFD (2010) provisions for the development length imply that the bond strength is reduced with increasing bar size. As mentioned in Chapter 2, Ichinose et al. (2004) have shown that the influence of the bar size on the bond strength depends on the level of confinement. To interpret and compare results from different tests with different confinement levels, a factor used in ACI 318-08 (ACI 2008) to calculate the required development length of deformed bars in tension is used as a confinement index. This index, which is denoted as *CI* here, is expressed as $\left(c_b + 40A_{tr} / s_{tr} n\right)/ d_b$, in which c_b is the distance of the center of a bar to the nearest concrete surface, s_{tr} is the spacing of the transverse reinforcement, A_{tr} is the transverse reinforcement area within distance s_{tr}, and n is the number of bars being spliced or developed at the plane of splitting. According to ACI 318-08, when *CI* is less than 2.5, splitting failure is likely, and for values above 2.5, pull-out failure is expected. Some studies have shown that when the confinement level was low enough that bond failure was governed by concrete splitting, the bond strength would increase significantly with the decrease of the bar size (Ichinose et al. 2004, Plizzari and Mettelli 2009). The value of *CI* considered in these studies ranges from 2 to 5. For pull-out tests with *CI* between 5 and 16 (Ichinose et al. 2004, Steuck et al. 2009), splitting failure was prohibited and the effect of the bar size was negligible. The tests reported in this chapter had *CI* between 11 and 17. A small increase in the bond strength with the bar size observed here is consistent with the observation made by Ichinose et al. (2004) for tests with *CI* greater than 5.

An explanation for the aforementioned observations is that larger bars have larger ribs, which induce a more severe wedging action and, thereby, a larger concrete splitting stress as a bar slips. With little or no confinement, this would result in an earlier splitting failure. With a high confinement level, not only splitting failure would be prohibited but the dilatation effect induced by the wedging action of the ribs would induce a higher passive confinement pressure. An increase of the confining pressure would result in a higher bond stress, based on results shown by other studies, e.g., Malvar (1991). Nevertheless, in the studies of Eligehausen et al. (1983) and Viwathanatepa et al. (1979), even though the specimens were well confined and the bond failed by the pull-out of the bars, there was a slight increase of the bond strength for smaller bars. It should be noted that the specimens used by Eligehausen et al. (1983) and Viwinathapea et al. (1979) had *CI* between 3 and 13, and 9 and 14, respectively, which are on average a little lower than that considered in the present study and the study of Steuck et al. (2009), which had *CI* between 9 and 16.

3.5.3 Effect of pull direction

The influence of the pull direction on the bond strength was examined in the tests of No. 11 bars, which have shown a lower bond strength and bond stiffness when a bar was pulled downward instead of upward (see Table 3.1 and Figure 3.5). This is consistent with what has been observed in other studies as discussed in Chapter 2, and it is related to the different qualities of the concrete above and beneath the ribs for bars casted vertically. The concrete right beneath a bar rib can be weaker due to the accumulation of bleed water.

3.5.4 Effect of slip history

The experimental results presented here have confirmed the observation made by Eligehausen et al. (1983) that the peak bond strength was reduced when a prior load cycle went beyond 70% to 80% of the peak of the monotonic bond stress-slip curve, indicating the damage of the concrete between the bar ribs. In addition, these tests have also shown that the decay of the bond resistance depends on the pattern of the load cycles (e.g., with

slip in one direction mainly or with fully-reversed cyclic slip reversals), the cumulative slip, and the number of slip reversals. A law to express the bond resistance as a function of the slip and slip history is presented in Chapter 4.

3.6 Summary and conclusions

The bond strength and bond-slip behavior of large-diameter bars embedded in well-confined concrete have been examined. Monotonic pull-out tests and cyclic pull-pull tests were conducted on No. 11 (36-mm), 14 (43-mm), and 18 (57-mm) bars. All the specimens failed by the pull-out of the bars from the concrete. The large-diameter bars exhibited a bond stress-slip relation similar to that of No. 8 (25-mm) and smaller bars, including the bond deterioration behavior under monotonic and cyclic loads. These tests have also shown that the bond strength tends to increase slightly with increasing bar size, and that the compressive strength of concrete has a notable effect on the bond strength. The bond strength observed here is proportional to $f_c'^{3/4}$. Results from this and other studies have indicated that the influence of the concrete strength and bar size on the bond strength depends on the level of confinement in the concrete specimen. However, data on this are limited, and a systematic and comprehensive investigation of the effects of the bar size and concrete strength on the bond strength under a wide range of confinement levels is needed to further confirm this observation and arrive at more definitive conclusions. Finally, for a bar positioned vertically during casting, the bond strength is smaller when the bar slips downward than when it slips upward. This observation is consistent with other studies.

Table 3.1: Test matrix and specimen properties

Series no.	Test no.	Bar size	Concrete compressive strength[1] f_c' MPa (ksi)	Tensile splitting strength[1] f_{cs} MPa (ksi)	Loading history	Peak bond strength τ_u MPa (ksi)
1	1	No. 11	33.8-36.5 (4.9-5.3)	3.2-3.2 (0.46-0.46)	Monotonic up	15.2 (2.2)
	2				Monotonic down	12.4 (1.8)
	3				Half cycles	13.8 (2.0)
	4				Half cycles	14.5 (2.1)
	5				Half cycles	11.7 (1.7)
	6				Full cycles	12.4 (1.8)
2	1	No. 14	33.8-37.2 (4.9-5.4)	2.8-2.9 (0.40-0.42)	Monotonic up	19.3 (2.8)[2]
	2				Half cycles	15.2 (2.2)
	3				Full cycles	15.2 (2.2)
	4				Monotonic up	16.5 (2.4)
	5				Half cycles	15.2 (2.2)
	6				Double half cycles	15.2 (2.2)
3	1	No. 18	34.5-40.7 (5.0-5.9)	3.0-3.5 (0.44-0.50)	Monotonic up	17.2 (2.5)
	2				Full cycles	13.1 (1.9)
	3				Full cycles	13.8 (2.0)
	4				Monotonic up	17.9 (2.6)
	5				Half cycles	14.5 (2.1)
	6				Half cycles	15.2 (2.2)
4	1	No. 14	54.5-56.5 (7.9-8.2)	3.7-3.8 (0.54-0.55)	Monotonic up	24.1 (3.5)
	2				Monotonic up	22.8 (3.3)
	3				Double full cycles	19.3 (2.8)
	4				Full cycles	20.0 (2.9)

[1] Strengths measured on the first and last day of testing for each series.

[2] Sealing in a PVC tube failed during construction resulting in a little concrete accumulated at the end of the tube and, thereby, an increase of the bonded length. Since the actual embedment length is unknown, the bond strength has been calculated with the specified embedment length of $5d_b$.

Table 3.2: Geometric properties of the bars

Bar size	d_b mm (in.)	Rib area ratio	Clear rib spacing mm (in.)
No. 11	36 (1.41)	0.070	19.1 (0.75)
No. 14	43 (1.69)	0.068	24.9 (0.98)
No. 18	57 (2.26)	0.095	24.4 (0.96)

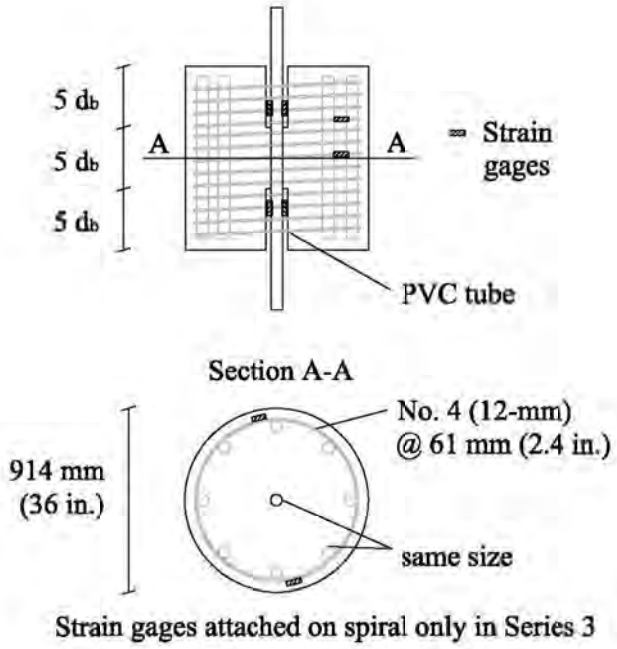

(a) Typical test specimen and strain gage locations

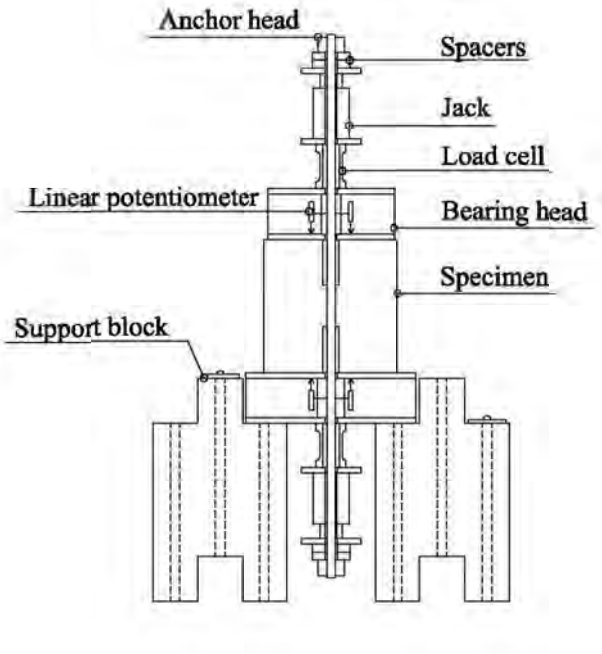

(b) Test setup and linear potentiometer locations

Figure 3.1: Test specimen, setup, and instrumentation

(a) Placing strain gages on test bars

(b) Assembling steel cages and placing strain gages on spiral

(c) Centering test bar, and placing PVC tubes and form

(d) Concrete pour

Figure 3.2: Construction sequence for each series of specimens

Figure 3.3: Test setup

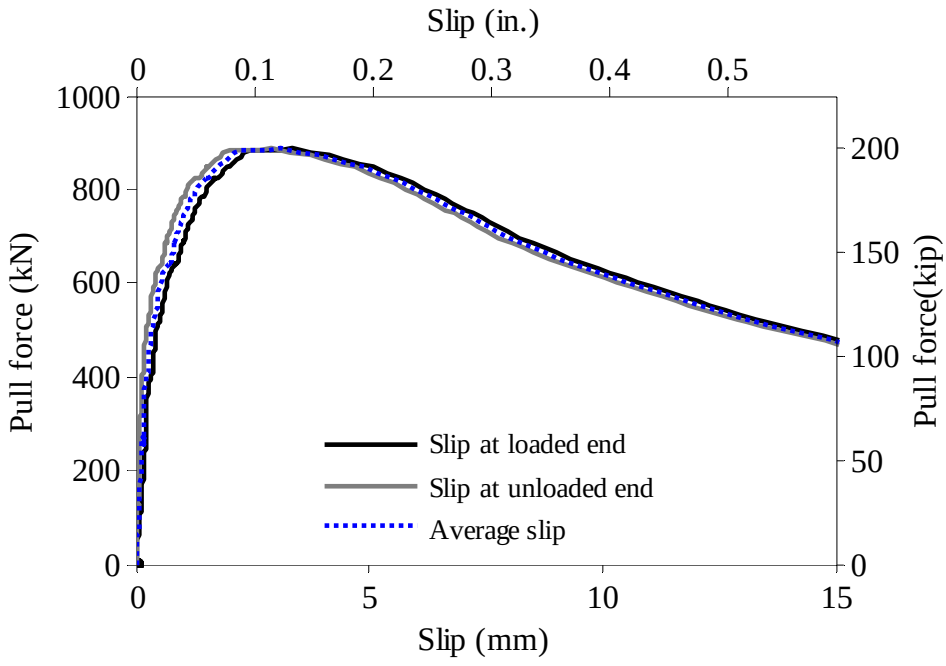

Figure 3.4: Pull force vs. slip for Test 1 of Series 3

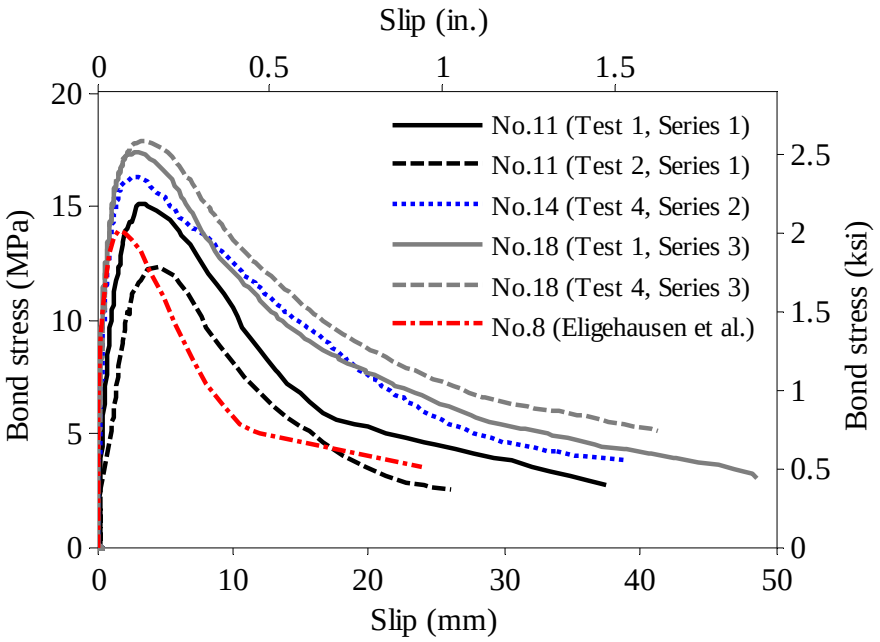

Figure 3.5: Average bond stress vs. slip from monotonic load tests

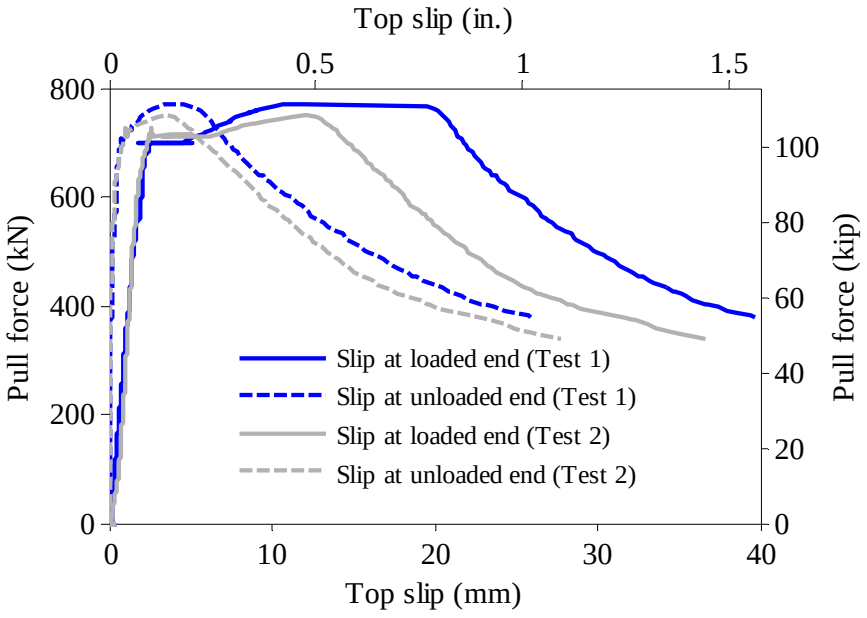

Figure 3.6: Pull force vs. slip for Test 1 and Test 2 of Series 4

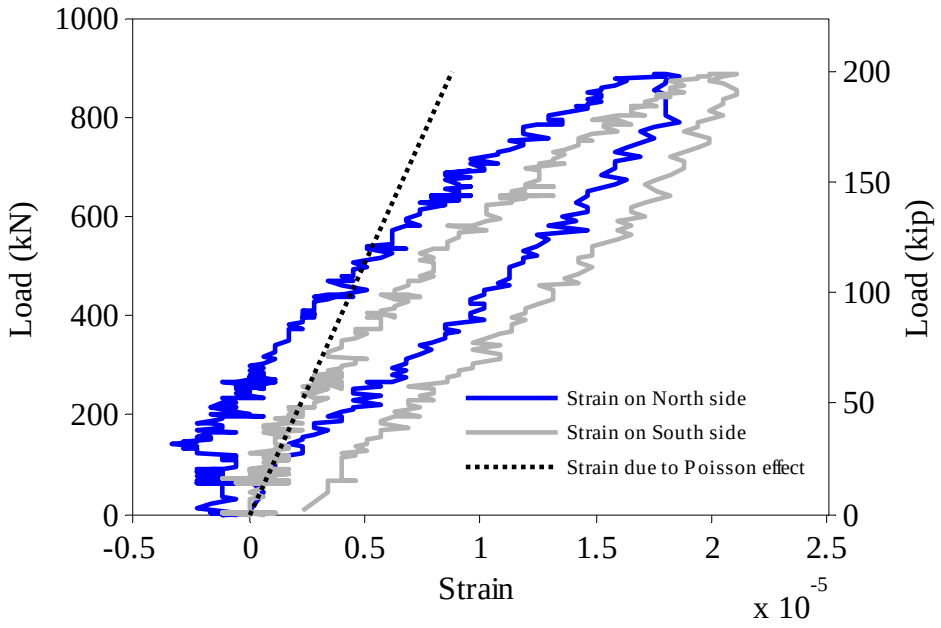

Figure 3.7: Strains in spiral at mid-height of the specimen for Test 1 of Series 3

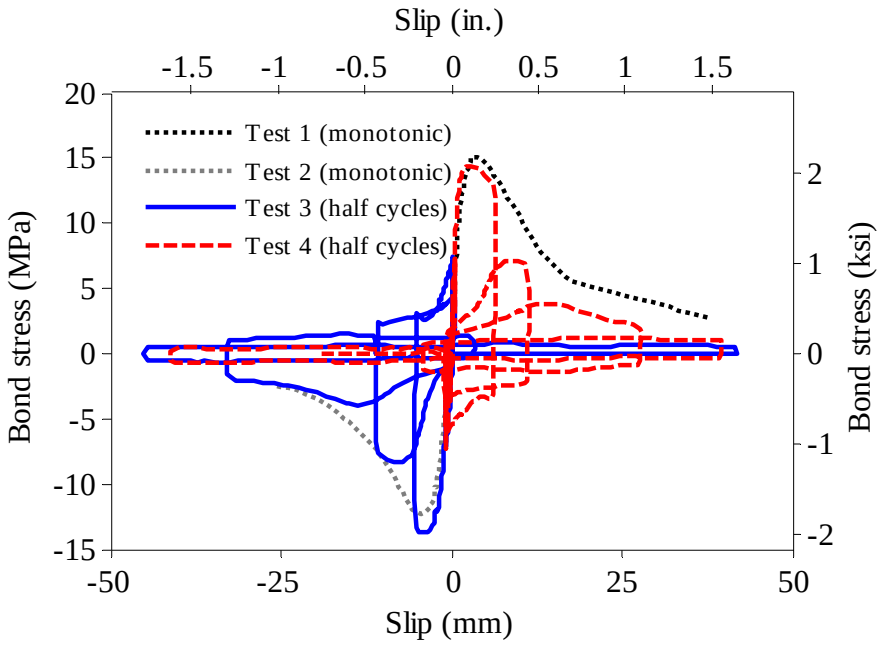

Figure 3.8: Tests on No. 11 bars (Series 1) under monotonic loads (Test 1 and Test 2) and cyclic loads with half cycles (Test 3 and Test 4)

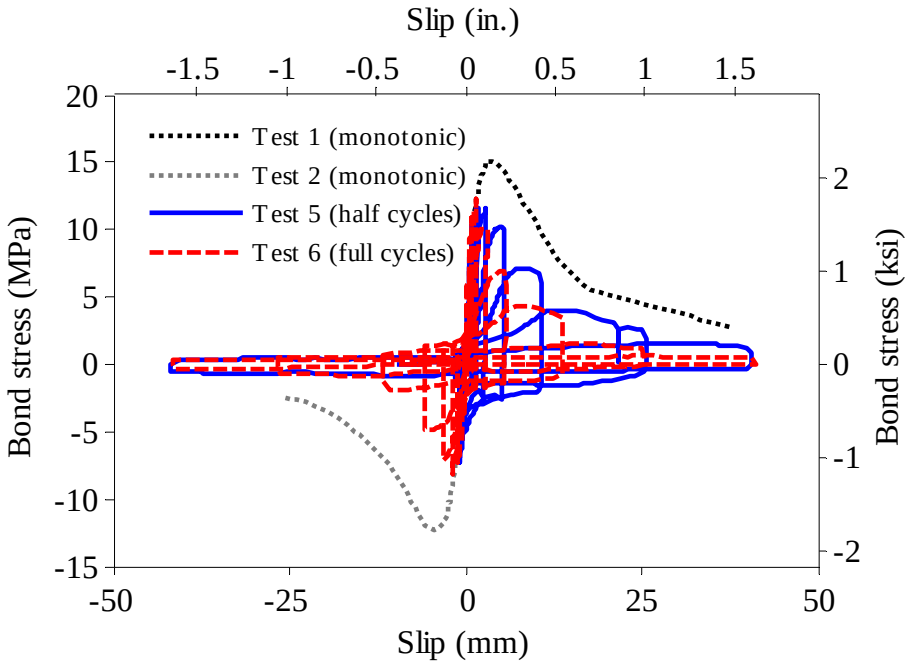

Figure 3.9: Tests on No. 11 bars (Series 1) under monotonic loads (Test 1 and Test 2) and cyclic loads with half cycles (Test 5) and full cycles (Test 6)

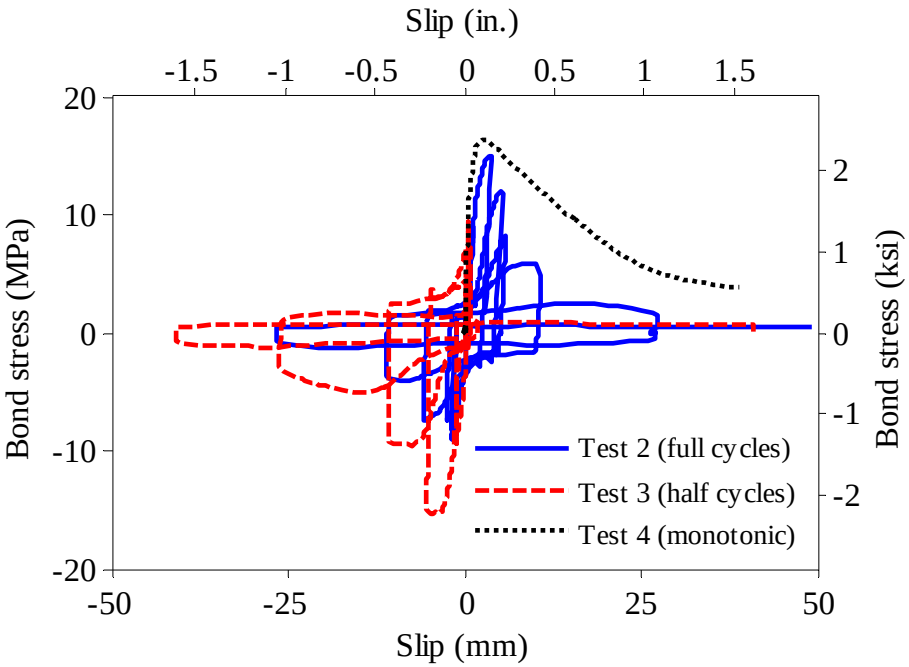

Figure 3.10: Tests on No. 14 bars (Series 2) under monotonic load (Test 4) and cyclic loads with full cycles (Test 2) and half cycles (Test 3)

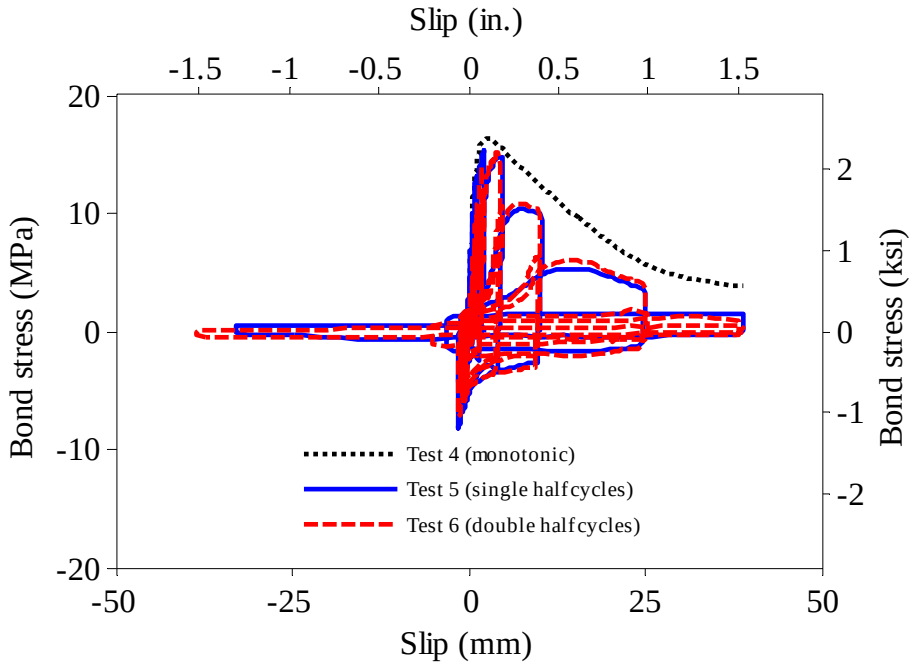

Figure 3.11: Tests on No. 14 bar (Series 2) under monotonic load (Test 4) and cyclic loads with single half cycles (Test 5) and double half cycles (Test 6)

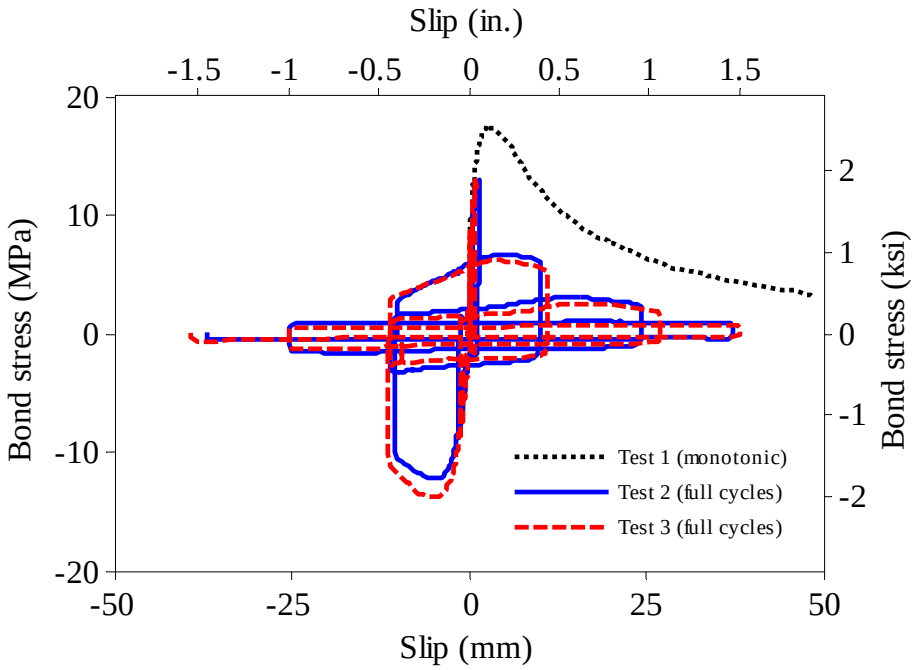

Figure 3.12: Tests on No. 18 bars (Series 3) under monotonic load (Test 1) and cyclic loads with full cycles (Test 2 and Test 3)

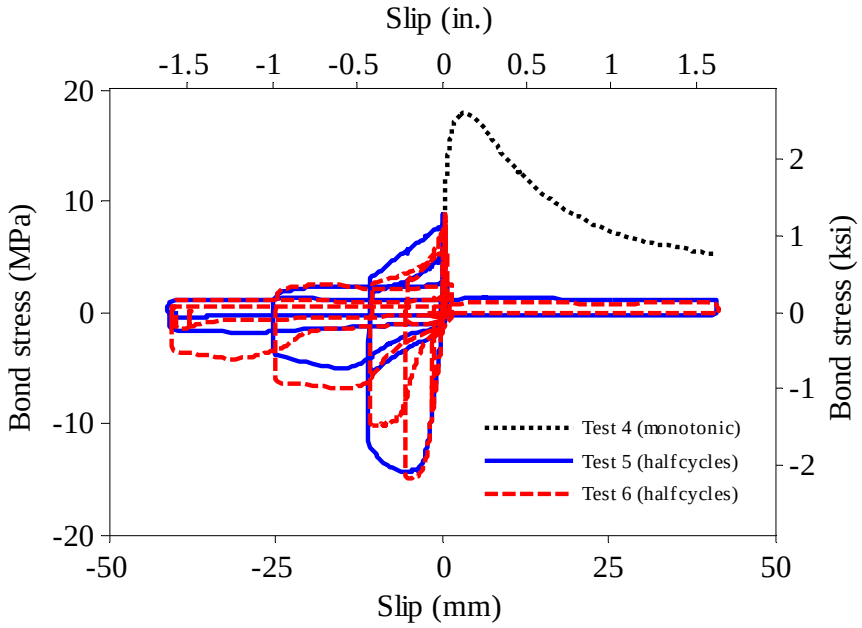

Figure 3.13: Tests on No. 18 bars (Series 3) under monotonic load (Test 2) and cyclic loads with half cycles (Test 5 and Test 6)

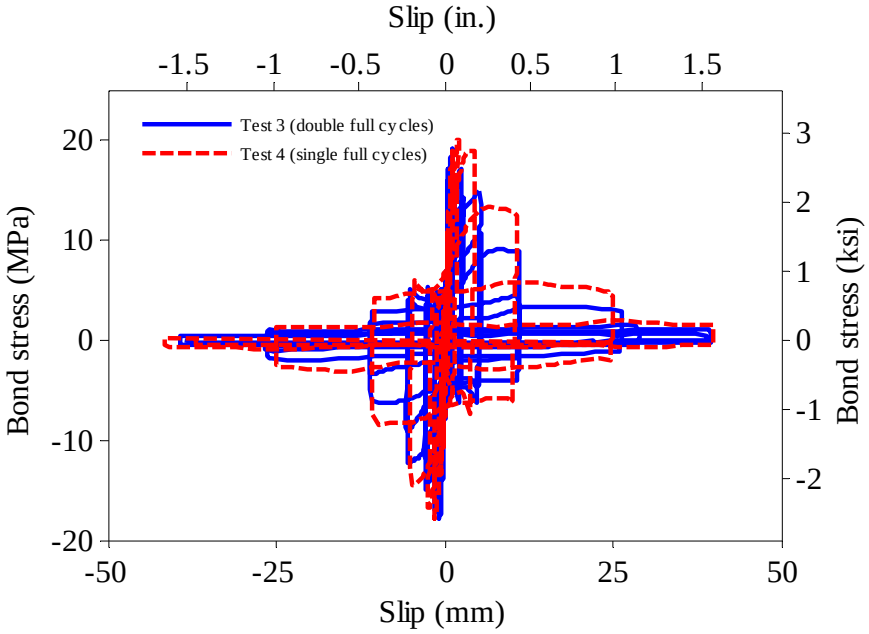

Figure 3.14: Tests on No. 14 bars (Series 4) under cyclic loads with single full cycles (Test 4) and double full cycles (Test 3)

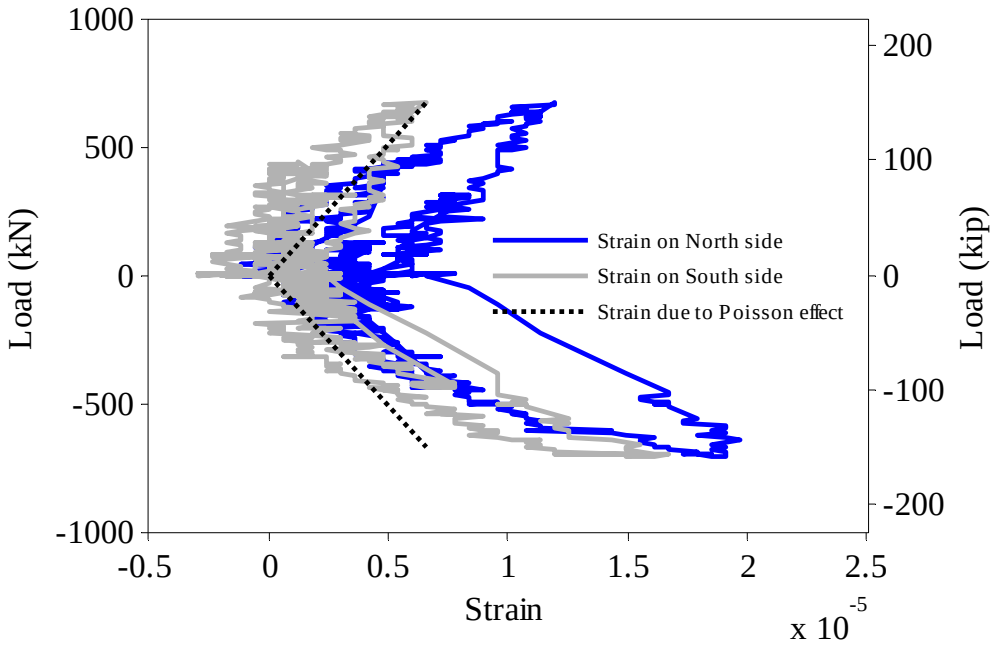

Figure 3.15: Strains in spiral at mid-height of the specimen for Test 3 of Series 3

CHAPTER 4

PHENOMENOLOGICAL BOND-SLIP MODEL FOR FINITE ELEMENT ANALYSIS

In this chapter, a newly developed model to simulate the bond-slip behavior of bars for the finite element analysis of reinforced concrete (RC) structures is presented. It is an enhanced version of a model presented in Murcia-Delso et al. (2013). This model is based on a semi-empirical phenomenological law and was originally developed to predict the bond stress-slip relations of bars embedded in well-confined concrete. It has been extended here to account for low confinement situations. However, its accuracy for very lightly confined situations is not expected to be as good. This law has been calibrated with the bond-slip test data presented in Chapter 3, as well as data obtained by others. The model has been implemented as a constitutive law in a dedicated interface element in the finite element (FE) program ABAQUS (Simulia 2010), and it has been validated by using it in the finite element analyses of various RC components tested in laboratories. These include bond-slip, development length, and RC column tests. The constitutive models for concrete and steel that are available in ABAQUS have been calibrated for these FE analyses.

4.1 Bond stress-vs.-slip law for bars in well-confined concrete

A phenomenological bond stress-vs.-slip law for bars embedded in well-confined concrete has been developed based on the experimental data presented in Chapter 3 and on concepts originally proposed by Eligehausen et al. (1983) and further extended by

others (Pochanart and Harmon 1989, Yankelevsky et al. 1992, and Lowes et al. 2004). However, it is distinct from other models in that it requires the calibration of only three parameters and can applied to bars of different sizes and concrete of different strengths.

In this model, the relation between the bond stress and slip for monotonic loading is described by a set of polynomial functions. For cyclic loading, a similar relation is used but the bond strength is reduced at each slip reversal by using two damage parameters, whose values are based on the slip history, to account for cyclic bond deterioration. In addition, cyclic unloading and reloading rules similar to those proposed by Eligehausen et al. (1983) are adopted to describe bond resistance right after slip reversal. The model is described in detail in the following sections.

4.1.1 Monotonic bond stress-slip relation

The monotonic bond stress (τ) - slip (s) relation assumed in this model is shown in Figure 4.1a. It is defined piecewise in terms of five polynomial functions, which depend on three governing parameters: the peak bond strength (τ_u) for an elastic bar, the slip at which the peak strength is attained (s_{peak}), and the clear spacing between the ribs (s_R). These functions are given below.

$$\tau(s)=\begin{cases} 4\dfrac{\tau_{\max}}{s_{peak}}s & \text{for } 0\le s<0.1s_{peak} \\ \tau_{\max}\left[1-0.6\left(\dfrac{s-s_{peak}}{0.9s_{peak}}\right)^4\right] & \text{for } 0.1s_{peak}\le s<s_{peak} \\ \tau_{\max} & \text{for } s_{peak}\le s<1.1s_{peak} \\ \tau_{\max}-\left(\tau_{\max}-\tau_{res}\right)-0.75\dfrac{s-1.1s_{peak}}{s_R-1.1s_{peak}} & \text{for } 1.1s_{peak}\le s<s_R \\ \tau_{res} & \text{for } s\ge s_R \end{cases} \tag{4.1}$$

in which $\tau_{\max}$ and τ_{res} are the maximum and residual bond strengths for the monotonic curve. For a bar that has not yielded, $\tau_{\max}=\tau_u$ and $\tau_{res}=0.25\tau_u$. Their relation to τ_u for a yielded bar will be formulated later in this section. Until reaching 40% of the maximum strength, $\tau_{\max}$, (point A in Figure 4.1a), the bond stress increases linearly with the slip.

The nonlinear hardening behavior is represented by a fourth-order polynomial (line A-B in Figure 4.1a), followed by a plateau at $\tau_{\max}$ (B-C). The bond strength decay is described by a linear descending branch (C-D). When the slip equals the clear rib spacing, s_R, of the bar (point D), a residual bond strength is reached and this value remains constant for larger slip values.

The use of the proposed law requires the determination of the values of the three governing parameters. The value of s_R is a known geometric property of the bar, and it is usually between 40 to 60% of the bar diameter. As discussed in Chapter 3, τ_u depends on many factors and no theoretical formulas are available to accurately estimate its value. The same situation applies to s_{peak}. Therefore, these values have to be determined experimentally for each case if possible. Table 4.1 shows the values of these parameters obtained from the bond-slip tests conducted on No. 11, 14, and 18 bars embedded in 34.5-MPa (5-ksi) concrete as presented in Chapter 3. The values of the bond strengths are the average values obtained from the monotonic pull-out tests. Values for smaller bars obtained in other studies are also shown.

When no experimental data are available, the following approximations, based on data obtained in this study and by others, can be used to determine τ_u and s_{peak}. The bond strength can be assumed to be 16.5 MPa (2.4 ksi) for 34.5-MPa (5-ksi) concrete regardless of the bar size. This is based on the average τ_u value obtained from Test Series 1 to 3, as shown in Table 4.1. The slight increase of the bond strength with the increase of the bar size observed in these tests can be ignored in the absence of comprehensive data that cover a broad range of bar sizes. For concrete strengths other than 34.5 MPa (5 ksi), τ_u can be scaled accordingly with the assumption that it is proportional to $f_c'^{3/4}$. As shown in Table 4.1, s_{peak} for the No. 11, 14, and 18 bars is about 1.7 times that for No. 8 (25-mm) bars (Eligehausen et al. 1983) and three times that for No.5 (16-mm) bars (Lundgren 2000). This seems to indicate a scale effect with respect to the bar size, but these values could also be influenced by other factors such as the confinement, concrete properties, and loading conditions. In addition, some studies (Eligehausen et al. 1983,

Pochanart and Harmon 1989) have indicated that that s_{peak} also depends on the relative rib area. Owing to the lack of more conclusive data, it is recommended that s_{peak} be taken to be 7% of the bar diameter, which is obtained by taking the average of the experimentally obtained s_{peak} values, presented in Table 4.1, normalized by the bar respective bar diameters.

The experimental results presented here and those obtained by Lundgren (2000) have shown that the bond strength and the bond stiffness are reduced when a vertically cast bar is pulled downward. Based on this data, the monotonic bond stress-slip relation for a vertically cast bar pulled downward is described by Equation 4.2. Note that for a bar pulled downward, the slip and bond stress have a negative sign here.

$$\tau(s) = \begin{cases} -2.3\dfrac{\tau_{\max}}{s_{peak}}|s| & \text{for } -0.15s_{peak} \le s < 0 \\ -\tau_{\max}\left[0.85 - 0.505\left(\dfrac{|s| - 1.5s_{peak}}{1.35s_{peak}}\right)^4\right] & \text{for } -1.5s_{peak} \le s < -0.15s_{peak} \\ -0.85\tau_{\max} & \text{for } -1.6s_{peak} \le s < -1.5s_{peak} \\ -0.85\tau_{\max} + (0.85\tau_{\max} - \tau_{res})\dfrac{|s| - 1.6s_{peak}}{s_R - 1.6s_{peak}} & \text{for } -s_R \le s < -1.6s_{peak} \\ -\tau_{res} & \text{for } s < -s_R \end{cases} \quad (4.2)$$

As mentioned in Chapter 2, the bond resistance can be considerably reduced after a reinforcing bar yields in tension. This behavior could not be quantified in this study although the bars yielded in two of the monotonically loaded specimens. The reason is that in these two cases, the concrete had a compressive strength of 55 MPa (8 ksi), and there were no other specimens tested monotonically that had the same concrete strength but no bar yielding. In addition, in these specimens, yielding occurred at the loaded end of the bar while the other end remained unstrained. As a result, yielding might have occurred only in the upper portion of the bonded region and the total bond force was probably only slightly affected by this. As discussed in Chapter 2, in pull-out tests carried out by Shima et al. (1987b) on bars with a long embedment length, the bond resistance dropped to approximately 25% of the peak bond strength at bar yielding, and it continued to decrease gradually as the inelastic deformation of the bar increased. To account for this

effect in the model, $\tau_{\max}$ and τ_{res} are defined as a function of the steel strain, ε_s, as shown in Equation 4.3. This equation assumes that once the bar yields in tension, the peak of the monotonic envelope will decrease linearly with respect to ε_s at such a rate that it reaches 25% of the peak bond strength, τ_u, of an unyielded bar when the bar strain attains the value ε_{sh}, which corresponds to the initiation of strain hardening and can be assumed to be 1%. As the bar strain further increases, both the peak and the residual resistances decrease linearly to zero, which is the point when the bar strain reaches the ultimate strain of the steel, ε_u, which can be assumed to be 15%.

$$\tau_{\max}(\varepsilon_s) = \begin{cases} \tau_u & \text{for } \varepsilon_s \le \varepsilon_y \\ \tau_u \left(1 - 0.75 \dfrac{\varepsilon_s - \varepsilon_y}{\varepsilon_{sh} - \varepsilon_y}\right) & \text{for } \varepsilon_y < \varepsilon_s \le \varepsilon_{sh} \\ 0.25\tau_u \dfrac{\varepsilon_u - \varepsilon}{\varepsilon_u - \varepsilon_{sh}} & \text{for } \varepsilon_s > \varepsilon_{sh} \end{cases} \tag{4.3a}$$

$$\tau_{res}(\varepsilon_s) = \begin{cases} 0.25\tau_u & \text{for } \varepsilon_s \le \varepsilon_{sh} \\ 0.25\tau_u \dfrac{\varepsilon_u - \varepsilon}{\varepsilon_u - \varepsilon_{sh}} & \text{for } \varepsilon_s > \varepsilon_{sh} \end{cases} \tag{4.3b}$$

4.1.2 Cyclic law

The extension of the bond stress-slip law to cyclic loading is based on the experimental evidence presented in this study and the bond-slip mechanism hypothesized by Eligehausen et al. (1983). It is assumed that at a large slip, part of the concrete in contact with the ribs on the bearing side is crushed and a gap has been created on the other side of the ribs. This gap needs to be closed before the bearing resistance in the opposite direction can be activated. Hence, the initial bond resistance developed upon slip reversal after a large slip can be attributed solely to friction. Once contact is resumed on the bearing side of the rib, the bond resistance increases. However, this resistance is lower than that under a monotonic load for the same level of slip due to the deterioration of the concrete around the ribs. The bond-slip law for cyclic loading is shown in Figure 4.1b.

In most phenomenological models, bond deterioration under cyclic slip reversals is simulated by scaling the monotonic bond stress-slip relation, and the scale factors are updated upon each slip reversal. Some of these models adopt a single damage parameter that is a function of the energy dissipated by bond-slip (Eligehausen et al. 1983) or of the slip history (Lowes et al. 2004) to determine a scale factor. Some models (Pochanart and Harmon 1989, Yankelevsky et al. 1992, and Lowes et al. 2004) distinguish the bearing and friction resistances. Pochanart and Harmon (1989) and Yankelevsky et al. (1992) scale independently these two contributions. The latter approach has been adopted here based on the experimental evidence that the reduction of the peak strength is in general more rapid than that of the residual strength. The peak strength in a monotonic bond stress-slip curve is mainly contributed by the bearing resistance, while the residual strength is entirely due to friction. Friction deterioration is caused by the smoothening of the interface between the steel and concrete, and, therefore, can be assumed to be dependent on the total cumulative slip. The deterioration of the bearing resistance is caused by the crushing and/or shearing of the concrete between the ribs. Therefore, it can be assumed to be dependent only on the maximum slips attained in the two loading directions. For sliding between previously attained levels of slip, there will be no bearing contact between the concrete and the ribs, and, therefore, no further crushing and shearing of concrete can occur. These mechanisms are consistent with the cyclic behavior observed in the tests presented in Chapter 3. Fully-reversed cycles are more damaging than half cycles because the maximum slip excursion and the total slip accumulated are larger, causing more deterioration in both the bearing and the friction resistances. Double cycles between the same slip levels induce slightly more damage than single cycles because the second cycle causes a further reduction of the friction resistance.

Based on the reasoning presented above, the monotonic bond stress-slip relation in this model is separated into a bearing component and a friction component as shown in Figure 4.1a. From the origin to the end of the plateau at the peak of the curve (point C), the bearing resistance, τ_b, is assumed to be 75% of the total bond resistance, and the remaining 25% is assumed to be contributed by the friction resistance, τ_f. After the peak, τ_b is assumed to decay linearly to zero, which corresponds to the point when the

slip is equal to s_R, i.e., when the concrete between the ribs has been completely crushed or sheared off. The friction resistance, τ_f, is assumed to remain constant as slip continues to increase after the peak. The maximum bearing and friction resistances are therefore $\tau_{b,\max} = 0.75\tau_{\max}$ and $\tau_{f,\max} = 0.25\tau_{\max}$, respectively. To model the cyclic bond deterioration, the following damage law is used.

$$\begin{aligned} \tau_{red} &= \tau_{b,red} + \tau_{f,red} \\ \tau_{b,red} &= \left(1-\hat{d}_b\right)\cdot\tau_b \\ \tau_{f,red} &= \left(1-\hat{d}_f\right)\cdot\tau_f \end{aligned} \tag{4.4}$$

in which τ_{red} is the reduced bond resistance, $\tau_{b,red}$ is the reduced bearing resistance, $\tau_{f,red}$ is the reduced friction resistance, $\hat{d}_b$ is the damage parameter for the bearing resistance, and $\hat{d}_f$ is the damage parameter for the friction resistance. The bond stress-slip relation is updated using Equation 4.4 when the load is reversed. The damage laws have been calibrated using the experimental data from Test Series 1, 2 and 3. Data from Series 4 cannot be used because the bars in the monotonic bond-slip tests yielded, and, therefore, it does not provide a direct comparison of the monotonic bond-slip behavior with the cyclic behavior.

The damage parameter for the bearing resistance, $\hat{d}_b$, is defined as a function of the maximum slip.

$$\hat{d}_b(\bar{s}_{\max}) = 1 - 1.2e^{-2.7\left(\frac{\bar{s}_{\max}}{s_R}\right)^{0.8}} \geq 0 \tag{4.5a}$$

where

$$\bar{s}_{\max} = 0.75\max\left(s^+_{\max}, s^-_{\max}\right) + 0.25\left(s^+_{\max} + s^-_{\max}\right) \tag{4.5b}$$

in which $s^+_{\max}$ and $s^-_{\max}$ are the absolute values of the maximum slips reached in the positive and negative directions. Since full cycles produce more damage than half cycles, the maximum slip $\bar{s}_{\max}$ considered here is a weighted average of the absolute maximum slip reached in any of the two directions and the sum of the maximum slips in the two directions. As mentioned previously, cyclic deterioration starts to become apparent after

the maximum bond stress in a previous cycle has reached 70% to 80% of the peak bond strength developed under a monotonic load. This is accounted for in the above damage index in the following way. Equation 4.1 stipulates that under monotonic loading, the bond stress reaches 70% of the peak bond strength when the slip $s = 0.034 s_R$ if $s_{peak} = 0.07 d_b$ and $s_R = 0.5 d_b$ as assumed here. Hence, Equation 4.5a is so formulated that $\hat{d}_b$ starts to increase only when $\bar{s}_{\max} / s_R > 0.034$.

The friction resistance decreases progressively as a result of the smoothening of the bond interface, which depends on the total cumulative slip. However, more severe deterioration has been observed in the residual bond strength as the maximum slip increases in a subsequent cycle. Therefore, the damage parameter for the friction resistance, $\hat{d}_f$, is assumed to be a function of both the absolute maximum slip attained in each loading direction and the cumulative slip, s_{acc}.

$$\hat{d}_f(s_{acc}, s^+_{\max}, s^-_{\max}) = \frac{\min\left(s^+_{\max} + s^-_{\max}, s_R\right)}{s_R}\left(1 - e^{-0.45\left(\frac{s_{acc}}{s_R}\right)^{0.75}}\right) \tag{4.6}$$

To avoid an overestimation of damage that could otherwise be caused by a large number of small cycles, s_{acc} is considered zero before the slip displacement has exceeded the slip at the peak stress, s_{peak}, for the first time. This is a reasonable assumption if one agrees that friction should play a minor role at the beginning when bearing resistance is significant.

As shown in Figure 4.1b, right after each slip reversal, unloading follows the initial stiffness of the monotonic curve until the friction resistance limit τ_{rev} in the opposite direction is reached. If the maximum slip ever achieved exceeds the slip at the peak resistance, s_{peak}, the resistance τ_{rev} right after slip reversal is equal to the reduced friction, $\tau_{f,red}$, given in Equation 4.4. Otherwise, it is a fraction of the reduced friction as shown in Equation 4.7, which is a modification of that suggested by Eligehausen et al. (1983).

$$\tau_{rev} = k_{rev} \tau_{f,red} \tag{4.7a}$$

where

$$k_{rev} = \frac{\max(s^{+}_{\max}, s^{-}_{\max})}{s_{peak}} \leq 1 \qquad (4.7b)$$

At slip reversal, $\tau = \tau_{rev}$ until the maximum slip previously attained in that direction ($s^{+}_{\max}$ or $s^{-}_{\max}$) is reached. After this point, the bond stress-slip relation will be governed by the reduced bond strength in Equation 4.4. The reloading branch from the horizontal line ($\tau = \tau_{rev}$) to the reduced envelope follows the initial stiffness of the monotonic curve.

4.1.3 Comparison of analytical and experimental results

The ability of the analytical model to reproduce the bond stress-slip relations obtained from the experiments presented in Chapter 3 and by others has been evaluated. The experimental and analytical results for two monotonic load tests from Chapter 3, and for No. 8 (25-mm) bars tested by Eligehausen et al. (1983) are presented in Figure 4.2. Two sets of analytical curves have been generated. The first set is based on the values of τ_u and s_{peak} directly obtained from the monotonic tests while the second set is based on the values estimated with the recommendations provided in Section 4.1.1. The values of τ_u and s_{peak} for both sets of curves are presented in Table 4.1. The results in Figure 4.2 show that once the values of τ_u and s_{peak} have been determined with experimental data, the ascending and descending branches are well represented by the proposed polynomial functions. The curves based on the estimated values also provide a satisfactory match in spite of the simplicity of the rules used to derive these values.

The cyclic bond stress-slip relations have been reproduced analytically using the parameters calibrated with the monotonic tests. The analytical and experimental results for selected tests in Series 1, 3, and 4 are compared in Figure 4.3. The model accurately reproduces the cyclic bond stress-slip relations, including the bond strength decay. Experiments by Eligehausen et al. (1983) and Lundgren (2000), which had smaller bars, more cycles per amplitude level, and cycles with finer amplitude increments, are also well reproduced by the analytical model, as shown in Figure 4.4.

4.2 Steel-concrete interface model for bond-slip

The bond stress-vs.-slip law presented in Section 4.1 has been implemented in an interface model to simulate the interaction between steel and concrete for the finite element analysis of reinforced concrete members. In the interface model, the relative displacement at the concrete-steel interface has three components: one normal, $\tilde{u}_1$, and two tangential components, $\tilde{u}_2$ and $\tilde{u}_3$, as shown in Figure 4.5. Likewise, the stress transfer at the interface is decomposed into one normal, σ_1, and two shear components, τ_2 and τ_3. The constitutive relations for the interface model are presented in Equations 4.8 through 4.10.

In Equation 4.8, the bond stress-vs.-slip law proposed in Section 4.1 is used to define the relation between the tangential relative displacement and shear stress in the longitudinal direction of the bar, i.e., between $\tilde{u}_2$ and τ_2. However, to introduce the capability of modeling bond resistance in low confinement situations and splitting failure, a bond stress reduction factor, ρ, has been introduced so that

$$\tau_2 = \rho(\tilde{u}_1) \cdot \tau(\tilde{u}_2, \varepsilon_s) \tag{4.8a}$$

in which the relation between τ and $(\tilde{u}_2, \varepsilon_s)$ are defined by the constitutive law presented in Section 4.1 with $\tilde{u}_2$ representing the bar slip s. The reduction factor ρ depends on the normal opening of the interface, $\tilde{u}_1$, with respect to the bar rib height, h_R, as follows.

$$\rho(\tilde{u}_1) = \begin{cases} 1 & \text{for } \tilde{u}_1 \le 0.5h_R \\ 2(1-\tilde{u}_1 / h_R) & \text{for } 0.5h_R < \tilde{u}_1 \le h_R \\ 0 & \text{for } \tilde{u}_1 > h_R \end{cases} \tag{4.8b}$$

When the opening of the interface is small as compared to the rib height, ρ is equal to one, which will be the case if the concrete surrounding the bar is well confined. If the interface opening is larger than the rib height, the bond resistance disappears, which will be the case when the confinement is low and the concrete splitting cracks open. A smooth transition is assumed between these two situations.

As shown in Equation 4.9, the normal stress is defined to be proportional to the bond stress with the assumption that the resultant bond force has a fixed angle of

inclination θ with respect to the longitudinal axis of the bar. A similar assumption was used in the bond-slip model proposed by Lowes et al. (2004). In addition, a penalty factor in terms of a stiffness parameter, $K_{pen,1}$, which is active only in compression, has been added to introduce the necessary normal resistance to minimize interpenetration between the steel and concrete.

$$\sigma_1 = -|\tau_2| \tan\theta + K_{pen,1} \min(\tilde{u}_1, 0) \tag{4.9}$$

For three-dimensional models, the rotation of the bar about its longitudinal axis is restrained by a penalty stiffness parameter, $K_{pen,3}$, as presented in Equation 4.10.

$$\tau_3 = K_{pen,3} \tilde{u}_3 \tag{4.10}$$

The steel-concrete model has been implemented in a user-defined interface element in ABAQUS (Simulia 2010). The element has linear shape functions and two integration points located at the ends of the element (see Figure 4.5). The force per unit length of the interface is obtained by multiplying the interface stresses by the tributary perimeter of the bar that the interface element represents. Finally, the axial strain of the bar required in the constitutive equations is calculated from the nodal displacements parallel to the bar axis at the nodes connected to the bar (nodes A and B in Figure 4.5) and the length of the element, L_e, as

$$\varepsilon_s = \frac{u_{2B} - u_{2A}}{L_e} \tag{4.11}$$

4.3 Three-dimensional modeling of plain concrete

In the finite element analyses presented in this study, plain concrete has been modeled with continuum elements and a plastic-damage constitutive model available in ABAQUS (Simulia 2000). Plastic-damage models are attractive to simulate the behavior of concrete because they combine salient features of plasticity theory and damage mechanics to account for plastic deformations and stiffness degradation. The model available in ABAQUS, called the concrete damaged plasticity, is based on the formulations proposed by Lubliner et al. (1989) and Lee and Fenves (1998). In this

section, the formulation of the plastic-damage model available in ABAQUS is briefly reviewed, and the model is validated and calibrated by experimental data.

4.3.1 Plastic-damage model formulation

Following the classical theory of plasticity, the strain tensor is decomposed into an elastic part and a plastic part, and the stress tensor is obtained as the double contraction of the elastic stiffness tensor and the elastic strain tensor.

$$\boldsymbol{\varepsilon} = \boldsymbol{\varepsilon}^e + \boldsymbol{\varepsilon}^p \tag{4.12a}$$

$$\boldsymbol{\sigma} = \mathbf{E} : \boldsymbol{\varepsilon}^e = \mathbf{E} : \left(\boldsymbol{\varepsilon} - \boldsymbol{\varepsilon}^p\right) \tag{4.12b}$$

To account for stiffness degradation, the elastic stiffness tensor is related to the initial stiffness tensor as

$$\mathbf{E} = (1-d)\mathbf{E_0} \tag{4.12c}$$

where d is a scalar parameter that controls the stiffness degradation. In damage theory, d represents the ratio of the damaged area to the original area. The effective stress in the undamaged area is given as

$$\overline{\boldsymbol{\sigma}} = \mathbf{E}_0 : \boldsymbol{\varepsilon}^e = \mathbf{E}_0 : \left(\boldsymbol{\varepsilon} - \boldsymbol{\varepsilon}^p\right) \tag{4.12d}$$

The yield surface for the damaged plasticity model is based on that proposed by Lubliner et al. (1989) with the modifications introduced by Lee and Fenves (1998) to account for the different behavior in tension and compression. The initial shape of the yield surface in the principal stress plane for a plane-stress situation is shown in Figure 4.6. The yield function is defined in terms of the invariants I_1 and J_2 as

$$F = \frac{1}{1-\alpha}\left[\alpha I_1 + \sqrt{3J_2} + \beta(\tilde{\varepsilon}_c^{\,p}, \tilde{\varepsilon}_t^{\,p}) < \hat{\sigma}_{\max} > -\gamma < -\hat{\sigma}_{\max} >\right] - c_c(\tilde{\varepsilon}_c^{\,p}) \tag{4.13}$$

in which $<\cdot>$ is the Macaulay bracket, $\hat{\sigma}_{\max}$ is the maximum principal stress, α and γ are constants, and β and c_c are parameters that depend on two history variables, $\tilde{\varepsilon}_c^{\,p}$ and $\tilde{\varepsilon}_t^{\,p}$, representing the equivalent plastic strains in compression and tension, respectively. These variables are later on defined in Equation 4.15.

A non-associated plastic potential, G, is adopted and the plastic strain rate is obtained as $\dot{\boldsymbol{\varepsilon}}^p = \dot{\lambda}\dfrac{\partial G}{d\boldsymbol{\sigma}}$, where $\dot{\lambda}$ is the plastic multiplier. The plastic potential is defined in Equation 4.14 using the Drucker-Prager criterion.

$$G = \sqrt{3J_2} + \frac{I_1}{3}\tan\psi \tag{4.14}$$

in which ψ is the dilation angle for concrete.

The history variables $\tilde{\varepsilon}_c^{\,p}$ and $\tilde{\varepsilon}_t^{\,p}$ are related to the plastic flow as follows:

$$\dot{\tilde{\varepsilon}}_t^{\,p} = r\left(\hat{\bar{\boldsymbol{\sigma}}}\right)\dot{\hat{\varepsilon}}_{\max}^{p} \tag{4.15a}$$

$$\dot{\tilde{\varepsilon}}_c^{\,p} = \left(1 - r\left(\hat{\bar{\boldsymbol{\sigma}}}\right)\right)\dot{\hat{\varepsilon}}_{\min}^{p} \tag{4.15b}$$

in which $\dot{\hat{\varepsilon}}_{\max}^{p}$ and $\dot{\hat{\varepsilon}}_{\min}^{p}$ are obtained from the principal plastic strains rates ($\dot{\varepsilon}_1^p$, $\dot{\varepsilon}_2^p$, $\dot{\varepsilon}_3^p$) as $\dot{\hat{\varepsilon}}_{\max}^{p} = \dot{\varepsilon}_1^p$ and $\dot{\hat{\varepsilon}}_{\min}^{p} = \dot{\varepsilon}_3^p$ with $\dot{\varepsilon}_1^p \geq \dot{\varepsilon}_2^p \geq \dot{\varepsilon}_3^p$, and

$$r\left(\hat{\bar{\boldsymbol{\sigma}}}\right) = \begin{cases} 0 & \text{if } \hat{\bar{\boldsymbol{\sigma}}} = 0 \\ \dfrac{\sum_{i=1}^{3}\left\langle\hat{\bar{\sigma}}_i\right\rangle}{\sum_{i=1}^{3}\left|\hat{\bar{\sigma}}_i\right|} & \text{otherwise} \end{cases} \tag{4.15c}$$

where $\hat{\bar{\sigma}}_i$ are the principal effective stresses.

The parameter β is defined as

$$\beta = \frac{c_c(\tilde{\varepsilon}_c^{\,p})}{c_t(\tilde{\varepsilon}_c^{\,p})}(1-\alpha) - (1+\alpha) \tag{4.16}$$

in which the functions $c_t\left(\dot{\tilde{\varepsilon}}_t^{\,p}\right)$ and $c_c\left(\dot{\tilde{\varepsilon}}_c^{\,p}\right)$ represent the tensile and compressive cohesions, and are calibrated from the uniaxial compression and tension test data.

The damage parameter d is a function of both the damage parameter in tension, $d_t\left(\dot{\tilde{\varepsilon}}_t^{\,p}\right)$, and the damage parameter in compression, $d_c\left(\dot{\tilde{\varepsilon}}_c^{\,p}\right)$, as follows:

$$(1-d) = (1-s_t d_c)(1-s_c d_t) \tag{4.17a}$$

where

$$s_t = 1 - w_t r\left(\hat{\bar{\boldsymbol{\sigma}}}\right) \tag{4.17b}$$

$$s_c = 1 - w_c\left(1 - r\left(\hat{\bar{\boldsymbol{\sigma}}}\right)\right) \tag{4.17c}$$

In Equation 4.17, w_t and w_c are constants that control stiffness degradation in tension and compression, respectively. The functions $d_t\left(\tilde{\varepsilon}_t^{\,p}\right)$ and $d_c\left(\tilde{\varepsilon}_c^{\,p}\right)$ are calibrated from cyclic uniaxial tension and compression tests, respectively. The uniaxial tension and compression stress-strain curves for this model are shown in Figure 4.7.

4.3.2 Validation and calibration of the plastic-damage model

Lee and Fenves (1998) validated the model for monotonic uniaxial and biaxial compression and tension. The model available in ABAQUS (Simulia 2010) has been calibrated and further validated here for the cyclic compression-tension behavior and compression under lateral confinement. Since cracks are modeled in a smeared fashion, the post-crack behavior of concrete is expressed in terms of a stress-strain relation with appropriate post-peak uniaxial stress-strain curves in tension and compression reflecting the fracture energies released in the failure processes. The yield function of the model, as given in Equation 4.13, accounts for the influence of the hydrostatic pressure on the yield and failure strengths of concrete. Together with a properly calibrated plastic potential, the yield function is able to represent the increase in the compressive strength of concrete due to lateral confinement. However, the model is not able to properly represent the post-peak compressive behavior of confined concrete, which is one limitation of the model. The approach taken in this study to overcome this limitation will be explained later in this section.

To calibrate the concrete model, one needs to input the uniaxial compressive stress-strain relation for the concrete. In this study, the stress-strain relation proposed by Karthik and Mander (2011) has been used. The tensile strength of the concrete also needs to be specified. In addition, there are other parameters that govern the properties of the yield function and plastic potential, and the evolution of the damage parameter. It is assumed that their values are independent of the concrete strength. The values of the key

parameters used in this study are presented in Table 4.2. They have been kept constant for all the analyses conducted in this study.

Figure 4.8 shows that the cyclic tension-compression tests carried out by Reinhardt (1984b) are sufficiently well reproduced by the model. The plastic-damage model is able to simulate the closing and opening of a tensile crack with reduced stiffness. However, with a large inelastic tensile strain, the complete closure of the crack requires a very large stiffness degradation (with the value of the damage parameter very close to one), which has led to irresolvable numerical problems. Hence, the model is not capable of simulating the closure of a crack in a realistic manner resulting in a large residual crack opening upon unloading. This can be observed in Figure 4.8 for the larger amplitude displacement cycles. To circumvent this problem, contact interfaces in ABAQUS can be introduced to represent cracks in a discrete manner. This is not entirely satisfactory in that the cohesive strength of concrete is completely ignored.

The parameters governing the yield function and plastic potential have been calibrated to match experimental results obtained by Hurblut (1985) and Mander et al. (1989) so that the model will be able to capture the behavior of confined concrete in compression. As shown in Figure 4.9, the model is capable of reproducing the effect of the lateral confining stress on the compressive strength and lateral expansion of concrete observed in the tests of Hurblut (1985). However, as mentioned previously, the model is not able to account for the influence of the confining pressure on the post-peak compressive stress-strain of concrete. This has also been observed when attempting to reproduce the experimental results obtained by Mander et al. (1989) on concrete cylinders that had different amounts of confining steel. To overcome this limitation, the decaying slope of the input uniaxial compressive stress-strain curve has been modified a priori for each case based on the level of the confining steel present, as shown in Figure 4.10a. This modification is based on the formula proposed by Karthik and Mander (2011). With this *ad hoc* approach, the model is capable of reproducing the tests results of Mander et al. (1989) reasonably well, as shown in Figure 4.10b.

4.4 Modeling of steel reinforcement

A rate-independent elasto-plastic model with kinematic hardening available in ABAQUS (Simulia 2010) has been used to simulate the behavior of steel reinforcement. This model uses the Von Mises yield condition with an associated flow rule. The yield surface and plastic potential are defined by the following function.

$$F(\boldsymbol{\sigma},\boldsymbol{\alpha}) = \sqrt{\frac{3}{2}(\boldsymbol{\sigma}'-\boldsymbol{\alpha}'):(\boldsymbol{\sigma}'-\boldsymbol{\alpha}')} - \sigma_y \tag{4.18}$$

in which $\boldsymbol{\sigma}'$ and $\boldsymbol{\alpha}'$ are the deviatoric part of the stress tensor, $\boldsymbol{\sigma}$, and backstress tensor, $\boldsymbol{\alpha}$, respectively, and σ_y is the yield strength. The backstress tensor controls the translation of the yield surface in the stress space due to kinematic hardening. Two types of kinematic hardening laws are available in ABAQUS: linear and exponential. The evolution of $\boldsymbol{\alpha}$ for linear kinematic hardening is defined as

$$\dot{\boldsymbol{\alpha}} = C_l \dot{\bar{\varepsilon}}^p \frac{1}{\sigma_y}(\boldsymbol{\sigma}'-\boldsymbol{\alpha}') \tag{4.19}$$

in which C_l is the linear hardening parameter and $\dot{\bar{\varepsilon}}^p$ is the equivalent plastic strain rate, defined as $\dot{\bar{\varepsilon}}^p = \sqrt{\frac{3}{2}\dot{\boldsymbol{\varepsilon}}^{\mathbf{p}}:\dot{\boldsymbol{\varepsilon}}^{\mathbf{p}}}$. This law requires the calibration of two parameters: σ_y and C_l. For exponential kinematic hardening, the hardening rate decreases exponentially with increasing strain, and the evolution of $\boldsymbol{\alpha}$ is defined as

$$\dot{\boldsymbol{\alpha}} = C_e \dot{\bar{\varepsilon}}^p \frac{1}{\sigma_y}(\boldsymbol{\sigma}'-\boldsymbol{\alpha}') - \gamma_e \boldsymbol{\alpha} \dot{\bar{\varepsilon}}^p \tag{4.20}$$

in which C_e and γ_e are the exponential kinematic hardening parameters. This law requires the calibration of three parameters: σ_y, C_e, and γ_e.

The ability of the steel model with linear and exponential kinematic hardening to simulate the monotonic and cyclic test results of Restrepo-Posada et al. (1993) for reinforcing bar coupons is shown in Figure 4.11. The exponential hardening law provides a better approximation of the strain hardening behavior of steel, without unlimited stress increase, as shown in Figure 4.11a. There is no stress limit in the linear kinematic

hardening law. However, none of the hardening laws simulates the yield plateau, the strength decay, and the bar rupture. As shown in Figure 4.11b, the model can capture the cyclic stress-strain relation well with either hardening law, but not the Bauschinger effect.

In this study, reinforcing bars are modeled with either truss or beam elements using the elasto-plastic constitutive model presented above. For cases where the bending of the reinforcement is negligible, truss elements are used; otherwise, beam elements are used. For truss elements, the exponential kinematic hardening law has been adopted because it provides a slightly better approximation of the strain-stress relation. For beam elements, the exponential hardening law is not available. Hence, the linear kinematic hardening law has to be employed.

4.5 Verification examples with finite element models

Finite element (FE) models employing the bond-slip interface element presented in this chapter and the concrete and steel models described above have been constructed to examine their ability to reproduce results of different RC component tests. For this purpose, the bond-slip tests presented in Chapter 3 and other tests reported in the literature including bond-slip tests, development length tests, and a test on a RC column are considered. For the bond-slip and development length tests, the reinforcing bars are modeled with truss elements, and for the RC column, the vertical bars are modeled with beam elements. In the bond-slip law, the inclination angle of the bond force, θ, is assumed to be 60 degrees unless indicated otherwise. While it is often assumed that the resultant of the bond resistance has a 45-degree angle with respect to the bar longitudinal axis (Cairns and Jones 1996), Tepfers and Olsson (1992) have observed from pull-out tests that this angle varied between 35 and 65 degrees, depending on the rib geometry and the intensity of the bond force. The use of a 60-degree angle is recommended based on the cases considered below.

Two of the basic bond-slip tests presented in Chapter 3 have been replicated with FE models. As shown in Figure 4.12a, only one fourth of a specimen is modeled by taking advantage of the axial symmetry of the specimen. The experimental and numerical results are compared in Figure 4.12b and Figure 4.12c. It can be seen that the force-vs.-

displacement relations measured during the monotonic and cyclic tests are well reproduced in the FE analysis.

To evaluate the capability of the bond-slip law to simulate the radial dilatation caused by the wedging action of the ribs, bond-slip tests carried out by Lundgren (2000) and Plizzari and Mettelli (2009) have been modeled. Figure 4.13 plots the comparison between the FE model and experimental results for the pull-out tests conducted by Lundgren (2000) on bars embedded in concrete cylinders confined by a steel casing. The FE analysis results show a good correlation with experimental results not only for the force-displacement relations, but also for the strains measured in the steel casing when the inclination angle of the bond forces, θ , is taken as 45 degrees. If θ is equal to 60 degrees, the force-displacement relations do not vary, but the steel strains increase significantly. As shown in Figure 4.14a, the FE analysis is also able to reproduce the splitting failure of a large-diameter bar in a poorly confined specimen tested by Plizzari and Mettelli (2009) when θ is equal to 60 degrees. The splitting crack caused by the expansion of the steel-concrete interface can be observed from the maximum principal strain in the concrete, as shown in Figure 4.14b. However, if θ is taken as 45 degrees, a higher bond strength is obtained and the bond fails by the pull-out of the bar from the concrete rather than concrete splitting. In conclusion, the model is capable of reproducing the radial dilatation of the concrete-steel interface in an approximate manner. Based on these results and on the range of values provided in the literature, it is recommended that θ be equal to 60 degrees. This is a more conservative assumption because it increases the chances of inducing a splitting failure.

The development length test results obtained by Shima et al. (1989b) on a bar with a long embedment length subjected to a pull action have also been well replicated by the FE model. Figure 4.15 compares the FE analysis and experimental results in terms of the force-displacement relations at the loaded end of the bar, and the bar strain distribution along the embedment length. The small differences observed are related to the absence of a plateau in the stress-strain relation of the steel model, which characterizes the behavior of mild steel right after yielding.

Finally, the FE model shown in Figure 4.16 has been created to simulate the

behavior of an RC column tested by Lehman and Moehle (2000) with quasi-static lateral loading. In this model, the vertical bars are modeled with beam elements. The finite element meshes for the column and the footing are independently created and a contact condition has been imposed at their interface (see Figure 4.16b). This is a simple way in ABAQUS to introduce a discrete crack in the model at a location where large cracking is expected, and to overcome the limitation of the concrete model to simulate the opening and closing of cracks, as discussed in Section 4.3.2. The results presented in

Figure 4.17a show that the model is successful in predicting the lateral load capacity and force-displacement envelope. The hysteretic behavior is fairly well captured, even though the reloading branches are stiffer in the model. This difference is caused by the early resumption of contact in crack closing because of the insufficient stiffness degradation introduced in the damage model as shown in Section 4.3.2. This problem is only partially mitigated by the introduction of the contact condition at the column base but not at other locations in the column. The load decay observed at the end of the test was caused by the buckling and fracture of vertical bars at the base of the column, where a plastic hinge had formed. The model predicts the formation of the plastic hinge at the column base, but does not simulate bar buckling and fracture. Hence, the load drop observed in the test is not captured by the model.

Figure 4.17b shows that the FE model provides a good prediction of the strain penetration along the development length inside the footing, which indicates that the bond-slip behavior of these bars is well captured. However, the steel strains at the column-footing interface are overestimated. These differences are considered acceptable knowing that a small difference in bar stress can produce a large variation in strain in the post-yield regime, and that the post-yield stress-strain relation is approximated by a straight line in the model.

4.6 Summary and conclusions

A semi-empirical phenomenological bond stress-vs.-slip model has been presented in this chapter. This model requires the calibration of only three parameters and can be applied to any bar size and concrete strength. The model successfully reproduces

the monotonic and cyclic bond-slip behavior of the large-diameter bars tested in this study, as well as that of smaller bars tested by others. Implemented in an interface element in ABAQUS, it has shown good accuracy in simulating the bond-slip behavior of bars in well-confined concrete members. Also, through a simple representation of the wedging action of the ribs, it can capture splitting failures and bond decay due to the lack of confinement in an approximate manner.

Table 4.1: Bond-slip model parameters

Test	Bar size (No.)	f_c' [3] MPa (ksi)	τ_u MPa (ksi)		s_{peak} mm (in.)		s_R mm (in.)
			from tests	estimated	from tests	estimated	measured
Series 1	11	34.5 (5)	15.2 (2.20)	16.5 (2.40)	3.0 (0.12)	2.5 (0.10)	19.1 (0.75)
Series 2	14	34.5 (5)	16.5 (2.40)	16.5 (2.40)	2.8 (0.11)	3.0 (0.12)	24.9 (0.98)
Series 3	18	34.5 (5)	17.6 (2.55)	16.5 (2.40)	3.0 (0.12)	4.0 (0.16)	24.4 (0.96)
Series 4	14	55.2 (8)	23.8 (3.45)	23.4 (3.40)	- [1]	3.0 (0.12)	24.9 (0.98)
Eligehausen et al.	8	30 (4.35)	13.9 (2.00)	14.8 (2.15)	1.8 (0.07)	1.8 (0.07)	10.2 (0.40)
Lundgren	5	36 (5.2)	20.0 (2.90)	17.2 (2.50)	1.0 (0.04)	1.1 (0.04)	7.6 [2] (0.30)

[1] Monotonic bond stress-slip curve not available.
[2] Value estimated.
[3] For Series 1 through 4, it is based on the specified strength, which is very close to the average of the actual strengths measured.

Table 4.2: Plastic-damage model calibration

Parameter	Description	Values
α	Controls biaxial compressive strength	0.12
ψ	Dilation angle	20º
γ	Controls shape of the yield surface	1.91
w_c	Compression recovery factor	0
w_t	Tension recovery factor	1

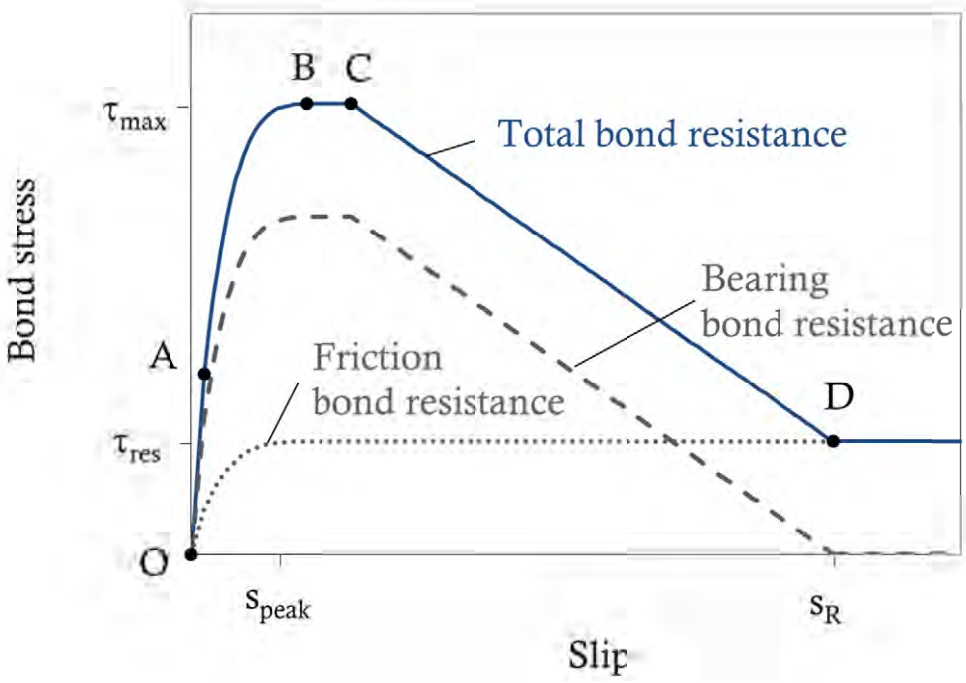

(a) Monotonic response

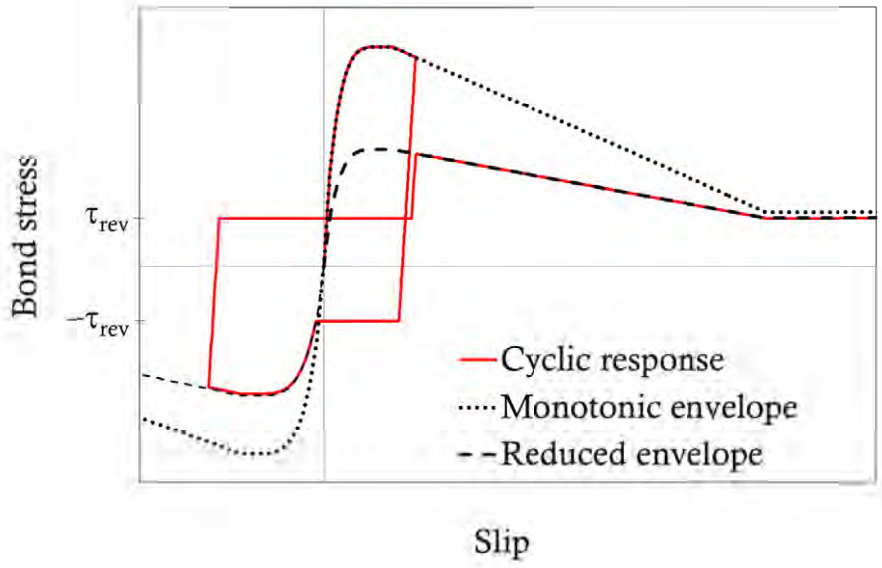

(b) Cyclic response

Figure 4.1: Analytical bond stress-slip law

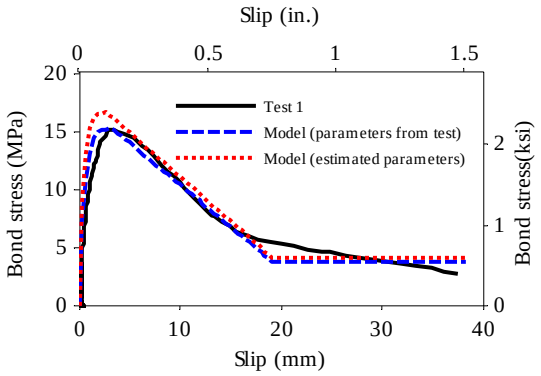

(a) No. 11, Series 1

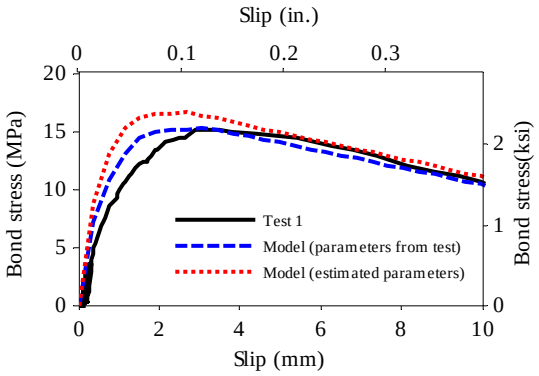

(b) Enlargement of (a) near origin

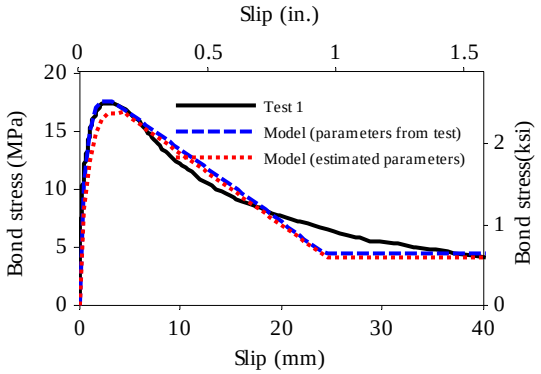

(c) No. 18, Series 3

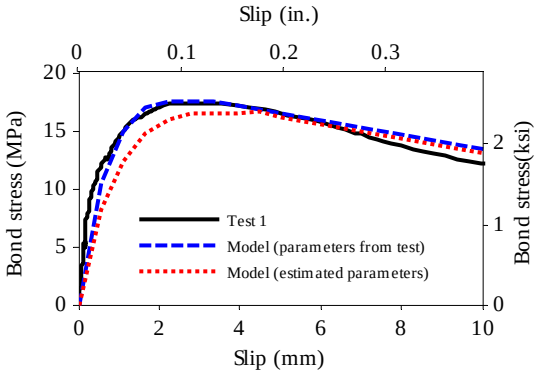

(d) Enlargement of (c) near origin

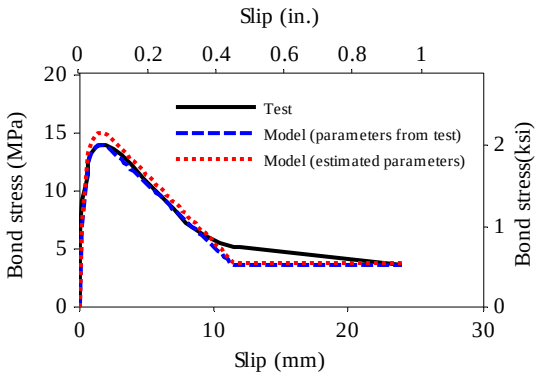

(e) No. 8, Eligehausen et al.

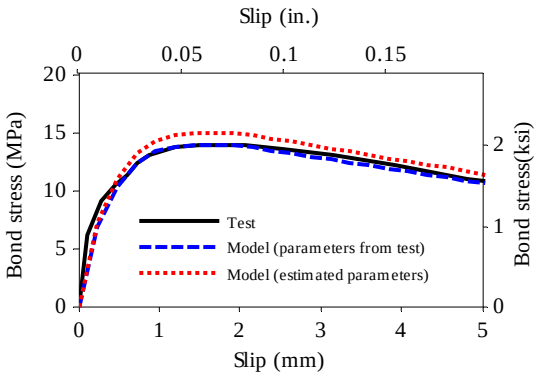

(f) Enlargement of (e) near origin

Figure 4.2: Analytical and experimental results for monotonic loading

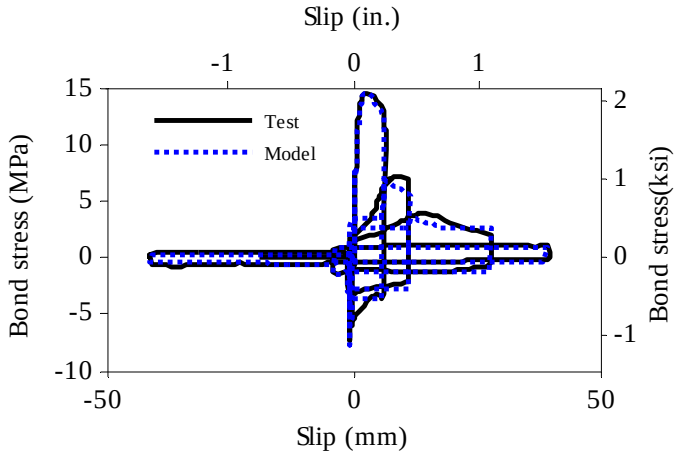

(a) Test 4, Series 1 (No. 11 bar, 5-ksi concrete)

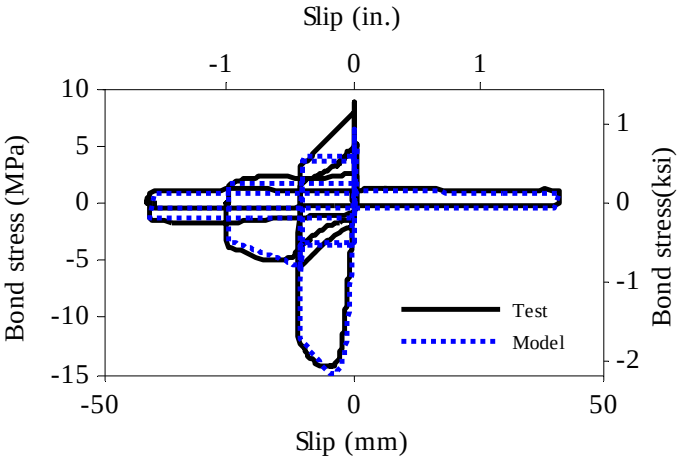

(b) Test 5, Series 3 (No. 18 bar, 5-ksi concrete)

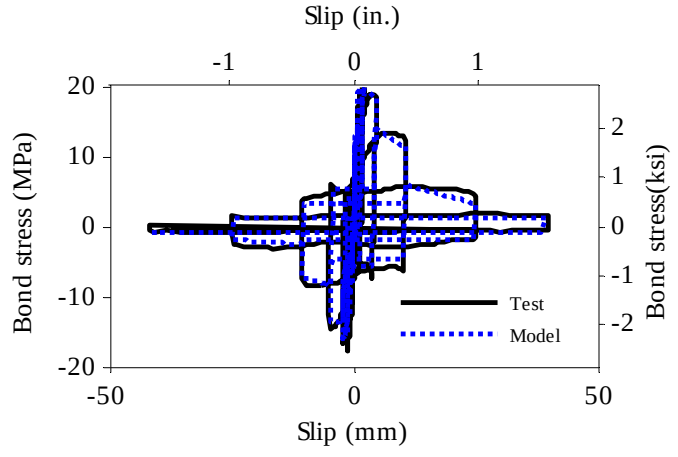

(c) Test 4, Series 4 (No. 14 bar, 8-ksi concrete)

Figure 4.3: Analytical and experimental results for cyclic loading

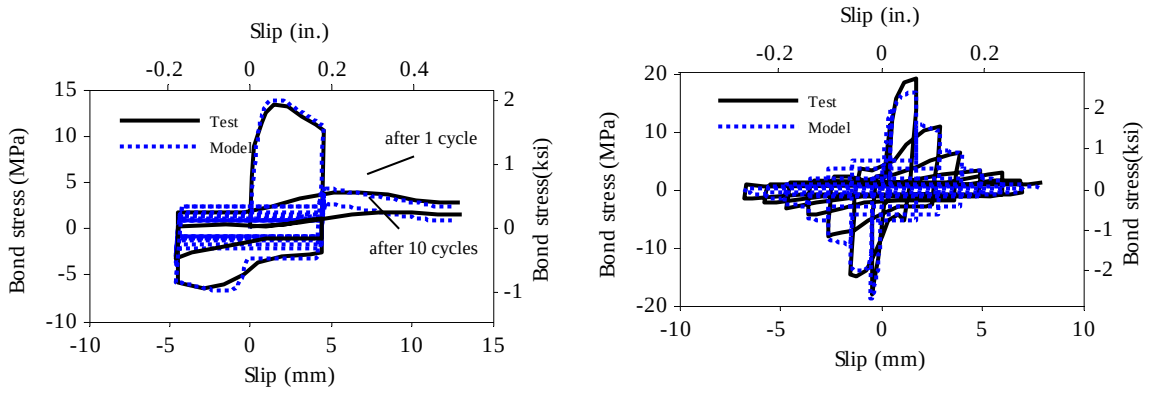

(a) No. 8 bar tested by Eligehausen et al. (b) No. 5 bar tested by Lundgren

Figure 4.4: Analytical and experimental results for tests conducted on No. 8 and 5 bars

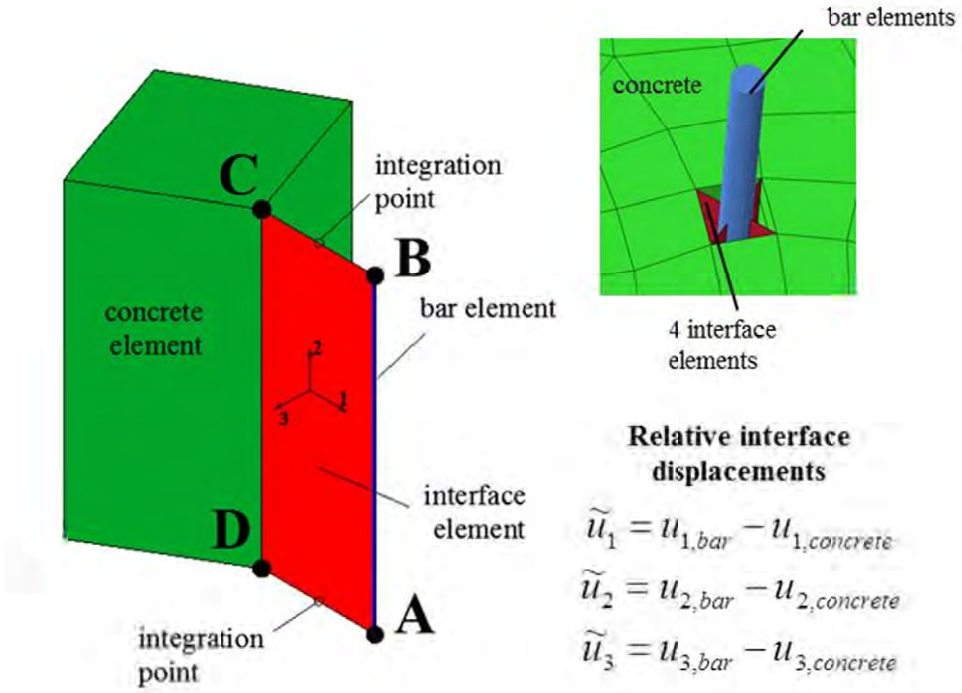

Figure 4.5: Interface element

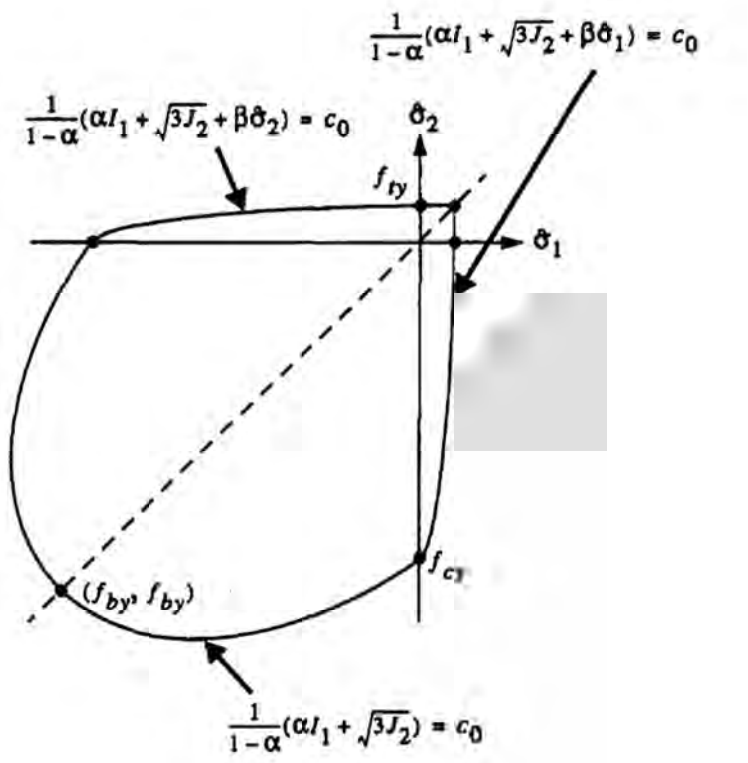

Figure 4.6: Initial yield function in plane-stress space (Lee and Fenves 1998)

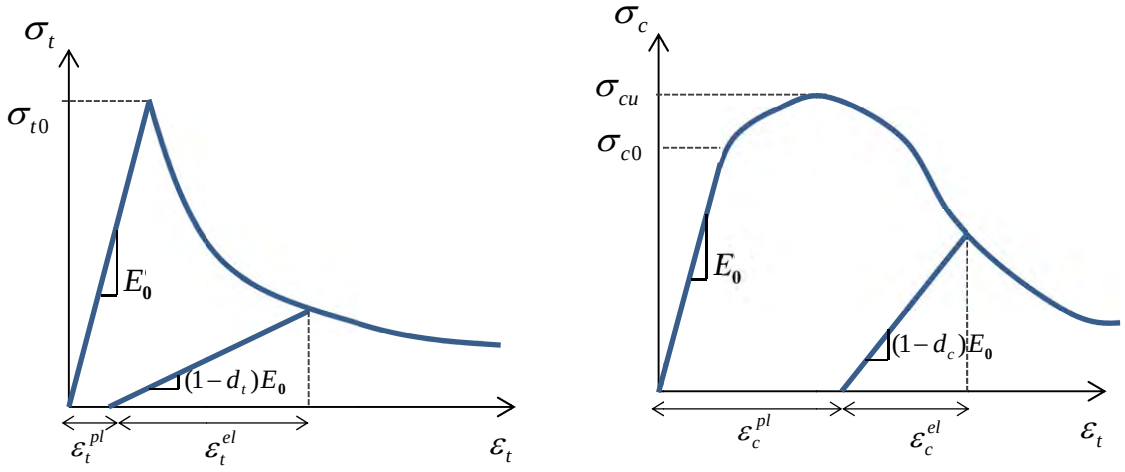

(a) Uniaxial tension

(b) Uniaxial compression

Figure 4.7: Uniaxial tension and compression behavior in plastic-damage model

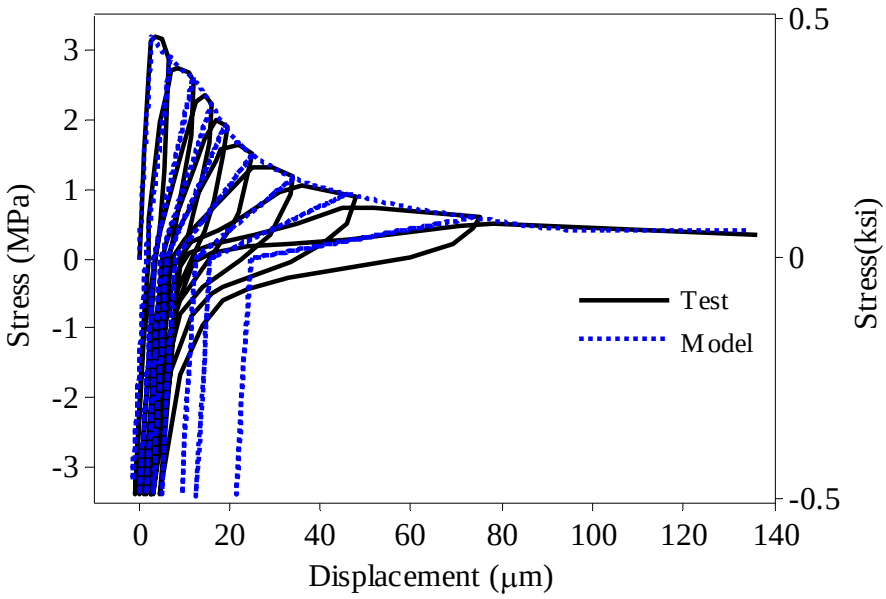

Figure 4.8: Tension-compression test by Reinhardt (1984b)

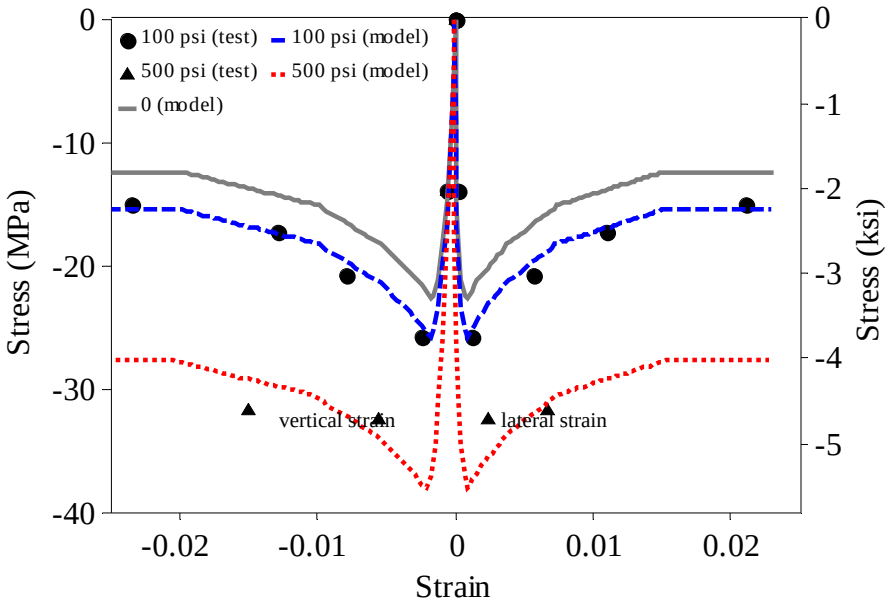

Figure 4.9: Confined compression tests by Hurblut (1985)

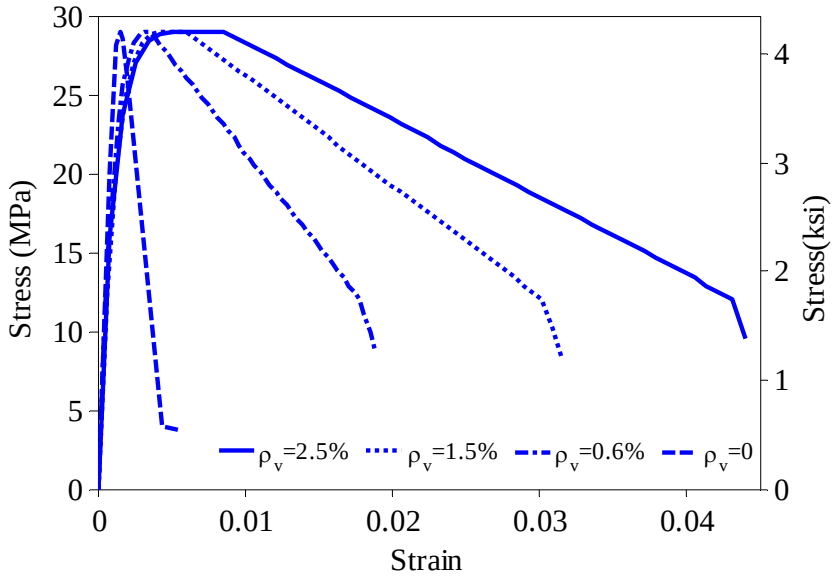

(a) Uniaxial compression curves input in concrete model

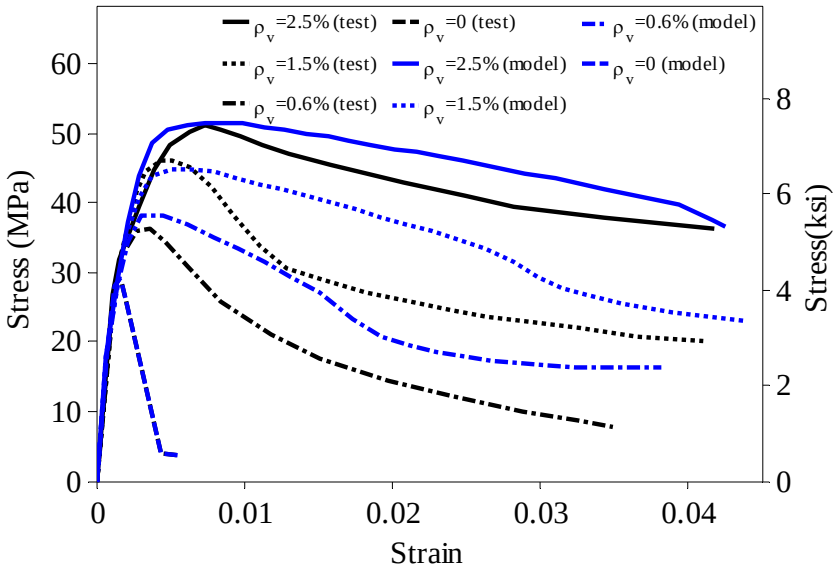

(b) Comparison between model and experimental results

Figure 4.10: Compression tests by Mander et al. (1989) on RC columns with different transverse reinforcement levels

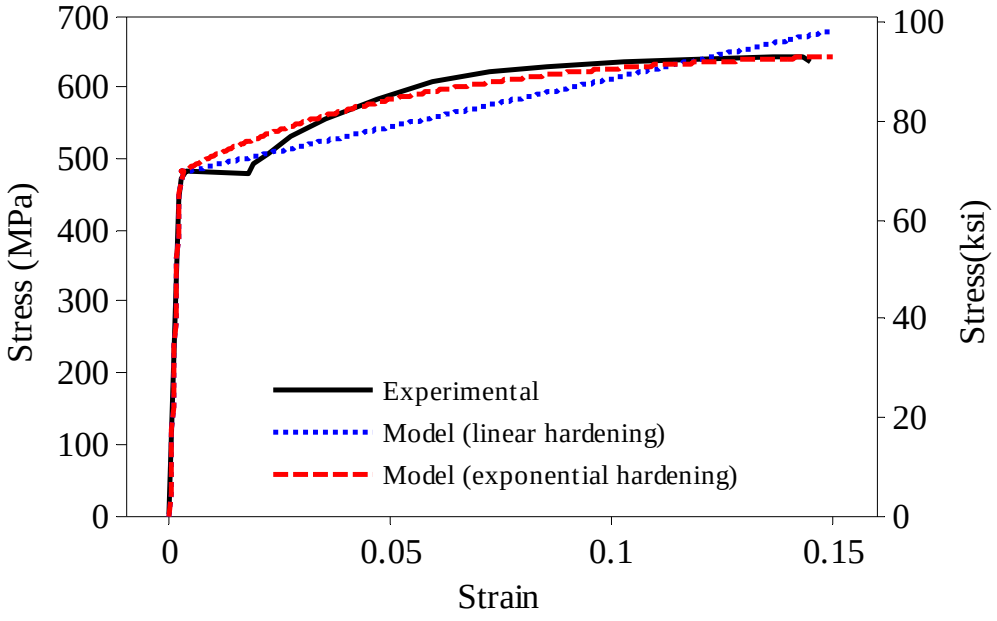

(a) Monotonic loading

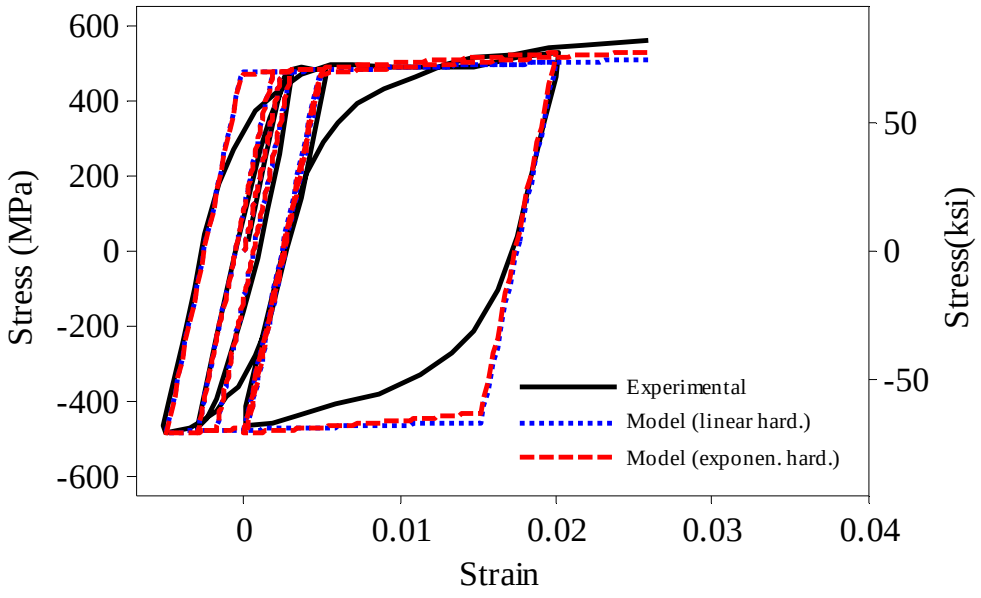

(b) Cyclic loading

Figure 4.11: Uniaxial tests on reinforcing steel coupons by Restrepo-Posada et al. (1993)

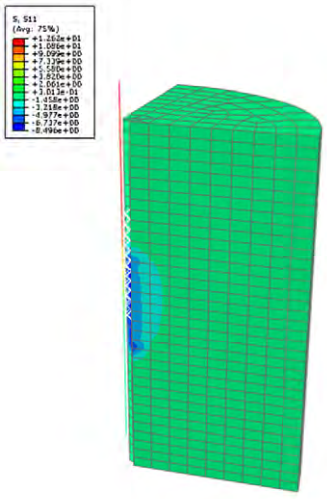

(a) FE model of test specimen

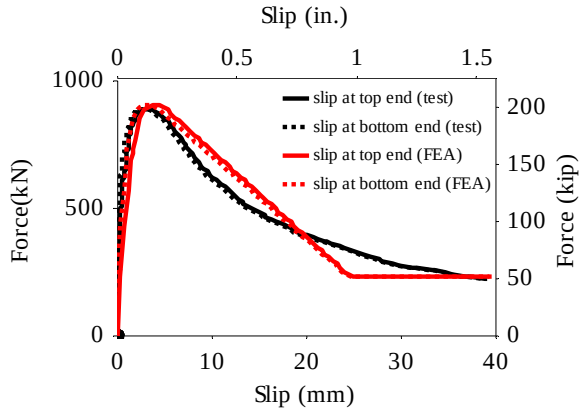

(b) Force vs. displacement for monotonic test (Test 1)

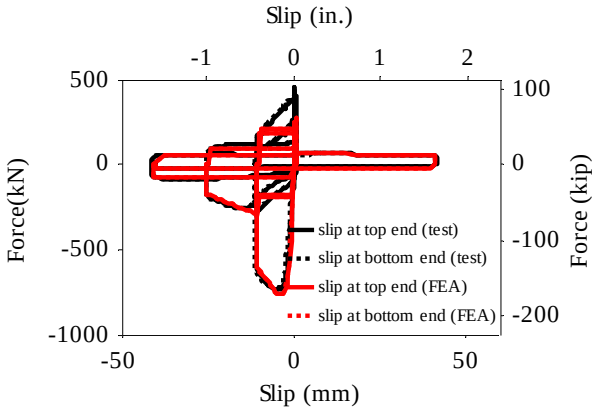

(c) Force vs. displacement for cyclic test (Test 5)

Figure 4.12: FE analysis of bond-slip tests on No. 18 bars (Series 3)

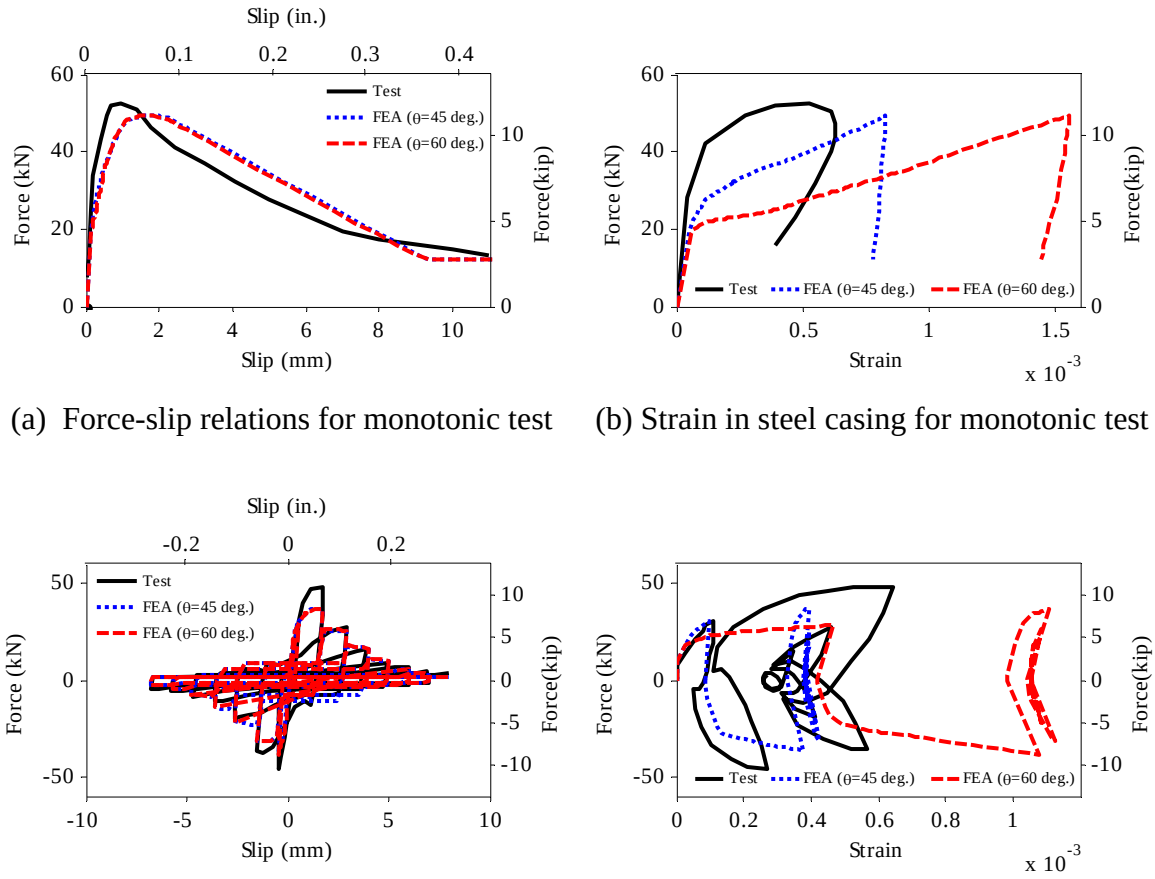

(a) Force-slip relations for monotonic test

(b) Strain in steel casing for monotonic test

(c) Force-slip relations for cyclic test

(d) Strain in steel casing for cyclic test

Figure 4.13: FE analysis of bond-slip tests by Lundgren (2000)

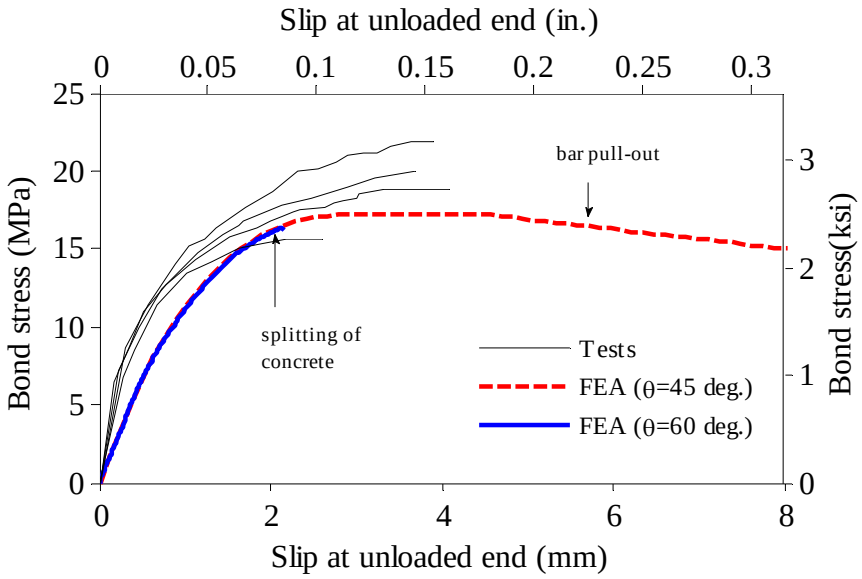

(a) Bond stress vs. slip at unloaded end

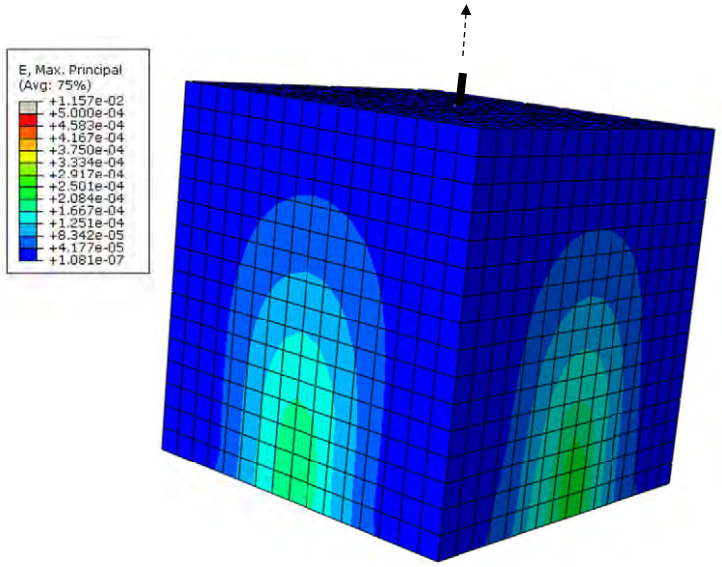

(b) Maximum principal strains in concrete from FE model at 2-mm (0.08-in.) slip (θ = 60 degrees)

Figure 4.14: FE analysis of bond-slip tests by Plizzari and Mettelli (2009)

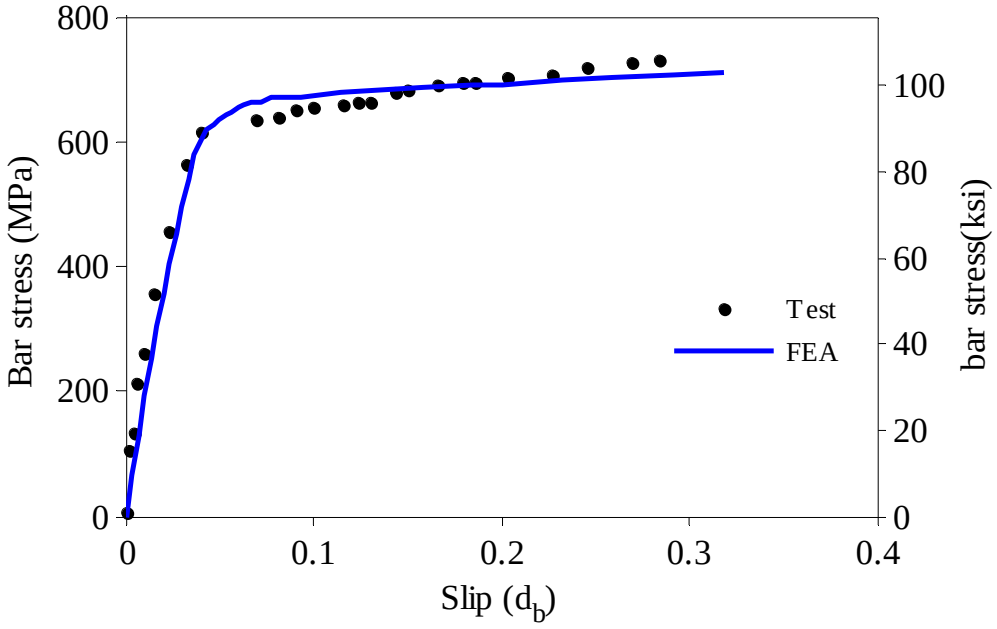

(a) Bar stress vs. displacement at loaded end

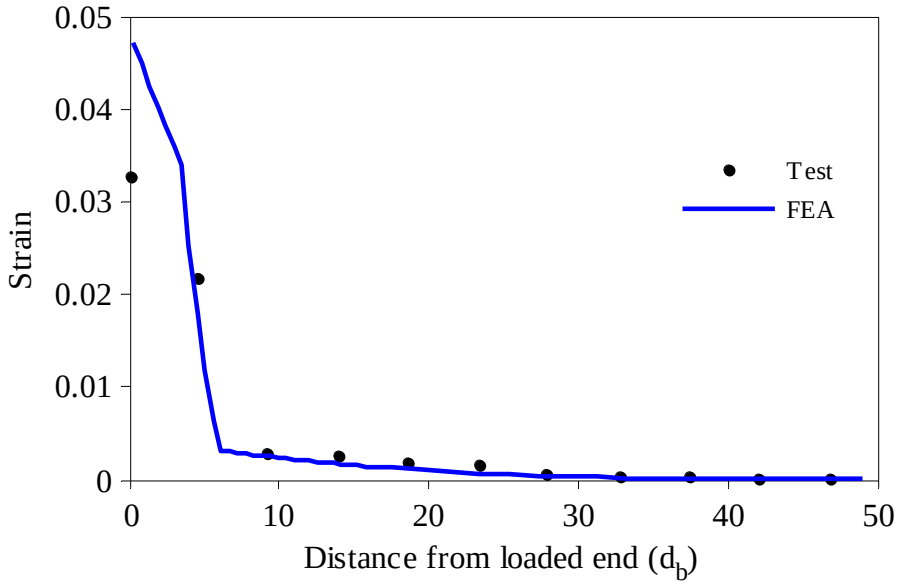

(b) Strain distribution at slip=0.225d_b

Figure 4.15: FE analysis of pull-out tests by Shima et al. (1989b)

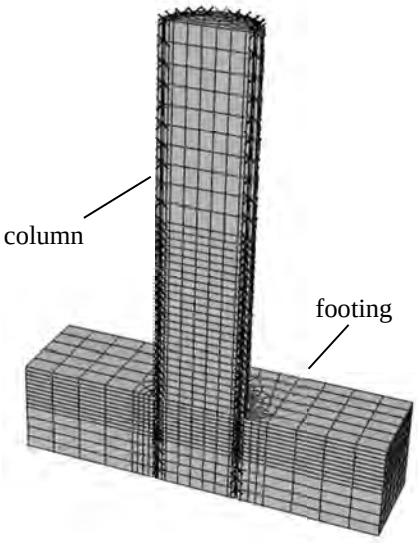

(a) Global view of the FE model

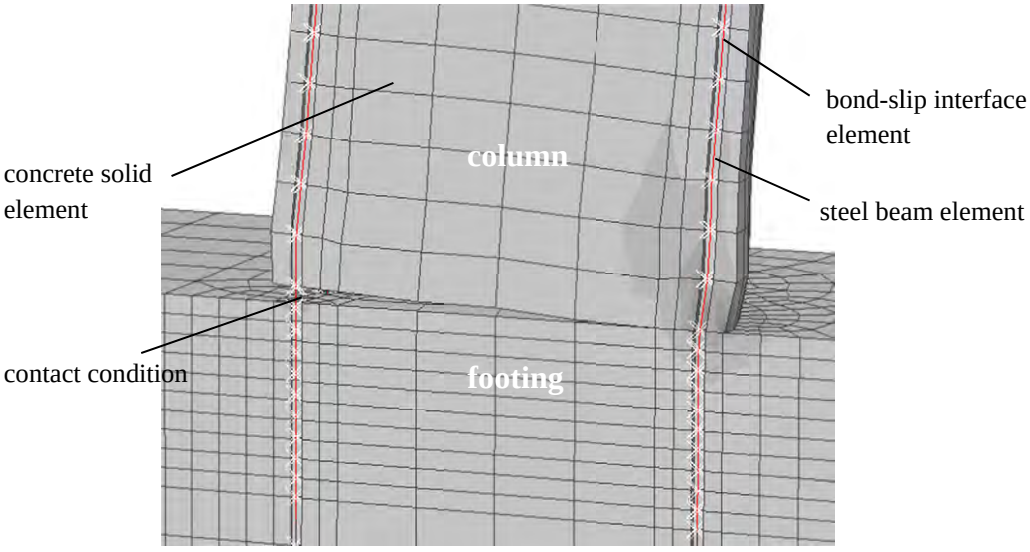

(b) Close-up view of the deformed shape near the column-footing interface

Figure 4.16: FE model of RC column tested by Lehman and Moehle (2000)

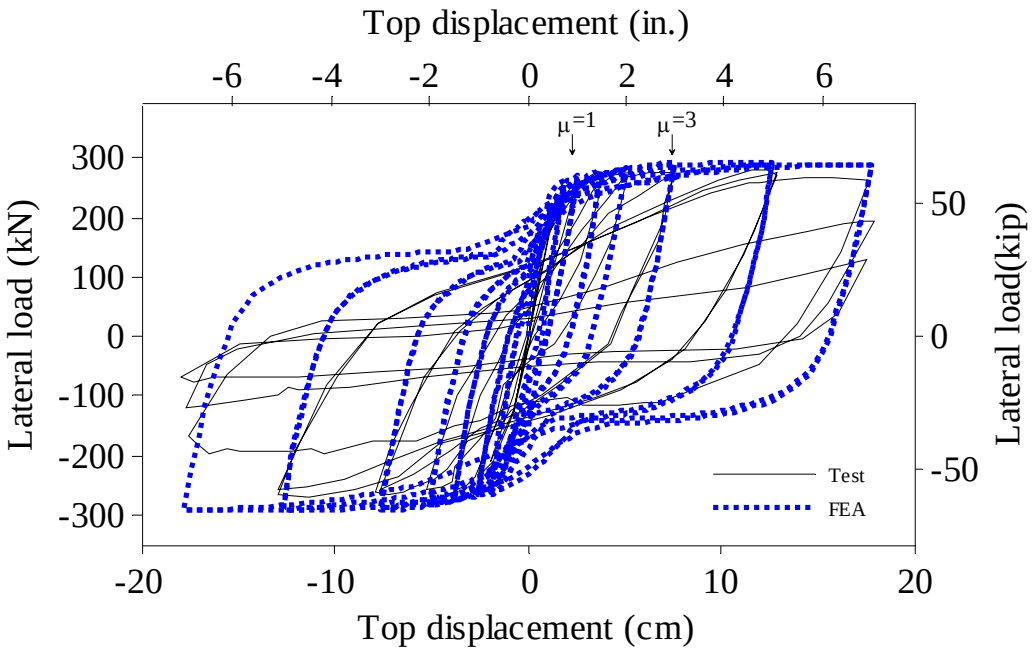

(a) Lateral load vs. top displacement

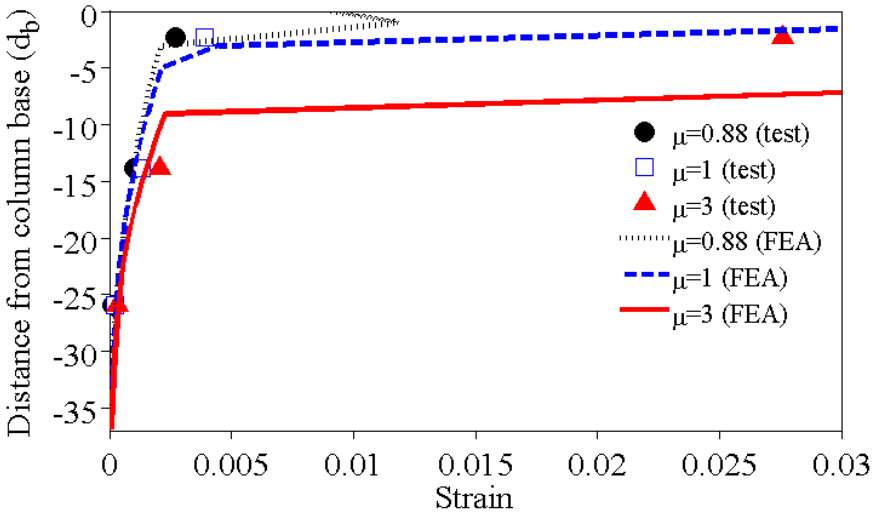

(b) Strain of vertical reinforcement embedded in footing

Figure 4.17: FE analysis of RC column tested by Lehman and Moehle (2000)

CHAPTER 5

DEVELOPMENT OF LARGE-DIAMETER BARS IN WELL-CONFINED CONCRETE

The development of large-diameter reinforcing bars embedded in well-confined concrete is studied in this chapter. Results of quasi-static pull-push tests conducted on No. 14 (43-mm) and 18 (57-mm) bars embedded in well-confined cylindrical concrete specimens are reported. These tests were to evaluate whether the tension development requirements stipulated in the AASHTO LRFD Bridge Design Specifications (AASHTO 2010) were adequate to develop the yield and tensile strengths of the bars under severe cyclic loading. These tests were also used to further evaluate the ability of a finite element (FE) model using the bond-slip element presented in Chapter 4 to capture the bond-slip behavior and predict the anchorage capacity of a bar. Once validated, additional FE analyses have been carried out in a parametric study to investigate how the tension capacity of bars anchored in well-confined concrete varies with the embedment length for bars of different sizes and steel and concrete of different strengths. Finally, a Monte Carlo simulation has been conducted to determine the reliability level of the AASHTO LRFD specifications on the development of large-diameter bars in well-confined concrete considering uncertainties in material properties and construction quality. Based on this study, a possible code improvement has been suggested.

5.1 Pull-push tests on large-diameter bars

Three cyclic pull-push tests were conducted on No. 14 (43-mm) and 18 (57-mm) bars embedded in well-confined cylindrical concrete specimens to check whether the development length requirements stipulated in the AASHTO LRFD Bridge Design Specifications (AASHTO 2010) were adequate to develop the yield and tensile strengths of the bars when they were subjected to severe cyclic tension and compression. Two tests, one for each bar size, were conducted with development lengths complying with the AASHTO specifications. An additional test was conducted on a No. 18 bar with a shorter embedment length. In these tests, the axial strains developed along the embedded portions of the bars were measured to deduce the extent of bond deterioration and to validate finite element models.

5.1.1 Test setup, instrumentation, and loading protocol

The geometries, reinforcing details, and instrumentation of the test specimens are shown in Figure 5.1. The same types of reinforcing bars, concrete mix design, and confinement level used in the basic bond-slip tests presented in Chapter 3 were employed. Tests No. 1 and 2 were conducted on a No. 14 bar and a No. 18 bar, respectively, with embedment lengths, l_e, equal to the tension development lengths required by the AASHTO LRFD Bridge Design Specifications (AASHTO 2010). The development lengths were determined based on the targeted concrete compressive strength of 34.5 MPa (5 ksi). They were obtained by multiplying the basic tension development lengths by a compounded reduction factor of 0.6 as permitted by AASHTO since the specimens met all the necessary conditions on the minimum clear concrete cover for the loaded bars, and the minimum diameter and maximum spacing of the transverse reinforcement. Test No. 3 was done on a No. 18 bar with an embedment length equal to 60% the development length required by the AASHTO specifications. This length was determined to be sufficient to yield the bar and sustain a small amount of strain hardening based on a pre-test FE analysis with a model that will be presented with more details in Section 5.2. Specimens 2 and 3 were tested when the compressive

strength of the concrete was very close to 34.5 MPa (5 ksi). For Specimen 1, the compressive strength of concrete was only 29.3 MPa (4.25 ksi) on the day of the test. The bar size, embedment length, actual material strengths, and test results for each specimen are summarized in Table 5.1. The yield strength (f_y) and tensile strength (f_u) of the bars were obtained from material tests on bar specimens.

All the specimens were cast with the bars in an upright position. However, Specimen 1 was later rotated and anchored to a strong wall to be tested horizontally. The bar was pulled from and pushed into the concrete using a servo-controlled hydraulic actuator attached to a reaction block, which was anchored to the strong floor. This test setup is shown in Figure 5.2a. The test setup was changed for Specimens 2 and 3, as shown in Figure 5.2b. These specimens were cast and tested in an upright position for the sake of convenience. In this setup, the actuator was attached to a steel reaction frame secured to the footing of the specimens. In both test setups, the reaction of the pull-push force was not transferred to the concrete surrounding the bar, which closely represented the situation for bar slip in a real structure.

The instrumentation of these specimens is presented in Figure 5.1. Strain gages were attached to the bar at different heights to obtain the longitudinal strain distribution along the embedded length during the test. In Specimens 1 and 2, strain gages were also placed in two perimeter bars to monitor the transfer of the tensile force from the pulled bar to these bars. In Specimen 3, strain gages were attached to the transverse reinforcement at two locations to monitor the hoops strains introduced by bar slip. The exact locations of the strain gages for each specimen are given in Table 5.2. In addition, the displacement of the bar at the loaded end was monitored during the test. Since the top concrete surface was expected to be damaged during the test, this displacement was measured relative to a point 150 mm (6 in.) below the top of the concrete cylinder. For this purpose, two displacement transducers were secured to the two opposite sides of the concrete cylinder at this elevation. The other end of each transducer was attached to a horizontal metal rod welded to a collar, which was secured to the bar at a position right above the concrete surface. Pictures of the setup to measure bar slip are shown Figure 5.2c and Figure 5.2d. Pictures of specimen construction are provided in Appendix A.

The loading protocol is presented in Table 5.3. The bars were subjected to load cycles of increasing displacements in tension with two cycles at each amplitude. The first six cycles of each test were under force control. The amplitudes of the tensile and compressive forces applied in each cycle were set to be fractions of the expected yield force of the bar, which was based on the expected yield strength of 469 MPa (68 ksi), while the maximum compressive force applied was limited to 50% of the expected yield to avoid bar buckling. After the tensile force applied to the bar reached 75% of the expected yield force, the test was switched to displacement control but with the maximum compressive force limited to 50% of the expected yield. In each cycle, the displacement amplitude in tension was specified in terms of an integer multiple of the maximum displacement reached in Cycle 5 (the first cycle at 75% of the yield force). Failures of the specimens occurred with either bar fracture or the pull-out of the bar from the concrete.

5.1.2 Test results

Plots of the bar stress against the displacement of the bar at the top of the anchorage zone for Tests No. 1 through 3 are presented in Figure 5.3 and Figure 5.4. In Test No. 1, the No. 14 bar yielded in tension and sustained significant inelastic deformation before it was pulled out from the concrete cylinder. As shown in Figure 5.3b, the stiffnesses exhibited by the stress-displacement relations in tension and compression were very similar before the bar yielded in tension at a displacement of 1 mm (0.04 in.). After yielding, the displacement at the loaded end increased with little increase in the pull force. The maximum pull force was reached at a displacement of 76 mm (3.0 in.). This load corresponds to 98% of the tensile strength of the bar, which was obtained from material tests. After this point, the load dropped with increasing displacement due to the failure of the anchorage. The load tended to stabilize at a residual resistance that was one third of the peak load when the displacement reached 140 mm (5.5 in.). This residual resistance was contributed by the friction bond strength of the bar as explained in Chapters 3 and 4. At this point, the test was stopped. As the bar was being pulled out from the cylinder, pulverized concrete remained attached to the bar between

the ribs, as shown in Figure 5.5. Furthermore, a cone-shaped concrete piece, approximately 50-mm (2-in.) deep and 125 mm (5 in.) in maximum diameter was detached from the top of the concrete cylinder as shown in Figure 5.5a.

In Test No. 2, the No. 18 bar yielded and reached its ultimate strength, which was followed by bar necking and fracture. The bar yielded in tension at a displacement of 1.5 mm (0.06 in), which is higher than that for the No. 14 bar. The tensile strength of the bar was reached at a displacement of 60 mm (2.35 in.). After this, the load dropped, which was not caused by the failure of the anchorage, but due to bar necking. The bar fractured at a location right below the surface of the concrete cylinder when the displacement was 93 mm (3.66 in.). Even though there was no anchorage failure, widely-open splitting cracks were visible at the top surface of the concrete cylinder, as shown in Figure 5.6. These cracks radiated from the bar to the outer surface of the concrete cylinder and extended vertically 125 mm (5 in.) down from the top surface (see Figure 5.6a). In addition, a circumferential horizontal crack was observed at this depth. Post-test inspection of the specimen revealed that this horizontal crack was an extension of a 200-mm (8-in.) deep cone-shaped crack. Figure 5.6c shows the shape of the crack surface after the upper concrete piece was removed. The use of a larger bar with larger ribs generates larger splitting forces in the concrete. This explains the more severe damage induced on the concrete specimen in Test No. 2. Results from these two tests indicate that the AASHTO LRFD Bridge Design Specifications (AASHTO 2010) on the development lengths of these bars are appropriate. The bars were able to yield and develop significant strain hardening with bar fracture occurring in Test No. 2.

Even though the bar in Test No. 3 had an embedment length significantly shorter than the development length required by the AASHTO specifications, it was able to yield and experience a small amount of strain hardening before the bar anchorage failed. The response before the bar yielded in tension was very similar to that of Test No. 2. However, the bar yielded in tension at a displacement of 1.9 mm (0.075 in), which is 25% larger than that in Test No. 2. This reduction in stiffness was caused by the shorter embedment length in Test No. 3. The maximum pull force was reached at a displacement of 5.9 mm (0.23 in.) when the bar stress was 10% higher than its actual yield strength

with a tensile strain of 1.7% at the pulled end. There was extensive bond failure, which resulted in larger displacements in compression as compared to Test No. 2, and a steady reduction of the load capacity in tension until the bar was completely pulled out from the concrete cylinder. Pictures of the specimen at the end of the test are shown in Figure 5.7. Pulverized concrete was observed between the ribs of the bar as it was being pulled out from the concrete cylinder. A crack pattern similar to that in Test No. 2 was observed in the upper portion of the concrete specimen, with widely-opened splitting cracks and a large concrete cone detached from the top of the specimen.

The strains measured in the loaded bars provide useful information to understand the bond deterioration along the embedment length. The strains at different locations along the length and at different stages of the tests are plotted in Figure 5.8. In this and subsequent figures, the reference position for the strain gages is the top surface of the concrete specimen (see Table 5.2), which is referred to as the "loaded end". The displacement at the loaded end of a bar is due to the strain penetration inside the embedment zone. After the anchorage failed in Tests No. 1 and 3, the displacement was mainly contributed by the rigid body displacement of the bar. Results obtained from the tests indicate that there was a significant penetration of plastic strain inside the embedment zone. As explained in Chapter 4, bond resistance will drop significantly at locations where the bar has yielded, which will exacerbate the plastic strain penetration as the bar undergoes strain hardening. For Test No. 1, plastic strains were measured up to a depth of $18\,d_b$ at a slip of 75mm (3 in.), prior to the anchorage failure, as shown in Figure 5.8a. With the total embedment length of $26\,d_b$, this means that the lowest $8\,d_b$ of the embedment length was sufficient to develop the yield stress in the bar. In Test No. 2, the maximum plastic strain penetration was at least $11\,d_b$, or 44% of the total embedment length, which is $25\,d_b$. Despite this significant plastic penetration, the bar was able to reach its tensile strength and fracture. In Test No. 3, the maximum plastic strain penetration was at least $3.5\,d_b$, or 30% of the total embedment length, which is $14\,d_b$, before the anchorage failed. This means that the lowest $10.5\,d_b$ of the embedment length was sufficient to develop the yield force but not the tensile strength. The bond resistance

in this region had probably suffered significant deterioration because of the more severe bar slip as compared to the other two specimens.

The strains measured in the perimeter bars provide further information to understand the damage observed in the test specimens and the transfer of the tensile force in the pulled bar to the surrounding concrete and reinforcing bars. The strains measured at two different heights of a perimeter bar at different stages of Tests No. 1 and 2 are plotted in Figure 5.9. These results show that the tensile strains in these bars increased with the depth. This was caused by the progressive transfer of the tensile force from the central bar with respect to the depth. These strains were much larger in Test No. 2 than in Test No. 1, as shown in Figure 5.9. To understand this difference, the strains measured in these bars close to the end of the tests are compared with the strain distributions calculated with two simple analytical models in Figure 5.10. In both models, the bond stress on the bar being pulled out is assumed uniform for simplicity. The first model assumes that the concrete is uncracked and that both the concrete and the perimeter bars remain linearly elastic. The tension force from the pulled bar is transferred to the concrete and perimeter bars, which experience the same axial strain at a given cross section. For this model, the modulus of elasticity of the concrete is estimated with the ACI 318-08 (ACI 2008) formula. In the second model, the tension force from the pulled bar is transferred to the perimeter bars through a truss mechanism as adopted by McLean and Smith (1997) and others. The force transfer mechanism in this model is shown in Figure 5.11. The struts in Figure 5.11 are assumed to have a 45-degree inclination and transmit a uniform force. As shown in Figure 5.10a, the strains in the perimeter bar for Test No. 1 show a better match with the first model. According to this model, the concrete would be subjected to a maximum vertical tensile stress of 1.2 MPa (0.18 ksi), which is half of the tensile strength of 2.5 MPa (0.36 ksi) obtained from split-cylinder tests. This is in agreement with the fact that no cracks perpendicular to the bars were observed in the concrete specimen. In Test No. 2, horizontal cracks were actually observed at different heights along the concrete cylinder. For this reason, the first model, which assumes that the concrete behaves elastically, significantly underestimates the strains in the perimeter bars, as shown in Figure 5.10b. For Test No. 2, the truss analogy results in a strain

variation that matches well the strain reading from the upper gage, but overestimates the strain at the lower gage. This can be explained by the fact that the bond stress and, thereby, the strut force along the splice length is not uniform in reality. Hence, results from these two tests indicate that the truss analogy assuming a uniform bond stress, as it has been often assumed, may not provide a good representation of the tensile force transfer in a non-contact lap splice.

The strains measured in the spiral reinforcement in Test No. 3 indicate that significant hoop strains were induced by bar slip. As shown in Figure 5.12, the tensile strains in the spiral reached 10^{-3} and $4 \cdot 10^{-4}$ at depths of $1.8\,d_b$ and $7.1\,d_b$, respectively, when the slip of the bar was 25 mm (1 in.). At a slip of 50 mm (2 in.), the strains dropped significantly because the concrete between the bar ribs was completed sheared off thus eliminating the wedging action of the ribs.

5.2 Finite element modeling of pull-push tests

Finite element analyses have been conducted to simulate the pull-push tests presented in Section 5.1. The purpose of these analyses is to validate the bond-slip constitutive law presented in Chapter 4 and gain more insight into the bond-slip behavior in the pull-push tests. For these analyses, three-dimensional models presenting one quarter of a test specimen have been employed by taking advantage of the axial symmetry of the specimens. Figure 5.13 shows the FE model for Test No. 3. The constitutive models for the concrete, steel, and bond-slip behavior used here are the same as those presented in Chapter 4. The reinforcing bars are modeled with elasto-plastic truss elements with the exponential hardening law. The concrete and steel models are calibrated to the material strengths obtained from the material samples of the respective specimens, while the bond-slip model is calibrated according to the method recommended in Chapter 4.

Results from the FE analyses for Tests No. 1, 2, and 3 are compared to the experimental results in Figure 5.14 in terms of the bar stress-vs.-displacement relations at the loaded end of the bar. Not only the experimentally obtained relations are well

replicated by the models, but the failure modes are also captured. For Test No. 1, the pull-out of the bar is predicted by the model. For Test No. 2, the model shows that the bar reaches its tensile strength as it actually happened in the test. However, the load degradation due to bar necking and bar fracture is not captured by the FE model because the steel model does not account for these features. For Test No. 3, the early pull-out of the bar after yielding and the cyclic deterioration of the anchorage capacity are well replicated.

The match between the FE analysis and experimental results in terms of the distributions of the tensile strain in the bar along the embedment zone at different stages of the tests is reasonably good, as shown in Figure 5.8. The analysis results complement the discrete data points obtained from the tests and provide a better estimation of the plastic strain penetration in the bars. These results show that the extents of the plastic strain penetration developed in Tests No. 1, 2, and 3 at the peak loads are $18\,d_b$, $13\,d_b$, and $4\,d_b$, respectively. For Test No. 2, in which the full tensile strength of the steel was reached, the extent of plastic strain penetration represents 52% of the total embedment length, while it is 69% for Test No. 1, in which the bar stress reached 98% of its tensile strength. This can be attributed to the fact that Test No. 1 has a weaker concrete and, thereby, a lower bond strength, which leads to a larger plastic strain penetration.

The distributions of the axial stresses in the bars along the embedment zones obtained from the FE analyses are plotted in Figure 5.15 through Figure 5.17. The bond stresses are calculated from the gradient of the axial stress distributions, and are plotted in Figure 5.18 through Figure 5.20. Tests No. 1 and 2, in which the bars had the embedment lengths satisfying the AASHTO LRFD Bride Design Specifications (AASHTO 2010), the bond stress distributions are highly nonlinear. The maximum bond stress develops at a location slightly below the top of the embedment zone when the bar behaves elastically. Once the bar yields in tension, the plastic strain penetrates inside the embedment zone and the location of the peak bond stress moves downward. The maximum bond stresses shown in Figure 5.18 through Figure 5.20 are smaller than the peak bond strength obtained in the basic bond-slip tests presented in Chapter 3. The reason is that the bars yield in tension before this peak strength has been reached. The yielding of the bars

introduces significant lateral contraction, which weakens the bond capacity. This is accounted for in an empirical fashion in the bond-slip law. In compression, the maximum bond stress is also smaller than the specified peak value due to the limited downward slip of the bar and the bond deterioration introduced by the large upward slip. Figure 5.18b and Figure 5.19b show that even though the compressive forces in the bar in the first and last cycles are the same, the bond stresses are quite different due to the progressive bond deterioration.

The bond stress distributions for Test No. 3, as plotted in Figure 5.20, are more uniform than those for the previous cases. This stems from the fact that the slip of the bar becomes more uniform once it starts to be pulled out from the concrete. Towards the end of the test, the bond resistance is very low due to the complete loss of the bearing resistance and the deterioration of the frictional resistance. Despite this severe deterioration, the bar is still able to develop 50% of the yield strength in compression at this stage (see Figure 5.20b) primarily due to the bearing of the tip of bar against the concrete at the bottom of the anchorage. The model is also successful in reproducing the dilatation caused by bar slip in a satisfactory way. As shown in Figure 5.12, the strains in the transverse reinforcement in Test No. 3 from FE analysis match the experimental measurements relatively well. However, the reduction of the dilatation effect observed experimentally at very large slips is not well captured due to the inability of the concrete model to adequately simulate the closing of the splitting cracks, as pointed out in Chapter 4. The FE model can reproduce the axial strain variation along the perimeter bars in Test No. 1, as shown in Figure 5.9a. These strains were very small in the test because the concrete was capable of carrying the tensile force developed by the pulled force. However, as shown in Figure 5.9b, the model underestimates the strains in the perimeter bars in Test No. 2 because it overestimates the tensile capacity of the concrete and, therefore, it does not capture the horizontal cracking of the concrete specimen.

5.3 Tension capacity of bars in well-confined concrete

Finite element analyses have been conducted to investigate how the tension capacity of bars anchored in well-confined concrete varies with the embedment length for

bars of different sizes and steel and concrete of different strengths, and to identify the minimum embedment length required to develop the yield and tensile strengths of a bar. For this purpose, a total of 120 pull-push tests have been simulated with FE models. The models have the same concrete cylinder dimensions and confining reinforcement as the test specimens presented in Section 5.1. The bar sizes considered are No. 11, 14, and 18 bars. For each bar size, ten different embedment lengths, namely, lengths equal to 4, 8, 12, 16, 20, 24, 28, 32, 36, and 40 times the bar diameter, have been considered. Three different compressive strengths of concrete have been used: 24.1 MPa (3.5 ksi), 34.5 MPa (5 ksi), and 48.3 MPa (7 ksi). The tensile strength of the concrete has been assumed to be equal to 10% of the compressive strength. The bond strength has been assumed to be 16.5 MPa (2.4 ksi) for 34.5-MPa (5-ksi) concrete and proportional to $f_c'^{3/4}$ for the other concrete strengths, as proposed in Chapter 4. Steel bars with yield strengths of 469 MPa (68 ksi) and 586 MPa (85 ksi) have been considered. The tensile strength of the steel has been assumed to be equal to 1.4 times the yield strength. The embedment length, bar size, and the concrete and steel strengths for each of the analyses are presented in Table 5.4.

The loading protocol used in the parametric study is presented in Table 5.5. This protocol is slightly different from that used in the tests. Since bars are not expected to yield in tension in some of the analyses, which have short embedment lengths, the positive (pull direction) displacement amplitude of each cycle is prescribed as a fraction or an integer multiple of the displacement at which the bar of the same size yielded in the actual test specimen that had the development length complying with the AASHTO LRFD specifications. For the No. 11 bar, which was not tested, this value has been estimated with a finite element analysis. The amplitude in compression is defined as a fraction of the expected yield force of the bar in the first few cycles; but for the later cycles, the compressive force imposed exceeds the yield force to have a more demanding situation.

Table 5.4 shows the ratios of the maximum tensile stress developed at the pulled end of the bar, $\sigma_{\max}$, to the yield strength of the steel, f_y, obtained from the analyses. These results show that the yielding of a bar can be achieved with an embedment length

as short as 8 to 12 times the bar diameter, and the tensile strength of the steel can be developed with an embedment length that is 20 to 32 times the bar diameter, depending on the compressive strength of the concrete and the yield strength of the bar. Figure 5.21 shows the plot of the $\sigma_{\max} / f_y$ ratio against the normalized embedment length l_e / d_b. While there is a general tendency that the normalized tensile strength increases with the increase of the normalized embedment length, there is a large scatter in the tensile capacities for a given normalized embedment length due to the variation in the compressive strength of the concrete and the yield strength of the steel. As expected, increasing the steel strength and decreasing the concrete strength decreases the $\sigma_{\max} / f_y$ ratio.

The relation between the tension capacity of a bar embedded in concrete and the embedment length, bar size, compressive strength of concrete, and yield strength of steel can be established as follows. For a bar of diameter d_b subjected to a tensile force at the free end, the following equilibrium condition holds when a pull-out failure occurs.

$$\sigma_{\max} \frac{\pi d_b^{\,2}}{4} = \tau_{u,av} \pi d_b l_e \tag{5.1}$$

in which $\sigma_{\max}$ is the maximum tensile stress developed in the bar, and $\tau_{u,av}$ is the average bond stress along the embedment length, l_e. Dividing both sides of Equation 5.1 by the yield strength of steel and rearranging the terms, one has

$$\frac{\sigma_{\max}}{f_y} = \frac{4\tau_{u,av} l_e}{f_y d_b} \tag{5.2}$$

Assuming that the average bond stress is proportional to the compressive strength of the concrete to the power κ, one can rewrite Equation 5.2 as

$$\frac{\sigma_{\max}}{f_y} = \chi \frac{f_c'^{\kappa} l_e}{f_y d_b} = \chi \lambda_e \tag{5.3}$$

in which χ is a proportionality constant and λ_e is defined as:

$$\lambda_e = l_e \frac{f_c'^{\kappa}}{f_y d_b} \tag{5.4}$$

Note that neither χ nor λ_e is dimensionless, and that the value of χ may vary with the embedment length and, thereby, λ_e because the bond stress distribution along the embedment zone may change as the embedment length changes. Therefore, it is more appropriate to express Equation 5.3 in the following general form.

$$\frac{\sigma_{\max}}{f_y} = f\left(\lambda_e\right) \tag{5.5}$$

To characterize the above relation, the values of $\sigma_{\max} / f_y$ obtained from the FE analyses are plotted against λ_e assuming different values of κ. Most design codes assume that the average bond strength is proportional to $f_c'^{1/2}$, while the local bond strength assumed in the FE models is proportional to $f_c'^{3/4}$. Figure 5.22 through Figure 5.24 show the plots of $\sigma_{\max} / f_y$ against λ_e for values of κ equal to 0.5, 0.75, and 1, respectively. It can be seen for all three cases that a tri-linear relation ending with a horizontal line provides a good correlation with the numerical results. The horizontal line corresponds to the tensile strength of the bars, which is assumed to be 1.4 times the yield strength in the analyses. The expressions for the other two lines that provide a best fit of the data are determined with the least-squares method. The goodness of fit is measured by the coefficient of determination, R^2, which is calculated for the lines obtained for the different values of κ. The R^2 values are shown in Figure 5.22 through Figure 5.24. It can be seen that κ equal to 0.75 results in the values of R^2 closest to one, which represents a perfect fit. This can be largely attributed to the fact that the local bond strength assumed in the FE models is proportional to $f_c'^{3/4}$. Based on the findings in Chapter 3 and the fact that this investigation focuses on the development length required for well-confined cases, for which the above assumption is appropriate, a tri-linear relation that has κ equal to 0.75 has been chosen to represent the normalized tensile strength as a function of the normalized embedment length. This relation is expressed as follows:

$$\frac{\sigma_{\max}}{f_y} = \begin{cases} 3.25\lambda_e & \text{for } \lambda_e \le 0.375 \\ (0.45\lambda_e + 1.05) \le 1.4 & \text{for } \lambda_e > 0.375 \end{cases} \tag{5.6a}$$

where

$$\lambda_e = l_e \frac{f_c'^{3/4}}{f_y d_b} \tag{5.6b}$$

in which f_c' and f_y are in MPa. With US customary units, this relation becomes

$$\frac{\sigma_{\max}}{f_y} = \begin{cases} 2.0\lambda_e & \text{for } \lambda_e \le 0.61 \\ (0.275\lambda_e + 1.05) \le 1.4 & \text{for } \lambda_e > 0.61 \end{cases} \tag{5.7}$$

in which f_c' and f_y are in ksi.

Based on Equation 5.6, the minimum values of λ_e required to develop the yield and tensile strengths of a bar are 0.31 and 0.78, respectively. These lead to the conclusion that for a reinforcing bar with an expected yield strength of 469 MPa (68 ksi) and embedded in 34.5-MPa (5-ksi) concrete, the minimum embedment lengths required to develop the yield and tensile strengths are $10.3d_b$ and $25.8d_b$, respectively. It should be noted that it is for a well-confined situation. Equation 5.6 also reveals that the tension capacity of a bar is linearly proportional to the embedment length up to a bar stress that is slightly beyond the yield point. This observation confirms the provisions in Article 12.2.5 of ACI 318-08 (ACI 2008) and Article 5.11.2.2.2 of the AASHTO LRFD Bridge Design Specifications (AASHTO 2010) that the development length can be reduced in proportion to the ratio of the required bar stress to the yield strength of the bar. However, the equation also shows that the ratio of the minimum embedment length required to develop the tensile strength of a bar to that required to develop the yield strength is 2.5, while the tensile strength is only 1.4 times the yield strength.

5.4 Reliability analysis of the tension capacity of bars anchored in well-confined concrete

The minimum embedment length required to develop the yield and ultimate capacities of a bar can be determined with Equation 5.6 based on the actual strengths of the concrete and steel. However, for design, one needs to ensure that an acceptable level of safety can be achieved under uncertainties related to the material properties, the geometry of the structure, the analytical models, etc. For this purpose, a probabilistic

analysis has been carried out using the analytical expression given in Equation 5.6 to (a) assess the level of reliability of the AASHTO LRFD Bridge Design Specifications (AASHTO 2010) in developing the yield and tensile strengths of large-diameter bars embedded in well-confined concrete; and (b) determine the minimum embedment length required for bars with the confinement condition considered here to develop their ultimate tensile capacity with an acceptable reliability level. The reliability analysis is based on the best estimates of the probability distributions for the compressive strength of concrete, the yield strength of steel, the embedment length, and the analytical prediction error. This analysis considers No. 11, 14, and 18 Grade 60 bars, and concrete with specified strengths of 24.8 MPa (3.6 ksi) and 34.5 MPa (5 ksi), which represent typical concrete strengths used for cast-in-place bridge structures.

The probability distributions of the random variables considered in the reliability analysis are provided in Table 5.6. The distributions of the material properties are obtained from the literature. The yield strength of steel is assumed to be normally distributed with a mean equal to 1.145 times the specified value and a coefficient of variation of 0.05, as reported by Nowak and Szerszen (2003). The compressive strength of concrete is also assumed to be normally distributed based on the study carried out by Unanwa and Mahan (2012) on concrete properties of recently constructed highway bridges in California. Based on that study, for 24.8-MPa (3.6-ksi) concrete, the mean is equal to 1.45 times the specified strength, and the coefficient of variation is 0.19. For 34.5-MPa (5-ksi) concrete, the mean is equal to 1.33 times the specified strength, and the coefficient of variation is 0.13. To account for construction errors, the actual embedment length is also treated as a normally distributed random variable with a mean equal to the specified length and a standard deviation equal to 16 mm (0.61 in.), as suggested by Darwin et al. (1998). The uncertainties related to the use of Equation 5.6 and FE analysis to predict the tensile capacity of a bar also need to be considered. To account for the uncertainty in using Equation 5.6, the difference between the value of $\sigma_{\max} / f_y$ calculated with the equation and that with a FE model is represented by a random error, e, which is assumed to have a normal distribution. Based on the data presented in Figure 5.23, the mean and standard deviation of e are calculated to be 0.0 and 0.05, respectively. In

addition, the ratio of the actual tensile capacity of an embedded bar to that predicted by a FE model is represented by a random variable r, which is also assumed to have a normal distribution. Due to the lack of sufficient experimental data, the mean value of r is taken to be 1.0 and the dispersion is determined with the following consideration. Based on the observation that the errors in the FE analysis results when compared to the three pull-push tests presented previously are less than 3%, it is deemed conservative to assume that there is a 90% probability that the error introduced by a FE model is no more than 10%. With this assumption, the standard deviation of r turns out to be 0.06. All random variables are statistically independent. The ratio of the ultimate to the yield strength of steel has been assumed to be a deterministic parameter.

For the reliability analysis, the limit-state functions, g_y and g_u, for the yield strength and the ultimate strength of a bar are defined in Equations 5.8 and 5.9, respectively. These functions are derived from Equation 5.6, and are defined in terms of the above-mentioned random variables and one deterministic variable, d_b.

$$g_y = \begin{cases} r\left(3.25 l_e \dfrac{f_c'^{3/4}}{f_y d_b} + e\right) - 1.0 & \text{for } l_e \dfrac{f_c'^{3/4}}{f_y d_b} \le 0.375 \\ r\left(0.45 l_e \dfrac{f_c'^{3/4}}{f_y d_b} + 1.05 + e\right) - 1.0 & \text{for } l_e \dfrac{f_c'^{3/4}}{f_y d_b} > 0.375 \end{cases} \tag{5.8}$$

$$g_u = \begin{cases} r\left(3.25 l_e \dfrac{f_c'^{3/4}}{f_y d_b} + e\right) - 1.4 & \text{for } l_e \dfrac{f_c'^{3/4}}{f_y d_b} \le 0.375 \\ r\left(0.45 l_e \dfrac{f_c'^{3/4}}{f_y d_b} + 1.05 + e\right) - 1.4 & \text{for } l_e \dfrac{f_c'^{3/4}}{f_y d_b} > 0.375 \end{cases} \tag{5.9}$$

in which f_c' and f_y are in MPa.

The reliability of the AASHTO LRFD specifications in developing the yield and tensile strengths of bars have been studied with the limit-state functions presented in Equations 5.8 and 5.9. The development lengths required by the AASHTO specifications for No.11, 14, and 18 Grade 60 bars and a specified concrete strength of 24.8 MPa (3.6 ksi) are $26\,d_b$, $31\,d_b$, and $30\,d_b$, respectively, for the best confined scenario. For a

specified concrete strength of 34.5 MPa (5 ksi), these lengths are $22d_b$, $26d_b$, and $25d_b$, respectively. These development lengths have been used as the median value of l_e.

The probabilities of failing to reach these two limit states, p_F, i.e., the probabilities of having $g_y < 0$ and $g_u < 0$, respectively, have been calculated through Monte Carlo simulations using the program CALREL (Liu et al. 1989). The probability of failing to reach a limit state is related to the reliability index, β, through the definition that $p_F = \Phi(-\beta)$, in which Φ is the cumulative probability function of the standard normal distribution. A higher reliability index means a higher safety level.

Results of the Monte Carlo simulations are presented in Table 5.7 and Table 5.8. The probabilities of not reaching bar yielding are between $3 \cdot 10^{-6}$ and $3.5 \cdot 10^{-5}$. Darwin et al. (1998) have suggested that the reliability index β for developing the yield strength of a bar should be around 3.5. This is equivalent to a probability of bond failure of no more than $2 \cdot 10^{-4}$, which is one fifth of that accepted for the failure of beams in bending and the failure of columns in combined bending and compression. Hence, the development length requirements in the AASHTO LRFD specifications for well-confined situations are clearly adequate for developing the yield strength of a bar. Nevertheless, the results in Table 5.7 and Table 5.8 have shown that the probabilities of not reaching the ultimate strengths of the bars are extremely high, between 24% and 47%. The lack of a safety margin in the AASHTO LRFD specifications to develop the full tensile capacity of a bar is also evident from the fact that the first specimen in the development length tests reported in Section 5.1 had a bond failure because the compressive strength of the concrete was 15% lower than that used to determine the development length.

Under severe seismic loading, the longitudinal reinforcement of an RC column is expected to yield and enter the strain-hardening regime. However it may experience low-cycle fatigue failure prior to reaching the ultimate tensile strength of the steel as a result of concrete cover spalling and bar buckling. The Caltrans Seismic Design Criteria (Caltrans 2010) defines the failure limit state for flexure as the state at which either the concrete reaches its ultimate compressive strain or the longitudinal reinforcement reaches a reduced ultimate tensile strain, which is 33% less than the expected ultimate tensile

strain. The tensile stress developed at the reduced ultimate strain is about 1.35 times the actual yield strength of a reinforcing bar, based on the tensile tests conducted in this study on the large-diameter bars. This can be considered as the minimum strength that needs to be developed in longitudinal reinforcing bars in a hinging column. Hence, a third limit-state, g_{ru}, as presented below, is introduced.

$$g_{ru} = \begin{cases} r\left(3.25 l_e \dfrac{f_c'^{3/4}}{f_y d_b} + e\right) - 1.35 & \text{for } l_e \dfrac{f_c'^{3/4}}{f_y d_b} \le 0.375 \\ r\left(0.45 l_e \dfrac{f_c'^{3/4}}{f_y d_b} + 1.05 + e\right) - 1.35 & \text{for } l_e \dfrac{f_c'^{3/4}}{f_y d_b} > 0.375 \end{cases} \tag{5.10}$$

in which f_c' and f_y are in MPa.

Monte Carlo simulations have been repeated using Equation 5.10 to study the reliability of the AASHTO LRFD specifications in developing the reduced ultimate tensile strength of a bar for specified concrete strengths of 24.8 MPa (3.6 ksi) and 34.5 MPa (5 ksi). As shown in Table 5.7 and Table 5.8, the probabilities of not reaching the reduced ultimate tensile strength vary between 12 and 30%. If one adopts a reliability level of $\beta = 1.75$ ($p_F = 4\%$) as suggested by Ellingwood et al. (1980) for earthquake loads, these development lengths are not adequate.

Reliability analysis has been conducted to solve an inverse problem, i.e., given a target level of reliability, the minimum embedment lengths required to develop the yield and reduced ultimate tensile strengths of a bar is to be determined. For developing the yield strength, the desired reliability index is $\beta = 3.5$ as suggested by Darwin et al. (1998) for ordinary loading conditions. For developing the reduced ultimate strength, the desired reliability index is $\beta = 1.75$, as suggested by Ellingwood et al. (1980) for earthquake loads. Monte Carlo simulations have been performed for different embedment lengths until the target value of β has been attained. The results have shown that embedment lengths of $21\,d_b$ and $17\,d_b$ satisfy the minimum reliability level of $\beta = 3.5$ for a bar to reach its yield strength when the specified compressive strengths of the concrete are 24.8 MPa (3.6 ksi) and 34.5 MPa (5 ksi), respectively. To develop the reduced ultimate tensile strength of a bar with a reliability level of $\beta = 1.75$, the

embedment length has to be increased to $38\,d_b$ and $31\,d_b$, respectively, for the above-considered concrete strengths. Considering that the required development length is proportional to f_y and inversely proportional to $f_c'^{3/4}$, as implied in Equation (5.6b), the minimum embedment length required to develop the reduced ultimate tensile strength of a bar can be expressed as

$$l_{e,\min} = \lambda_{e,\min} \frac{d_b f_y}{f_c'^{3/4}} \tag{5.11a}$$

in which $\lambda_{e,\min}$ is 1.05 based on the above results, f_y is the specified yield strength of the steel (in MPa), and f_c' is the specified compressive strengths of the concrete (in MPa). With US customary units, Equation 5.11a becomes

$$l_{e,\min} = \lambda_{e,\min} \frac{d_b f_y}{f_c'^{3/4}} \tag{5.11b}$$

in which $\lambda_{e,\min}$ is 1.70, and f_y and f_c' are in ksi. Equation (5.11) provides a more adequate reliability level than the AASHTO LRFD specifications to develop the reduced tensile strength of a bar.

Even though only No. 11, 14, and 18 bars are considered in this study, the formulas derived should also be applicable to smaller bars. The parametric study presented here has shown that the bar size has a negligible influence on the constants in the limit-state functions, and the bond-slip test data presented in Chapter 3 have shown that the bar size has a very small influence on the bond strength for well-confined situations.

5.5 Summary and conclusions

The development length tests presented in this chapter have shown that the AASHTO LRFD Bridge Design Specifications (AASHTO 2010) are adequate to develop the yield strengths of large-diameter bars subjected to severe cyclic loads with a large margin of safety. The test specimens had bars embedded in well-confined concrete,

which is representative of the confinement condition in a Type II shaft. They are also adequate to develop tensile stresses up to or very close to the tensile strengths of the bars.

A formula to calculate the tensile capacity of a bar, based on the given embedment length, and the specified concrete and steel strengths, has been derived using results of a parametric study conducted with a FE model. Monte Carlo simulations conducted with this formula have confirmed that the margin of safety of the AASHTO specifications is sufficient to develop tensile yielding, but insufficient to develop the full tensile capacity of a bar when uncertainties in material strengths and construction quality are introduced. Furthermore, it has been shown that to develop the reduced ultimate tensile strength of the longitudinal reinforcement in a hinging column (defined in Caltrans Seismic Design Criteria) with an adequate reliability level, the development lengths specified in the AASHTO specifications have to be increased. To this end, a new development length formula for bars in well-confined concrete has been proposed. The formulas derived in this chapter are also applicable to bars of smaller diameters.

The experimental and FE analysis results presented in this chapter have provided a better understanding of the bond-slip behavior in the anchorage zone of a bar under severe cyclic loading. These results have shown that bar slip and plastic strain penetration can be significant even for a well-anchored bar. The FE analysis results have shown that the bond stress distributions along the anchorage length are highly nonlinear.

Table 5.1: Specimen properties, actual material strengths, and test results

	Specimen properties							Test results		
Test no.	Bar diameter mm (in.)	l_e (d_b)	f'_c MPa (ksi)	f_{cs} MPa (ksi)	f_y MPa (ksi)	f_u MPa (ksi)	Slip at bar yield mm (in.)	Bar peak stress MPa (ksi)	Slip at peak stress mm (in.)	Failure mode
1	43 (1.41)	26	29.3 (4.25)	2.5 (0.36)	450 (65)	630 (91.5)	1 (0.04)	616 (89)	76 (3.0)	Bar pullout after yielding
2	57 (1.69)	25	35.9 (5.2)	3.0 (0.44)	470 (68)	655 (95)	1.5 (0.06)	655 (95)	60 (2.35)	Bar fracture
3	57 (2.25)	14	34.5 (5.0)	2.8 (0.40)	470 (68)	655 (95)	1.9 (0.075)	513 (74)	5.9 (0.23)	Bar pullout after yielding

l_e: embedment length, f'_c: compressive strength of concrete, f_{cs}: tensile splitting strength of concrete, f_y: yield strength of steel, f_u: tensile strength of steel.

Table 5.2: Distance of strain gages from top surface of concrete specimen in mm (in.)

Specimen 1		Specimen 2		Specimen 3	
Center bar	North and south perimeter bars	Center bar	North and south perimeter bars	Center bar	North and south sides of spiral
25 (1)		25 (1)		25 (1)	
-203 (-8)	-203 (-8)	-203 (-8)		-203 (-8)	-102 (-4)
-508 (-20)	-508 (-20)	-406 (-16)	-508 (-20)	-406 (-16)	-508 (-20)
-812 (-32)		-610 (-24)		-610 (-24)	
		-914 (-36)	-914 (-36)		
		-1219 (-48)			

Note: positive distance indicates that the strain gage is located above the concrete surface, i.e., outside the anchorage.

Table 5.3: Pull-push tests loading protocol

Specimen 1			Specimens 2 and 3		
Cycle no.	+ peak	- peak	Cycle no.	+ peak	- peak
1,2	$0.25\,F_y$	$0.25\,F_y$	1,2	$0.25\,F_y$	$0.25\,F_y$
3,4	$0.50\,F_y$	$0.50\,F_y$	3,4	$0.50\,F_y$	$0.50\,F_y$
5,6	$0.75\,F_y$	$0.50\,F_y$	5,6	$0.75\,F_y$	$0.50\,F_y$
7,8	$2u_5$	$0.50\,F_y$	7,8	$2u_5$	$0.50\,F_y$
9,10	$4u_5$	$0.50\,F_y$	9,10	$4u_5$	$0.50\,F_y$
11,12	$8u_5$	$0.50\,F_y$	11,12	$8u_5$	$0.50\,F_y$
13,14	$12u_5$	$0.50\,F_y$	13,14	$12u_5$	$0.50\,F_y$
15,16	$20u_5$	$0.50\,F_y$	15,16	$16u_5$	$0.50\,F_y$
17,18	$32u_5$	$0.50\,F_y$	17,18	$20u_5$	$0.50\,F_y$
19	Load to failure		19,20	$32u_5$	$0.50\,F_y$
			21	Load to failure	

F_y : expected yield force of the bar.

u_5: displacement measured at the positive peak of Cycle 5.

Table 5.4: Parametric study variables and results

Model parameters			Analysis results, σ_{max} / f_y		
l_e (d_b)	f_c' MPa (ksi)	f_y MPa (ksi)	No. 11 bar	No. 14 bar	No. 18 bar
4	34.5 (5)	469 (68)	0.35	0.31	0.33
8			0.79	0.82	0.71
12			1.18	1.23	1.02
16			1.26	1.27	1.28
20			1.31	1.33	1.33
24			1.38	1.38	1.38
28			1.40	1.40	1.40
32			1.40	1.40	1.40
36			1.40	1.40	1.40
40			1.40	1.40	1.40
4	48.3 (7)	469 (68)	0.47	0.44	0.46
8			1.07	1.13	0.98
12			1.29	1.29	1.29
16			1.34	1.34	1.36
20			1.39	1.39	1.39
24			1.40	1.40	1.39
28			1.40	1.40	1.40
32			1.40	1.40	1.40
36			1.40	1.40	1.40
40			1.40	1.40	1.40
4	23.1 (3.5)	469 (68)	0.29	0.23	0.29
8			0.59	0.54	0.63
12			0.97	1.02	0.93
16			1.22	1.25	1.26
20			1.31	1.25	1.26
24			1.32	1.32	1.31
28			1.36	1.37	1.37
32			1.38	1.39	1.37
36			1.38	1.40	1.39
40			1.40	1.40	1.40
4	34.5 (5)	586 (85)	0.28	0.25	0.26
8			0.63	0.65	0.56
12			1.04	1.04	0.80
16			1.26	1.28	1.14
20			1.28	1.29	1.29
24			1.31	1.34	1.32
28			1.38	1.38	1.37
32			1.39	1.39	1.40
36			1.40	1.40	1.40
40			1.40	1.40	1.40

Table 5.5: Loading protocol for parametric study

Cycle no.	+ peak	- peak
1	$0.25u_y$	$0.25F_y$
2	$0.50u_y$	$0.50F_y$
3	$0.75u_y$	$0.75F_y$
4,5	u_y	$1.0F_y$
6,7	$2u_y$	$1.0F_y$
8,9	$4u_y$	$1.0F_y$
10,11	$8u_y$	$1.1F_y$
12,13	$12u_y$	$1.1F_y$
14,15	$16u_y$	$1.1F_y$
16,17	$20u_y$	$1.2F_y$
18,19	$32u_y$	$1.2F_y$
20	$50u_y$	

F_y: expected yield force of the bar.

u_y: displacement at first tension yielding with l_e=$l_{d,AASHTO}$.

Table 5.6: Random variables used in Monte Carlo simulations

Variable	Symbol	Probability distribution	Mean	Standard deviation
Compressive strength of concrete, specified = 24.8 MPa (3.6 ksi)	f_c'	Normal	36.0 MPa (5.22 ksi)	6.84 MPa (0.99 ksi)
Compressive strength of concrete, specified = 34.5 MPa (5 ksi)	f_c'	Normal	45.9MPa (6.65 ksi)	5.97 MPa (0.86 ksi)
Yield strength of steel, specified = 414 MPa (60 ksi)	f_y	Normal	474 MPa (68.7 ksi)	23.7 MPa (3.44 ksi)
Embedment length	l_e	Normal	Specified length	15.5 mm (0.61 in.)
Error in analytical equation as compared to FE analysis	e	Normal	0.0	0.05
Ratio of the actual tensile capacity to FE prediction	r	Normal	1.0	0.06

Table 5.7: Probabilistic analysis results for $l_e = l_{d,AASHTO}$ and specified concrete strength of 24.8 MPa (3.6 ksi)

Bar size	Probability of not yielding the bar	Probability of not reaching ultimate tensile strength of the bar	Probability of not reaching reduced ultimate tensile strength of the bar
No. 11	$3.5 \cdot 10^{-5}$	0.47	0.30
No. 14	$7 \cdot 10^{-6}$	0.26	0.14
No. 18	$8 \cdot 10^{-6}$	0.29	0.16

Table 5.8: Probabilistic analysis results for $l_e = l_{d,AASHTO}$ and specified concrete strength of 34.5 MPa (5 ksi)

Bar size	Probability of not yielding the bar	Probability of not reaching ultimate tensile strength of the bar	Probability of not reaching reduced ultimate tensile strength of the bar
No. 11	$1.9 \cdot 10^{-5}$	0.44	0.27
No. 14	$3 \cdot 10^{-6}$	0.24	0.12
No. 18	$4 \cdot 10^{-6}$	0.28	0.14

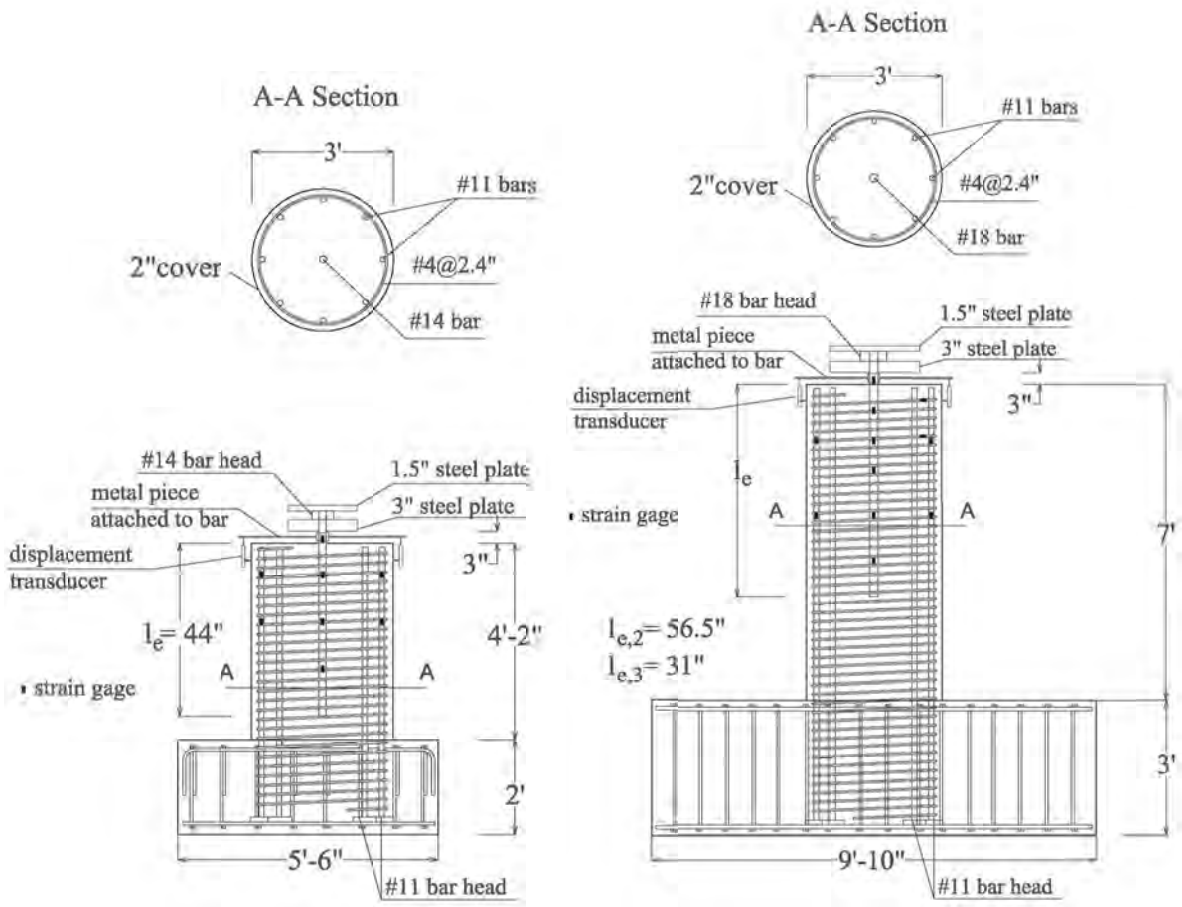

(a) Specimen 1 (b) Specimens 2 and 3

Figure 5.1: Test specimens and instrumentation (1'=304.8 mm, 1"=25.4 mm)

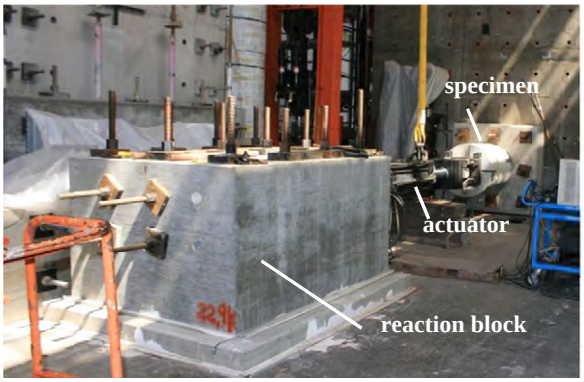

(a) Setup for Specimen 1

(b) Setup for Specimens 2 and 3

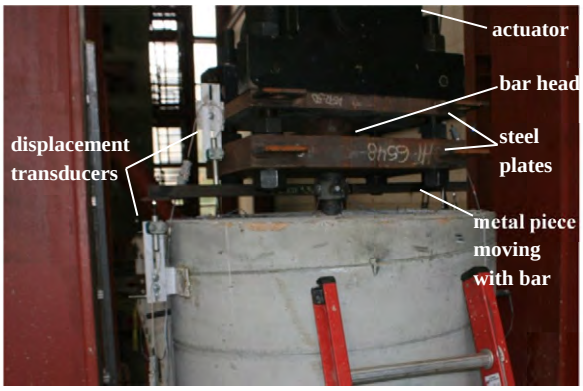

(c) Close-up view of test setup at pulled end

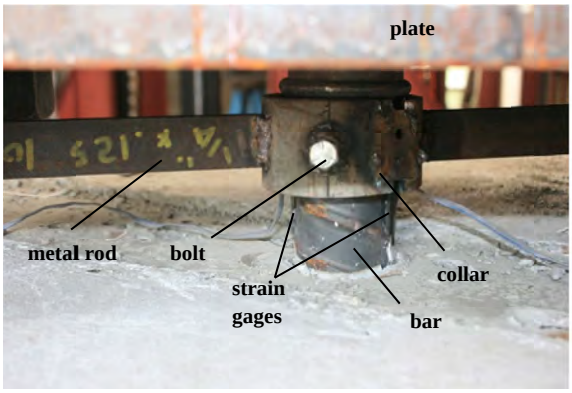

(d) Metal piece used to measure bar slip

Figure 5.2: Test setup

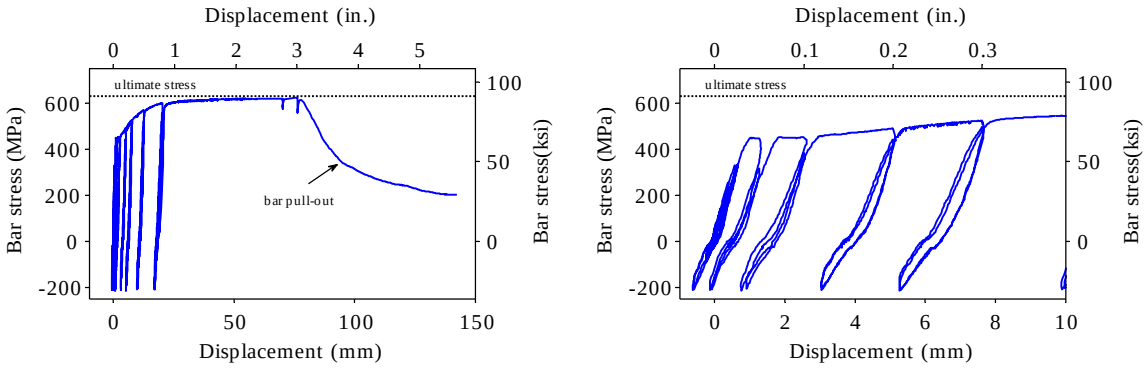

(a) Bar stress vs. displacement at loaded end

(b) Close-up view of curve in (a)

Figure 5.3: Results of Test 1

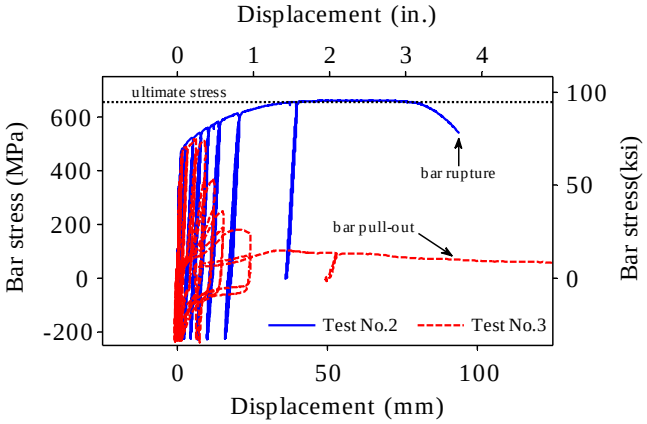

(a) Bar stress vs. displacement at loaded end

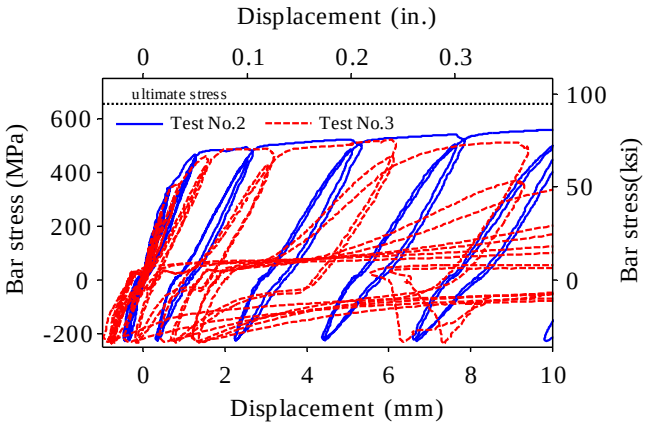

(b) Close-up view of curve in (a)

Figure 5.4: Results of Tests 2 and 3

(a) Pull-out and cone failure

(b) Concrete powder between ribs

Figure 5.5: Bar pull-out in Test No. 1

(a) Splitting and circular cracks in the concrete specimen

(b) Bar fracture and damage atop of the concrete specimen

(c) Cone-shaped fracture surface

Figure 5.6: Bar fracture and damage in concrete specimen in Test No. 2

(a) Splitting and circular cracks in the concrete specimen

(b) Bar pull-out and damage atop of the concrete specimen

(c) Cone-shaped fracture surface

Figure 5.7: Bar pull-out and damage in concrete specimen in Test No. 3

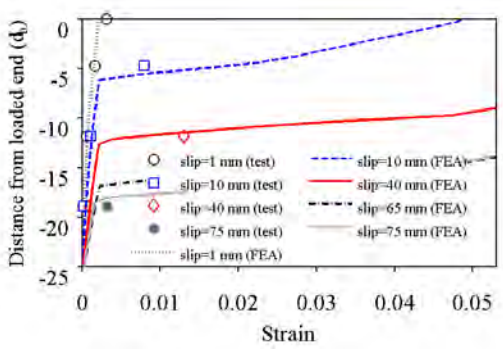

(a) Test No. 1

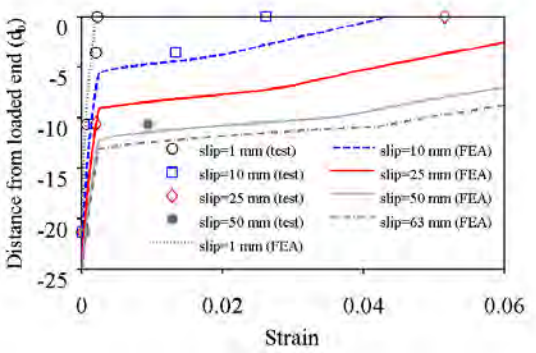

(b) Test No. 2

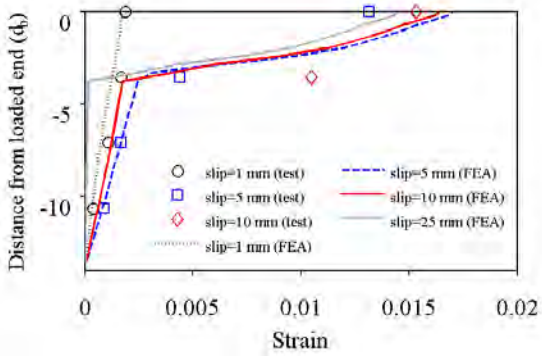

(c) Test No. 3

Figure 5.8: Strain penetration in tests and FE analyses (loaded end is the top surface of the concrete specimen)

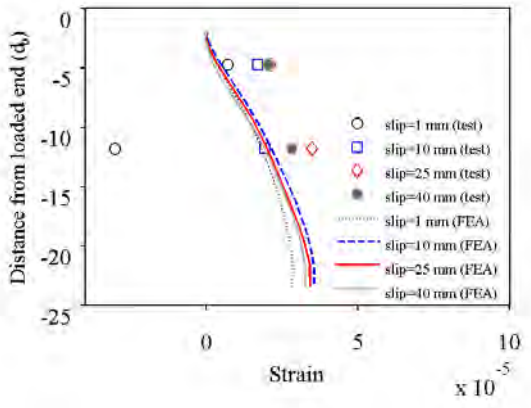

(a) Test No. 1

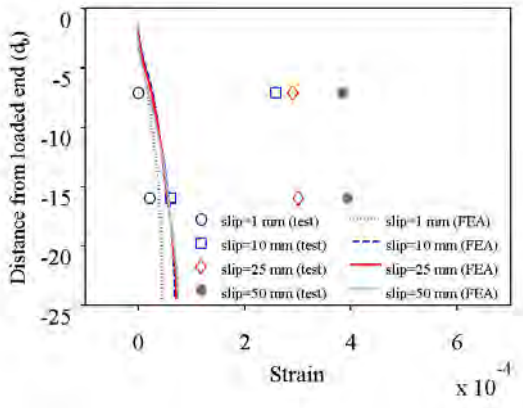

(b) Test No. 2

Figure 5.9: Strain in perimeter bars in tests and FE analyses

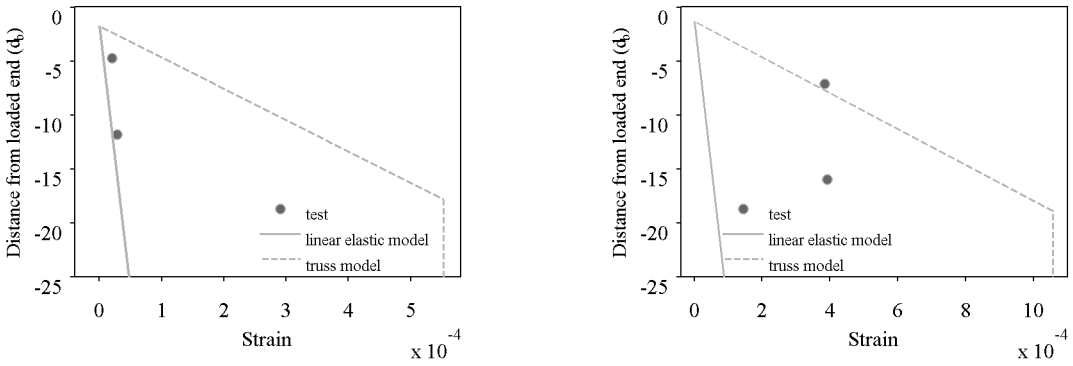

(a) Test No. 1 (slip=40mm) (b) Test No. 2 (slip=50mm)

Figure 5.10: Strains in perimeter bars from tests and simple analytical models

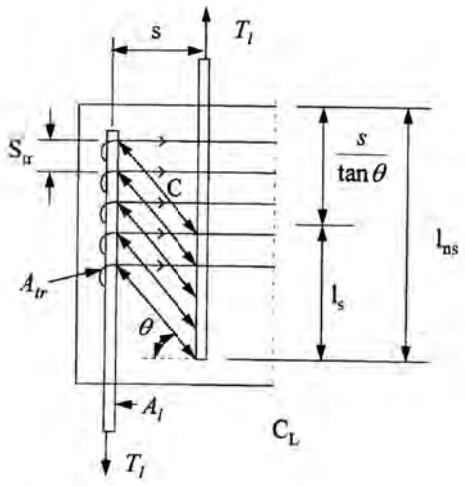

Figure 5.11: Truss analogy used by McLean and Smith (1997) for non-contact lap splices

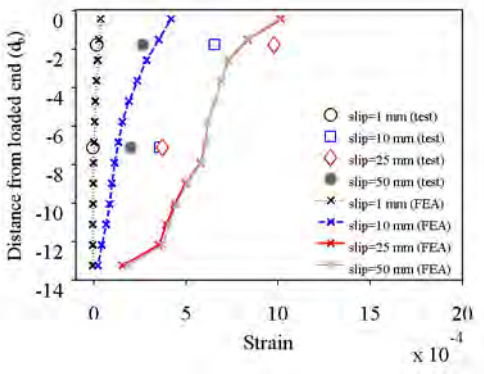

Figure 5.12: Strains in hoops in Test No. 3 and FE analysis

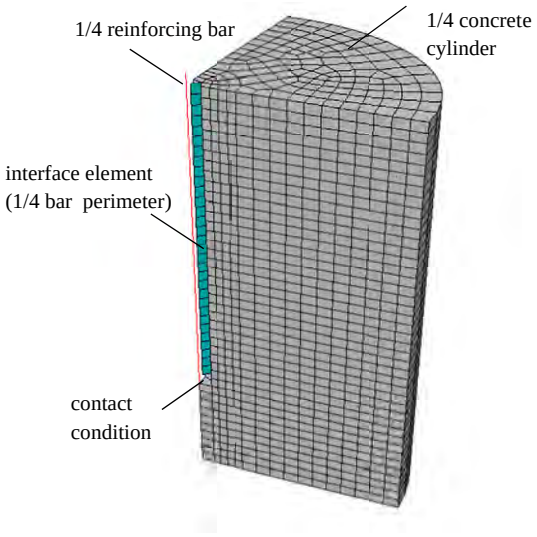

Figure 5.13: FE model for Test No. 3

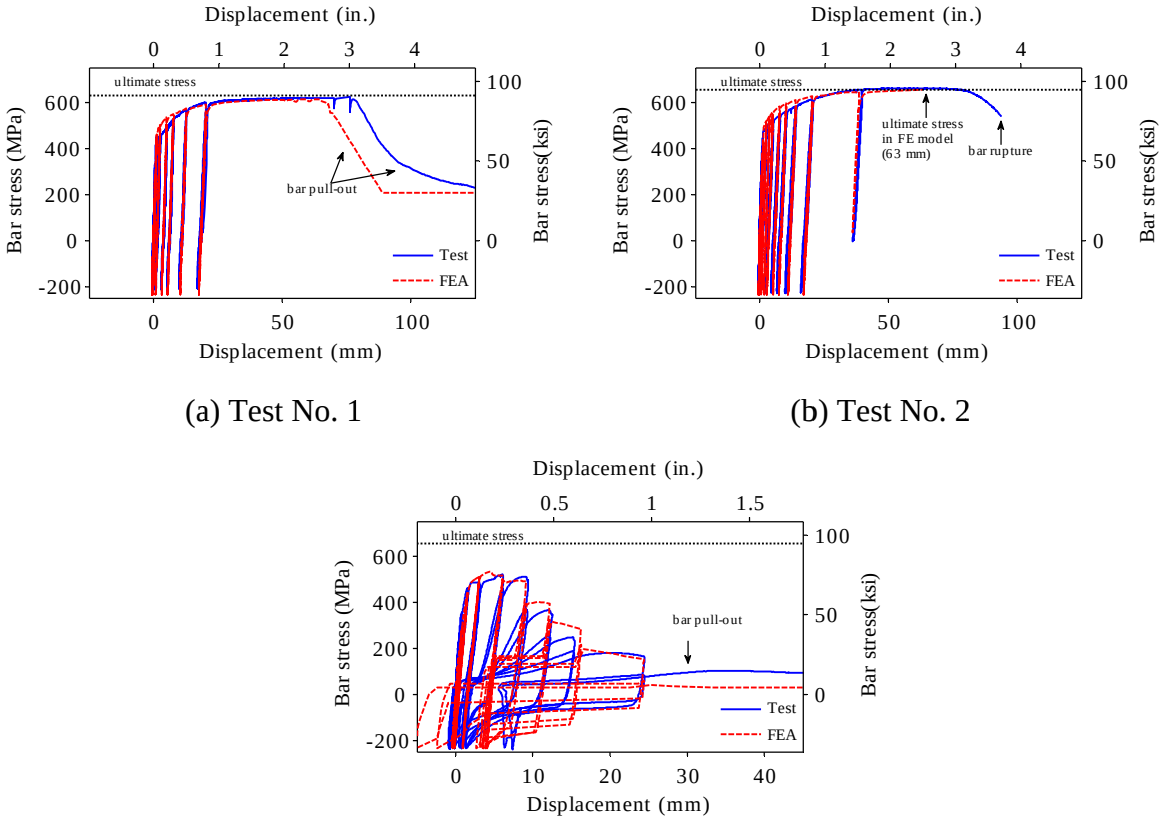

(a) Test No. 1

(b) Test No. 2

(c) Test No. 3

Figure 5.14: Bar stress – bar displacement curves from FE analyses and tests

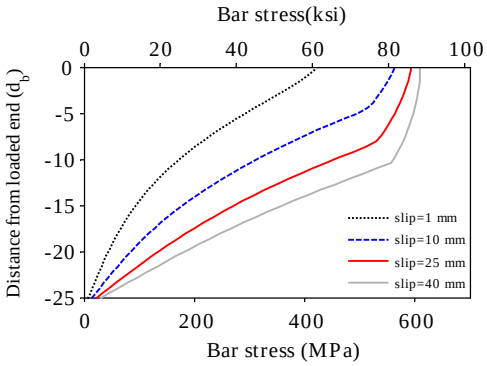

(a) Tension

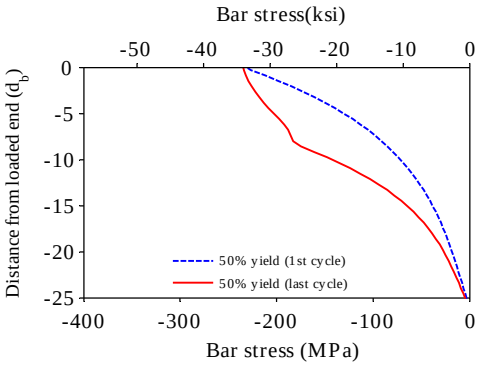

(b) Compression

Figure 5.15: Bar axial stress distributions from FE analysis for Test No. 1

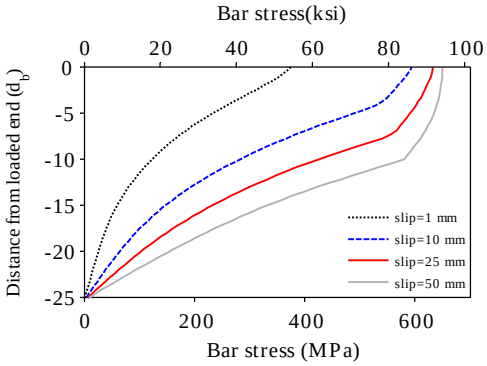

(a) Tension

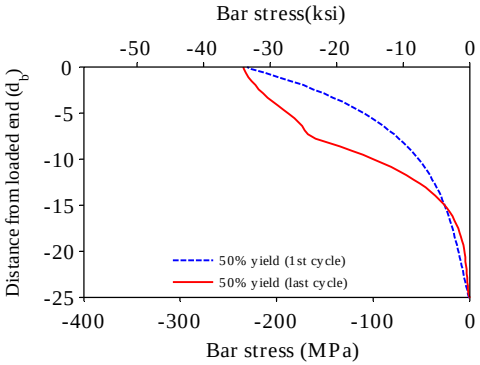

(b) Compression

Figure 5.16: Bar axial stress distributions from FE analysis for Test No. 2

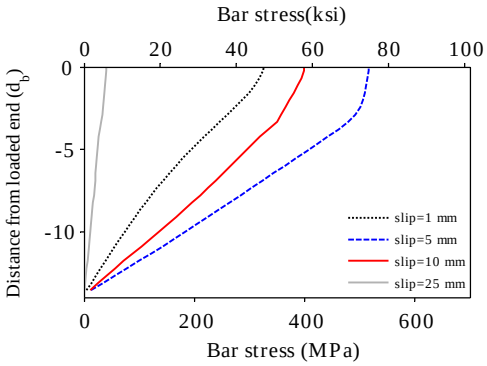

(a) Tension

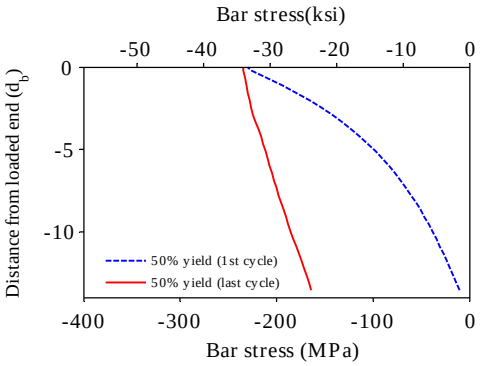

(b) Compression

Figure 5.17: Bar axial stress distributions from FE analysis for Test No. 3

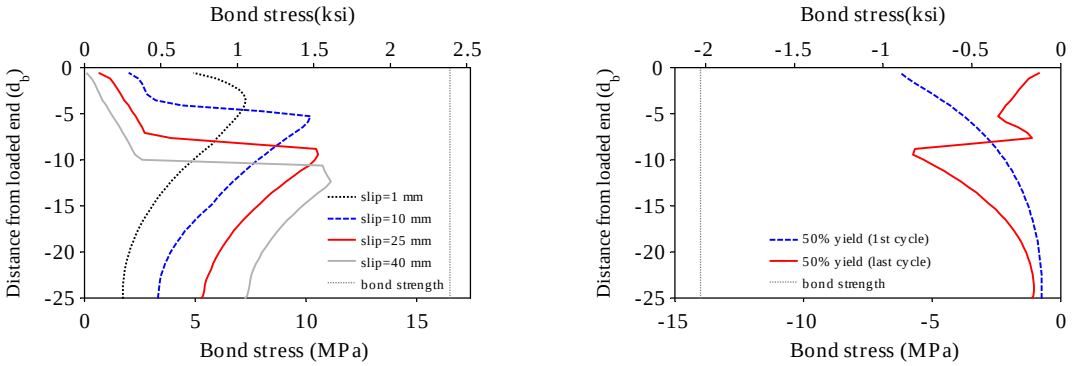

(a) Tension (b) Compression

Figure 5.18: Bond stress distributions from FE analysis for Test No. 1

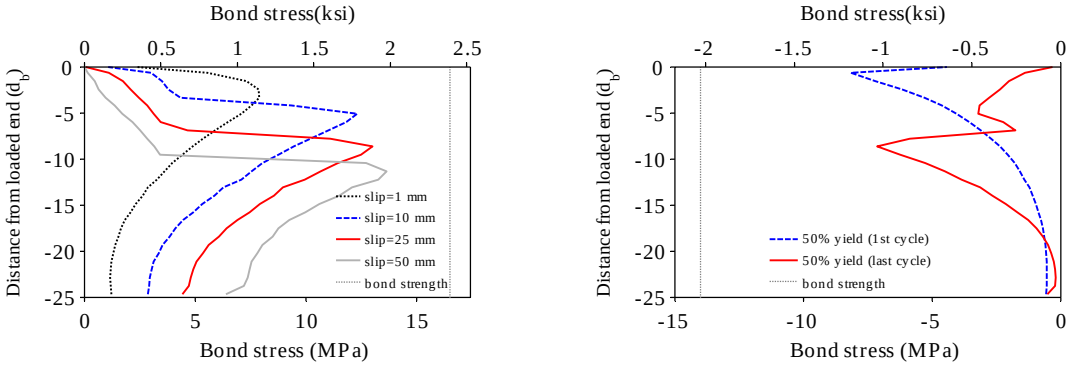

(a) Tension (b) Compression

Figure 5.19: Bond stress distributions from FE analysis for Test No. 2

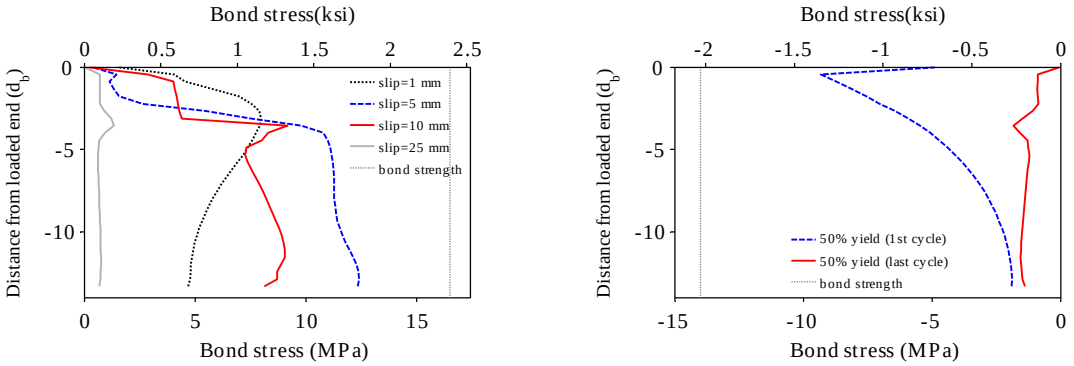

(a) Tension (b) Compression

Figure 5.20: Bond stress distributions from FE analysis for Test No. 3

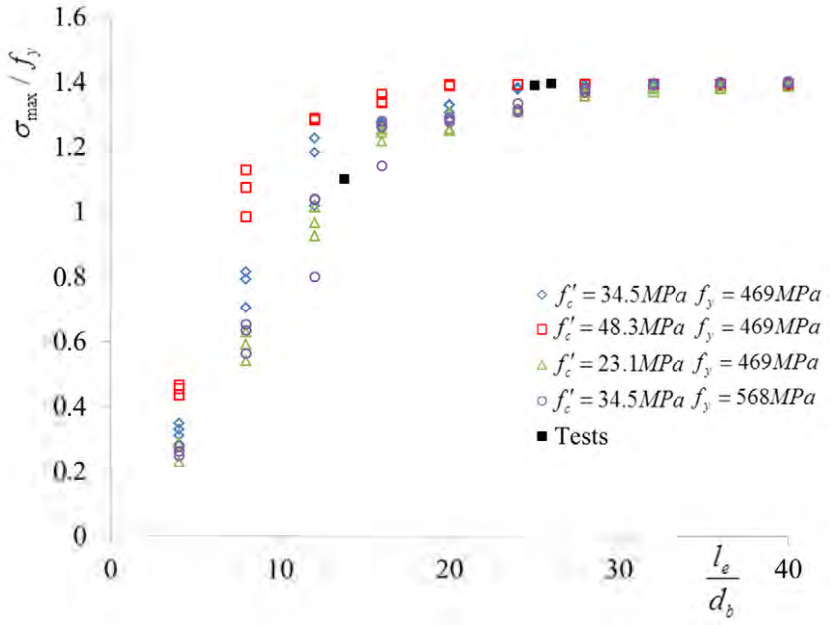

Figure 5.21: Normalized tensile capacity vs. normalized development length

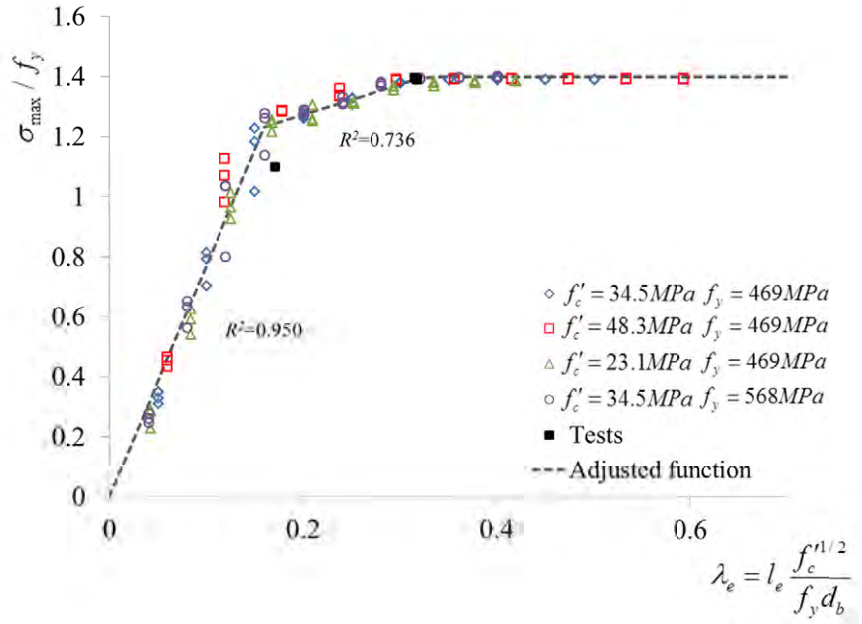

Figure 5.22: Normalized tensile capacity vs. development length index with $\kappa = 0.5$

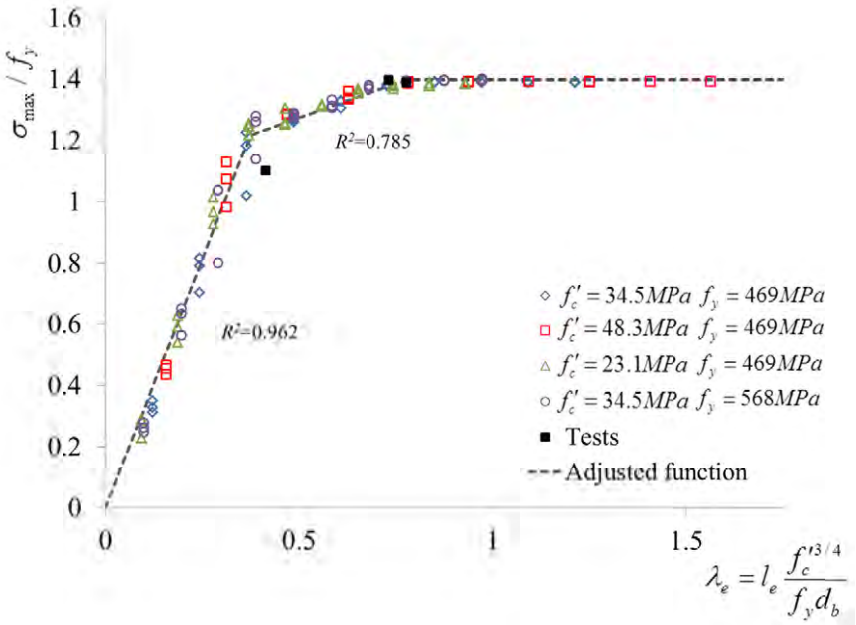

Figure 5.23: Normalized tensile capacity vs. development length index with $\kappa = 0.75$

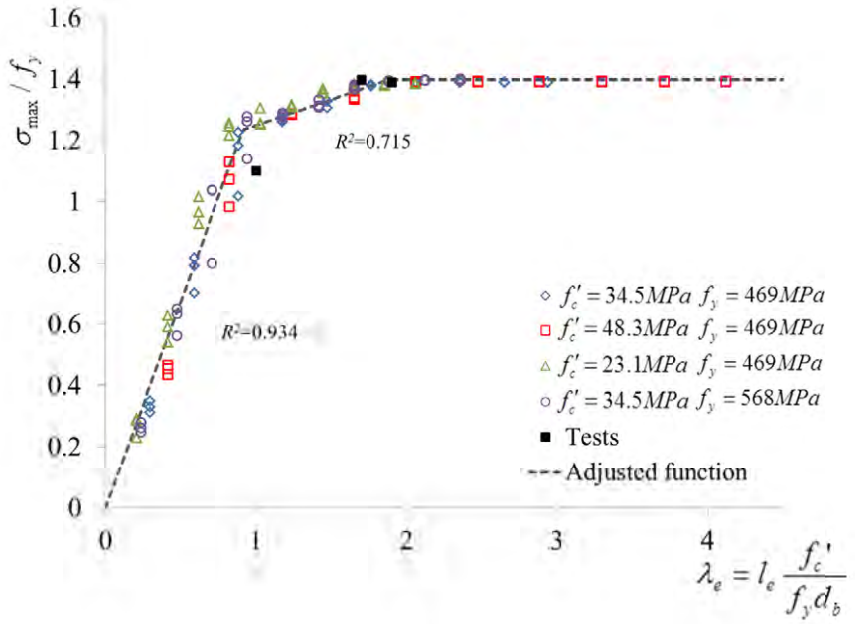

Figure 5.24: Normalized tensile capacity vs. development length index with $\kappa = 1$

CHAPTER 6

LARGE-SCALE LABORATORY TESTING OF COLUMN – ENLARGED PILE SHAFT ASSEMBLIES: TEST PROGRAM

Prior to 2010, Section 8.2.4 of the Caltrans Seismic Design Criteria (SDC) required that column longitudinal reinforcement extended into enlarged (Type II) CIDH shafts be terminated in a staggered manner with the minimum embedment lengths of $2D_{c,\max}$ and $3D_{c,\max}$, where $D_{c,\max}$ is the larger cross-sectional dimension of the column. This was to ensure adequate anchorage of the reinforcement when a plastic hinge forms at the bottom of the column. With this specification, the longitudinal reinforcement in columns with cross-sectional dimensions more than 2.14 m (7 ft) would require embedment lengths over 6.4 m (21 ft). This would significantly increase the construction costs in that for workers working in drilled holes more than 6.1 m (20 ft) deep, the stringent Cal/OSHA safety requirements needs to be followed. That embedment length requirement was recognized by Caltrans engineers to be over-conservative, and a new requirement was introduced in 2010, which specifies that the minimum embedment lengths for the staggered bars be $D_{c,\max} + l_d$ and $D_{c,\max} + 2l_d$, respectively, where l_d is the required development length for a straight bar in tension. According to the Caltrans SDC, this development length is the basic tension development length l_{db} specified in the AASHTO LRFD Bridge Design Specifications (AASHTO 2010) multiplied by a compounded modification factor of 0.9 for epoxy-coated bars and 0.6 for non epoxy-

coated bars. To calculate l_{db}, the SDC specifies that the expected yield strength of 469 MPa (68 ksi) for Grade 60 bars and the expected concrete compressive strength of 34.5 MPa (5 ksi) shall be used. This new requirement reduces the required embedment lengths to be within 6.1 m (20 ft) for columns with cross-sectional dimensions as large as 3.05 m (10 ft) and bars as large as No. 14 (43 mm), and it is still considered conservative according to the analytical study conducted by Chang and Dameron (2009).

In the Caltrans SDC, the required embedment length is governed by the column dimension $D_{c,\max}$ to account for possible damage penetration into the embedment zone, which could shorten the effective development length. However, there has been no convincing justification for this addition, which makes the requirement very conservative. A study by McLean and Smith (1997) has shown that non-contact lap splices in enlarged shafts can perform satisfactorily with splice lengths equal to $l_s + s$, where s is the bar spacing in the non-contact splice, and l_s is the splice length required for Class C lap splices in AASHTO (2010), which is $1.7l_d$. This recommendation has been derived by idealizing the force transfer in a non-contact slip with a truss model, as illustrated in Figure 6.1. Assuming that this force transfer is through 45-degree angle struts, the lap splice length has to be increased by s to make up for the ineffective force transfer region. However, McLean and Smith (1997) considered only No. 4 and 8 (12-mm and 25-mm) bars and reduced-scale specimens in their study; hence, it has not been clear as to whether their conclusion applies to larger bars. Based on the truss analogy, the transverse reinforcement in a shaft should be sufficient to resist the horizontal component of the strut forces. To this end, the spacing of the transfer reinforcement should not be more than that calculated with the following equation.

$$s_{tr,\max} = \frac{2\pi A_{tr} f_{y,tr} l_s}{A_l f_u} \tag{6.1}$$

in which $s_{tr,\max}$, A_{tr}, and $f_{y,tr}$ are the maximum spacing, cross-sectional area, and yield strength of the transverse reinforcement, respectively; and A_l and f_u are the total cross-

sectional area and ultimate tensile strength of the longitudinal reinforcement, respectively.

As compared to the recommendation of McLean and Smith (1997), the minimum embedment length required by the Caltrans SDC is very conservative. To acquire the necessary data to improve the current SDC specifications, four large-scale column-shaft assemblies were tested. The design of these tests was supported by the basic experimental data on bond-slip and development lengths, which have been presented in previous chapters, and by nonlinear finite element analyses using the constitutive models presented in Chapter 4. This chapter presents the test program, including the specimen design, test setup, instrumentation, and loading protocol. The test results and finite element modeling of the test specimens are discussed in Chapters 7 and 8, respectively.

6.1 Design of test specimens

Four full-scale reinforced concrete bridge column - enlarged shaft assemblies were tested with quasi-static cyclic lateral loading in the Powell Structural Systems Laboratory at UCSD. The main differences among the test specimens were the longitudinal reinforcement in the columns, the embedment lengths of the column cages, and the transverse reinforcement in the shafts. For Specimen 1, an embedment length of $D_{c,\max} + l_d$ was used, which is very similar to the Caltrans requirement, but the specimen had all the column longitudinal bars terminated at the same distance and l_d was determined according to AASHTO (2010). Specimens 2 through 4 had an embedment length of $l_d + s + c$, in which s is the center-to-center spacing between the longitudinal bars extending from the column and those of the shaft, and c is the concrete cover at the top of the shaft. This differs from the recommendation of McLean and Smith (1997) in that $1.7l_d$ was replaced by l_d. The rationale for arriving at these embedment lengths will be explained later.

Each test specimen consisted of a bridge column and the bar anchorage region of a pile shaft. It was subjected to fully-reversed cyclic lateral loading applied at the top of the column with the base of the shaft fixed onto the strong floor in the laboratory. The

portion of a shaft to be included in the specimens was determined with the following considerations. First, it should be sufficient to accommodate the specified embedment length, and second, the moment and shear demand on the shaft would be close to that on an actual shaft embedded in soil. To access the moment and shear demand, Liu (2012) conducted nonlinear pushover analyses on column-pile-soil systems with different dimensions and soil conditions. The column and the shaft were modeled with fiber-section beam-column elements and the soil was modeled with p-y springs using the software platform OpenSees (PEER 2012). Results of these analyses have shown that inelastic deformation will concentrate at the base of the column, and that the maximum bending moment will occur in the shaft at a depth of about two times the column diameter from the soil surface. Figure 6.2 compares a sketch of a moment diagram from the analysis to that for a cantilever test specimen. It can be seen that having a shaft height larger than two times the column diameter in a test specimen might induce an unduly large moment demand on the shaft. Hence, it was decided that a shaft height of about two times the column diameter or less would be appropriate. It would still result in a slightly higher moment and shear demand in the lap splice region of the specimen as compared to reality. However, this was not expected to induce any inelastic deformation in the shaft but would put the test results on the conservative side.

As to the reinforcing details, the column and the shaft in Specimen 1 were designed to represent existing bridges in California and they complied with the Caltrans Bridge Design Specifications (Caltrans 2008) and Caltrans SDC (Caltrans 2010), with the exception of the embedment length of the column cage inside the shaft as mentioned previosuly. Specimens 2 through 4 were designed to represent the current practice of Caltrans, which follows the AASHTO LRFD Bridge Design Specifications (AASHTO 2010) and the Caltrans SDC (Caltrans 2010), with the exception of the embedment length of the column cage and the transverse reinforcement in the lap splice region of the shaft. Details on the embedment lengths and transverse reinforcement are provided in the following sections. The moment capacities of the shafts satisfy Section 7.7.3.2 of the Caltrans SDC, which requires that the ratio of the expected nominal moment capacity of a pile shaft to the moment demand generated by the over-strength moment applied at the

base of the column be greater than 1.25 at any section. This ratio calculated at the base of the shaft is 1.67 for Specimen 1, 1.98 for Specimens 2 and 3, and 1.26 for Specimen 4.

6.1.1 Determination of embedment lengths of column reinforcement

For Specimen 1, the embedment length of the column cage inside the shaft was $D_{c,\max} + l_d$, in which l_d was determined with the AASHTO LRFD Bridge Design Specifications (2010) and AASHTO LRFD Seismic Bridge Design Specifications (2011) rather than the Caltrans SDC (2010). The current SDC requirement to terminate half of the bars at $D_{c,\max} + 2l_d$ was not followed. This reduction in embedment length was considered safe based on a pre-test nonlinear finite element analysis of the column-shaft assembly.

Specimens 2 through 4 had an embedment length of $l_d + s + c$, which is significantly less than that used in Specimen 1. The development length l_d was determined with the AASHTO LRFD BDS (2010) and AASHTO LRFD Seismic BDS (2011). As shown in Chapter 5, without the consideration of uncertainties in material properties and construction quality, the development lengths specified in AASHTO (2010) for large-diameter bars are appropriate to develop the tensile capacity of a bar. Based on this, the embedment length of $1.7l_d + s$ as recommend by McLean and Smith (1997) was considered unwarranted. This assertion was supported by the bond-slip data obtained from the column-shaft Specimen 1 and additional finite element analysis. Hence, it was subsequently decided that $l_d + s + c$ be first tried in Specimen 2.

6.1.2 Determination of transverse reinforcement in bar anchorage region of a shaft

For Specimen 1, the transverse reinforcement in the lap splice region of the shaft was no different from that in the rest of the shaft, which was determined according to the design requirements for compression members in Article 5.7.4.6 of the AASHTO LRFD BDS.

For Specimen 2, the amount of transverse reinforcement in the lap splice region of the shaft was based on Equation 6.1, proposed by McLean and Smith (1997), but with l_s replaced by l_d to be consistent with the actual embedment length used.

The transverse reinforcement in Specimens 3 and 4 was determined with an analytical model developed in this study, which is presented below. The transverse reinforcement in Specimen 4 was calculated with Equation 6.9 derived below to counteract the splitting forces introduced by bar slip, and prevent the tensile splitting failure of the bar anchorage. For Specimen 3, a more stringent criterion presented in Equation 6.14 was followed not only to prevent the tensile splitting failure but also limit the width of the tensile splitting cracks. The derivation of these formulas is presented below.

Splitting and confining forces in lap splice region

The transverse steel in the lap splice region has to counteract the splitting forces caused by the slip of the longitudinal bars. A bar that is being developed exerts a uniform pressure, σ, on the surrounding concrete due to the wedging action of the bar ribs, as shown in Figure 6.3a. The uniform radial stress for a unit length of the bar can be represented by a set of four splitting forces, as suggested by Cairns and Jones (1996) and shown in Figure 6.3b. Each force is calculated as $f = \sigma d_b$.

The confining pressure (hoop stress) required to develop the bond resistance after the occurrence of tensile splitting in the surrounding concrete can be determined with the following equilibrium considerations. Figure 6.4 presents a typical cross section of a pile shaft and the splitting forces induced by the longitudinal bars. It has two sets of bars. One consists of the longitudinal bars close to the perimeter of the shaft and the other consists of bars extending from the column. For simplicity, it is assumed that all the column bars are subjected to uniform tension. In reality, some could be in compression, and compression bars could also induce splitting forces as they slip. Hence, it can be assumed that both sets of bars can slip and generate splitting forces.

Assuming that the magnitude of the radial stress σ is equal to the bond stress τ, as suggested by Tepfers (1973), one can express the splitting force per unit length of the

bar as $f = |\tau_{col}| d_{b,col}$ for the column bars and $f' = |\tau_{sh}| d_{b,sh}$ for the shaft bars. Since the forces from the column longitudinal bars have to be transferred to the shaft longitudinal bars, the total bond force per unit length of the column bars and that of the shaft bars have to be equal over the lap splice region. Hence,

$$N_{col} |\tau_{col}| \pi d_{b,col} = N_{sh} |\tau_{sh}| \pi d_{b,sh} \tag{6.2}$$

in which N_{col} is the total number of bars in the column and N_{sh} is the number of bars in the shaft. The above equation results in

$$f' = \frac{N_{col}}{N_{sh}} |\tau_{col}| d_{b,col} \tag{6.3}$$

Equilibrium is considered for the free bodies represented by the ABCD and CDEF portions of the pile shaft section shown in Figure 6.4. The free-body diagrams of these portions are presented in Figure 6.5. The forces acting on the two free bodies are the splitting forces of the bars being spliced (f and f') and the tensile forces in the shaft and column (outer and inner) hoops (t_{ext} and t_{int}). The line AB is a free surface with no loads applied, and the concrete is assumed to be splitted along the lines AD, DC, CB, DE, EF, and FC (marked as dashed lines in Figure 6.5). Therefore, the concrete cannot transfer any forces along these lines.

For the free body ABCD, the splitting forces in the tangential direction can be ignored because these forces from two adjacent bars practically cancel each other since they have the same magnitude and the same direction but with opposite signs. The splitting forces pointing in the radial direction result in an equivalent pressure, p_{ext}, which is given by Equation 6.4.

$$p_{ext} = \frac{N_{sh} f'}{\pi D_{ext}} = \frac{N_{col} |\tau_{col}| d_{b,col}}{\pi D_{ext}} \tag{6.4}$$

in which D_{ext} is the diameter of the outer (shaft) reinforcing hoops. Based on the equilibrium of the free body ABCD, the tensile force, t_{ext}, to be provided by the hoops per unit length of the shaft to balance p_{ext} is

$$t_{ext} = p_{ext}\frac{D_{ext}}{2} = \frac{N_{col}|\tau_{col}|d_{b,col}}{2\pi} \tag{6.5}$$

In the free body CDEF, the splitting forces in the tangential direction can be ignored based on the same argument presented for ABCD. Based on the equilibrium of the free body CDEF, the tensile force, t_{int}, to be provided by the hoops to compensate for the difference in pressures, p_{ext} and p_{int}, generated by the splitting radial forces of the inner bars and outer bars, respectively, is

$$t_{\text{int}} = p_{\text{int}}\frac{D_{\text{int}}}{2} - p_{ext}\frac{D_{ext}}{2} \tag{6.6}$$

in which D_{int} is the diameter of the inner (column) reinforcing hoops. The internal pressure, p_{int}, generated by the slip of the column bars, is given by

$$p_{\text{int}} = \frac{N_{col}f'}{\pi D_{\text{int}}} = \frac{N_{col}|\tau_{col}|d_{b,col}}{\pi D_{ext}} \tag{6.7}$$

Substituting Equations 6.4 and 6.7 in Equation 6.6, we have

$$t_{\text{int}} = \frac{N_{col}|\tau_{col}|d_{b,col}}{\pi D_{\text{int}}}\frac{D_{\text{int}}}{2} - \frac{N_{col}|\tau_{col}|d_{b,col}}{\pi D_{ext}}\frac{D_{ext}}{2} = 0 \tag{6.8}$$

Hence, the inner hoops will not develop tension, and can be considered ineffective for confining the lap splices. For this reason, they will be ignored here.

Minimum transverse reinforcement to prevent tensile splitting failure

The transverse steel in the lap splice region of a shaft should provide the tensile hoop force given by Equation 6.5 for a unit length of the shaft. As shown by the FE analysis results, the bond stress distribution along the development length of a bar is not uniform and the location of the peak stress depends on the extent of the plastic strain penetration. However, the maximum bond stress cannot exceed the ultimate bond strength τ_u obtained from monotonic bond-slip tests. Hence, to determine the quantity of the transverse steel required to provide the hoop force, it is conservative to assume that the peak bond stress be τ_u. This is conservative because the actual bond stress will be much lower due to the tensile yielding of the bars. With the above-mentioned assumption, the following equation can be obtained from Equation 6.5 to determine the

quantity of transverse reinforcement required to balance the splitting force and, thereby, maintain the bond resistance.

$$A_{tr} = \frac{1}{2\pi} \frac{N_{col} \tau_u d_{b,col} s_{tr}}{f_{y,tr}} \tag{6.9}$$

in which s_{tr} is the spacing of the transverse reinforcement, A_{tr} is the cross-sectional area of transverse reinforcing within spacing s_{tr}, τ_u is the ultimate bond strength of the column longitudinal reinforcement, which can be assumed to be 16.5 MPa (2.4 ksi) for a 34.5-MPa (5-ksi) concrete, $f_{y,tr}$ is the nominal yield stress of the transverse reinforcement, $d_{b,col}$ is the diameter of the longitudinal bars in the column, and N_{col} is the number of longitudinal bars in the column. For concrete strengths other than 34.5 MPa (5 ksi), τ_u can be scaled with the assumption that it is proportional to $f_c'^{3/4}$, as suggested in Chapter 4.

Given the uncertainty in the location of the peak bond stress, it is suggested that the transverse steel calculated with Equation 6.9 be distributed along the entire lap splice length. This equation remains valid when bundled bars are used. In the case that the shaft has a steel casing, the tensile forces developed in the transverse reinforcement and steel casing should satisfy Equation 6.10.

$$\frac{A_{tr}}{s_{tr}} f_{y,tr} + t_{cas} f_{y,cas} = \frac{1}{2\pi} N_{col} \tau_u d_{b,col} \tag{6.10}$$

in which t_{cas} is the thickness of the casing and $f_{y,cas}$ is the nominal yield strength of the steel casing.

Transverse reinforcement to limit crack opening

The quantity of the transverse reinforcement determined by Equation 6.9 or Equation 6.10 is to prevent the degradation of the bond strength after the development of tensile splitting cracks and, thereby, prevent premature bar anchorage failure. However, it does not necessarily provide an adequate control of the opening of a splitting crack, which can be significant as observed in some of the tests described in Chapter 7. Hence, an additional requirement is proposed here to control the opening of the splitting cracks.

In this development, it is assumed that a radial splitting crack develops along every shaft longitudinal bar. As it will be seen in Chapter 7, this assumption is consistent with the splitting crack patterns observed in the column-shaft tests. The opening of this crack will induce strain in the transverse reinforcement. As shown in Figure 6.6, assuming that the strain in a transverse reinforcing hoop is uniform and all the cracks have the same widths, we have the following relation between the strain in the transverse reinforcement and the opening of a radial crack, u_{cr}:

$$u_{cr} = \frac{\pi D_{ext}}{N_{sh}} \varepsilon_s \tag{6.11}$$

The maximum allowable strain, $\varepsilon_{s,\max}$, in the transverse reinforcement is then related to the maximum allowable crack opening as follows:

$$\varepsilon_{s,\max} = \frac{u_{cr,\max} N_{sh}}{\pi D_{ext}} \tag{6.12}$$

The transverse reinforcement required to control the crack width can then be established with Equation 6.9 by replacing $f_{y,tr}$ with $\varepsilon_{s,\max} f_{y,tr} / \varepsilon_y \le f_{y,tr}$. This results in

$$A_{tr} = \frac{1}{2\pi} \frac{N_{col} \tau_u d_{b,col} s_{tr}}{\alpha f_{y,tr}} \tag{6.13a}$$

where

$$\alpha = \frac{\varepsilon_{s,\max}}{\varepsilon_y} = \frac{u_{cr,\max} N_{sh}}{\pi D_{ext} \varepsilon_y} \le 1 \tag{6.13b}$$

Here, the maximum allowable crack opening is taken to be 0.3 mm (0.012 in.), which is based on the recommendation from ACI (2001) for RC members in constant contact with soil. For the case that the shaft has a steel casing, we have

$$\frac{A_{tr}}{s_{tr}} f_{y,tr} \alpha_1 + t_{cas} f_{y,cas} \alpha_2 = \frac{1}{2\pi} N_{col} \tau_u d_{b,col} \tag{6.14a}$$

where

$$\alpha_1 = \frac{u_{cr,\max} N_{sh}}{\pi D_{ext} \varepsilon_{y,tr}} \le 1 \tag{6.14b}$$

$$\alpha_2 = \frac{u_{cr,\max} N_{sh}}{\pi D_s \varepsilon_{cas}} \leq 1 \qquad (6.14c)$$

in which ε_{cas} is the nominal yield strain of the steel casing. In the above equation, the diameter of the casing is assumed to be the same as that of the shaft, which is denoted by D_s.

6.2 Specimen dimensions, reinforcing details, and materials

The dimensions and reinforcing details of the test specimens are summarized in Table 6.1.

6.2.1 Specimen 1

The design details of Specimen 1 are shown in Figure 6.7. It consisted of a 1219-mm (4-ft) diameter column that had a height of 4877 mm (16 ft), measured from the column base to the point of the horizontal load application, resulting in an aspect ratio (H/D) of 4. The pile shaft was 1829 mm (6 ft) in diameter and 2743-mm (9-ft) tall. The development length l_d required for the column bars was $30\,d_b$. Hence, the embedment length of the column cage, given by $D_{c,\max} + l_d$, was 2286 mm (7 ft - 6 in.), which is 762 mm (2 ft - 4 in.) shorter than that what would have been required per Caltrans SDC. The column longitudinal reinforcement consisted of 18 No. 11 (36-mm) bars (with a reinforcement ratio of 1.55%), and the transverse reinforcement consisted of double No. 5 (16-mm) hoops spaced at 165 mm (6.5 in.) on center (with a volumetric reinforcement ratio of 0.87%). The transverse reinforcement of the column cage embedded in the shaft consisted of single No. 5 hoops spaced at 165 mm (6.5 in.) on center. The shaft longitudinal reinforcement consisted of 28 No. 14 (43-mm) bars (with a reinforcement ratio of 1.55%), and the transverse reinforcement consisted of double No. 6 (19-mm) hoops spaced at 165 mm (6.5 in.) on center (with a volumetric reinforcement ratio of 0.82%). The transverse reinforcement complies with the design requirements for compression members in Article 5.7.4.6 of the AASHTO LRFD BDS.

6.2.2 Specimen 2

Specimen 2 consisted of a 1219-mm (4-ft) diameter and 6486-mm (18-ft) tall column (with an aspect ratio of 4.5), and a 1829-mm (6-ft) diameter and 2337-mm (8-ft) tall pile shaft, as shown in Figure 6.8. The column longitudinal reinforcement consisted of 18 No. 14 bars (with a reinforcement ratio of 2.25%), and the transverse reinforcement consisted of double No. 5 hoops spaced at 102 mm (4 in.) on center in the plastic-hinge region (with a volumetric reinforcement ratio of 1.41%), and single No. 5 hoops spaced at 152 mm (6 in.) on center in the rest of the column (with a volumetric reinforcement ratio of 0.94%). The development length l_d required for the column bars was $34d_b$. Hence, the embedment length of the column cage, given by $l_d + s + c$, was 1829 mm (6 ft), which is half of that what would have been required per Caltrans SDC. In the top 610 mm (2 ft) of the shaft, the transverse reinforcement for the column cage was the same as that for the plastic-hinge region of the column, and for the rest of the embedment length, single No. 5 hoops spaced at 152 mm (6 in.) on center were used. The shaft longitudinal reinforcement consisted of 26 No. 18 (57-mm) bars (with a reinforcement ratio of 2.55%), and the transverse reinforcement consisted of double No. 7 (22-mm) hoops spaced at 178 mm (7 in.) on center (with a volumetric reinforcement ratio of 1.01%). The quantity of the transfer reinforcement was determined with Equation 6.1, but with l_s replaced by l_d to be consistent with the actual embedment length used.

6.2.3 Specimen 3

Specimen 3 had the same geometry and reinforcement as Specimen 2, including the embedment length of the column reinforcement in the shaft, but it had different quantity of transverse reinforcement for the shaft, as shown in Figure 6.9. The shaft transverse reinforcement consisted of No. 8 (25-mm) hoops spaced at 165 mm (6.5 in.) on center (with a volumetric reinforcement ratio of 0.74%), complying with the transverse reinforcement requirements for compression members in Article 5.7.4.6 of the AASHTO LRFD BDS. In addition to the hoops, a 0.25-in.-thick steel casing made of

A36 steel was provided to comply with Equation 6.14 to resist the splitting forces generated in the anchorage region and control the width of the splitting cracks.

6.2.4 Specimen 4

Specimen 4 consisted of a 1219-mm (4-ft) diameter and 4877-mm (16-ft) tall column (with an aspect ratio of 4), and a 1524-mm (5-ft) diameter and 1829-mm (6-ft) tall shaft, as shown in Figure 6.10. The column longitudinal reinforcement consisted of 16 pairs of bundled No. 8 bars (with a reinforcement ratio of 1.40 %), and the transverse reinforcement consisted of No. 6 hoops spaced at 102 mm (4 in.) on center in the plastic-hinge region (with a volumetric reinforcement ratio of 1.0 %), and single No. 6 hoops spaced at 140 mm (5.5 in.) on center in the rest of the column (with a volumetric reinforcement ratio of 0.73%). The development length l_d required for the column bars was $29\,d_b$. The embedment length of the column cage was 940 mm (3 ft - 1 in.), which is $l_d + s + c$. In the top 610 mm (2 ft) of the shaft, the transverse reinforcement for the column cage was the same as that for the plastic-hinge region of the column, and for the rest of the embedment length, No. 6 hoops spaced at 152 mm (6 in.) on center were used. The shaft longitudinal reinforcement consisted of 20 pairs of bundled No. 11 (43-mm) bars (with a reinforcement ratio of 2.21%), and the transverse reinforcement consisted of double No. 7 (22-mm) hoops spaced at 140 mm (5.5 in.) on center (with a volumetric reinforcement ratio of 1.62%) in the anchorage region to comply with Equation 6.13. In the rest of the shaft, the transverse reinforcement consisted of double No. 7 (22-mm) hoops spaced at 178 mm (7 in.) on center (with a volumetric reinforcement ratio of 1.27%).

6.2.5 Footings and load stubs

Each specimen had a 4267-mm x 2438-mm x 1219-mm (14-ft x 8-ft x 4-ft) footing to anchor the shaft onto the strong floor. On top of the column, a 2438-mm x 2438-mm x 610-mm (8-ft x 8-ft x 2-ft) load stub was constructed for the application of the vertical and horizontal loads. The reinforcement in the footing and load stub was designed to sustain the maximum loads expected during the tests without damage.

6.2.6 Material Properties

Concrete with a specified compressive strength of 31 MPa (4500 psi) at 28 days, a slump of 178 mm (7 in.), and a maximum aggregate size of 9.5 mm (3/8 in.) was used in the shafts of all four specimens. Concrete with a specified compressive strength of 31 MPa (4.5 ksi) at 28 days, a slump of 102 mm (4 in.), and a maximum aggregate size of 25 mm (1 in.) was used in the columns. The specimens were to be tested after the concrete strength in the column and the shaft had reached 34.5 MPa (5.0 ksi). The actual strengths of the concrete measured on the days of the structural tests are presented in Table 6.2. All the reinforcement was Grade 60 complying with the ASTM A706 standards. Results from material tests on the steel reinforcement are presented in Table 6.3. The yield and tensile strengths of the A36 steel used for the casing of Specimen 3 are 324 MPa (47.0 ksi) and 472 MPa (68.4 ksi), respectively, based on material testing,

6.3 Construction

The specimens were casted in five stages: footing, lower portion of the shaft, upper portion of the shaft, column, and load stub. After each pour, some roughness was introduced to the cold joint with chisels. Before the following pour, steel brushing was applied to the joint to partially expose the aggregates. The joint was cleaned from debris and dust, and wetted immediately before receiving the fresh concrete. Pictures of the construction of the specimen are presented in Appendix B.

6.4 Instrumentation

The specimens were internally and externally instrumented to monitor the deformations during testing. Internal instrumentation consisted of electrical resistance strain gages attached to the longitudinal and transverse reinforcement in the shaft and the column. For Specimen 3, strain gages were also placed on the steel casing. External instrumentation consisted of displacement transducers attached to the specimens to measure the lateral displacements and different deformations, namely, the flexure

deformation, shear deformation, base rotation, and sliding at the interfaces. Pictures of the instrumentation are shown in Appendix B.

Strain gages were placed at different elevations in selected column and shaft longitudinal bars near the north and south faces of the specimens (the specimens were loaded in the north-south direction) to monitor the strain distributions along these bars, including the strains in the lap splice regions inside the shafts. The strain gages were placed on the longitudinal ribs of the bars to avoid disturbing the transverse ribs, which could affect the bond characteristics. In addition, strain gages were attached on selected column and shaft hoops, with special attention to the anchorage region in the shaft to monitor the concrete dilatation caused by bar slip. For Specimen 3, gages were also installed on the steel casing to measure its vertical and hoop strains. Drawings on the exact locations of the strain gages are shown in Appendix C.

For each specimen, the curvature distribution along the height of the column and of the shaft was measured with vertical displacement transducers mounted along two parallel lines on the east and west faces of each specimen. These transducers measured the vertical elongation between two rods embedded in the column and shaft concrete at different heights. The same rods were used as reference points to measure the horizontal and diagonal elongation on one side of the specimen to estimate the shear deformation of the column. Vertical displacement transducers were mounted at the base of the column to measure the base rotation with respect to the top of the shaft. Similar measurements were made on the base rotation of the shaft with respect to the footing. In addition, transducers were mounted to measure potential sliding between the different components of the specimen (which include the footing, shaft, column, and load stub), and potential sliding and uplift at the footing with respect to the strong floor. Drawings on the exact locations of the displacement transducers are shown in Appendix C.

6.5 Test setup and loading protocol

The test setup is shown in Figure 6.11. The specimens were secured onto the strong floor using 16 rods post-tensioned to a force of 1334 kN (300 kips) each. This force was determined to avoid sliding and decompression at any point in the floor-footing

interface during a test. In a test, the column was subjected to a constant vertical load of 3559 kN (800 kips). Together with the self-weight of the specimen, this load subjected the base section of the column to an axial stress equal to 9.4% of the targeted compressive strength of the concrete (which is 5,000 psi). The vertical load was applied on top of the specimen using four post-tensioned rods placed symmetrically around the column. Anchored at the top of the load stub, these rods passed through holes in the load stub, the footing, and the strong floor, and were subjected to a constant force using four center-hole hydraulic jacks located beneath the strong floor. The hole in the footing was trapezoid-shaped to allow the free rotation of the rod as it moved at its top end together with the load stub. Pictures of the test setup are presented in Appendix B.

The specimens were subjected to cyclic lateral displacements in the north-south direction using two 979-kN (220-kip) capacity, 1219-mm (48-in.) stroke actuators placed at the mid-height of the load stub on the north side of the specimen. The actuators were attached to a strong wall at a height of 8.84 m (29 ft) for Specimen 1, 9.1 m (30 ft) for Specimens 2 and 3, and 7.9 m (26 ft) for Specimen 4. The loading protocol used for the tests is shown in Figure 6.12a. Initially, each specimen was subjected to four fully-reversed force-controlled load cycles, with load amplitudes of 25, 50, 75, and 100% of the lateral load, F_y', that corresponds to the theoretical first yield of the longitudinal reinforcement at the base of the column. The specimen was then subjected to fully-reversed displacement-controlled load cycles with increasing system ductility demands of 1, 2, 3, 4, and so forth until the lateral load resistance dropped significantly due to the fracture of the longitudinal bars in the column. There were two cycles at each ductility level. The system ductility demand is defined as $\mu = \Delta / \Delta_y$, in which Δ is the lateral displacement of the specimen at the level of the horizontal actuators, and Δ_y is the effective yield displacement. As shown in Figure 6.12b, Δ_y is defined as the displacement at the intersection of the secant line passing through the point (Δ_y', F_y') that corresponds to the theoretical first yield of the column longitudinal bars and the horizontal line passing through the theoretical ultimate load (F_y). Hence,

$$\Delta_y = \frac{F_y}{F'_y}\Delta'_y \tag{6.15}$$

To define the loading protocol, F'_y and F_y were estimated from finite element analyses, and Δ'_y was taken as the average of the absolute maximum displacements measured in both loading directions in Cycle 4 of the test, in which the theoretical first yield was reached.

6.6 Summary

The test program in which four full-scale column-shaft assemblies were subjected to quasi-static cyclic loading has been presented in this chapter. These tests were intended to determine the minimum required embedment length of column longitudinal reinforcement extended into enlarged (Type II) shafts, and the transverse reinforcement required for the bar anchorage region of a shaft. In Specimen 1, an embedment length equal to $D_{c,\max} + l_d$, which is similar to the minimum requirement in current Caltrans SDC (Caltrans 2010), was used. In Specimens 2 through 4, the embedment lengths were reduced to $l_d + s + c$. New design recommendations for the transverse reinforcement in the bar anchorage region of a shaft have been proposed and were adopted for Specimens 3 and 4. Results of these tests are presented in Chapter 7.

Table 6.1: Dimensions and reinforcing details of test specimens

	Specimen 1	Specimen 2	Specimen 3	Specimen 4
Column diameter, mm (ft)	1219 (4)	1219 (4)	1219 (4)	1219 (4)
Shaft diameter, mm (ft)	1829 (6)	1829 (6)	1829 (6)	1524 (5)
Column longitudinal reinforcement (reinforcement ratio)	18 No. 11 (1.55%)	18 No. 14 (2.24%)	18 No. 14 (2.24%)	32 No. 8 (1.40%)
Shaft longitudinal reinforcement (reinforcement ratio)	28 No. 14 (1.55%)	26 No. 18 (2.55%)	26 No. 18 (2.55%)	40 No. 11 (2.21%)
Formula for embedment length of column reinforcement	$D_{c,\max} + l_d$	$l_d + s + c$	$l_d + s + c$	$l_d + s + c$
Embedment length of column reinforcement, mm (ft)	2286 (7.5)	1829 (6)	1829 (6)	940 (3.08)
Formula for transverse reinforcement in bar anchorage region of shaft	Compression Member, AASHTO	McLean and Smith's	Equation 6.9	Equation 6.14
Transverse reinforcement in bar anchorage region of shaft	2 No. 6 at 165 mm (6.5 in.)	2 No. 7 at 178 mm (7 in.)	No. 8 at 165 mm (6.5 in.) and 6.3-mm (0.25-in.) steel casing	2 No. 7 at 140 mm (5.5 in.)
Volumetric ratio of transverse reinforcement in bar anchorage region of shaft	0.82%	1.04%	1.65%[1]	1.62%
Transverse reinforcement plastic-hinge region of column	2 No. 5 at 165 mm (6.5 in.)	2 No. 5 at 102 mm (4 in.)	2 No. 5 at 102 mm (4 in.)	No. 6 at 102 mm (4 in.)
Volumetric ratio of transverse reinforcement in plastic-hinge region of column	0.87%	1.41%	1.41%	1.0%

[1] Total equivalent amount of Grade 60 transverse reinforcement.

Table 6.2: Compressive strength of concrete on the day of test

Specimen no.	Region	Compressive strength of concrete, MPa (ksi)
1	Shaft - lap splice region	34.5 (5.0)
	Shaft - below lap splice region	42.8 (6.2)
	Column - lower 2.8 m (9 ft)	34.0 (4.9)
	Column - upper 2.1 m (7 ft)	38.6 (5.6)
2	Shaft - lap splice region	37.0 (5.4)
	Shaft - below lap splice region	39.7 (5.8)
	Column - lower 2.8 m (9 ft)	38.6 (5.6)
	Column - upper 2.4 m (8 ft)	40.7 (5.9)
3	Shaft - lap splice region	36.2 (5.3)
	Shaft - below lap splice region	34.1 (4.9)
	Column - lower 2.8 m (9 ft)	35.0 (5.1)
	Column - upper 2.4 m (8 ft)	33.2 (4.8)
3	Shaft - lap splice region	36.6 (5.3)
	Shaft - below lap splice region	33.0 (4.8)
	Column - lower 2.8 m (9 ft)	35.5 (5.1)
	Column - upper 2.1 m (7 ft)	33.9 (4.9)

Table 6.3: Yield and tensile strengths of longitudinal reinforcement

Specimen no.	Bar	Yield strength, MPa (ksi)	Tensile strength, MPa (ksi)
1	No. 11	448 (65.0)	629 (91.2)
	No. 14	484 (70.1)	672 (97.4)
2	No.14	462 (67.0)	638 (92.5)
	No. 18	462 (67.0)	641 (93.0)
3	No. 14	462 (67.0)	641 (93.0)
	No. 18	462 (67.0)	652 (94.5)
4	No. 8	459 (66.5)	650 (94.3)
	No. 11	445 (64.5)	634 (92.0)

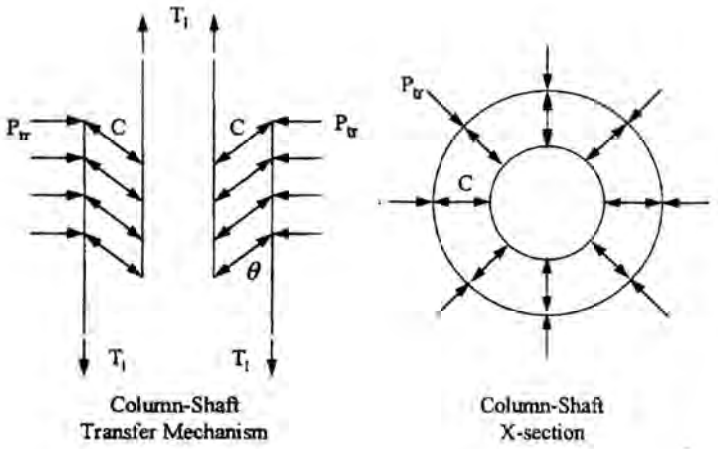

Figure 6.1: Truss analogy proposed by McLean and Smith (1997)

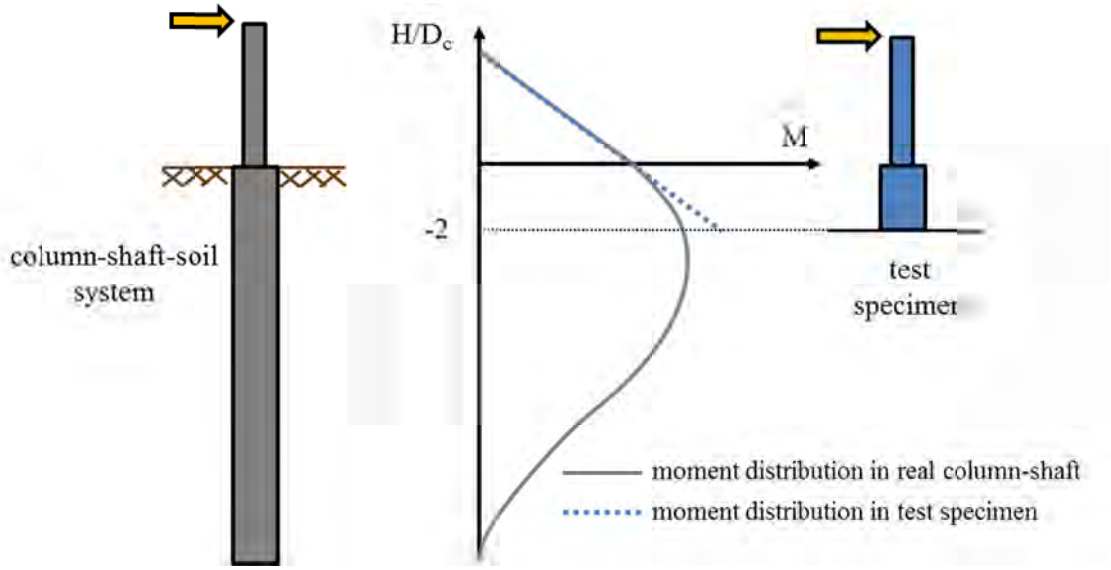

Figure 6.2: Bending moment distributions in a actual column-shaft and a test specimen

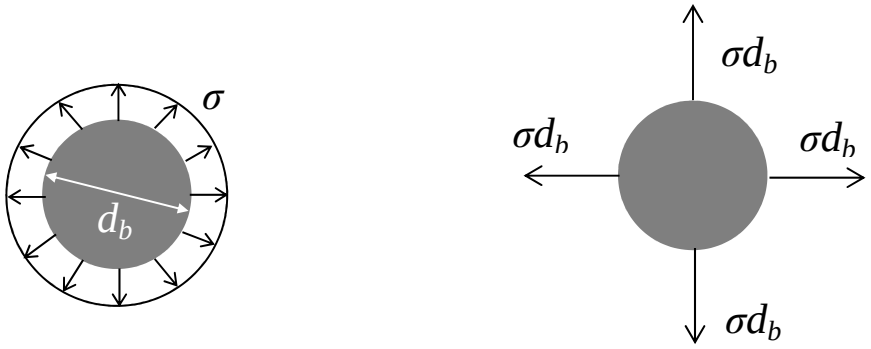

(a) Radial stress (b) Splitting forces per unit length of bar

Figure 6.3: Splitting stress and forces in developed bar

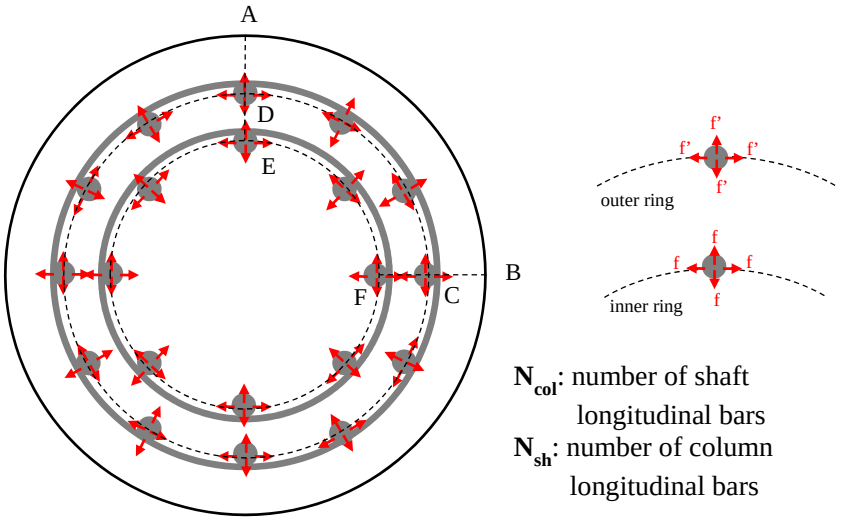

Figure 6.4: Cross section of pile shaft and splitting forces

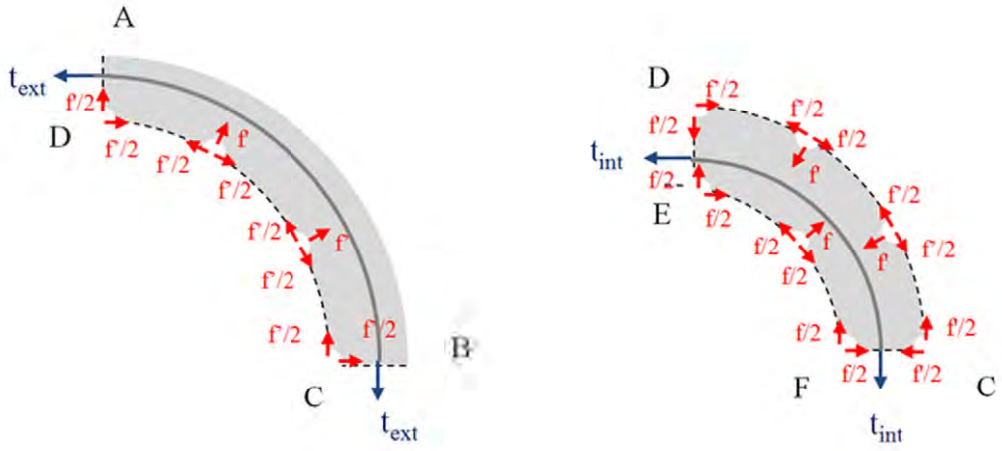

Figure 6.5: ABCD and CDEF free-body diagrams

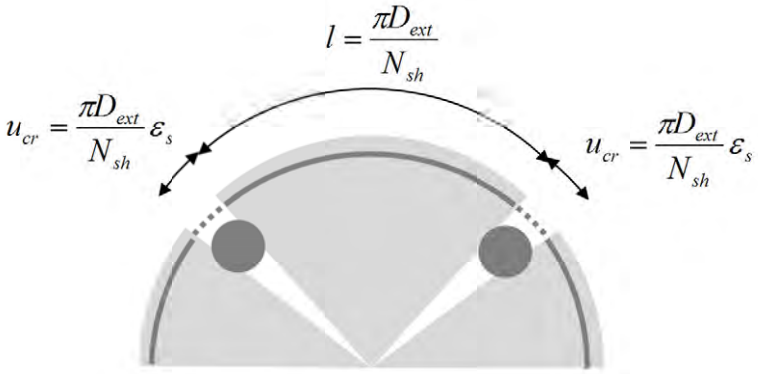

Figure 6.6: Splitting crack opening and strain in hoop reinforcement

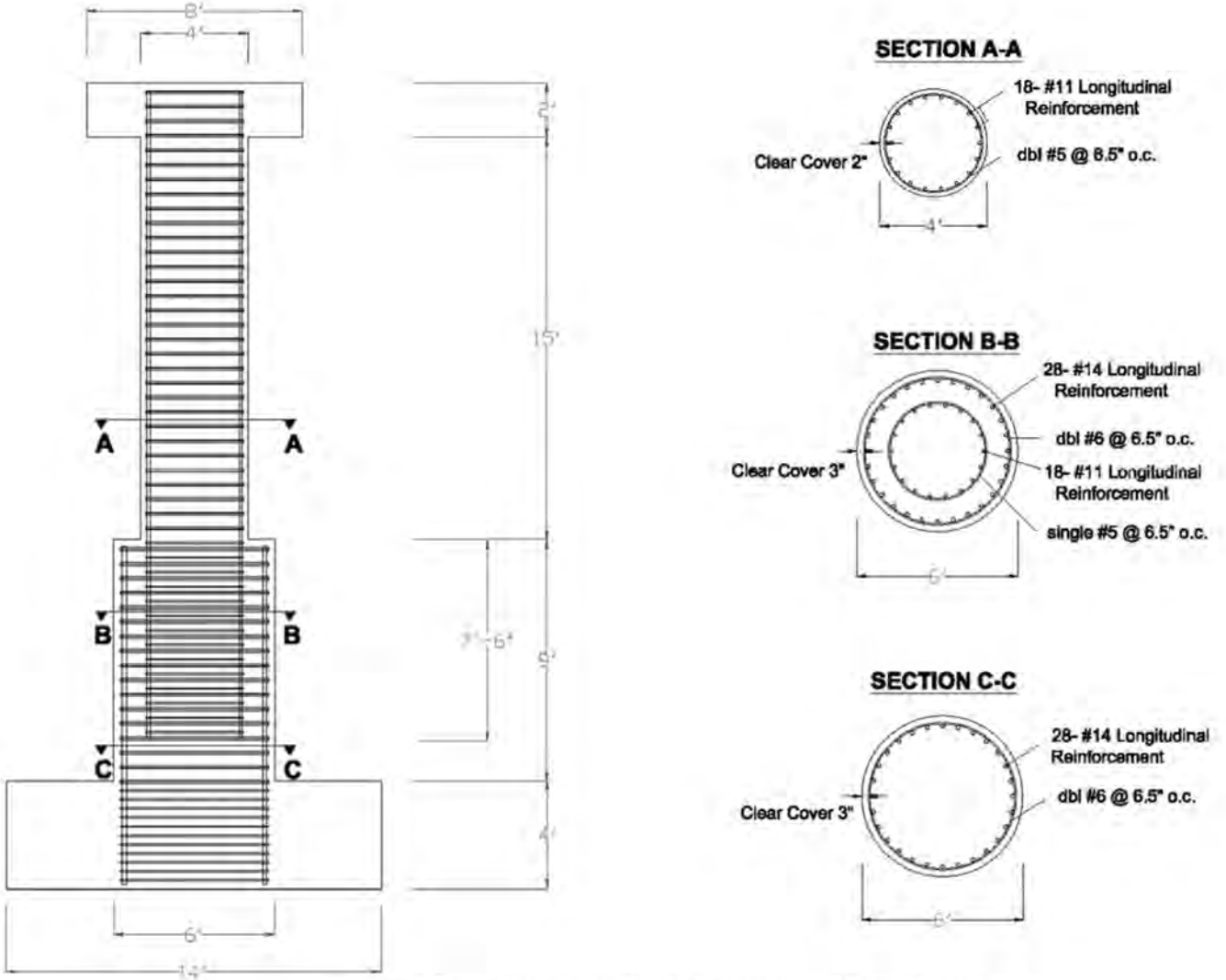

Figure 6.7: Geometry and reinforcement of Specimen 1
(1'=304.8 mm, 1"=25.4 mm)

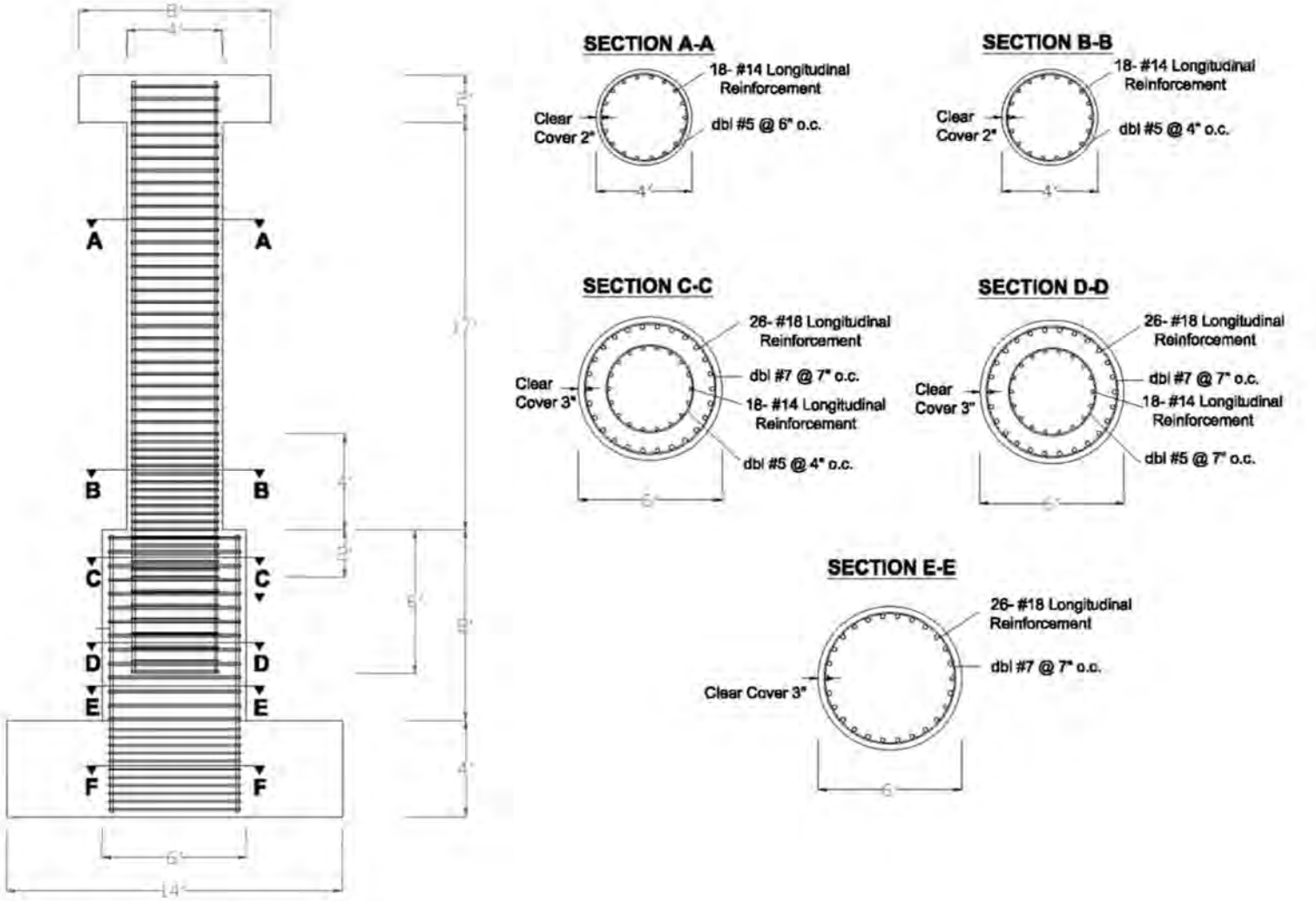

Figure 6.8: Geometry and reinforcement of Specimen 2
(1'=304.8 mm, 1"=25.4 mm)

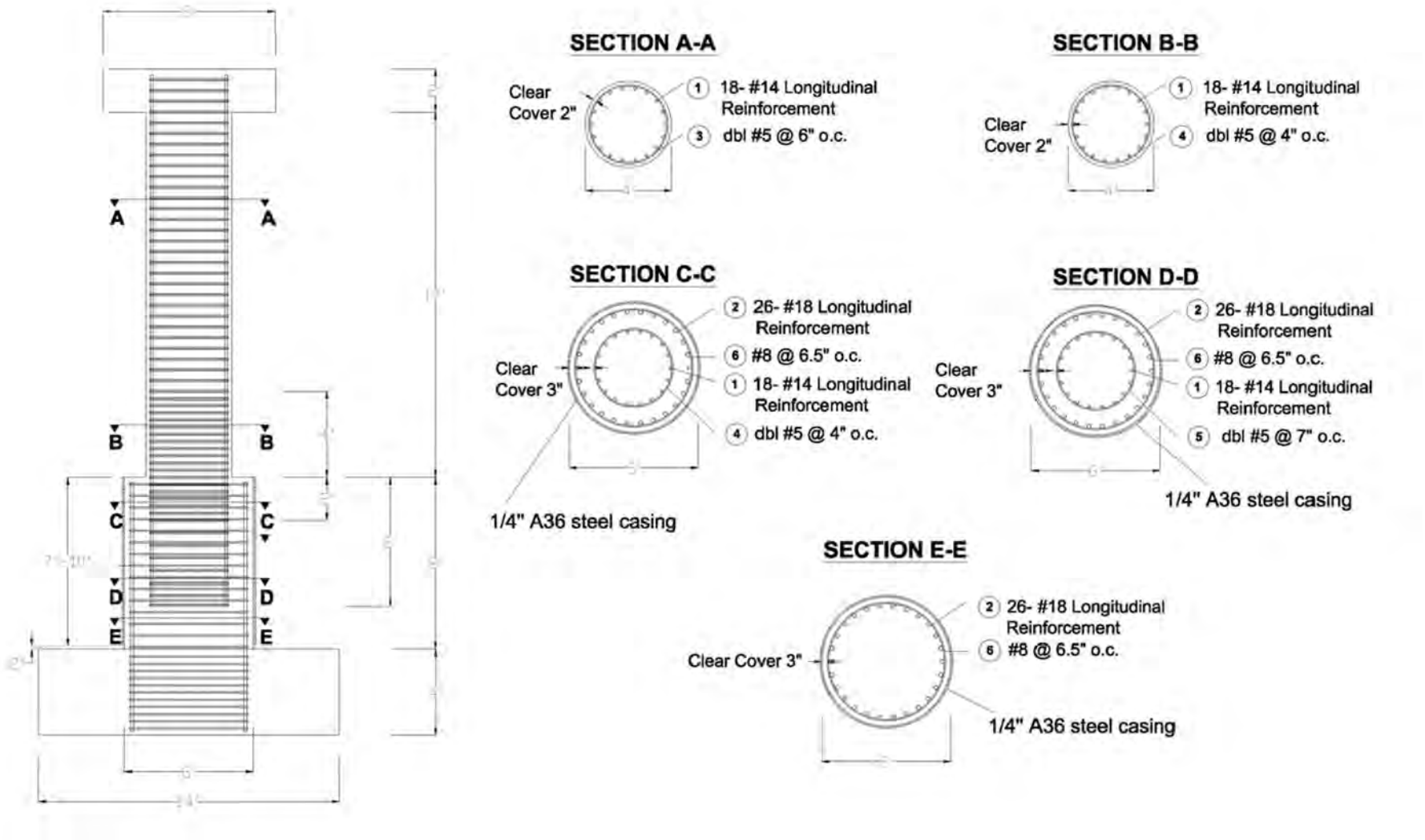

Figure 6.9: Geometry and reinforcement of Specimen 3
(1'=304.8 mm, 1"=25.4 mm)

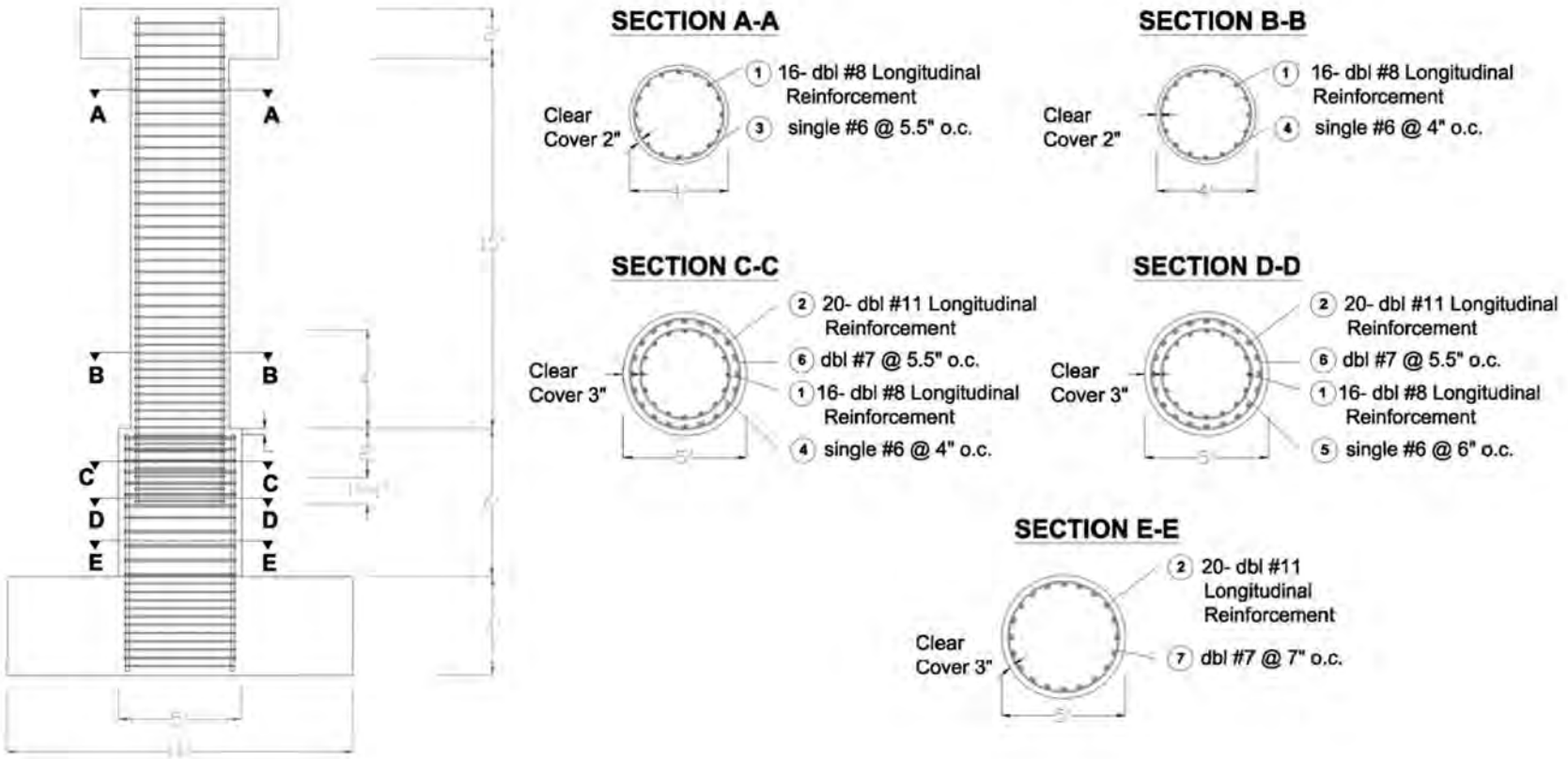

Figure 6.10: Geometry and reinforcement of Specimen 4
(1'=304.8 mm, 1"=25.4 mm)

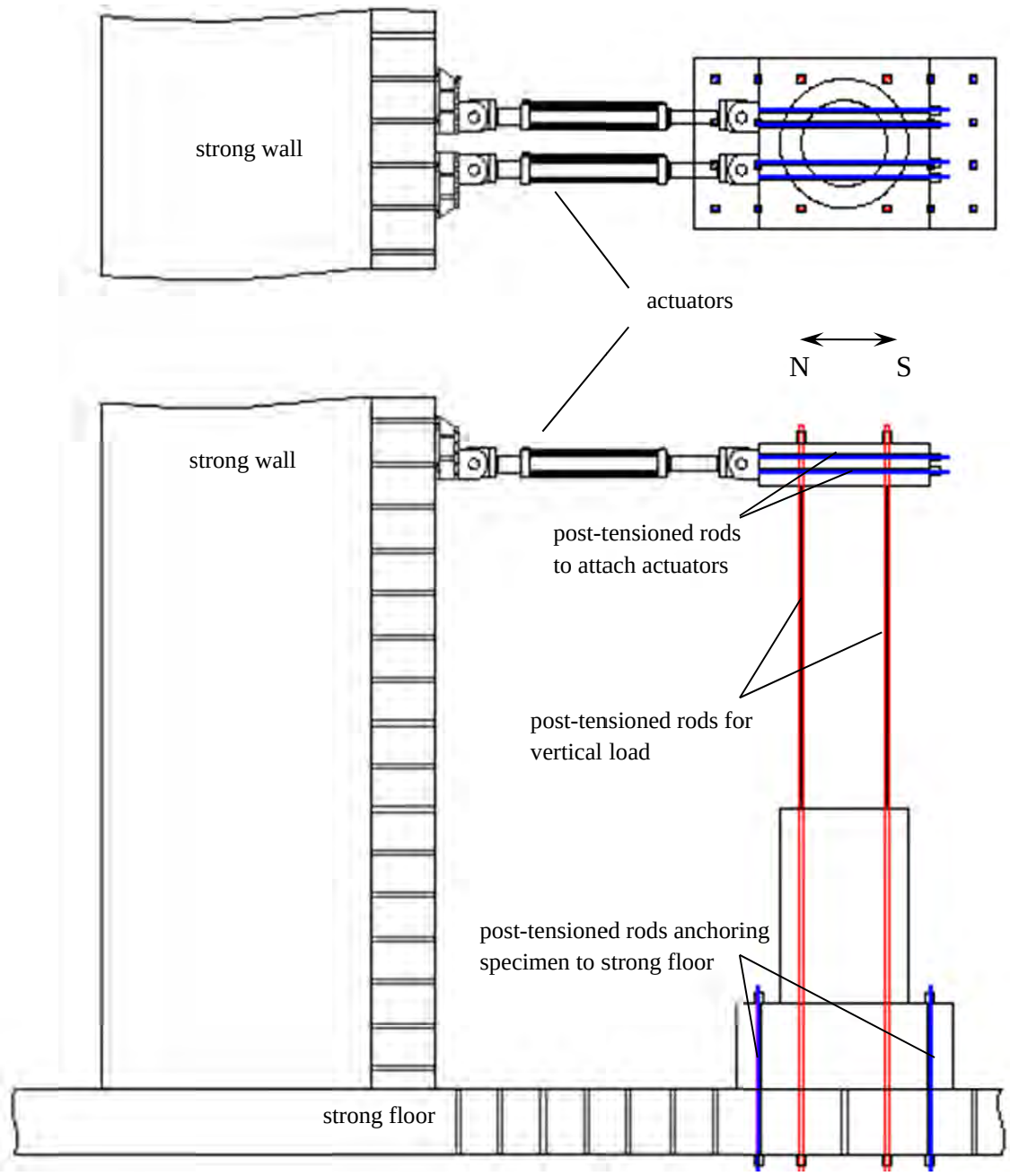

Figure 6.11: Test setup

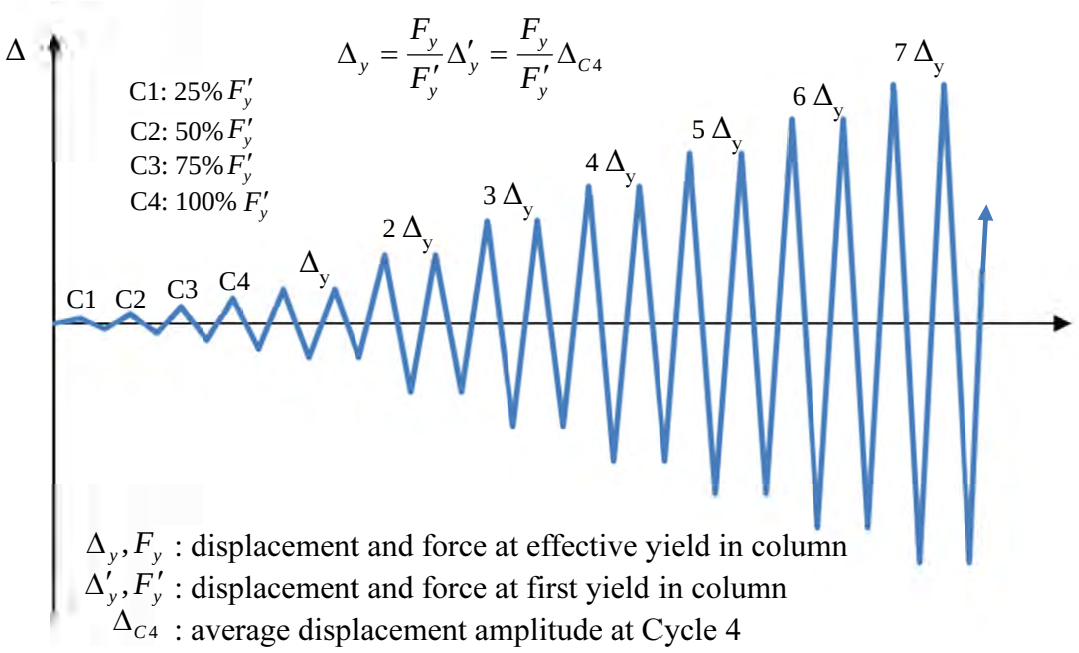

(a) Loading history

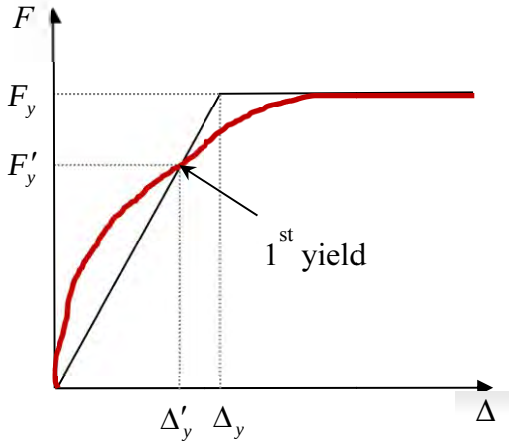

(b) First yield and effective yield

Figure 6.12: Loading protocol

CHAPTER 7

LARGE-SCALE LABORATORY TESTING OF COLUMN – ENLARGED PILE SHAFT ASSEMBLIES: TEST RESULTS

In this chapter, results of the tests conducted on four large-scale column – enlarged pile shaft assemblies are presented. For each of these specimens, the load-displacement response, main test observations, global lateral deformations, and strains in the reinforcing bars are presented and discussed. Emphasis is given to the strain measurements and damage observed in the bar anchorage region of the shafts. The maximum displacement and ductility reached in each cycle of the test are summarized in Table 7.1. The ductility values presented in this section are calculated with the effective yield displacement Δ_y, which is defined in the same way as that in Equation 6.15 but based on the actual maximum load and the actual displacement at the first yield attained in the tests instead of the theoretical values.

7.1 Specimen 1

7.1.1 Load-displacement response

The lateral load-vs.-top drift relation obtained for Specimen 1 is plotted in Figure 7.1. For the plots and the following discussion of the results, the positive direction of loading is defined to be towards the south, and the negative to be towards the north. The maximum lateral load attained was 1063 kN (239 kip). The gradual drop of the lateral resistance with drift was caused by the P-delta effect of the vertical force. The test was

stopped after the system displacement ductility had reached a value of 5.5 when the lateral load capacity started to decrease significantly due to the buckling and subsequent fracture of several longitudinal bars at the base of the column. The displacement ductility of the column itself reached a maximum value of 6.8, according to the calculation conducted by Liu (2012).

7.1.2 Test observations

Flexural cracks in the column started to be visible in the lower 1 m (3 ft) of the column at Cycle 2, i.e., at a force equal to 50% of that corresponding to the theoretical first yield. At Cycle 4, whose maximum load corresponds to the theoretical first yield, flexural cracking increased significantly in the column. The cracks developed in Cycle 2 propagated, and more flexural cracks appeared with a more or less uniform spacing of 250 mm (10 in.). However, the crack spacing increased slightly as they appeared farther away from the column base. Cracks were observed as far as 3 m (10 ft) from the base of the column or over 60% of the column height, as shown in Figure 7.2a. Some flexural cracks also appeared on both sides of the shaft (with about 600-mm [2-ft] spacing), as shown in Figure 7.2b and Figure 7.2c. In addition, several radial cracks extended from the column base to the edge of the shaft and continued vertically 300 mm (1 ft) to 600 mm (2 ft) down the surface of the shaft, as shown in Figure 7.2d and Figure 7.2e. These cracks were the result of the splitting forces generated by bar slip.

From Cycles 5 through 9, no new cracks were observed but the existing ones further propagated and opened. These cracks did not propagate further after Cycle 9. At Cycle 7, which was the first cycle at a system ductility of 2.2, the concrete at the base of the column started to be crushed on the north and south faces, as shown in Figure 7.3a. At Cycle 9, which was the first cycle at a system ductility of 3.3, spalling of the concrete cover at the base of the column started (see Figure 7.3b), and cracks with significant residual opening were observed. At Cycle 11, which was the first cycle at a system ductility of 4.4, spalling occurred in the lower 600 mm (2 ft) of the column with the hoop reinforcement exposed, as shown in Figure 7.3c. At Cycle 13, which was the first cycle at a system ductility of 5.5, spalling became more severe and exposed some of the

longitudinal bars on both sides of the column (see Figure 7.3d). On the north side, bars started to buckle at about 1 ft above the base of the column, as shown in Figure 7.3e. Upon load reversal in Cycle 14, which was the second cycle at a ductility of 5.5, these bars were placed in tension, and two of them fractured, as shown in Figure 7.3f. At the same time, two of the bars exposed on the south side started to buckle, and they fractured once the load was reversed. At this moment, the lateral load resistance had dropped significantly and the test was stopped. Finally, when bringing the column back to a zero residual drift, a third bar that had buckled on the north side fractured. The buckling and subsequent fracture of longitudinal reinforcement were also observed in previous tests on well-confined bridge columns, e.g., Lehman and Moehle (2000), Restrepo et al. (2006), and Carrea (2010). This type of fracture is the result of stress concentration in the extreme compression fiber of a buckled bar, which creates micro-cracks that will propagate when the bar is straightened up in tension again (Carrea 2010).

At the end of the test, after the rubbles formed by the crushing of the concrete at the column base had been removed, a circular crack was observed on the top of the shaft, as shown in Figure 7.4a and Figure 7.4b. This crack was the result of a cone shaped failure at the top of the embedment length of the column longitudinal reinforcement. Radial cracks due to the splitting forces introduced by bar slip at the top of the shaft are also visible in Figure 7.4a and Figure 7.4b. The maximum residual width measured in one of these cracks at the end of the test was 3 mm (1/8 in.). The splitting cracks extended vertically on the lateral surface of the shaft with lengths between 600 mm (2 ft) and 1200 mm (4 ft), as shown in Figure 7.4c.

7.1.3 Global lateral deformations

The lateral displacements of the specimen, plotted in Figure 7.5, at the peak displacements of different cycles, reveal that the lateral deformation of the shaft was very small, and that most of the displacement in the column was due to the curvature in the plastic-hinge region of the column and the rotation at the column base due to bar slip. The flexural and shear deformations, as well as the base rotation due to bar slip, were calculated with the displacement transducers readings. Description of how these

deformations were computed can be found in Liu (2012). The shear deformation was found negligible as compared to the flexural deformation and the base rotation of the column due to bar slip. According to Liu (2012), between 50% and 75% of the total displacement at the top of the column with respect to the top of the shaft was due to flexure; the base rotation accounts for about 20% to 50% of the total displacement of the column. The curvature measurements are compared to the yield curvature calculated by the expression $2.25\frac{\varepsilon_y}{D_c}$, which is an approximation suggested by Priestley (2003), where D_c is the diameter of the column and ε_y is the yield strain of the longitudinal reinforcement. At Cycle 13, the curvature in the lower 1.45 m (4.8 ft) of the column (30% of the column height), where most of the damage occurred, was higher than the estimated yield curvature. The maximum curvature occurred in the lower 300 mm (1 ft) of the column; and at the last cycle, it reached a value equal to 12 times the estimated yield curvature. The curvature in the shaft was much smaller than the estimated yield curvature.

7.1.4 Strains in reinforcing bars

The strain distributions along the column longitudinal bars at the peak displacements of different cycles are plotted in Figure 7.7 and Figure 7.8 for two bars located at the north face and two at the south face of the specimen, respectively. Two of the bars were located at the extreme north and south faces of the column, and the other two were adjacent to them. The strain was measured in these bars at different heights in the lower half of the column and along the embedment length in the shaft, l_e. Only one of the longitudinal bars (northwest bar) yielded at the base of the column before the peak load of Cycle 4 had been reached, as it had been predicted. After yielding, the maximum tensile strains along the bar occurred at a height of 610 mm (2 ft), but this does not necessarily mean that the maximum tensile stresses were developed at this height because the strain gages below experienced significantly higher residual compressive strains. Figure 7.7 and Figure 7.8 also show consistent trends in the strain penetration along the

embedment length. The maximum plastic strain penetration developed in the bars at a system ductility of 5.5 was 610 mm (2ft), which is equivalent to 17 times the bar diameter, d_b, or 27% of the total embedment length. The bond stresses in these bars are calculated with a finite element model, which will be discussed in Chapter 8.

The strain distributions along four of the longitudinal perimeter bars in the shaft at the peak displacements of different cycles are plotted in Figure 7.9. Two of the bars were located at the extreme north and south faces of the shaft, and the other two were adjacent to them. All these bars remained elastic. The strain varied practically linearly along the splice length. From the strain measurements, the axial stresses in the bars have been calculated; and from the difference in the stresses at two adjacent gage locations, the average bond stress has been calculated. The bond stresses in this region are small, less than 15% of the maximum bond strength obtained from the tests presented in Chapter 3.

The strains in the column cage hoops located at different heights of the column and inside the embedment length at the peak displacements of different cycles are plotted in Figure 7.10. These strains were measured near the north and south faces of the specimen. All the hoops except those located in the plastic hinge area remained elastic. The hoop located approximately 1 ft above the column base yielded at a system ductility of 4.4. This corresponds to the onset of buckling of some of the longitudinal bars in this region. Before a system ductility of 5.5 was reached, these strain gages were damaged. The column hoop located at a depth of 203 mm (8 in.) inside the embedment length area also experienced significant strains on the north side and yielded at a system ductility of 5.5, before the strain gages were damage. The rest of the column hoops inside the shaft remained elastic with strains significantly smaller than the yield strain.

Figure 7.11 presents the strains in the shaft hoops at the peak displacements of different cycles. These strains were measured near the north and south faces of the specimen. The strain is higher for the hoops in the upper portion of the lap splice. This could be partly due to the bar slip and partly to the plying action of the confined column core. The hoop located at 305 mm (1 ft) from the top of the shaft reached its yield strain in Cycle 13. No strain gages were placed in hoops above this level. The hoops located in the lower half of the embedment length experienced practically no strain.

7.2 Specimen 2

7.2.1 Load-displacement response

The lateral load-vs.-top drift relation obtained for Specimen 2 is plotted in Figure 7.12. The maximum lateral load reached 1223 kN (275 kips), and the test was stopped after the specimen had reached a system displacement ductility of 6.9, when one of the longitudinal bars fractured at the base of the column. The maximum displacement ductility of the column itself reached a value of 8, according to the analysis conducted by Liu (2012).

The lateral loads normalized by the respective peak loads are plotted against a system ductility for Specimens 1 and 2 in Figure 7.13. The difference in the embedment length does not seem to affect the global behavior of the columns. However, Specimen 2 shows a higher ductility than Specimen 1 because bar buckling and fracture were delayed due to the more closely spaced hoops at the base of the column.

7.2.2 Test observations

The behavior of Specimen 2 during the early cycles was very similar to that of Specimen 1. Flexural cracks appeared in the column and the shaft as early as Cycle 2, i.e., at a force equal to 50% of that corresponding to the theoretical first yield. Figure 7.14 shows the distribution of flexural cracks in the column and shaft right after Cycle 4, at which the theoretical first yield was reached. Radial cracks at the top of the shaft appeared as early as Cycle 3, i.e., at a force equal to 75% of that corresponding to the theoretical first yield, as shown in Figure 7.15. As in Specimen 1, the number of flexural and radial cracks did not increase after Cycle 5.

The evolution of damage on the north and south faces near the base of the column is shown in Figure 7.16 and Figure 7.17, respectively. At Cycle 7, which was the first cycle at a system ductility of 2, the concrete at the base of the column started to be crushed on both sides of the column (see Figure 7.16a and Figure 7.17a). At Cycle 8, which was the second cycle at a ductility of 2, spalling of the concrete cover started on the south side (see Figure 7.17b), while spalling did not occur on the north side until

Cycle 11, which was the first cycle at a system ductility of 3 (see Figure 7.16c). At Cycle 13, which was the first cycle at a system ductility of 5, the concrete cover over the lower 600 mm (2 ft) to 900 mm (3 ft) of the column spalled on both sides exposing the hoop reinforcement, as shown in Figure 7.16d and Figure 7.17d. At this stage, the damage at the top of the shaft was significant with a circular crack (cone failure) and radial (splitting) cracks widely opened, as shown in Figure 7.18a. The maximum residual crack opening measured at the splitting cracks after unloading was 6 mm (1/4 in.), twice as much as that measured in Specimen 1 at the same system ductility level. Subsequent cycles induced further spalling of the concrete at the base of the column exposing some of the longitudinal bars. The damage at the top of the shaft increased, with the cone-shaped fracture and splitting cracks developing to such an extent that pieces of concrete started to be detached (see Figure 7.18b). At the beginning of Cycle 18, which was the second cycle at a targeted system ductility of 6.9, one of the column longitudinal bars on the north side fractured at the column-shaft interface (see Figure 7.16f). A drop of the load carrying capacity of the column was observed, and the test was stopped before the cycle was completed.

Post-test inspection of the column indicated that some of the adjacent bars had started to buckle at the location where one bar fractured, as shown in Figure 7.16f. Buckling was not as severe as in Specimen 1 due to the better confinement provided by the hoops in the plastic-hinge region. The detached pieces of concrete at the top of the shaft caused by the cone formation and splitting cracks were removed by hand after the test. Figure 7.18c and Figure 7.18d show pictures of the shaft after these pieces were removed. A cone shaped surface with an average inclination of 25 degrees with respect to a horizontal plane had formed between the column and the shaft cages, and splitting cracks connecting radially the longitudinal bars in the column and the shaft were visible, as shown in Figure 7.18c. More splitting cracks were observed in this specimen than in Specimen 1, and they extended vertically with lengths between 900 mm (3 ft) to 1200 mm (4 ft) on the lateral surface of the shaft, as shown in Figure 7.18e. The more severe damage observed on the top of the shaft as compared to Specimen 1 can be explained by the larger splitting forces generated by the larger diameter bars and by the higher ductility

demand attained in the test. It is also possible that this was caused by a larger slip experienced by the bars.

7.2.3 Global lateral deformations

The lateral displacements of the specimen at the peak displacements of different cycles are plotted in Figure 7.19, and the curvatures are plotted in Figure 7.20. As in Specimen 1, these plots reveal that most of the displacement at the top of the column with respect to the top of the shaft was due to the curvature in the plastic-hinge region of the column and the rotation at the column base due to bar slip. Displacement measurements at the top of the shaft are not available after Cycle 9. After this load cycle, the rod connected to the displacement transducer started to be detached from the shaft due to the widely opened cracks at the top of the shaft. Curvature measurements at the top portion of the shaft are not available for the same reason. According to Liu (2012), between 50% and 80% of the total displacement at the top of the column with respect to the top of the shaft was due to flexural deformation; base rotation contributed between 15% and 50%, and shear deformation contributed less than 3% to the total displacement. As shown in Figure 7.20, the curvature distributions at the peak displacements of different cycles are not perfectly symmetrical in that the maximum curvature in the positive direction is higher than that obtained in the negative direction. This difference can be related to the unsymmetrical damage observed at the base of the column. The higher curvature in the positive direction, i.e., when the north face of the specimen was subjected to compression, is consistent with the fact that there was more concrete spalling on the north side. Figure 7.20 also shows that plastic flexural deformation developed near the column base over a distance of 2.1 m (6.8 ft), i.e., 38% of the effective height of the column, and that the maximum curvature ductility demand was 20 (with respect to the yield curvature estimated with the empirical expression presented in Section 7.1.3), which occurred at 305 mm (1 ft) above the column-shaft interface. Like in Specimen 1, the curvature in the shaft was much smaller than the theoretical yield curvature.

7.2.4 Strains in reinforcing bars

The strain values along the column longitudinal bars at the peak displacements of different cycles are plotted in Figure 7.21 and Figure 7.22 for two bars located at the north face and two at the south face of the specimen, respectively. The strain variations are similar to those for Specimen 1. The maximum strains are obtained in the lower 610 mm (2ft) of the column. For most of the bars, the maximum plastic strain penetration observed inside the embedment length is 610 mm (2 ft), which corresponds to $14\,d_b$, at a system ductility of 5. In two of the bars, the plastic strain penetration reached 915 mm (3 ft), or $21\,d_b$. Hence, even though the embedment length was reduced significantly with respect to Specimen 1, the plastic strain penetration observed at the same ductility demand was very similar. However, given the shorter embedment length of the column reinforcement in Specimen 2, the above-mentioned plastic penetrations represent 33% and 50% of the embedment length, respectively. For higher ductility demand levels, strain gages along the entire embedment length were damaged in all the bars. This indicates that bar slips started to be significant at this stage. The strain and bond stress distributions along these bars are further analyzed with a finite element model in Chapter 8.

The strain distributions along the longitudinal perimeter bars in the shaft at the peak displacements of different cycles are plotted in Figure 7.23. All the bars remained elastic, and the average bond stresses along the lap splice length calculated from the strain readings in this region varied between 5 and 30% of the maximum bond strength obtained from the tests presented in Chapter 3.

The strains in the column cage hoops located at different heights of the column and inside the embedment length at the peak displacements of different cycles are plotted in Figure 7.24. The strains were measured near the north and south faces of the specimen. For two of the hoops located near the base of the column, strains were also measured on the west side of the specimen. Like in Specimen 1, only the hoops located near the column base yielded on the north and south sides of the specimen. These hoops reached the nominal yield strain at a system ductility of 5. There were located in the region where

severe concrete crushing and bar buckling occurred. However, the strains on the west side of these same hoops did not even reach 50% the yield strain. All the column hoops inside the shaft remained elastic and experienced little strain.

Figure 7.25 presents the strains in the shaft hoops at the peak displacements of different cycles. These strains were measured near the north and south faces of the specimen. For three of the upper hoops, strains were also measured on the west side of the specimen. Like in Specimen 1, strain is higher for the hoops in the upper portion of the lap splice. The uppermost hoop, located at 75 mm (3 in.) below the top of the shaft, reached its yield strain in Cycle 13. The strains varied almost linearly along the height, and the hoop located at the bottom of the lap splice area experienced practically no strain. The strains on the west side of the uppermost hoop are very close to those obtained on the north and south sides. This is in agreement with the assumption of a uniform hoop strain adopted in the derivation of Equations 6.13 and 6.14.

7.3 Specimen 3

7.3.1 Load-displacement response

The lateral load-vs.-top drift relation obtained for Specimen 3 is plotted together with that of Specimen 2 in Figure 7.12. For Specimen 3, the maximum lateral load reached 1205 kN (271 kips); and the test was stopped after the specimen had reached a system ductility of 7.3, when several longitudinal bars had fractured and the lateral load resistance had dropped significantly. The lateral load-vs.-displacement response for Specimen 3 is very similar to that for Specimen 2, but Specimen 3 had some longitudinal bars fractured at the base of the column at an earlier cycle than Specimen 2, as the load drops shown in Figure 7.12 indicate.

7.3.2 Test observations

The behavior of the column in Specimen 3 is very similar to that in Specimen 2. The evolution of damage on the north face near the bottom of the column is plotted in Figure 7.26. Flexural cracks appeared in the column as early as Cycle 2, i.e., at a force

equal to 50% of that corresponding to the theoretical first yield. Figure 7.26a shows the distribution of flexural cracks at the base of column at Cycle 3. At Cycle 7, which was the first cycle at a system ductility of 2.1, the concrete at the base of the column started to be crushed, as shown in Figure 7.26b. At Cycle 9, the first cycle at a system ductility of 3.1, spalling of the concrete cover started (see Figure 7.26c). The severity of spalling in the subsequent cycles increased such that the transverse reinforcement was exposed at Cycle 13 (see Figure 7.26d) and longitudinal bars were exposed at Cycle 15 (see Figure 7.26e). During Cycle 16, which was the second cycle at a system ductility of 6.3, one of the column longitudinal bars on the south side fractured at about 0.3 m (1 ft) above the column base. A drop of the load carrying capacity of the column was observed. The test was continued until the end of Cycle 17, resulting in the fracture of three longitudinal bars per side, and a significant deterioration of the lateral load resistance. The bars fractured on the north side of the specimen are shown in the picture in Figure 7.26f taken at the end of the test.

In the shaft, flexural cracks could only be observed at the base because the rest of the shaft was covered by the steel casing. Similarly to those in Specimen 2, radial cracks appeared at the top of the shaft as early as Cycle 3, i.e., at a force equal to 75% of that corresponding to the theoretical first yield, as shown in Figure 7.26a. However, the width of these cracks remained small during the entire test. As shown in Figure 7.27a and Figure 7.27b, damage on the top face of the shaft at the end of Cycle 13 was less severe than that for Specimen 2 (see Figure 7.18a). The maximum residual width of the radial cracks on the top face of the shaft at this stage was 0.3 mm (0.012 in.), which is significantly smaller than the 6-mm (1/4-in.) wide cracks observed in Specimen 2 at a similar ductility demand. At the end of the test, the damage on the top face of the shaft was much less severe than that in Specimen 2, as shown in Figure 7.27c and Figure 7.27d. The maximum residual width of the splitting cracks observed was 1 mm (0.04 in.) and a much shallower cone-shaped crack was observed. After the test, the steel casing was removed and the maximum width of the cracks a few inches below the top of the shaft, where the shaft hoops were also effective in restraining these cracks, was measured to be 0.2 mm (0.008 in.), as shown in Figure 7.27e and Figure 7.27f. Hence, the higher

quantity of transverse reinforcement provided in this specimen by the hoops and steel casing according to Equation 6.14 was effective in restraining the opening of the splitting cracks and limiting damage in the shaft.

7.3.3 Global lateral deformations

The lateral displacements of the specimen at the peak displacements of different cycles are plotted in Figure 7.28. Like in the previous specimens, most of the displacement at the top of the column with respect to the top of the shaft was due to the curvature in the plastic hinge region and the rotation at the column base due to bar slip. The curvature distributions at the peak displacements of different cycles are plotted in Figure 7.29. Plastic flexural deformation occurred over a distance of 1.55 m (5.1 ft) near the base of the column, i.e., 28% of the effective height of the column; and the curvature ductility reached near the base of the column during Cycle 16 was 24 (with respect to the yield curvature estimated with the empirical expression presented in Section 7.1.3). Larger curvatures were measured in Cycle 17, but the column had already failed with the buckling and fracture of several bars. No curvature measurements were taken in the shaft. Due to the steel casing, no target rods could be inserted in the shaft except at the base. Based on the results from the previous specimens, the curvature developed in the shaft was expected to remain small.

7.3.4 Strains in reinforcing bars

The strain distributions along the column longitudinal bars at the peak displacements of different cycles are plotted in Figure 7.30 and Figure 7.31 for two bars located at the north face and two at the south face of the specimen, respectively. The penetration of plastic strains inside the embedment length is slightly smaller than that in Specimen 2. The maximum plastic strain penetration measured inside the embedment length is 610 mm (2 ft), which occurred at a system ductility of 6.3. This corresponds to $14\,d_b$. In Specimen 2, the plastic penetration reached 915 mm (3 ft), or $21\,d_b$, in some bars at a system ductility of 5, and the strain gages were damaged at higher ductility levels due to the large slip of the bars. The strain gages in Specimen 3 were not damaged.

Hence, the higher quantity of confinement in the shaft with respect to Specimen 2 seems to improve the bond of the longitudinal column bars.

The strain distributions along two of the longitudinal perimeter bars on the north side of the shaft at the peak displacements of different cycles are plotted in Figure 7.32. The strains in these bars are similar to those in the corresponding bars in Specimen 2. The strain data is incomplete because several strain gages were damaged. The strain readings on the south face of the specimens were not obtainable because of unreliable gage readings.

The column hoops remained elastic except those located near the base of the column, which yielded during Cycle 13 at a system ductility of 5.2, as shown in Figure 7.33. At this stage, severe concrete crushing and spalling had occurred at the base of the column, and transverse reinforcement had been exposed. The yielding of the hoops could indicate that the longitudinal bars had started to buckle.

The shaft hoops experienced a significantly smaller strain than those in Specimen 2. As shown in Figure 7.34, the maximum strain was measured at the uppermost hoop, located at about 75 mm (3 in.) from the column base, and it was only 65% of the yield strain. Like in Specimen 2, the hoop strains were smaller towards the bottom of the embedment length. The hoop strains measured in the steel casing are similar to those in the hoops at the same elevations, as shown in Figure 7.35. Yielding of the casing was measured on the north, south, and west faces of the specimen only at one elevation, which is 25 mm (1 in.) below the column base. This occurred at Cycle 13 at a system ductility of 5.2. These results show that the steel casing can reduce the hoop strains in the shaft, providing a good control of the opening of splitting cracks.

7.4 Specimen 4

7.4.1 Load-displacement response

The lateral load-vs.-top drift relation obtained for Specimen 4 is plotted in Figure 7.36. The maximum lateral load reached 1023 kN (230 kips). The test was stopped after

the specimen had reached a system ductility of 6.6, when several longitudinal bars had fractured and the lateral load resistance had dropped significantly.

7.4.2 Test observations

The behavior of the column in Specimen 4 is very similar to that in the previous specimens, even though the shaft diameter was smaller. However, cracking in the shaft was more severe than that in the other specimens. The evolution of damage at the column base on the north face of the specimen is shown in Figure 7.37. Flexural cracks appeared in the column and shaft as early as Cycle 2 at a force equal to 50% of that corresponding to the theoretical first yield. Figure 7.37a shows the distribution of flexural cracks at the base of the column at Cycle 4, which corresponded to the theoretical first yield. At Cycle 7, which was the first cycle at a system ductility of 2.2, the concrete at the base of the column started to be crushed. Spalling at the base of the column started at Cycle 9, the first cycle at a system ductility of 3.3, and became severe by Cycle 11, the first cycle at a system ductility of 4.4, as shown in Figure 7.37c. During Cycle 13, which was the first cycle at a system ductility of 5.5, longitudinal and transverse reinforcement was exposed at the base of the column, and some column longitudinal bars had started to buckle, as shown in Figure 7.37d. During Cycle 14, which was the second cycle at a system ductility of 5.5, one pair of bundled bars that had buckled fractured, as shown in Figure 7.37e, and a drop of the load carrying capacity of the column was observed (see Figure 7.36). The test was continued until the end of Cycle 16, resulting in the fracture of three pairs of bundled bars per side, and a significant drop of the lateral load resistance. The bars fractured on the north side of the specimen are shown in the picture in Figure 7.37f, which was taken at the end of the test.

In the shaft, severe splitting cracking was observed during the test, as shown in Figure 7.38. Like those in Specimen 2, splitting cracks appeared near the top of the shaft as early as Cycle 3 at a force equal to 75% of that corresponding to the theoretical first yield. At Cycle 13, some of these splitting cracks were widely opened at the top of the shaft (with the maximum residual crack width equal to 10 mm [0.4 in.]) and had already propagated through the entire embedment length, as shown in Figure 7.38a and Figure

7.38b. At the end of the test, these cracks were wide open on the top of the shaft (with the maximum residual crack width larger than 15 mm [0.6 in.]) with pieces of concrete starting to be detached, as shown in Figure 7.38c and Figure 7.38d. Also, a circular crack was observed around the column cage, indicating the formation of a small cone-shaped breakoff.

7.4.3 Global lateral deformations

The lateral displacements of the specimen at the peak displacements of different cycles are plotted in Figure 7.39. Like that in the previous specimens, most of the displacement at the top of the column was due to the curvature in the plastic-hinge region of the column and rotation at the column base due to bar slip. The curvature distributions at the peak displacements of different cycles are plotted in Figure 7.40. Plastic flexural deformation developed over a length of 1.1 m (3.6 ft) near the column base, which was 23% of the effective height of the column; and the curvature ductility near the base of the column reached 21 (with respect to the yield curvature estimated with the empirical expression presented in Section 7.1.3) during Cycle 13. Like that in the previous specimens, the curvature in the shaft was much smaller than the theoretical yield curvature.

7.4.4 Strains in reinforcing bars

The strain distributions along column longitudinal bars at the peak displacements of different cycles are plotted in Figure 7.41 and Figure 7.42 for pairs of bundled bars located at the north and south faces of the specimen, respectively. The maximum plastic strain penetration measured inside the embedment length was 457 mm (1.5 ft), which occurred at a system ductility of 5.5. This corresponds to $18\,d_b$, and like that in Specimen 2, represents 50% of the total embedment length.

The strain distributions along the longitudinal perimeter bars in the shaft at the peak displacements of different cycles are plotted in Figure 7.43. All the bars remained elastic. The average bond stresses along the lap splice length calculated from the strain

readings were less than 25% of the maximum bond strength obtained from the bond-slip tests presented in Chapter 3.

The strains in the column cage hoops located at different heights of the column and inside the embedment length at the peak displacements of different cycles are plotted in Figure 7.44. Like those in the previous specimens, the hoops remained elastic, except those located at the base of the column.

As shown in Figure 7.45, the shaft hoop located at 0.64 m (2.1 ft) from the base of the column yielded during the test. Yielding started in Cycle 5 at a system ductility of 1.0, and Cycle 7, at a ductility of 2.2, on the south and north faces of the specimen, respectively. No yielding was measured on the west side of this hoop. The maximum strain measured in the hoop was less than 0.025. Hence, the hoop did not undergo much strain hardening. The other hoops above and below this one did not yield but developed relatively large strains. In general, the strains developed in the shaft hoops are more severe than those in the other specimens. This could be due to the smaller diameter of the shaft in this specimen, which resulted in a thinner concrete ring to resist the splitting action induced by bond slip, and also the plying action exerted by the confined concrete core of the column.

7.5 Summary and conclusions

The behavior of four full-scale column-shaft assemblies subjected to quasi-static cyclic loading has been studied. These tests were intended to identify the minimum required embedment length of column longitudinal reinforcement in enlarged (Type II) shafts. For Specimen 1, an embedment length equal to $D_{c,\max} + l_d$, which is close to the minimum requirement in the current Caltrans SDC (Caltrans 2010), was adopted. For Specimens 2 through 4, the embedment length was reduced to $l_d + s + c$. Despite the difference in the embedment lengths between Specimen 1 and the rest, all the specimens showed a very similar behavior. The columns developed a plastic hinge at the base and failed by bar buckling and the subsequent fracture of longitudinal bars in the plastic-hinge region. Damage in the shafts was limited to cone-shaped failure and splitting cracks

near the base of the column. The damage in the shaft was significantly reduced in Specimen 3 owing to the increased confinement provided by a steel casing.

The maximum tensile plastic strain penetration measured in the column longitudinal bars inside the shafts was between $14\,d_b$ and $21\,d_b$, with the lowest strain penetration occurring in Specimen 3, which had a steel casing for the shaft. For Specimens 1 through 3, the strains in the shaft hoops were in general relatively small and below the yield limit except for the first hoop at the top. However, the maximum strains in top hoops were not large enough to develop strain hardening. The shaft hoops in Specimen 3, which had a steel casing around the shaft, did not yield at all. The hoop strains in the steel casing are similar to those in the hoops at the same elevations, but they exceed yield level at the very top of the casing. Specimen 4 had more or less uniform strains, which were below the yield level, in the shaft hoops along the height, except for a hoop that was about 0.64 m (2.1) ft below the top of the shaft, whose strain way exceeded the yield level. The level of the strain measured in that hoop and its change during unloading indicate that the hoop bar could be bent as the splitting cracks in the shaft opened. This could be attributed to the wider splitting cracks developed in the smaller diameter shaft as compared to the other specimens.

The comparison of the test results for Specimens 1 with those for the other specimens indicates that the embedment length can be reduced from $D_{c,\max} + l_d$ to $l_d + s + c$ without affecting the behavior of a column-shaft assembly. The comparison between Specimens 2 and 3 indicates that increasing the confinement of the shaft with a steel casing improved the bond along the anchored bars. Furthermore, the test results for Specimens 3 and 4 show that the design recommendations presented in Chapter 6 for the transverse reinforcement in the bar anchorage region of a shaft are adequate. However, the more severe splitting cracks developed in the shaft of Specimen 4, in spite of its relatively high quantity of transverse reinforcement, could be due to the smaller diameter of the shaft as compared to that of the other specimens, which provided less resistance to the splitting forces induced by bar slip and to the plying action of the confined concrete

core of the column. The plying action is not accounted for in the design formulas presented in Chapter 6.

The bond slip and development of the column longitudinal bars in enlarged shafts are further studied in Chapter 8 with finite element analyses.

Table 7.1: Maximum displacement and system ductility in each cycle

Cycle no.	Specimen 1		Specimen 2		Specimen 3		Specimen 4	
	Δ_{max} mm (in.)	μ_{max}	Δ_{max} mm (in.)	μ_{max}	Δ_{max} mm (in.)	μ_{max}	Δ_{max} mm (in.)	μ_{max}
1	5 (0.2)	0.1	7 (0.27)	0.1	7 (0.27)	0.1	5 (0.2)	0.1
2	12 (0.5)	0.2	18 (0.71)	0.2	17 (0.68)	0.2	12 (0.5)	0.2
3	28 (1.1)	0.4	38 (1.5)	0.5	36 (1.4)	0.5	25 (1.0)	0.5
4	50 (2.0)	0.8	64 (2.5)	0.8	60 (2.35)	0.8	47 (1.86)	0.8
5	71 (2.8)	1.1	83 (3.25)	1.0	79 (3.1)	1.0	61 (2.4)	1.1
6	71 (2.8)	1.1	83 (3.25)	1.0	79 (3.1)	1.0	61 (2.4)	1.1
7	142 (5.6)	2.2	165 (6.5)	2.0	157 (6.2)	2.1	122 (4.8)	2.2
8	142 (5.6)	2.2	165 (6.5)	2.0	157 (6.2)	2.1	122 (4.8)	2.2
9	213 (8.4)	3.3	248 (9.75)	3.0	236 (9.3)	3.1	183 (7.2)	3.3
10	213 (8.4)	3.3	248 (9.75)	3.0	236 (9.3)	3.1	183 (7.2)	3.3
11	284 (11.2)	4.4	330 (13.0)	4.0	315 (12.4)	4.2	244 (9.6)	4.4
12	284 (11.2)	4.4	330 (13.0)	4.0	315 (12.4)	4.2	244 (9.6)	4.4
13	356 (14.0)	5.5	413 (16.25)	5.0	394 (15.5)	5.2	305 (12.0)	5.5
14	356 (14.0)	5.5	413 (16.25)	5.0	394 (15.5)	5.2	305 (12.0)	5.5
15	-	-	495 (19.5)	6.0	472 (18.6)	6.3	361 (14.4)	6.6
16	-	-	495 (19.5)	6.0	472 (18.6)	6.3	361 (14.4)	6.6
17	-	-	572 (22.5)	6.9	551 (21.7)	7.3	-	-

Δ_{max}: maximum lateral displacement at the top of the column.

μ_{max}: maximum system ductility.

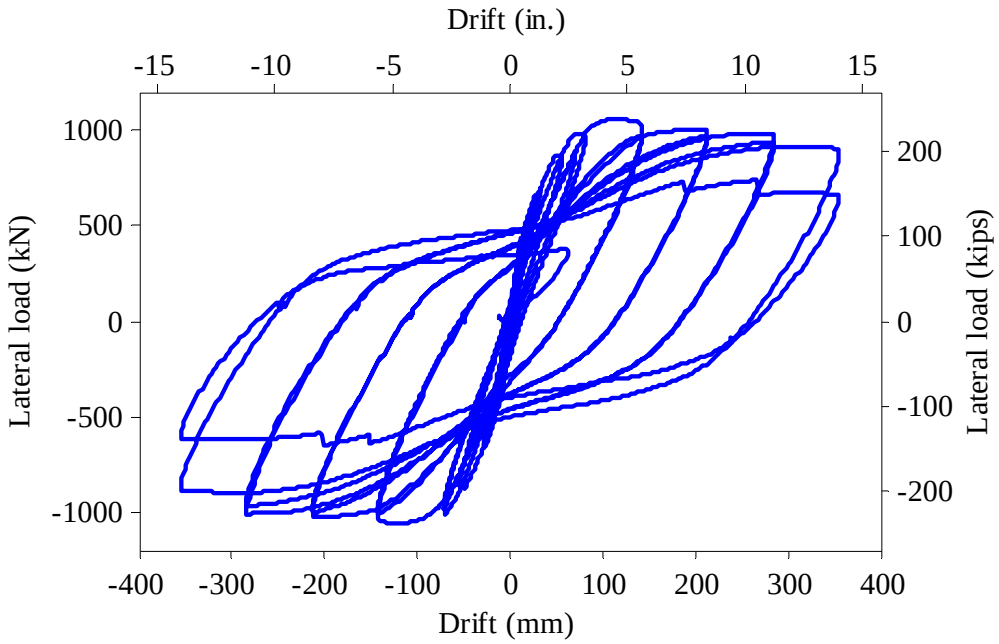

Figure 7.1: Lateral force vs. drift for Specimen 1

(a) Column (west face)

(b) Shaft (north face)

(c) Shaft (south face)

(d) Column-shaft interface (north face)

(e) Column-shaft interface (south face)

Figure 7.2: Cracks in Specimen 1 at Cycle 4 (1st yield)

(a) Cycle 7

(b) Cycle 9

(c) Cycle 11

(d) Cycle 13

(e) Cycle 13

(f) Cycle 14

Figure 7.3: Evolution of damage at the column base in Specimen 1 (north face)

(a) Top of the shaft (north side)

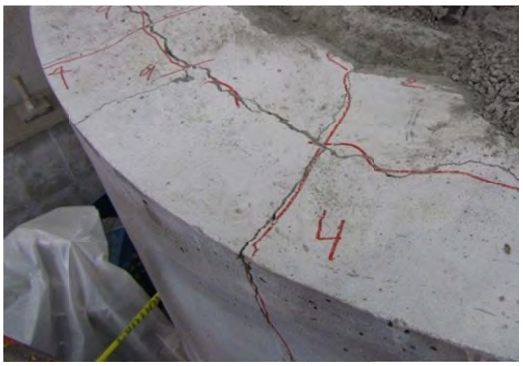

(b) Top of the shaft (south side)

(c) Lateral view of the shaft (south face)

Figure 7.4: Damage at the end of the test in the shaft of Specimen 1

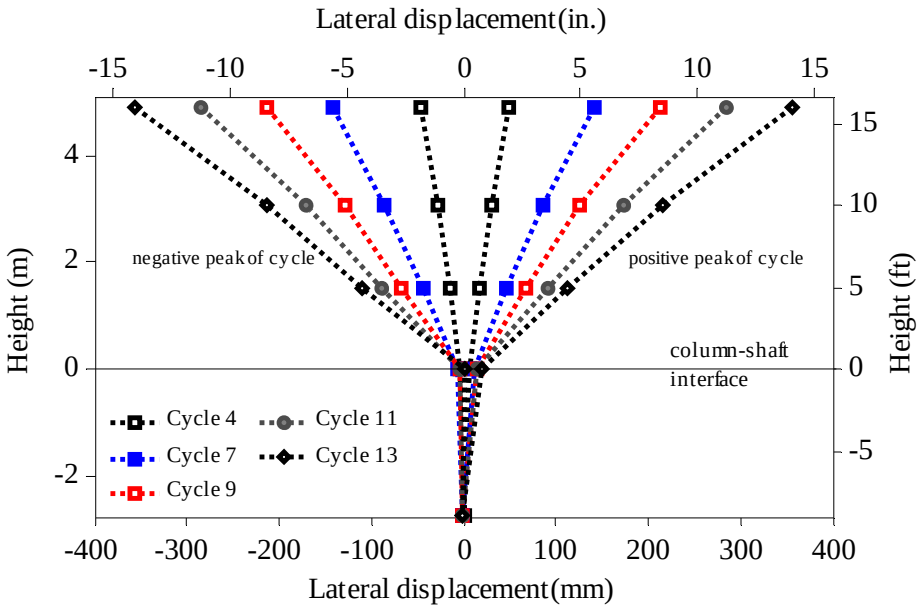

Figure 7.5: Lateral displacements of Specimen 1

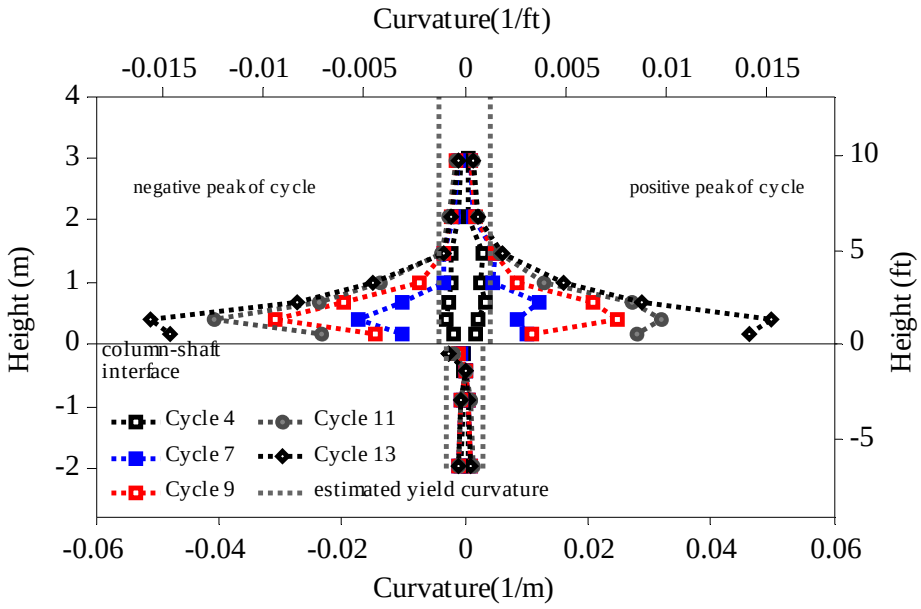

Figure 7.6: Curvatures along the height of Specimen 1

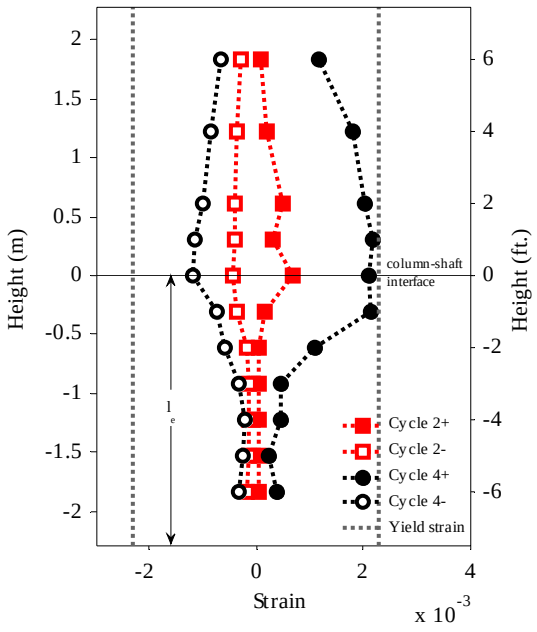

(a) North bar (early cycles)

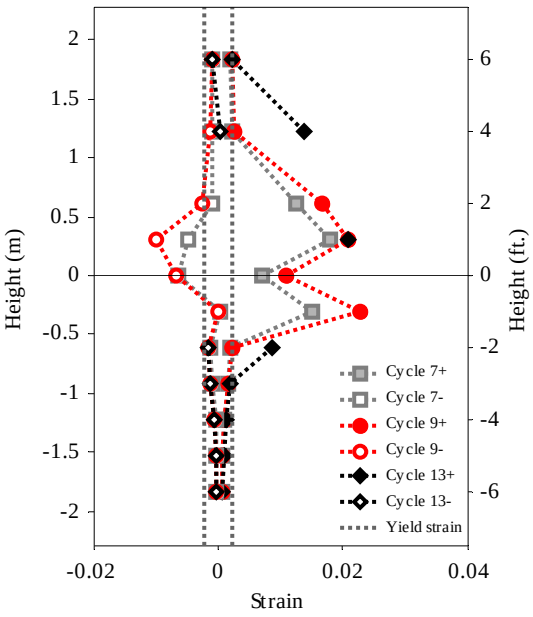

(b) North bar (final cycles)

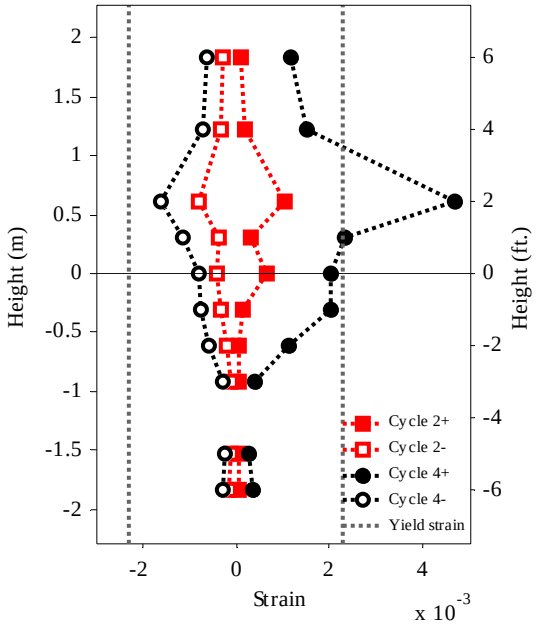

(c) Northwest bar (early cycles)

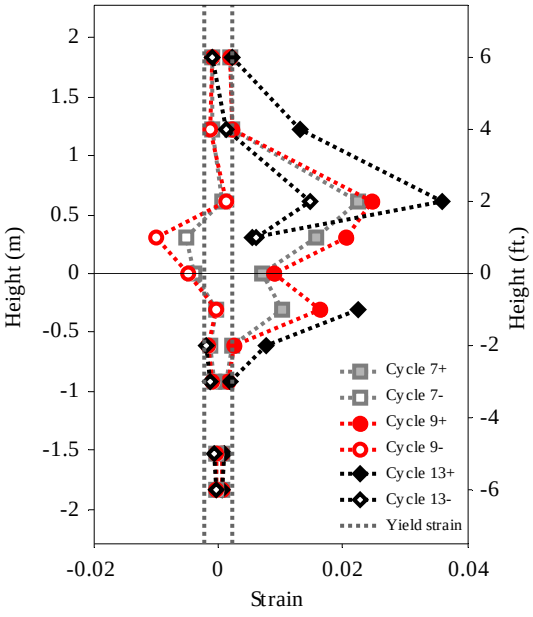

(d) Northwest bar (final cycles)

Figure 7.7: Strains in column longitudinal bars in Specimen 1 (north face)

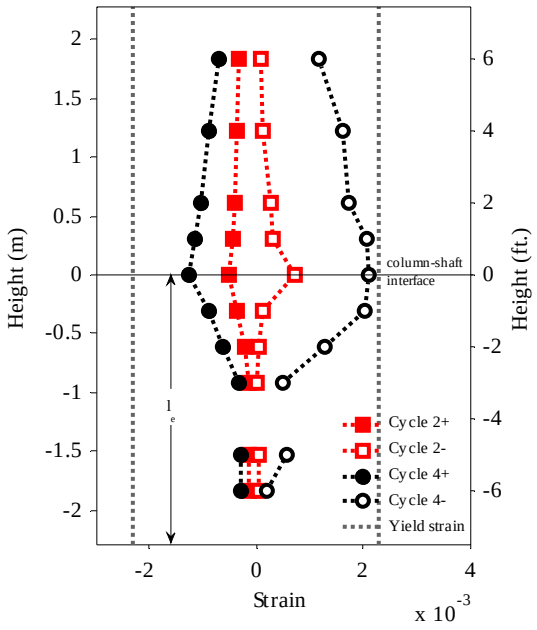

(a) South bar (early cycles)

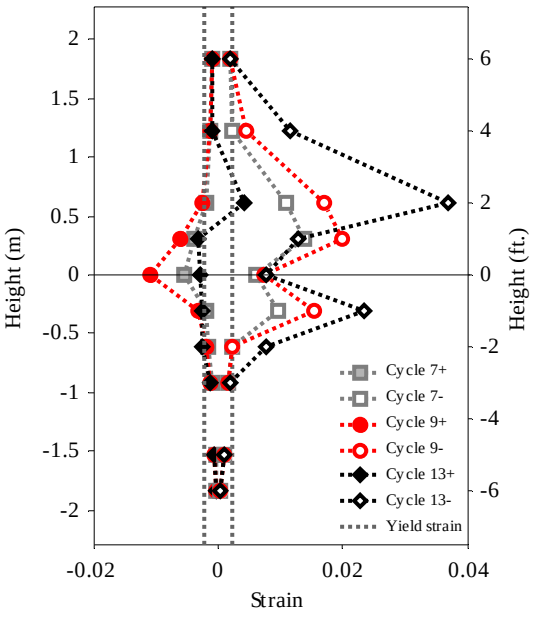

(b) South bar (final cycles)

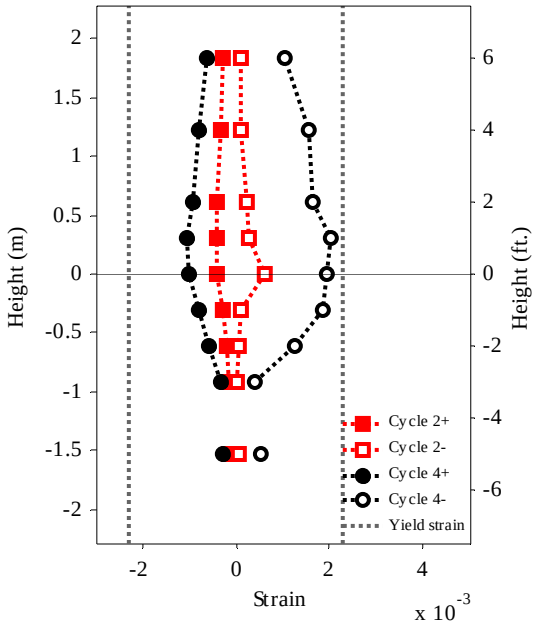

(c) Southwest bar (early cycles)

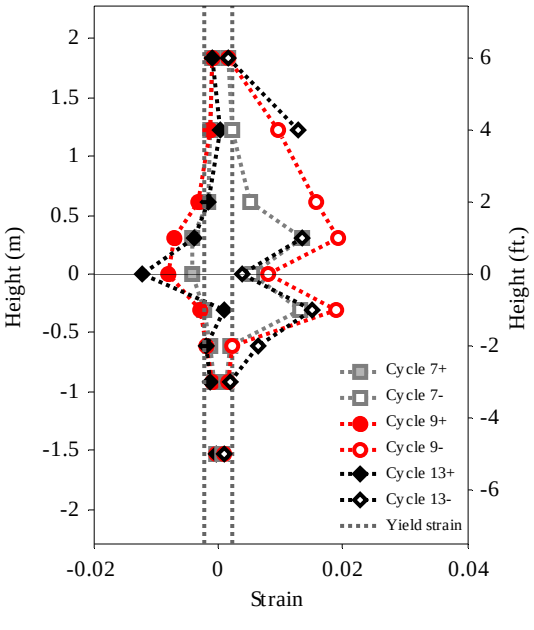

(d) Southwest bar (final cycles)

Figure 7.8: Strains in column longitudinal bars in Specimen 1 (south side)

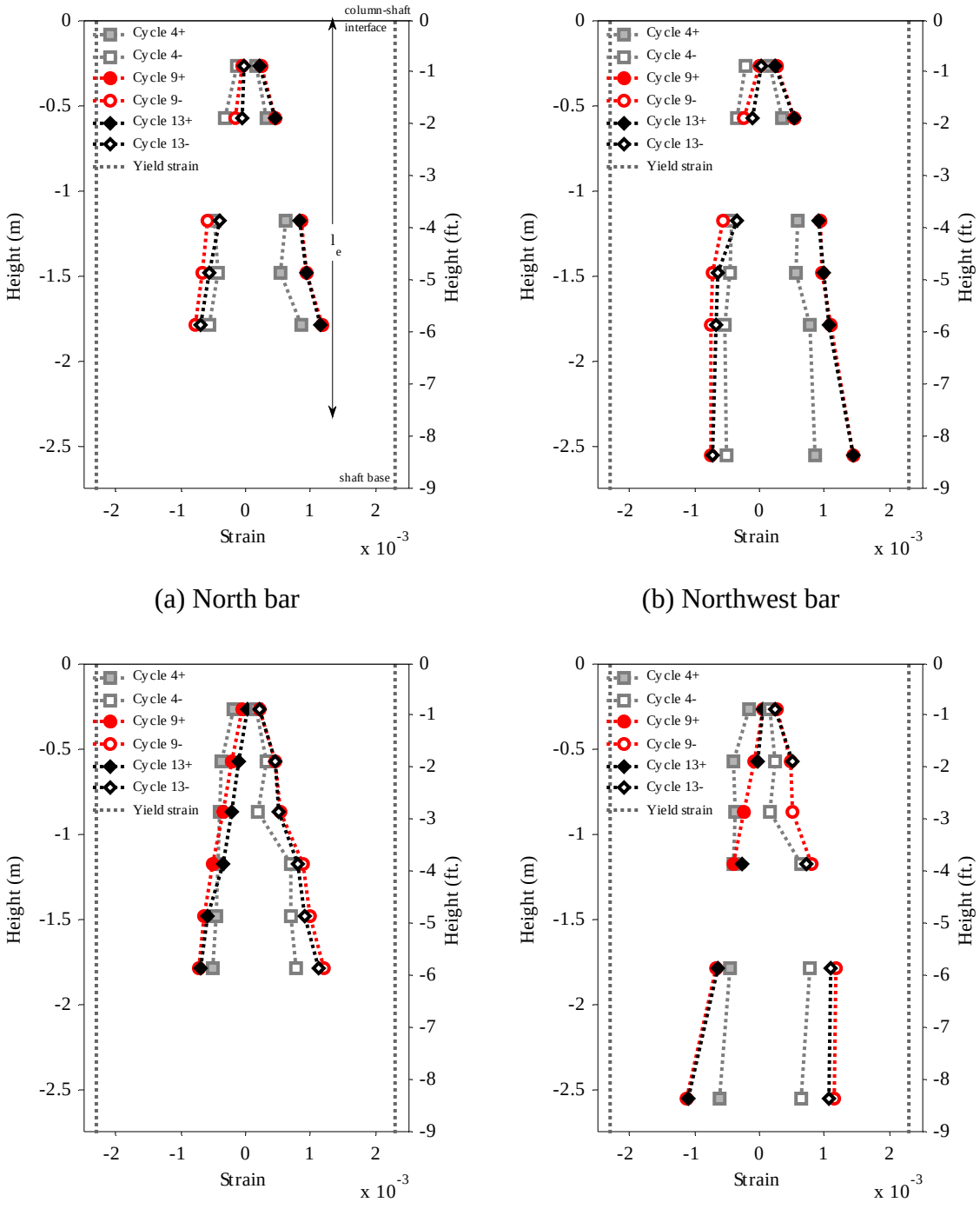

(a) North bar

(b) Northwest bar

(c) South bar

(d) Southwest bar

Figure 7.9: Strains in shaft longitudinal bars in Specimen 1

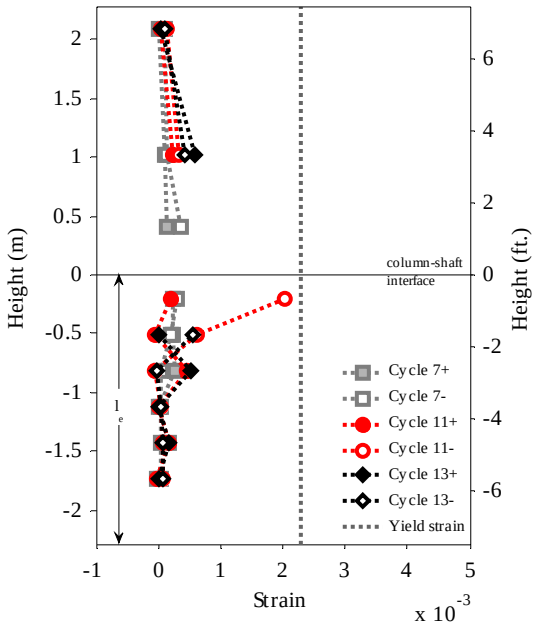

(a) North face

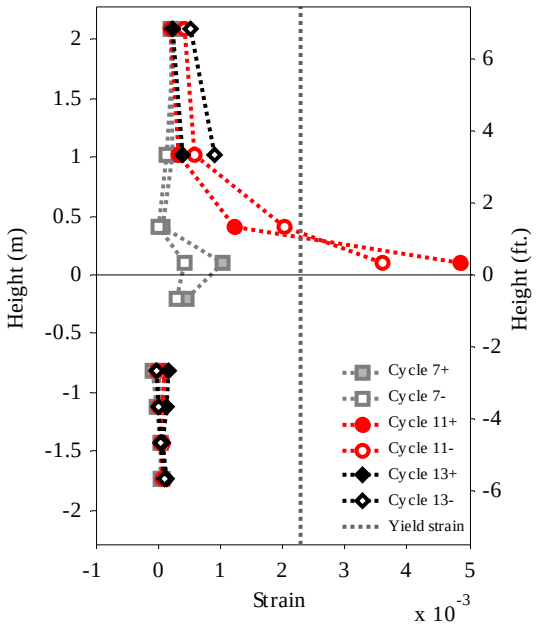

(b) South face

Figure 7.10: Strains in column hoops in Specimen 1

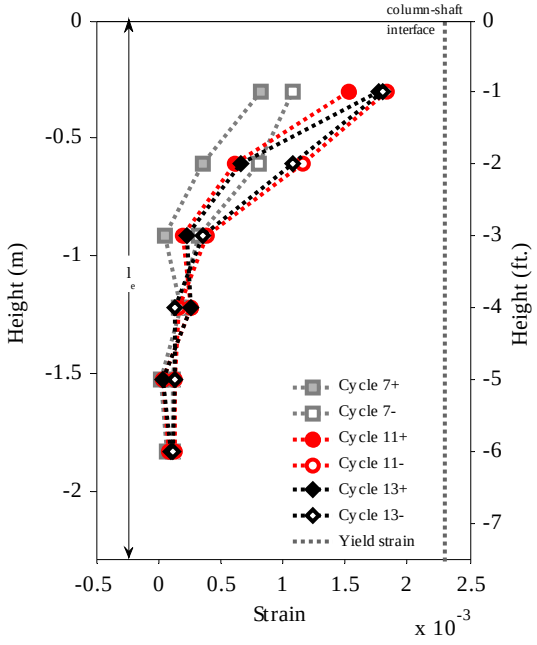

(a) North face

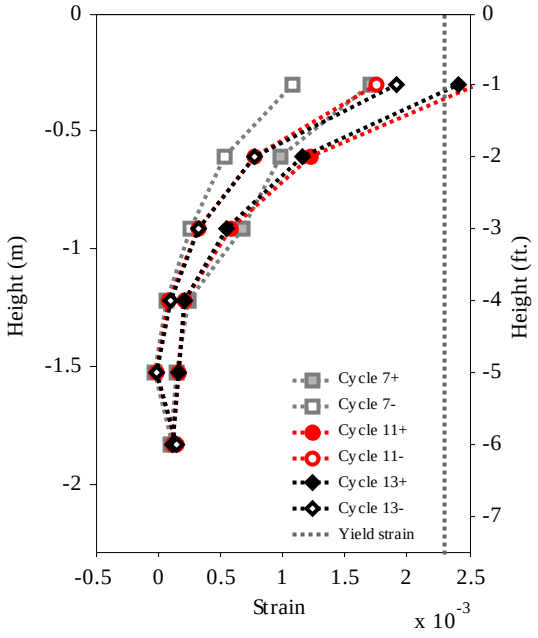

(b) South face

Figure 7.11: Strains in shaft hoops in Specimen 1

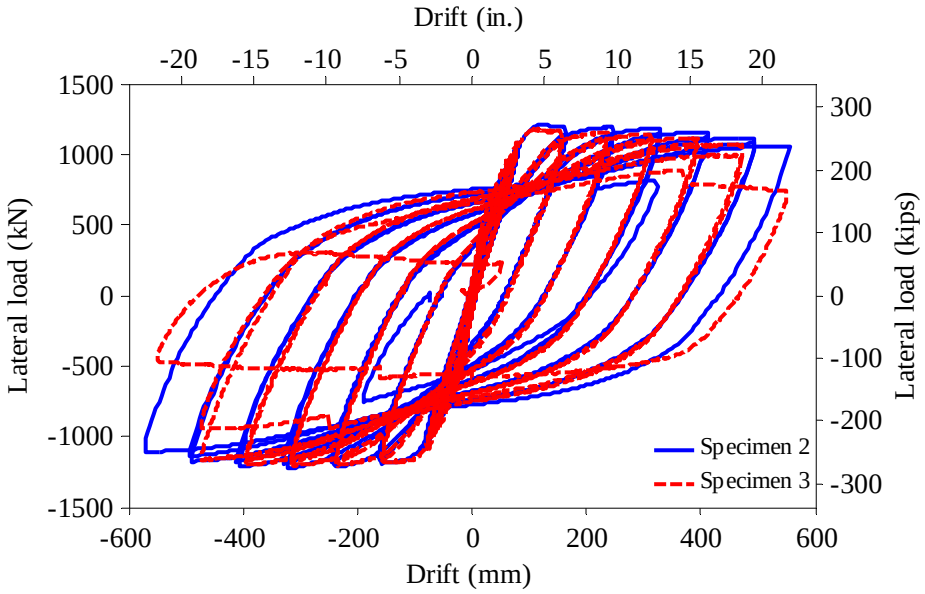

Figure 7.12: Lateral load vs. drift for Specimens 2 and 3

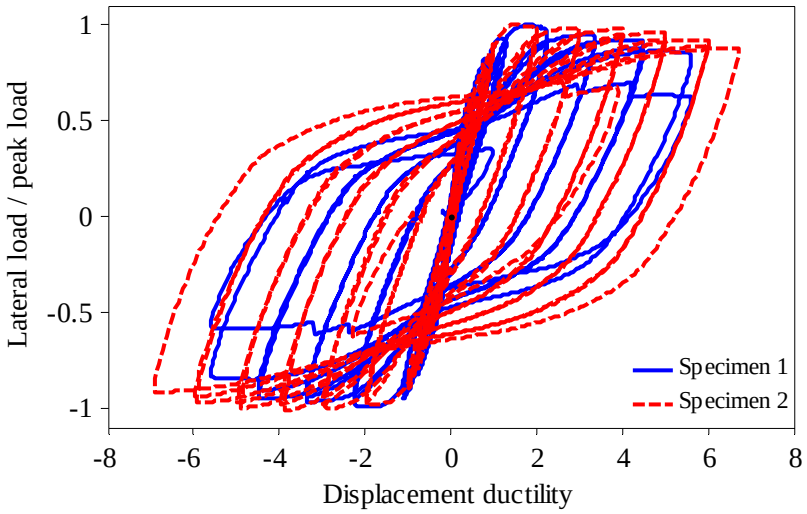

Figure 7.13: Normalized lateral load vs. system ductility for Specimens 1 and 2

(a) Column (southeast view)

(b) Shaft (north face)

(c) Shaft (south face)

Figure 7.14: Flexural cracks in Specimen 2 at Cycle 4 (1st yield)

(a) Cycle 3 (north face)

(b) Cycle 3 (south face)

Figure 7.15: Splitting cracks at the top of the shaft in Specimen 2 at Cycle 3

(a) Cycle 7 (b) Cycle 9 (c) Cycle 11

(d) Cycle 13 (e) Cycle 15 (f) Cycle 18 (end)

Figure 7.16: Evolution of damage at the column base in Specimen 2 (north face)

(a) Cycle 7 (b) Cycle 8 (c) Cycle 11

(d) Cycle 13 (e) Cycle 15 (f) Cycle 18 (end)

Figure 7.17: Evolution of damage at the column base in Specimen 2 (south face)

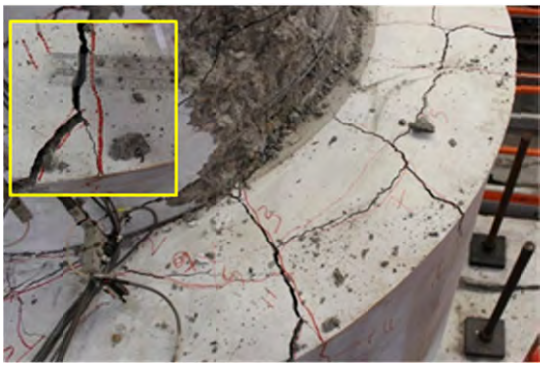

(a) Cycle 13 (south face)

(b) End of the test (south face)

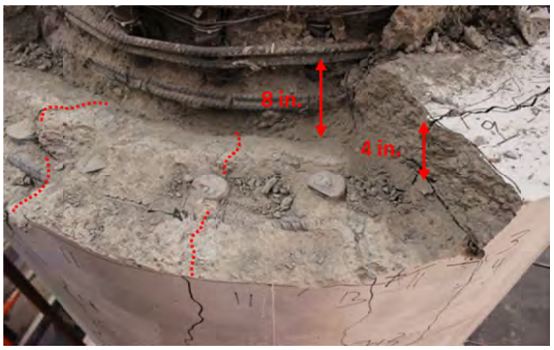

(c) Post-test inspection (Top of north face)

(d) Post-test inspection (Top of south face)

(e) Post-test inspection (north face)

Figure 7.18: Damage in the shaft of Specimen 2

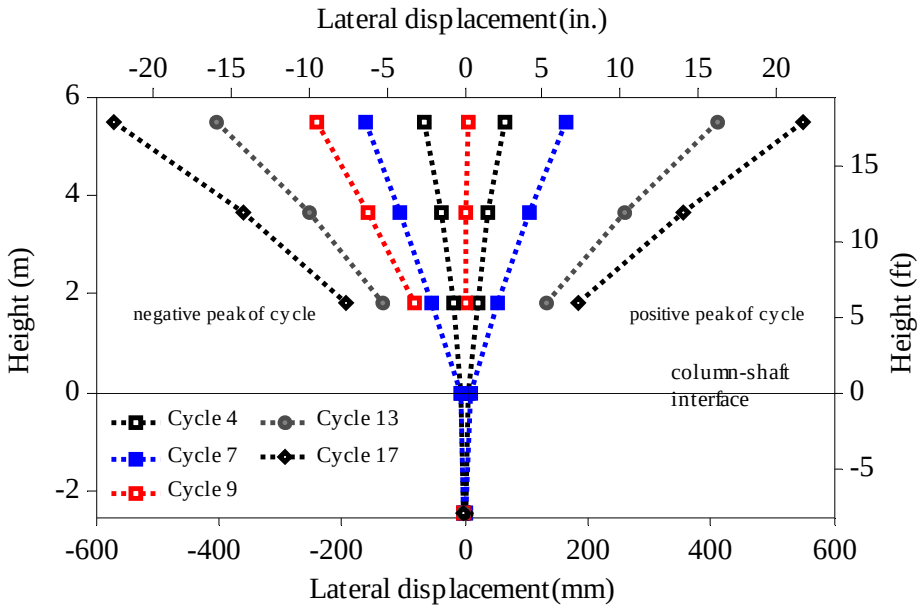

Figure 7.19: Displacements of Specimen 2

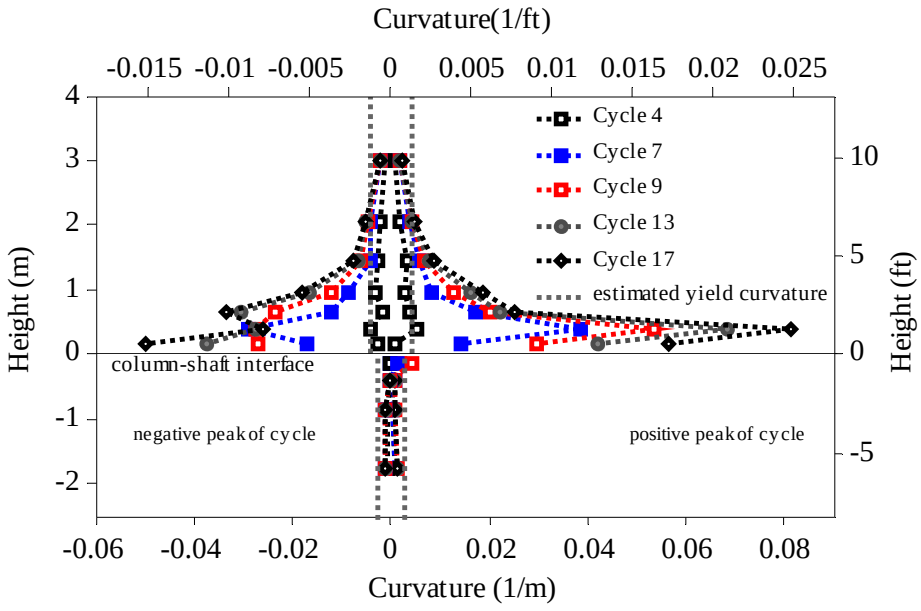

Figure 7.20: Curvatures along the height of Specimen 2

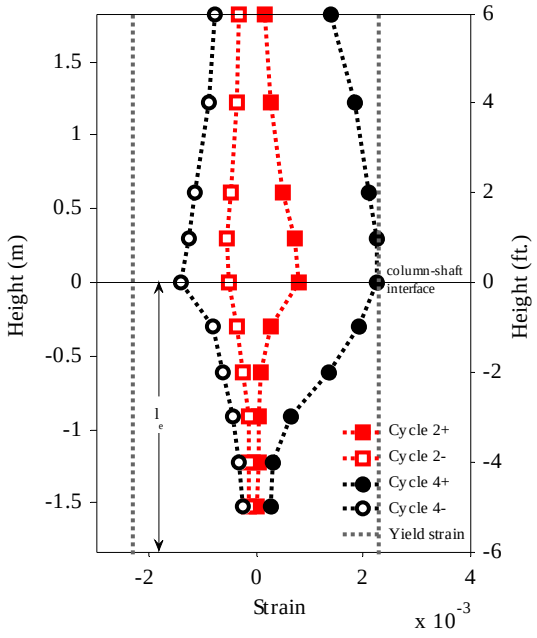

(a) North bar (early cycles)

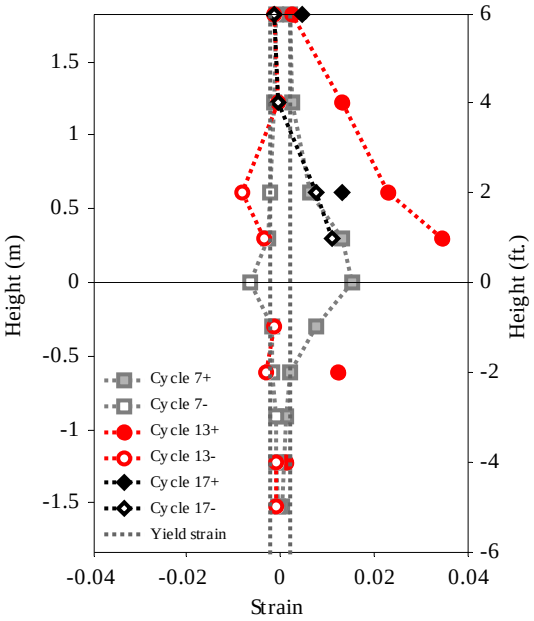

(b) North bar (final cycles)

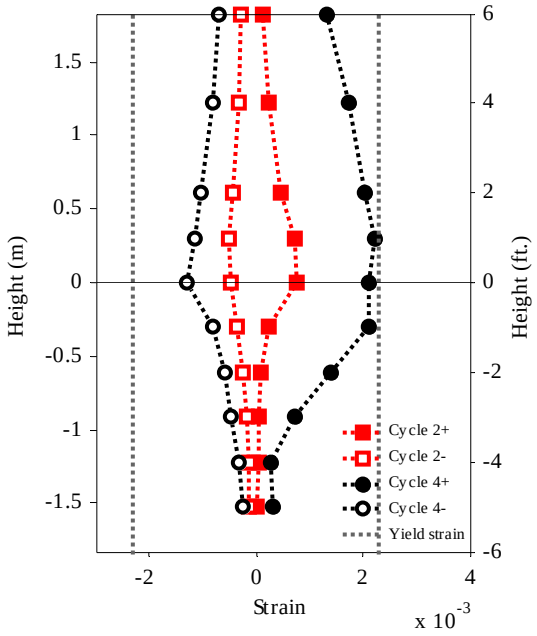

(c) Northwest bar (early cycles)

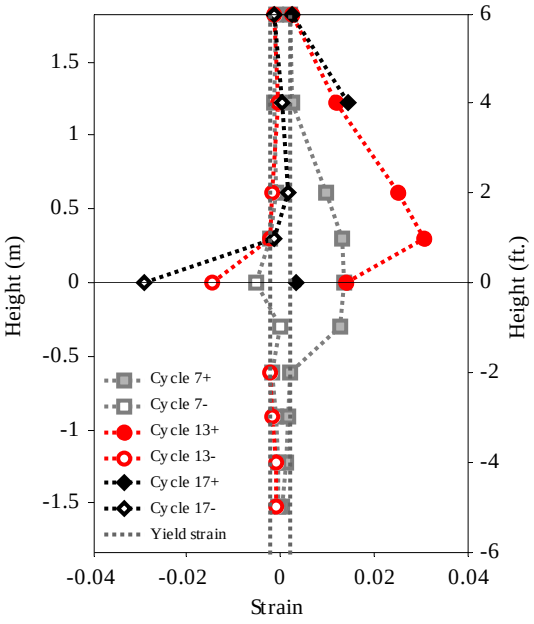

(d) Northwest bar (final cycles)

Figure 7.21: Strains in column longitudinal bars in Specimen 2 (north face)

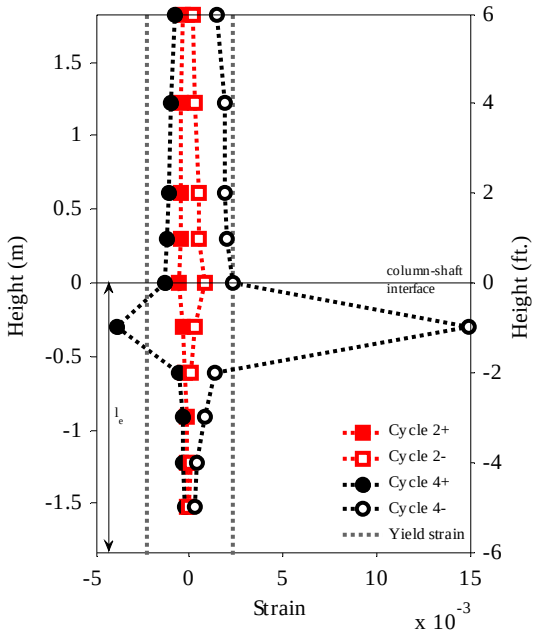

(a) South bar (early cycles)

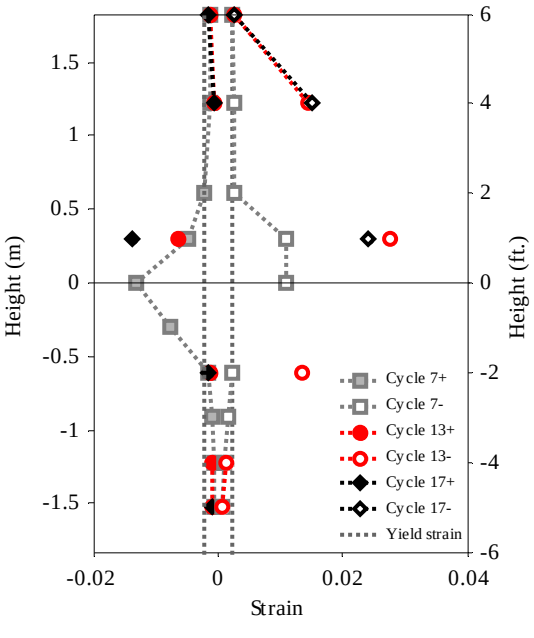

(b) South bar (final cycles)

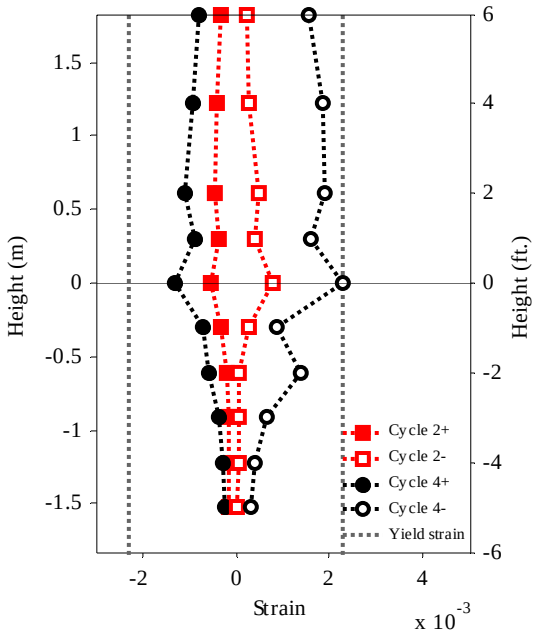

(c) Southwest bar (early cycles)

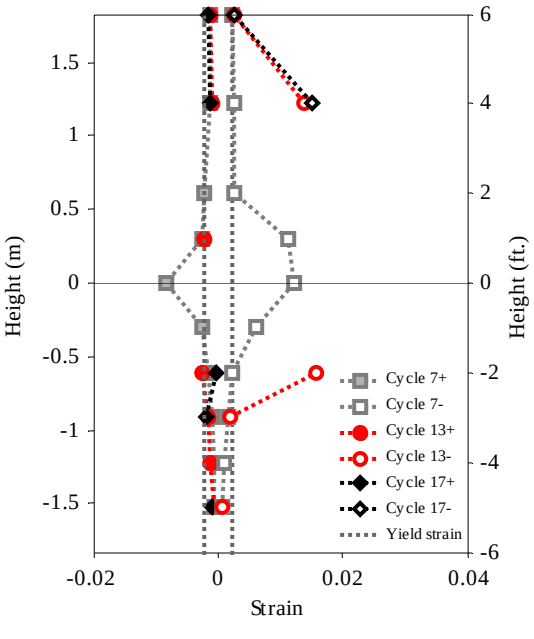

(d) Southwest bar (final cycles)

Figure 7.22: Strains in column longitudinal bars in Specimen 2 (south face)

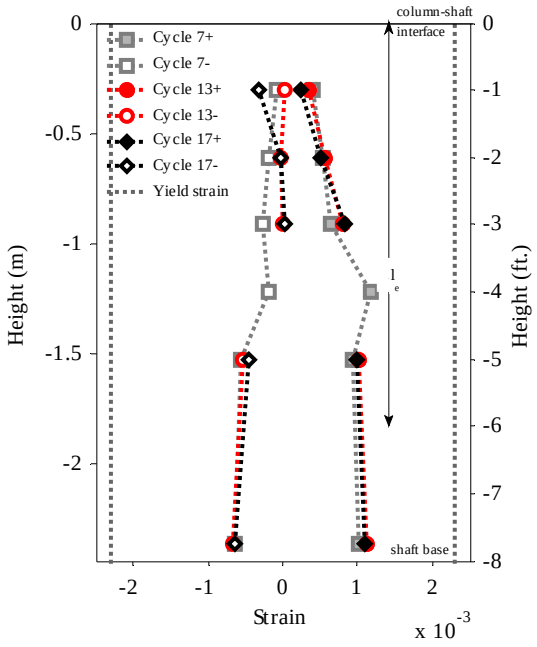

(a) North bar

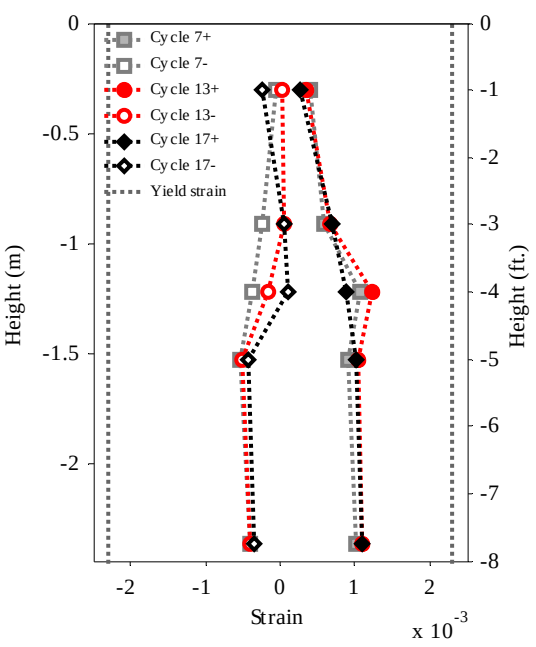

(b) Northwest bar

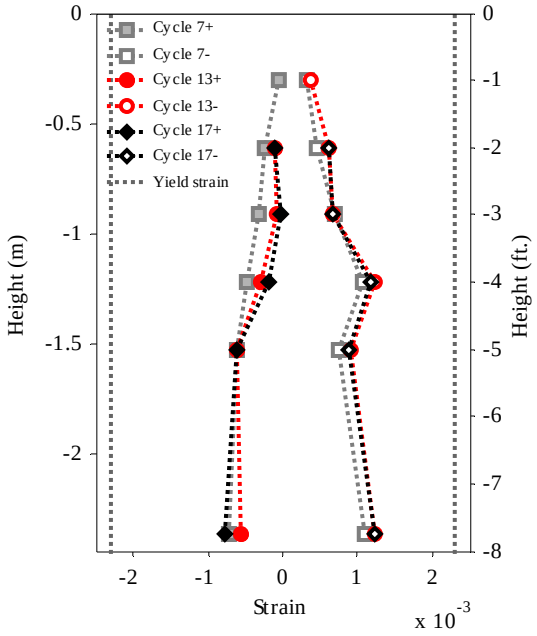

(c) South bar

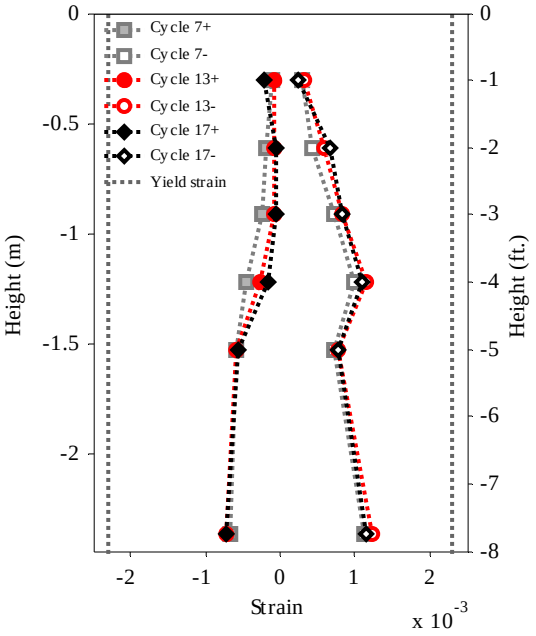

(d) Southwest bar

Figure 7.23: Strains in shaft longitudinal bars in Specimen 2

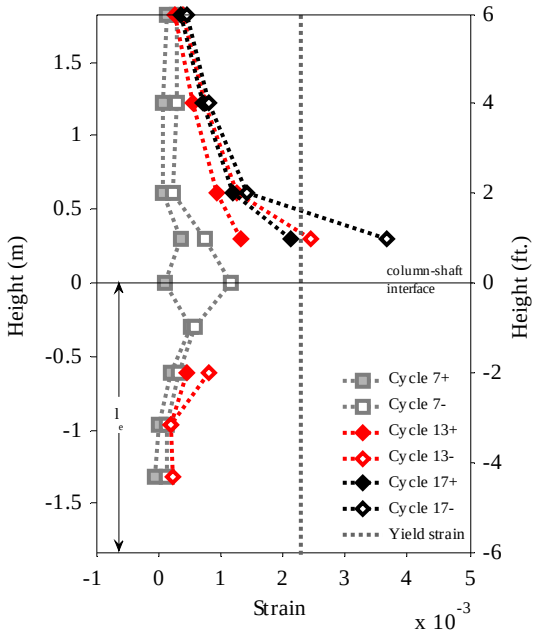

(a) North face

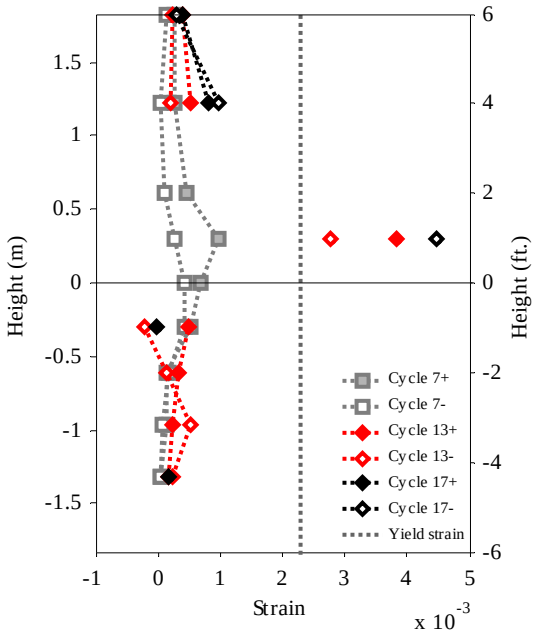

(b) South face

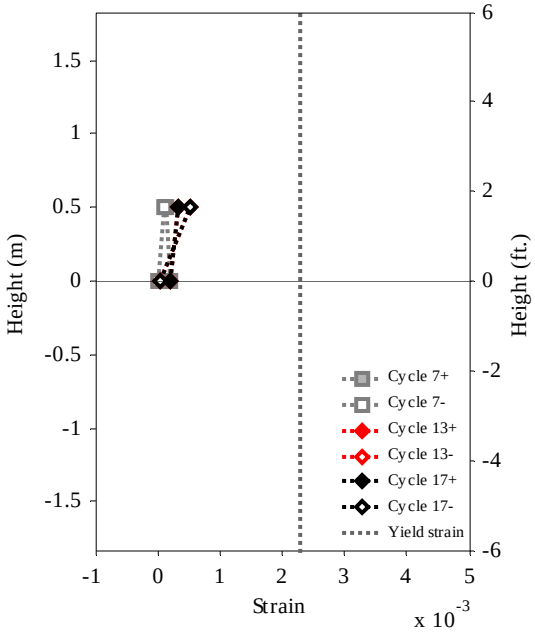

(c) West face

Figure 7.24: Strains in column hoops in Specimen 2

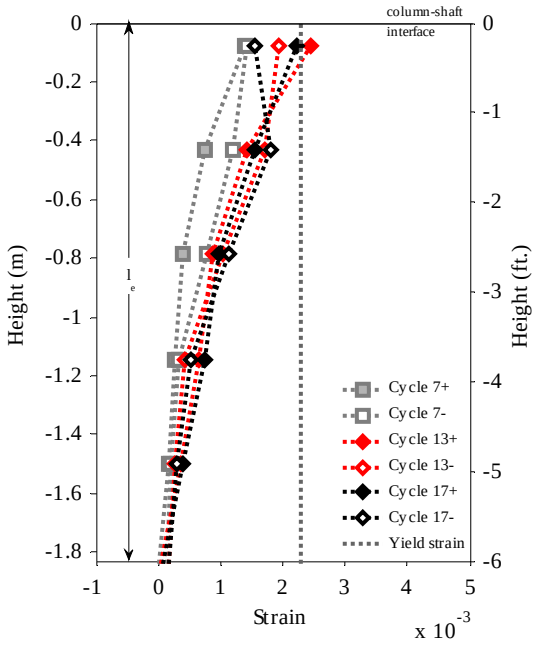

(a) North face

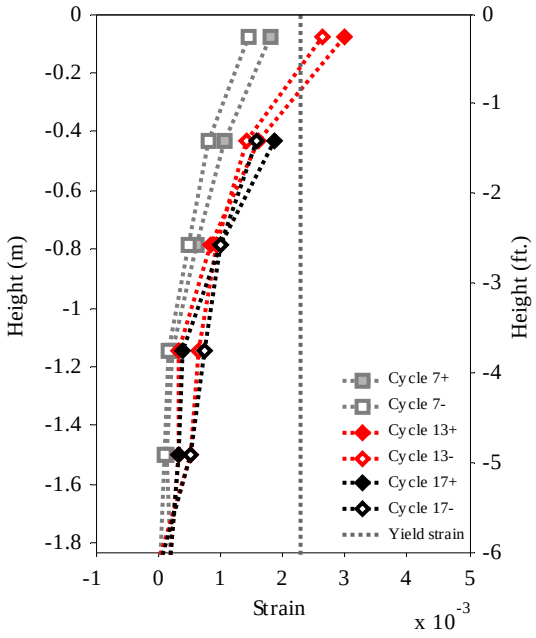

(b) South face

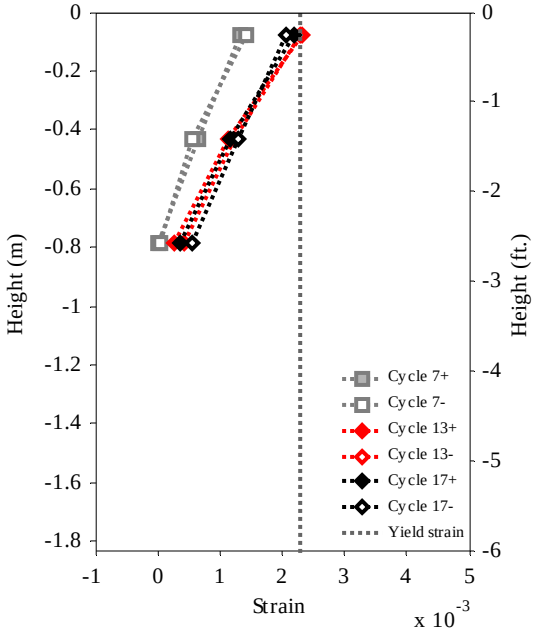

(c) West face

Figure 7.25: Strains in shaft hoops in Specimen 2

(a) Cycle 3

(b) Cycle 7

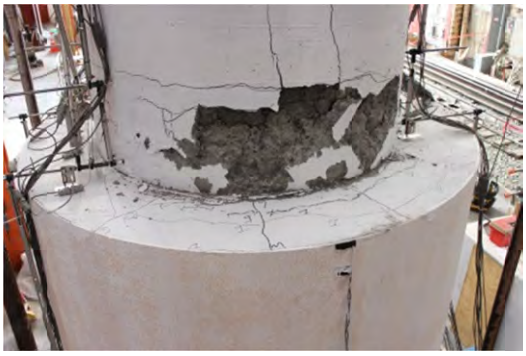

(c) Cycle 9

(d) Cycle 13

(e) Cycle 17 (end)

Figure 7.26: Evolution of damage at the column base in Specimen 3 (north face)

(a) North face at Cycle 13

(b) South face at Cycle 13

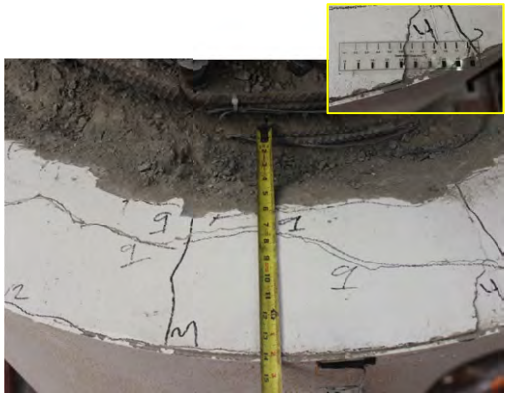

(c) North face at Cycle 17 (end of test)

(d) South face at Cycle 17 (end of test)

(e) North face after steel casing removal

(f) South face after steel casing removal

Figure 7.27: Damage in the shaft of Specimen 3

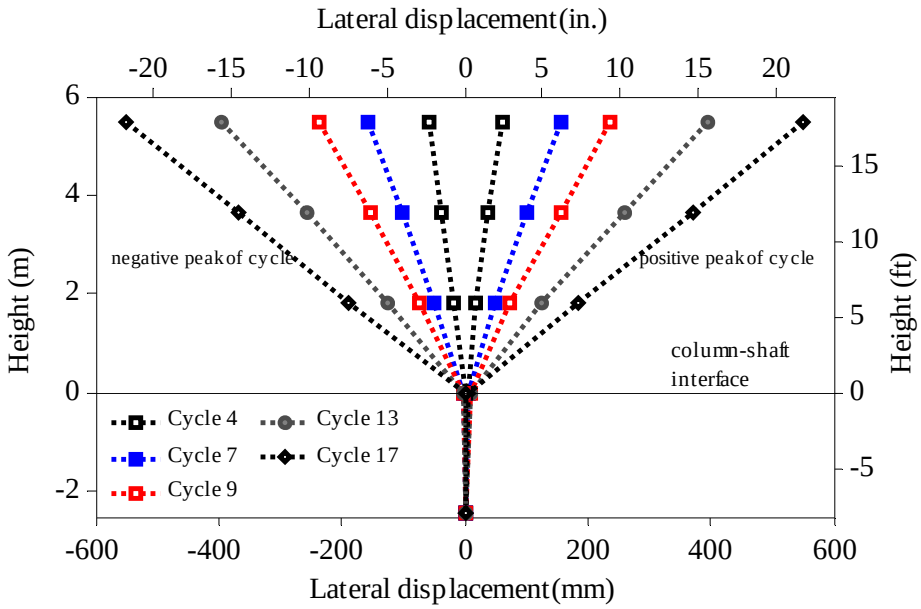

Figure 7.28: Displacements of Specimen 3

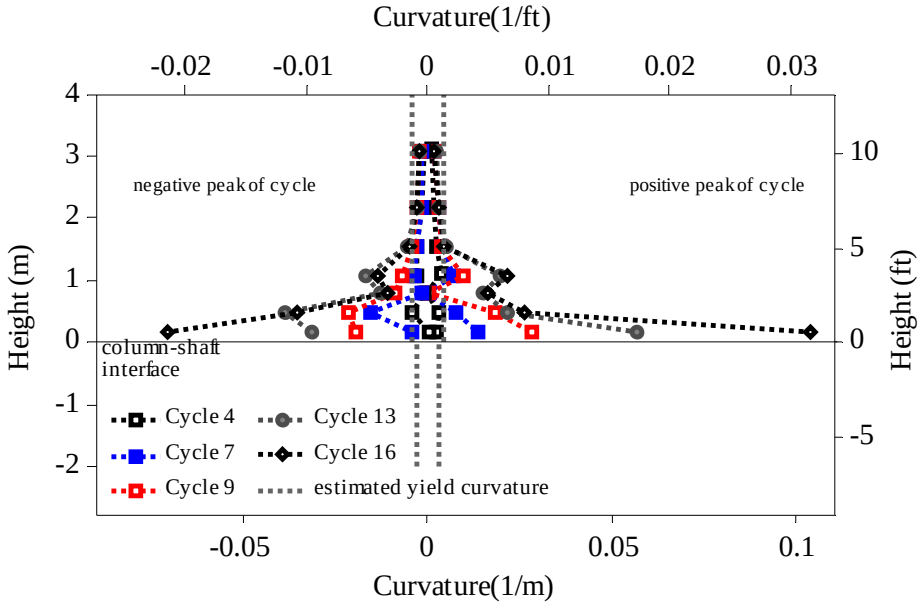

Figure 7.29: Curvatures along the height of Specimen 3

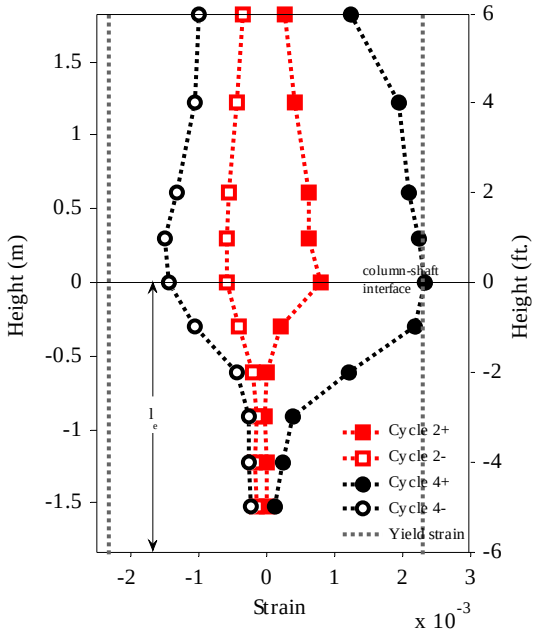

(a) North bar (early cycles)

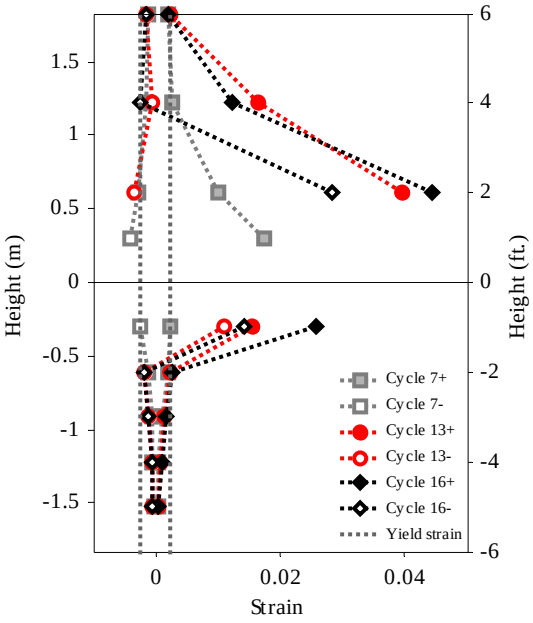

(b) North bar (final cycles)

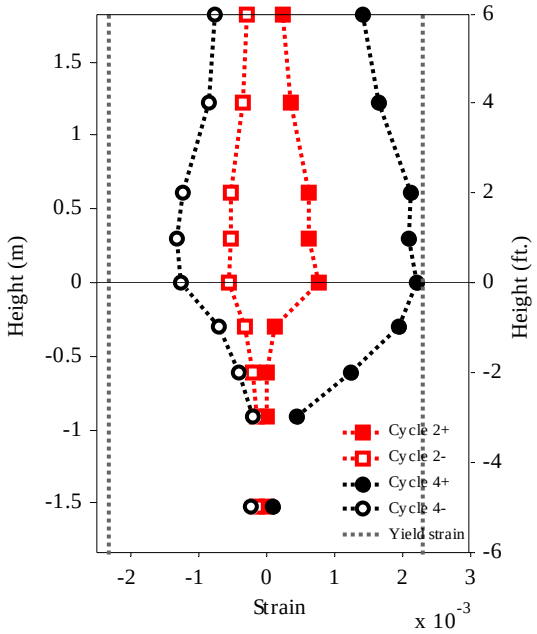

(c) Northwest bar (early cycles)

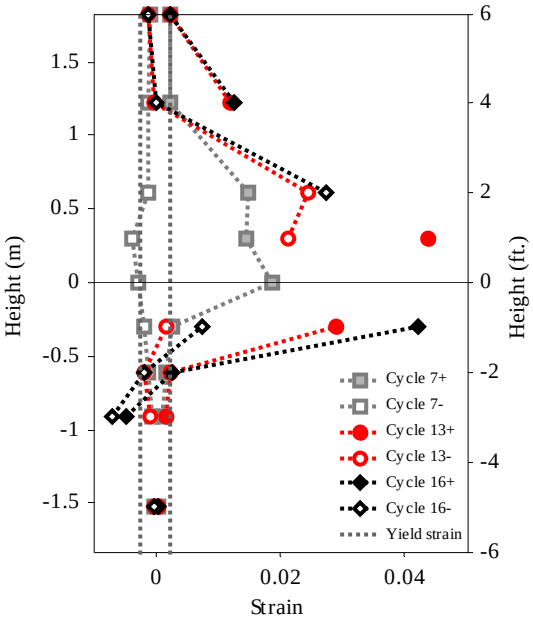

(d) Northwest bar (final cycles)

Figure 7.30: Strains in column longitudinal bars in Specimen 3 (north face)

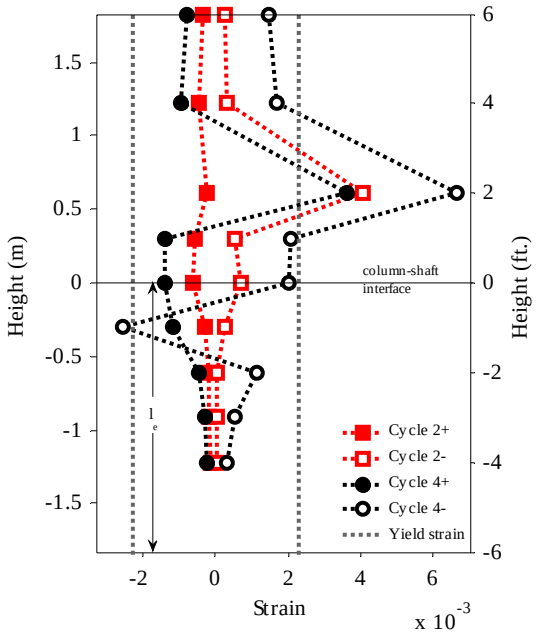

(a) South bar (early cycles)

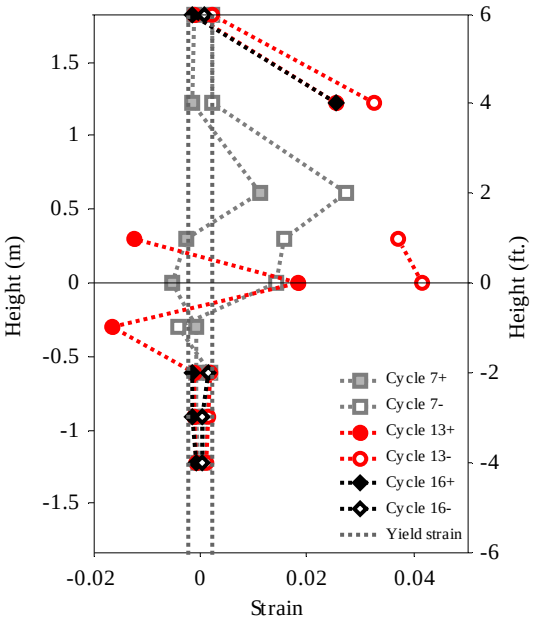

(b) South bar (final cycles)

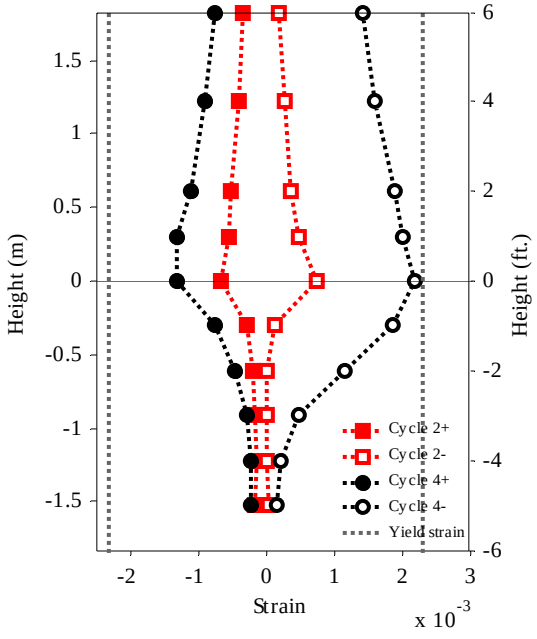

(c) Southwest bar (early cycles)

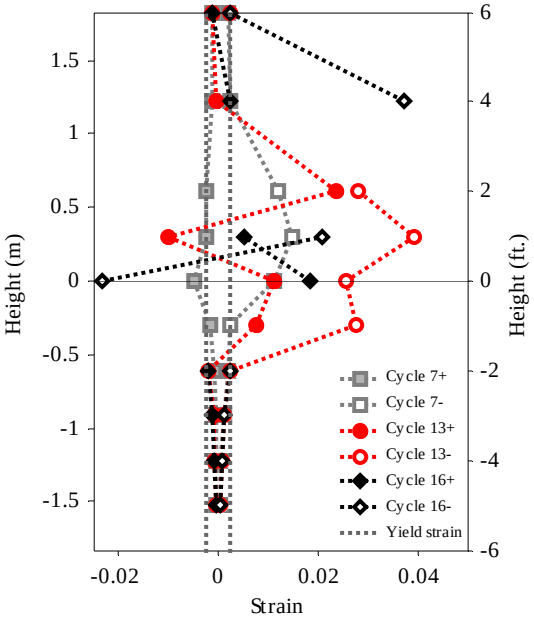

(d) Southwest bar (final cycles)

Figure 7.31: Strains in column longitudinal bars in Specimen 3 (south face)

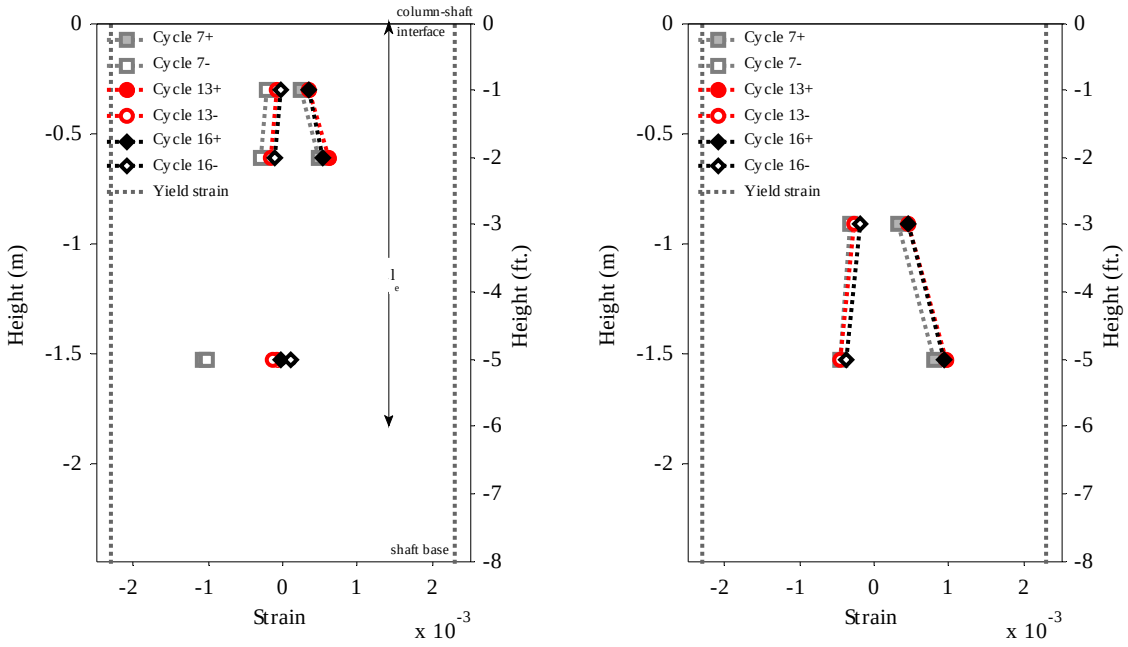

(a) North bar (b) Northeast bar

Figure 7.32: Strains in shaft longitudinal bars in Specimen 3

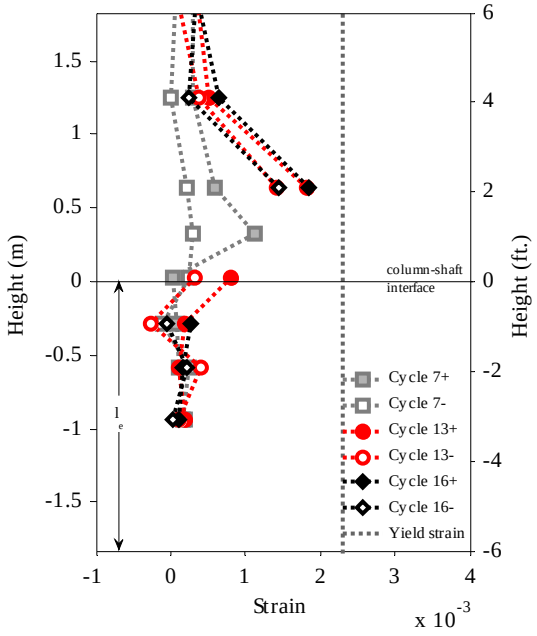

(a) North face

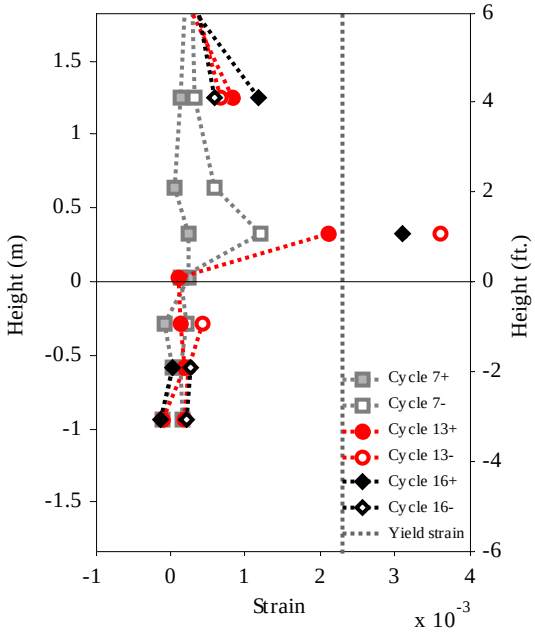

(b) South face

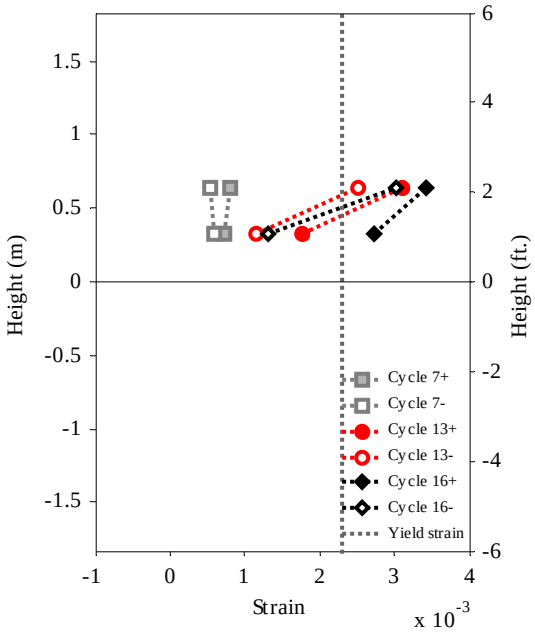

(c) West face

Figure 7.33: Strains in column hoops in Specimen 3

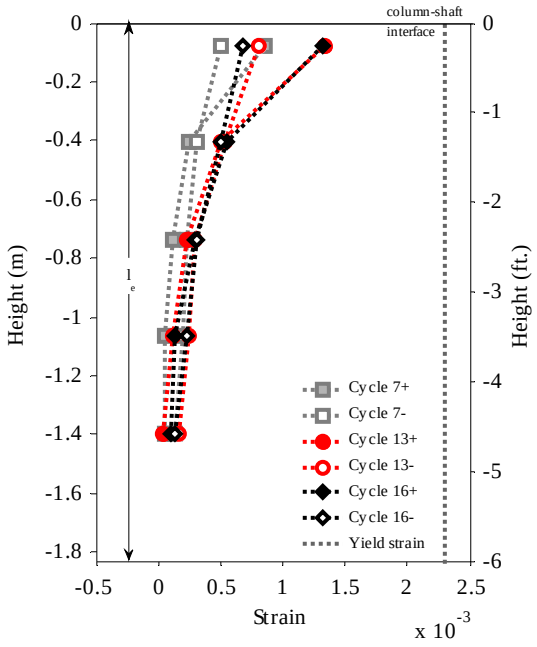

(a) North face

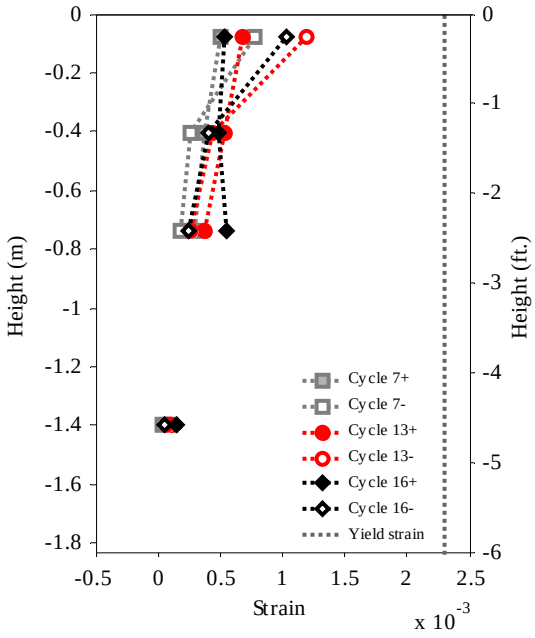

(b) South face

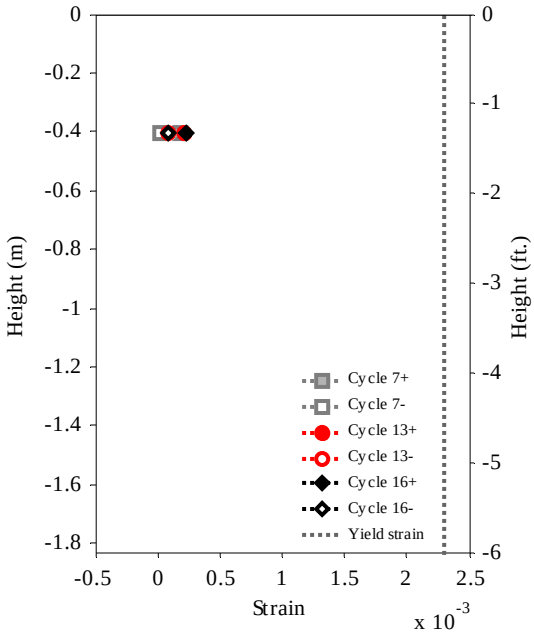

(c) West face

Figure 7.34: Strains in shaft hoops in Specimen 3

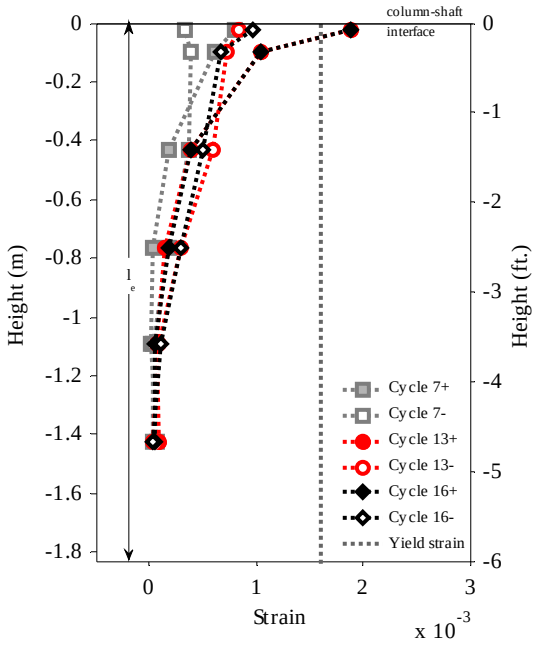

(a) North face

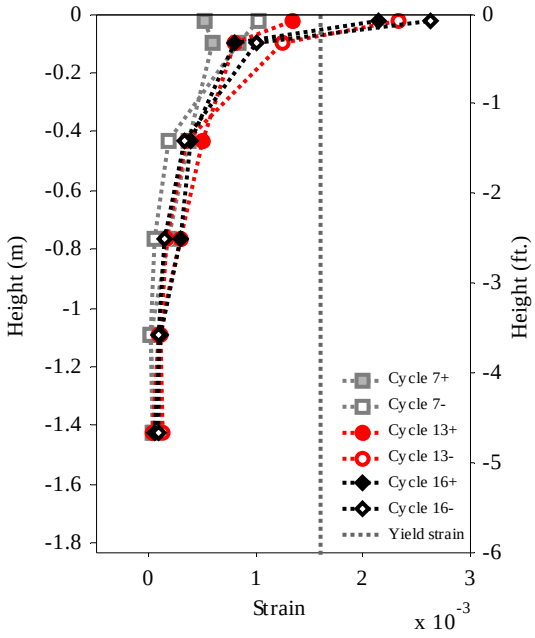

(b) South face

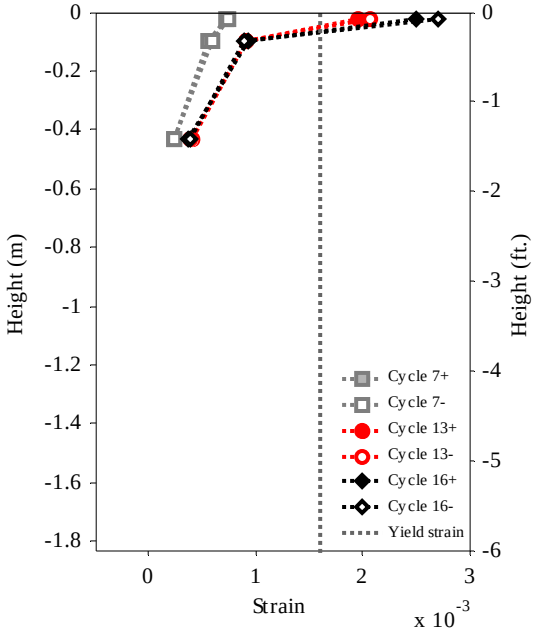

(c) West face

Figure 7.35: Hoop strains in steel casing in Specimen 3

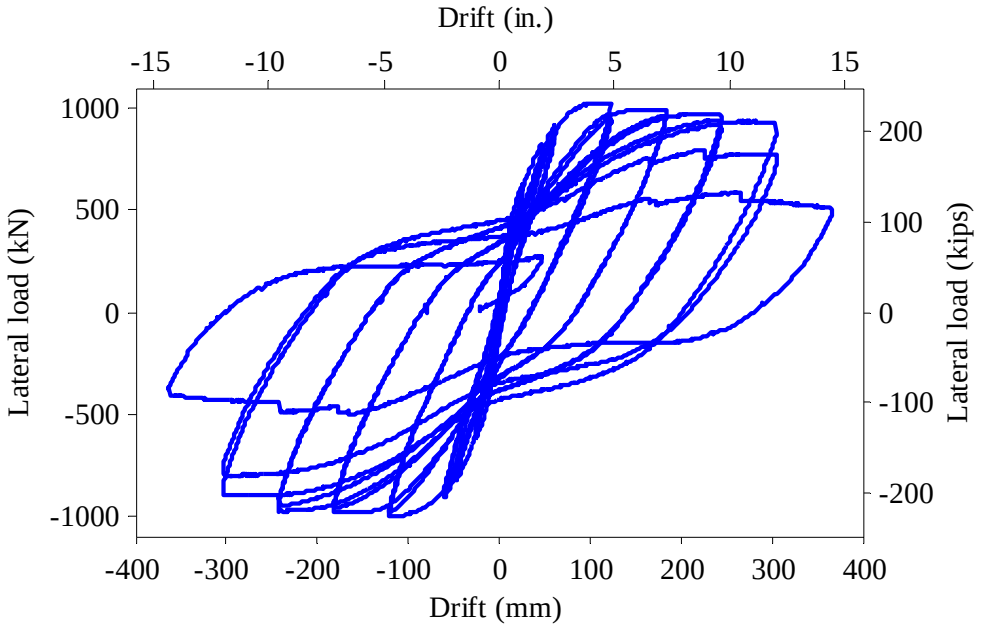

Figure 7.36: Lateral force vs. drift for Specimen 4

(a) Cycle 4

(b) Cycle 7

(c) Cycle 11

(d) Cycle 13

(e) Cycle 14

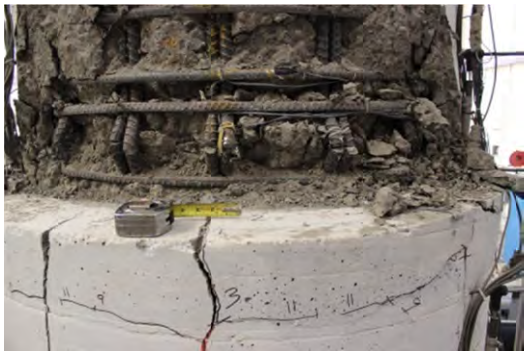

(f) Cycle 15

Figure 7.37: Evolution of damage at the column base in Specimen 4 (north face)

(a) North face at Cycle 13

(b) South face at Cycle 13

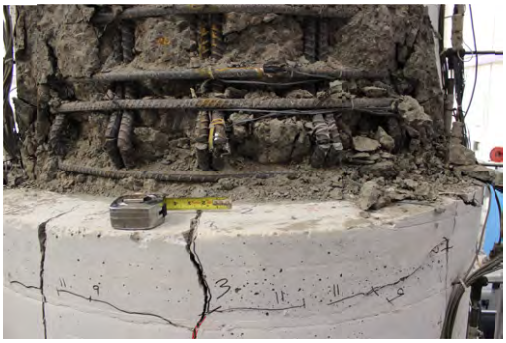

(c) North face at Cycle 16 (end of test)

(d) South face at Cycle 16 (end of test)

(e) Post-test inspection of north face

(f) Post-test inspection of north face

Figure 7.38: Damage in the shaft of Specimen 4

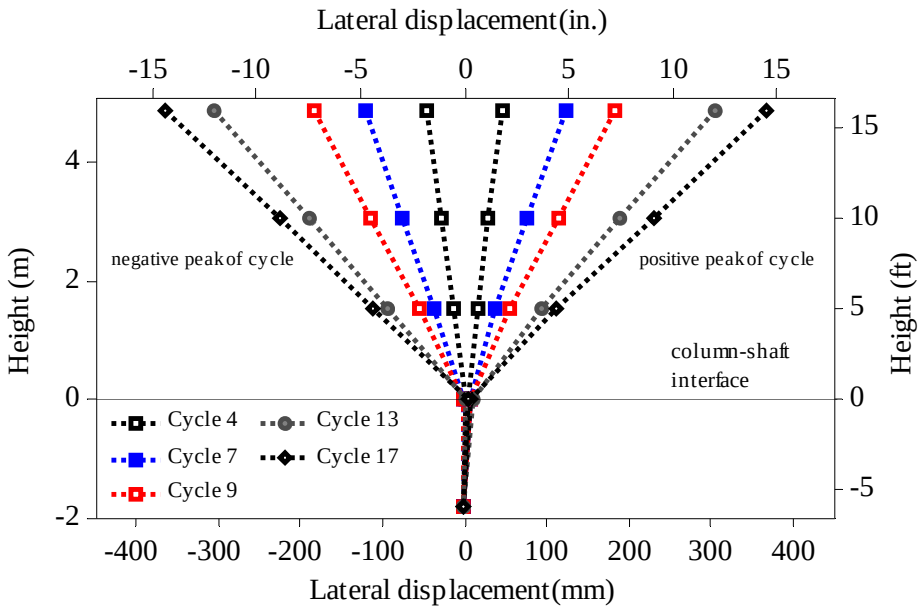

Figure 7.39: Displacements of Specimen 4

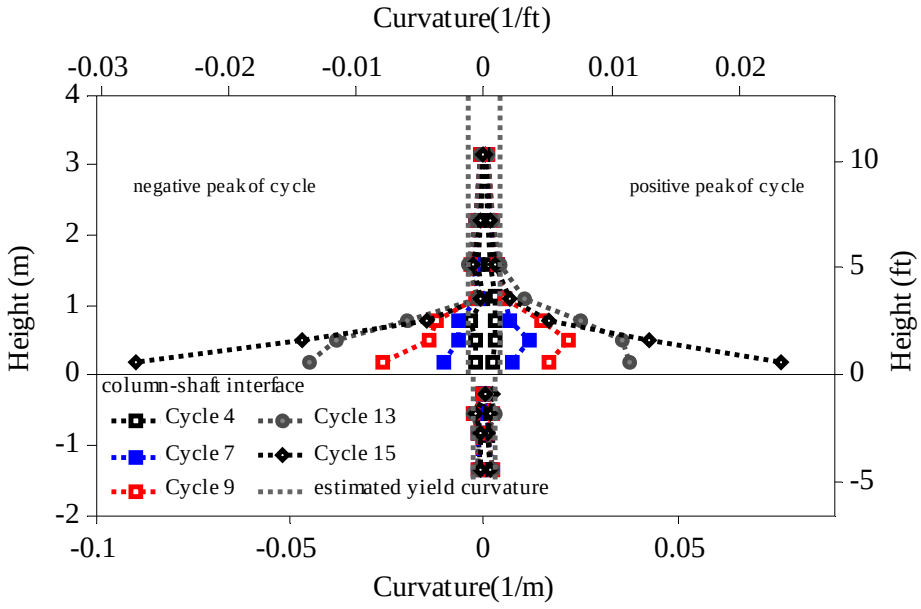

Figure 7.40: Curvatures along the height of Specimen 4

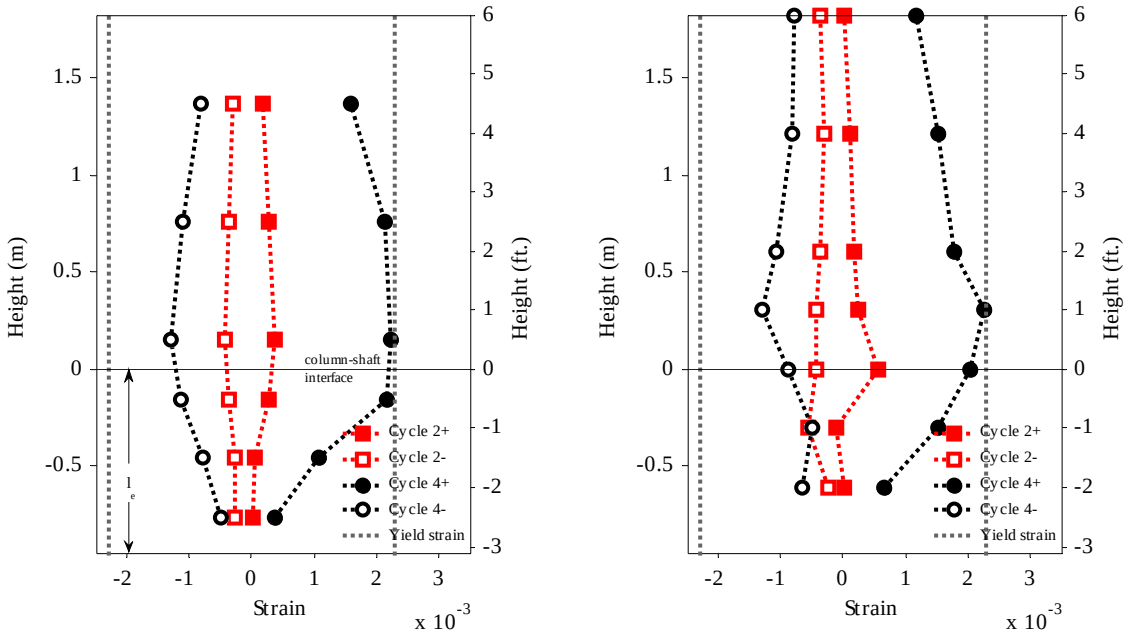

(a) Bar 1 (early cycles)

(b) Bar 2 (early cycles)

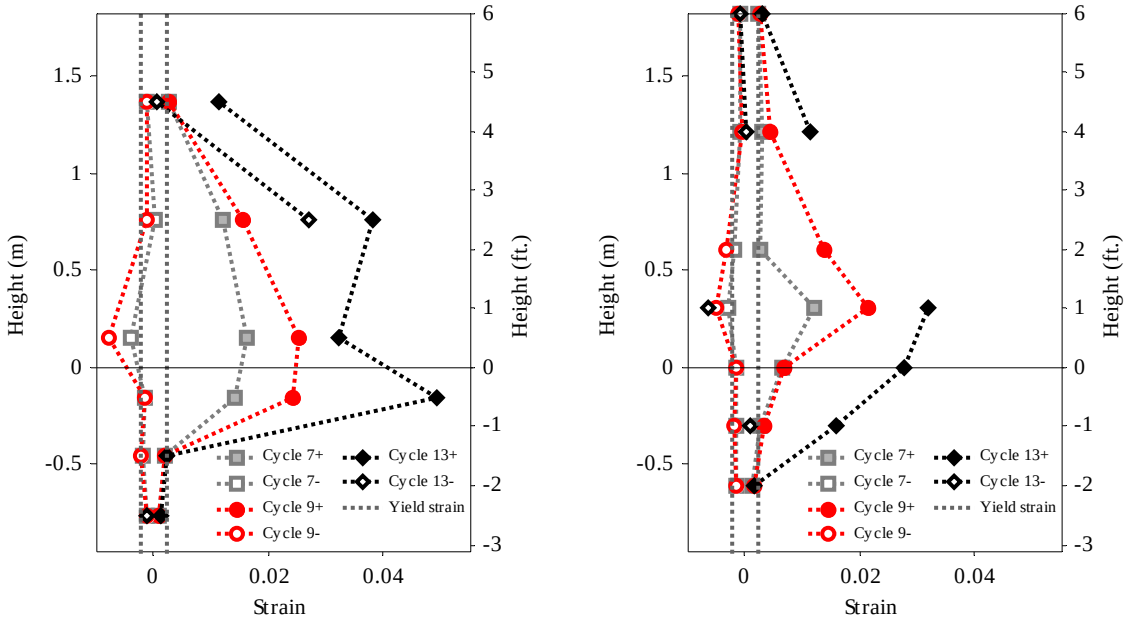

(c) Bar 1 (final cycles)

(d) Bar 2 (final cycles)

Figure 7.41: Strains in column longitudinal bars in Specimen 4 (a pair of bundled bars at north face)

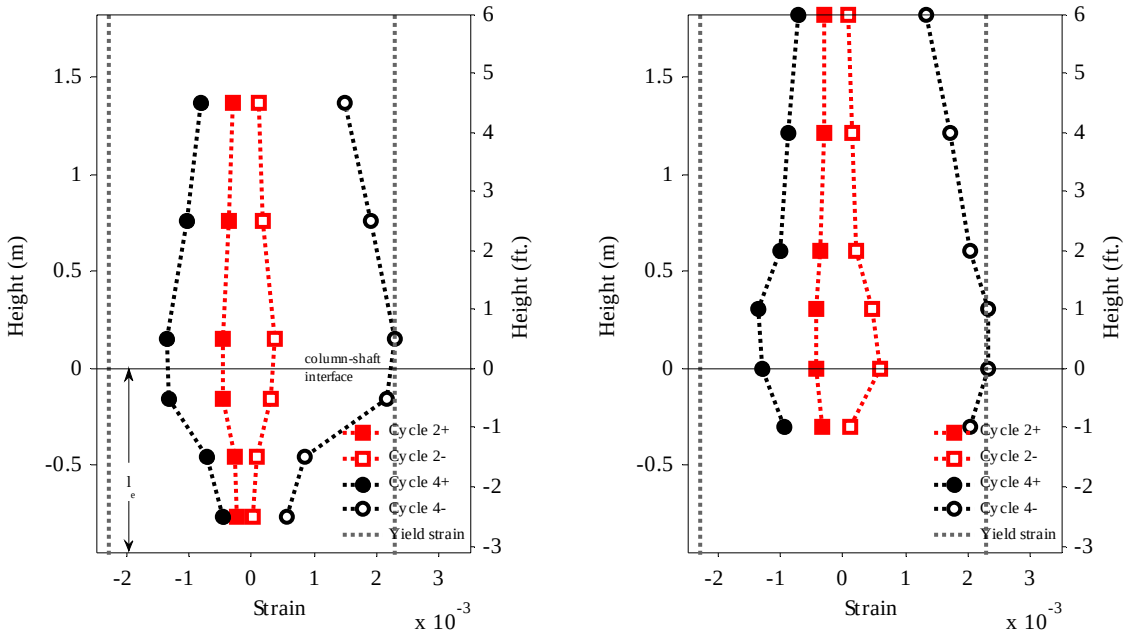

(a) Bar 1 (early cycles)

(b) Bar 2 (early cycles)

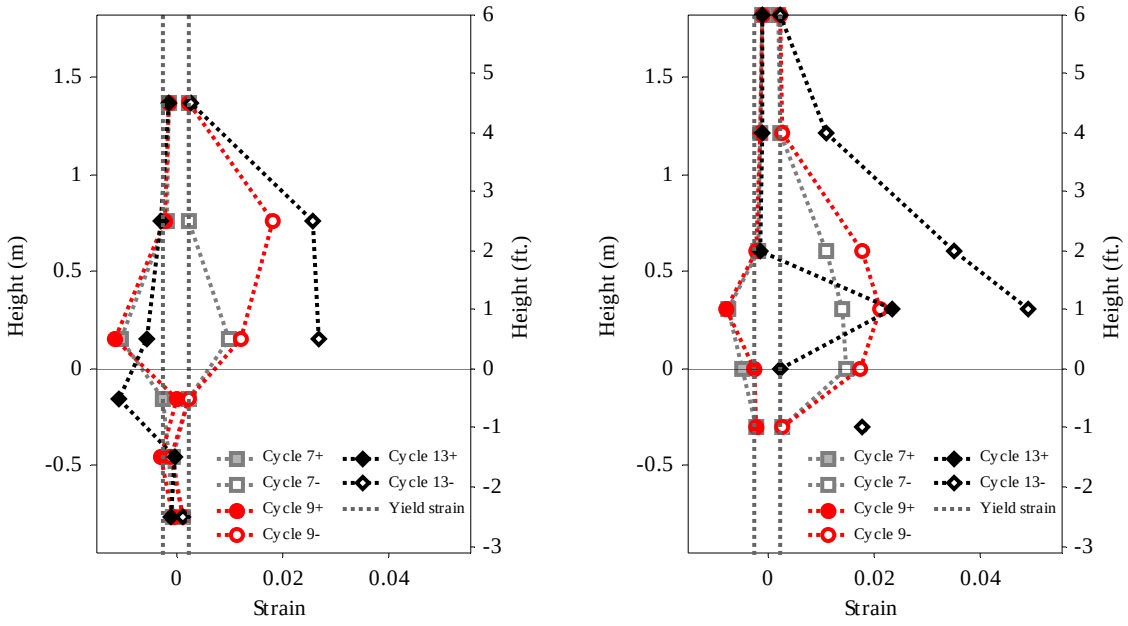

(c) Bar 1 (final cycles)

(d) Bar 2 (final cycles)

Figure 7.42: Strains in column longitudinal bars in Specimen 4 (a pair of bundled bars at south face)

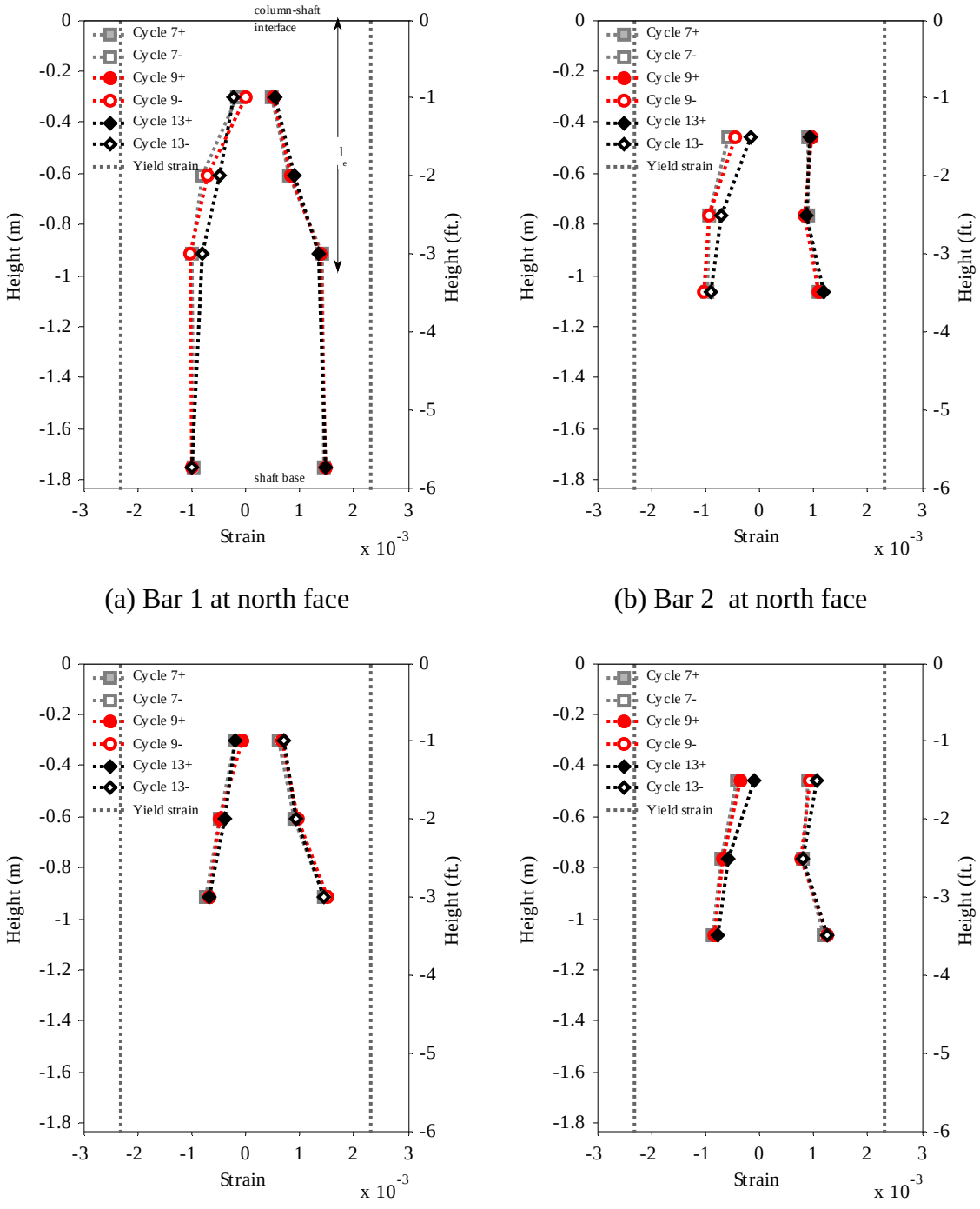

(a) Bar 1 at north face

(b) Bar 2 at north face

(c) Bar 1 at south face

(d) Bar 2 at south face

Figure 7.43: Strains in shaft longitudinal bars in Specimen 4 (two pairs of bundled bars)

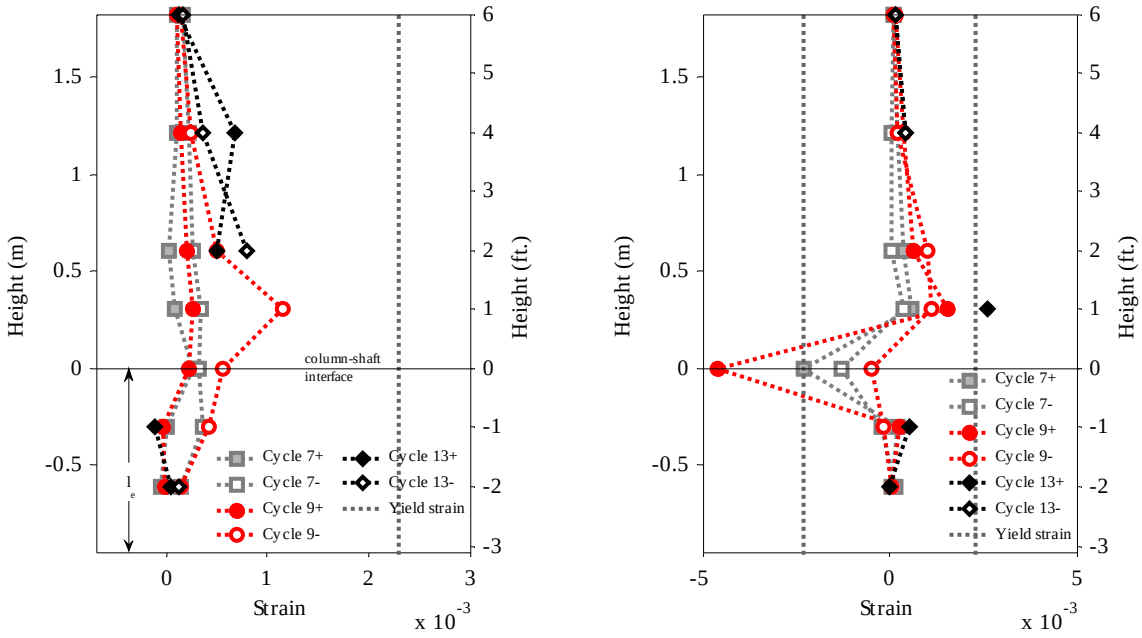

(a) North face (b) South face

Figure 7.44: Strains in column hoops in Specimen 4

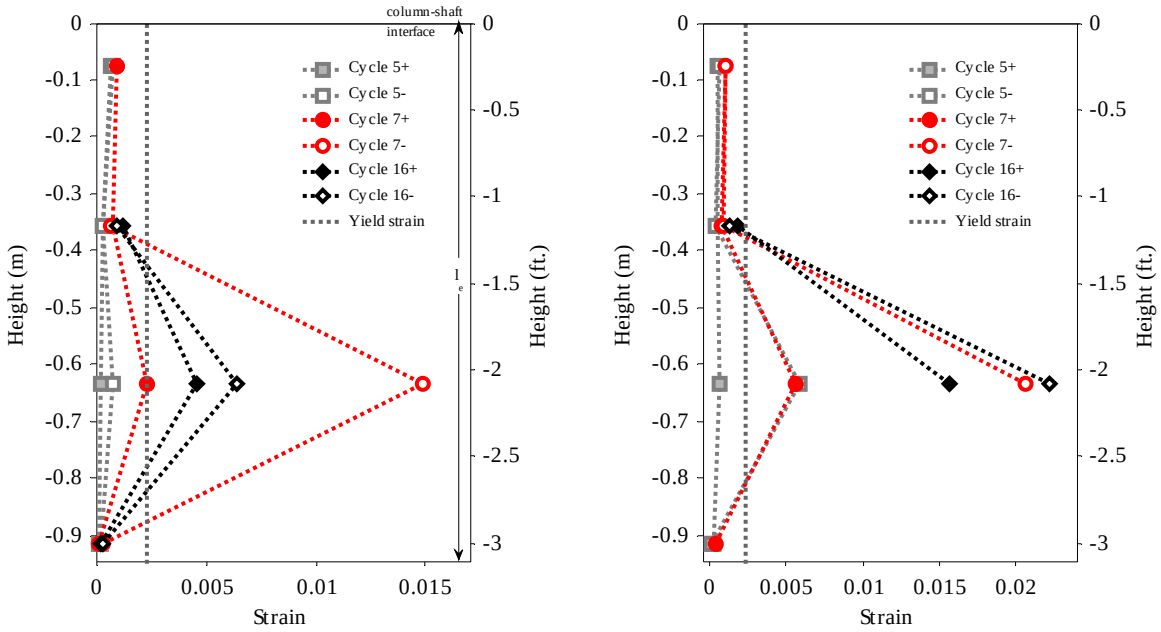

(a) North face

(b) South face

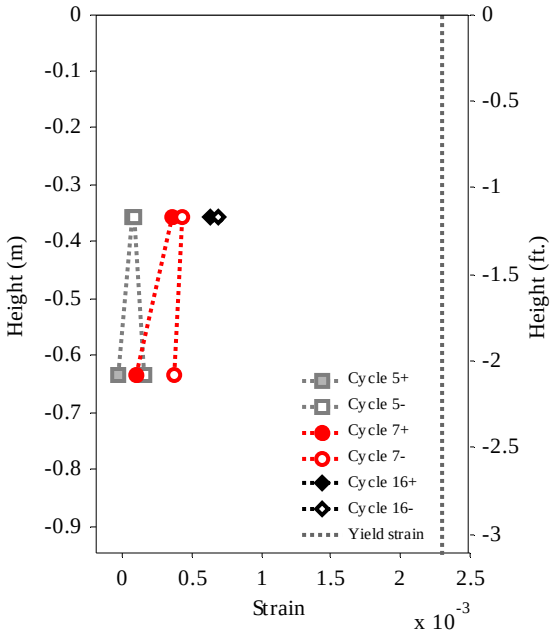

(c) West face

Figure 7.45: Strains in shaft hoops in Specimen 4

CHAPTER 8

FINITE ELEMENT ANALYSIS OF COLUMN – ENLARGED PILE SHAFT ASSEMBLIES

Finite element (FE) analyses have been used together with the results of the large-scale tests presented in Chapter 7 to determine the minimum embedment length required for column longitudinal reinforcement extending into enlarged pile shafts. Initially, FE models were used for the pre-test assessment of the performance of the column-shaft assemblies and to assist the development of the loading protocols for the tests presented in Chapter 6. In particular, the analyses confirmed that the embedment lengths used in Specimen 2 and subsequent specimens, which were determined with the new formula $l_d + s + c$, were close to the minimum required to develop the column longitudinal reinforcement. Once validated by the test results and further refined, the FE models have been used to obtain detailed information, such as the bar stress and bond stress distributions along the longitudinal column reinforcement, which were not obtainable from the tests but are crucial for gaining a good understanding the bond-slip behavior of the column reinforcement in the shaft and for determining the adequacy of the embedment length. Finally, the FE models have been used in a parametric study to further verify if the formula used to determine the embedment lengths for Specimens 2, 3, and 4 is adequate in general for column-shaft assemblies of different dimensions and with different longitudinal reinforcement ratios and bar sizes.

8.1 Finite element modeling of the column-shaft tests

A FE model of a column-shaft assembly like those tested in the laboratory is shown in Figure 8.1. Only half of the specimen is represented in the model by taking advantage of the symmetry plane along the north-south (loading) direction. The constitutive models for concrete and steel, which are available in ABAQUS and have been calibrated as discussed in Chapter 4, are used. Bond slip in the column and shaft longitudinal bars is considered. The bars are modeled with beam elements, and bond slip is modeled with the phenomenological bond-slip law presented in Chapter 4. Perfect bond is considered for the transverse reinforcement, which is modeled with truss elements embedded in the concrete elements. In Specimen 3, the steel casing is modeled with solid elements. The strength parameters for the concrete and steel models are calibrated with the material test data presented in Chapter 7, while the bond-slip model is calibrated with the method described in Chapter 4 based on the compressive strength of the concrete, the diameters of the reinforcing bars and rib spacing. Contact conditions are imposed at the interface between the column and the shaft, whose meshes are constructed independently, and also at the interface between the shaft and the footing. This is to improve the simulation of the opening and closing of large flexural cracks possible at these locations, which cannot be well represented by the concrete model, as discussed and explained in Chapter 4.

8.1.1 Load-displacement response

The FE models are subjected to the same vertical load and displacement demands at the top of the column as the test specimens. Geometric nonlinearity is considered in the analyses. The lateral load-vs.-drift relations obtained from the tests and the analyses for Specimens 1 through 4 are shown in Figure 8.2 through Figure 8.5, respectively. The FE analysis results provide a good match with the experimental load-displacement curves, except for the last cycle of the tests. The lateral load carrying capacities obtained from the tests and finite element analyses are compared in Table 8.1. It can be observed that the FE analyses overestimate the maximum loads by 2% (for Specimen 4) to 13% (for Specimen 3). The gradual drop of the load carrying capacity caused by the P-delta effect is well predicted analytically. The models reproduce the inelastic mechanisms developed

in the columns and shafts, such as the concrete crushing at the base of the columns, flexural cracking, bar yielding, bond slip, and splitting cracking in the shafts. Cracking in the shafts is similar to the patterns observed experimentally, as shown in Figure 8.6 by the contour plots of the maximum principal strains in the four shafts at the peak displacement of Cycle 13. Figure 8.6 also shows that the levels of damage in Specimens 1, 2 and 4 are similar, while it is less severe in Specimen 3 owing to the additional confining action of the steel casing. The models cannot simulate bar buckling and subsequent bar fracture observed near the base of the columns towards the end of the tests. For this reason, the sudden load drop observed in the last cycle of the tests cannot be reproduced, as shown in Figure 8.2 through Figure 8.5. Unloading and reloading behaviors are fairly well represented because of the contact condition introduced at the column-shaft interface. However, the numerical results still show a smaller deterioration of the stiffness in the unloading branches due to the limitation of the concrete model to simulate the closing of cracks accurately in locations other than the column-shaft and shaft-footing interfaces.

8.1.2 Strains and stresses in column longitudinal reinforcement

Figure 8.7 through Figure 8.10 plot the numerical and experimental strain values for the column longitudinal bar at the north face of Specimens 1 through 4, respectively. A good correlation can be seen between the numerical and experimental results for bar strains in the columns and along the embedment length in the shafts. Only for Specimen 1, the severity of strain penetration seems to be underestimated slightly by the FE model. As shown in Figure 8.7b, according to the FE analysis, tension yielding of the column longitudinal bars in Specimen 1 penetrates 0.5 m (1.63 ft) into the shaft at the peak displacement of Cycle 13 (the first cycle at a system ductility of 5.5 and the last cycle before bar fracture occurred in the test). This plastic strain penetration is 14 times the bar diameter, d_b. In the test, the plastic strain penetration was measured to be 0.61 m (2 ft) at this same cycle. Thus, the model underestimates the plastic strain penetration along this bar by 18%. However, for the other specimens, the strain penetrations in the FE models match the test results well. In Specimen 2, strain gages were damaged in the last few

cycles, so the final plastic strain penetration could not be obtained. According to the FE analysis, the plastic penetration in Cycle 17 (the first cycle at a system ductility of 7 and the last cycle before bar fracture occurred in the test) for Specimen 2 is 0.72 m (2.4 ft), which is $17\,d_b$, as shown in Figure 8.8. The FE analysis have shown that Specimens 3 and 4 have similar extents of normalized plastic strain penetration, with respect to the bar diameter, at the end of the tests. For Specimen 3, it is $15\,d_b$, or 0.65 m (2.1 ft), and for Specimen 4, it is $16\,d_b$ or 0.4 m (1.3 ft).

Figure 8.11 plots the axial stress distributions along the column longitudinal bars for Specimens 1 through 4 at the peak displacements of different cycles, as predicted by the FE analysis. Table 8.2 shows the maximum tensile stresses developed for each of the specimens at the peak displacement of the cycle prior to failure in the test, as obtained from FE analysis. The maximum stresses developed in these bars are smaller than the tensile strength of the bars, which was obtained from material testing. For example, the maximum bar stresses developed at the base of the column in Specimen 1 are 550 MPa (80 ksi) in tension and 485 MPa (70 ksi) in compression, while the yield strength and tensile strengths of the bar are 448 MPa (65 ksi) and 629 MPa (91.2 ksi), respectively. As mentioned in Chapter 7, the fracture of these bars during the tests was not caused by exhaustion of the tensile capacity but by the propagation of micro-cracks created when the bar buckled, which is a feature that the FE model cannot capture.

8.1.3 Bond stresses and slip in column longitudinal reinforcement

The bond stresses along the column longitudinal bars obtained from the FE analyses provide valuable information to understand the bond-slip behavior of these bars along their anchorage. The bond stress distributions along the embedment length of the column bars located at the north face of Specimen 1 through Specimen 4 are plotted in Figure 8.12 through Figure 8.15, respectively. It is possible to calculate the average experimental bond stresses based on the readings from two adjacent strain gages as long as the bar had not yielded, which was the case for the lower portions of the bar anchorage zones. As shown in Figure 8.12 through Figure 8.15, the numerically obtained bond

stresses compare relatively well to the average bond stresses obtained from the experimental data in these lower anchorage regions.

For Specimen 1, the bond stress distribution is highly nonlinear when the bar is subjected to tension and compression, as shown in Figure 8.12. The peak bond stress occurs near the top of the embedment length, and it moves downward as the ductility demand is increased. Even though the bar slip is maximum at the top of the embedment length, the peak bond resistance occurs at a lower section. This is mainly due to the severe bond deterioration caused by bar yielding occurring in the upper region of the embedment length. This behavior is similar to that observed in the development length tests presented in Chapter 5. As shown in Figure 8.12b, the peak bond resistance in Cycle 13 is located 0.53 m (1.75 ft) below the column base, practically at the same location where the plastic strain penetration ends as shown in Figure 8.7. This peak resistance is 6.9 MPa (1 ksi) or 40% of the maximum bond strength. At the peak displacement of Cycle 13, most of the bond resistance is provided in a region located approximately between 0.3 m (1 ft) and 1 m (3.3 ft) below the base of the column. In the remaining 2.3 m (4.2 ft) below this region, little bond resistance is activated, with the bond stress less than 2.5 MPa (0.35 ksi) (i.e., 15% of the bond strength), because the bar has not slipped much. This indicates that there is a significant portion of the embedment length that is not utilized to develop the stress in the bar in the last load cycle, at which the load dropped significantly due to bar rupture in the test.

Figure 8.13 plots the bond stress distributions along the embedment length of the longitudinal bar located at the north face of Specimen 2. The distribution is highly nonlinear when the bar is subjected to compression. However, the bond resistance is more uniform when the bar is subjected to tension. At the peak displacement of Cycle 17, the bond resistance along the upper 0.6 m (2 ft) of the embedment length has deteriorated significantly. For the rest of the bar anchorage length, the bond resistance is more uniformly distributed than that for Specimen 1 when the bar is in tension, with the bond stress varying from 2.8 MPa (0.4 ksi) to 6.4 MPa (0.93 ksi), i.e., from 17% to 39% of the maximum bond strength. This implies that the bar has experienced more slip along the

anchorage. These results show that the embedment length for Specimen 2 can be close to the minimum required.

The increase of confinement in the anchorage region of Specimen 3 as compared to Specimen 2 affects the bond stress distributions, as shown in Figure 8.14. At the peak displacement of Cycle 15, bond deterioration in the upper part of the bar anchorage is similar to that for Specimen 2. However, for Specimen 3, the peak bond stress reaches 45% of the maximum bond strength, slightly higher than that for Specimen 2 (which has the peak bond stress at 39% of the maximum bond strength), and the bond stress mobilized drops much faster with depth and is equal to 8% of the maximum bond strength near the bottom of the anchorage zone. These results indicate that an increase in confinement improves the bond along the embedment length and reduces bond slip. Thus, this specimen has more reserve anchorage capacity than Specimen 2.

For Specimen 4, the shape of the bond stress distribution in tension is similar to that for Specimen 2, as shown in Figure 8.15. At the peak displacement of Cycle 13, the bond resistance along the upper 0.4 m (1.3 ft) of the embedment length has deteriorated significantly mainly due to bar yielding in tension. For the rest of the anchorage length, the bond stresses variation is small (it varies from 25% to 42% of the maximum bond strength), and the maximum bond resistance occurs at the bottom of the anchorage. As for Specimen 2, this indicates that the embedment length for this specimen was close to the minimum required.

The bar slip with respect to the surrounding concrete is plotted in Figure 8.16 through Figure 8.19 for the same bars in Specimens1, 2, 3, and 4, whose bond stress is considered above. In the upper regions of the bar anchorage zones, in which the bars have yielded, large levels of slip are measured. Below the plastic strain penetration regions, the bar slips are smaller than the slip, s_{peak}, at which the maximum bond resistance is mobilized in the monotonic bond stress-slip curves of for the respective bars. In Specimen 1, the bar practically does not slip (with the slip smaller than 5% of s_{peak}) in the lower 1.4 m (4.5 ft), or $38\,d_b$, of the bar anchorage length, as shown in Figure 8.16. In the other specimens, the regions with little slip are shorter and the magnitude of the slips

in these regions is larger. In Specimens 2, the slip in the lower 1 m (3.5 ft), or $25d_b$, is between 5% and 10% of s_{peak}, as shown in Figure 8.17. Over the same length, this slip is between 3% and 8% of s_{peak} in Specimen 3, as shown in Figure 8.17. In Specimen 4, the slip in the lower 0.9 m (2.8 ft), or $33d_b$, is between 8% and 12% of s_{peak}, as shown in Figure 8.18. It should be noted that according to monotonic stress-slip relation adopted in the model, as presented in Chapter 4, the bond stress will reach 40% of the maximum bond strength at a slip of 10% of s_{peak}. Hence, the bar slip in Specimen 4 can be considered relatively significant.

8.1.4 Strain and stresses in shaft longitudinal reinforcement

The numerical and experimental strain values for the shaft longitudinal reinforcement are plotted in Figure 8.20 through Figure 8.23 for Specimens 1 through 4, respectively. The FE models underestimate the strain levels in these bars. The discrepancies in the tensile strains could be attributed to the fact that the concrete in the models is able to carry higher tensile stresses than that in the actual specimens, for which flexural cracks were observed in the shafts. As shown in Figure 8.21 and Figure 8.23, the bar strains at the base of the shafts show a better correlation. This is because the contact interface at the shaft base cannot develop tensile stresses, and the tensile stresses are transferred to the footing through the bars.

8.1.5 Strains in the column hoops

Figure 8.24 compares the numerical and experimental strain values for the column hoops at the south face of the specimens. The models predict correctly the yielding of the hoops at the base of the column in the late few cycles. However, they overestimate the hoop strains at other locations along the height of the column. This could be attributed to an overestimation of the plastic dilatation in the concrete model.

8.1.6 Strains in the shaft hoops

The numerical and experimental strain values for the shaft hoops in Specimen 1 are compared in Figure 8.25. The model provides a fairly good representation of the peak

strains for the north side of the shaft, but overestimates these strains near the top of the embedment length region, as shown in Figure 8.25a. The lateral load-vs.-hoop strain curves for the north side of the hoop located at 0.3 m (1 ft) below the column base are plotted in Figure 8.25b. During the test, the hoop strain increased when the column was pushed and pulled laterally, i.e., when the column longitudinal bar near the north face was pulled and pushed, and decreased when the column was unloaded. The strain increase was largely caused by the radial expansion induced by the bar slip as it was pulled or pushed. However, when a bar is pushed, additional dilatation can be introduced by the lateral elastic or plastic expansion of the concrete due to vertical compression. As shown in Figure 8.25b, the FE model shows a different hysteretic behavior in hoop strains. In the FE model, the strain near the north face increases only when the column is pulled towards north (which corresponds to negative loading), i.e., when the longitudinal bar located on the north side is pushed into the shaft. When the column is unloaded and pushed towards south, the strain remains practically constant. For the shaft hoop located at about 1 m (3 ft) below the base of the column, the strain increases when the column is pushed and decreases when it is pulled.

The problems in replicating the hoop strains in the shaft, as shown in Figure 8.25, could be attributed to the deficiencies of the concrete model, which is not able to simulate accurately the plastic dilatation in concrete and the closing of tensile splitting cracks, and also to the inaccuracy of the bond-slip model in simulating the radial dilatation caused by bar slip. Similar trends have been observed for Specimen 2, as shown in Figure 8.26. The magnitude of the strains at the north side of the hoops correlates well with the experimental results, as shown in Figure 8.26a. Nevertheless, the lateral load-vs.-hoop strain curves for the north side of the uppermost hoop, as plotted in Figure 8.26b, show similar discrepancies. For the west side of this hoop, the numerical strain values increase when the column is either pushed or pulled laterally, as plotted in Figure 8.26c. However, it is unclear if this is caused by the radial stress introduced by the slip of the column bars or by the lateral expansion of concrete due to compression on the north and south sides of the column as it was pulled and pushed.

The peak hoop strains in the transverse reinforcement and steel casing of the shaft in Specimen 3 are reasonably well captured with the FE analysis, as shown in Figure 8.27 and Figure 8.28. The smaller hoop strains as compared to those measured in Specimen 2 are well predicted. However, these strains are underestimated at the top of the bar anchorage zone, where the maximum hoop strains develop.

The hoop strain distribution in the shaft of Specimen 4 predicted with the FE analysis is similar to that of Specimen 2, as shown in Figure 8.29. However, during the test, the peak strains were measured in a hoop located 0.64 m (2.1 ft) below the top of the shaft rather than the hoop near the top.

8.1.7 Concluding remarks

The FE analysis results presented have shown good correlation with the experimental results in terms of the global lateral load-displacement behavior of the column-shaft assemblies and strain variations in the column longitudinal bars within the columns and embedment regions. However, some modeling limitations have also been identified. One is that the failure of a column caused by the buckling and subsequent fracture of the bars is not simulated. Also, the concrete model is not able to simulate the closing of tensile cracks in an accurate manner. However, these deficiencies have no significant impact on the bond-slip behavior of bars, which is the focus of this study. Moreover, the finite element models are not able to capture the strains in the shaft hoops in a very accurate manner. At the top of the shaft, the models tend to show hoop strains lower than those observed in the tests. This can be attributed to the fact that the models cannot well simulate the plying action of the confined concrete core of the column within the shaft. Hence, these models may not have the desired resolution to determine the minimum quantity of transverse reinforcement required for the bar anchorage region of a shaft.

8.2 Parametric study to verify the minimum embedment length of column reinforcement in enlarged pile shafts

Three of the four column-shaft assemblies tested in this project and the finite element analyses presented in Section 8.1 have shown that an embedment length of

$l_d + s + c$ for the column reinforcement extended into an enlarged shaft is sufficient to develop the full bending capacity of a column. Further finite element analyses have been conducted to investigate if this is true for column-shaft assemblies of different geometric configurations and reinforcing details, and its level of conservatism against the pull-out failure of the reinforcing bars. As summarized in Table 8.3, results from 12 column-shaft models are discussed here. Additional analyses have been conducted to establish the limiting conditions for the embedment length, but their results will not be presented. The nomenclature for the models is based on a set of four numbers. The first two numbers correspond to the column diameter (D_c) and shaft diameter (D_s), respectively, in feet. The third number corresponds to the size of the column longitudinal bars. Wherever needed, a forth number is added to distinguish models with the same dimensions and reinforcement, but with different embedment lengths for the column reinforcement and/or different quantities of transverse reinforcement in the shafts. Based on the first three numbers in the nomenclature, the models are divided into five groups. Three of these models, Models *4-6-11-1*, *4-16-14-1*, and *4-6-14-4* correspond to Specimens 1, 2, and 3 tested in the laboratory, respectively. Results from these three models have been discussed in detail in Section 8.1. Nine more analyses have been carried out on column-shaft models with different embedment lengths, column and shaft diameters, quantities of longitudinal reinforcement, and quantities of transverse reinforcement in the shafts. The concrete, steel, and bond-slip properties used in these models are the same as those for the analyses presented in Section 8.1. The same loading protocol was used, except that an extra half cycle was added at the end to subject the system to a maximum ductility demand of 10.

Of the 9 new models, five have embedment lengths of $l_d + s + c$ and the quantities of transverse reinforcement in the bar anchorage region of the shaft determined with Equation 6.9. These are Models *4-6-11-2*, *4-6-14-2*, *8-10-14-1*, *8-12-14*, and *8-12-18* shown in Table 8.3. They include small-size (D_c =1219 mm [4 ft]) and large-size (D_c= 2438 mm [8 ft]) columns, and have bar sizes between No. 11 and 18.

The columns and shafts in Models *4-6-11-2* and *4-6-14-2* have the same dimensions, with D_c=1219 mm (4 ft) and D_s=1829 mm (6 ft), and the same longitudinal reinforcement as Specimens 1 and 2, respectively. Model *8-10-14-1* corresponds to an assembly with D_c= 2438 mm (8 ft) and D_s= 3048 mm (10 ft), and has No. 14 (43-mm) and 18 (57-mm) longitudinal bars in the column and shaft, respectively. In the above three models, the shaft diameter is 610 mm (2 ft) larger than the column diameter, which is the minimum difference required in Caltrans SDC (Caltrans 2010). As a result, the separation between the column and shaft cages is slightly less than 305 mm (1 ft). Two additional models have been analyzed with D_c= 2438 mm (8 ft) and D_s= 3658 mm (12 ft) to verify the embedment length formula when a larger separation between the column and shaft cages is provided. In one of the models, Model *8-12-14*, No. 14 and 18 longitudinal bars are used in the column and shaft, respectively. In the other, Model *8-12-18*, both the column and the shaft have No. 18 longitudinal bars.

Analysis results from the aforementioned five models show that an embedment length of $l_d + s + c$ is sufficient to develop the full bending capacity of the columns. The remaining four of the 9 new models have either shorter embedment lengths or different quantities of transverse reinforcement to examine the level of conservatism in the embedment length formula. Analysis results obtained with these models are summarized in the following sections.

8.2.1 Smaller-size column-shaft assemblies

Model *4-6-11-2* has the same column and shaft dimensions and reinforcement as Specimen 1 but with $l_e = l_d + s + c$. Figure 8.30 shows that it has identical force-displacement curves as the model for Specimen 1 (Model *4-6-11-1*), in which $l_e = D_{c,\max} + l_d$. Hence, the reduction of the embedment length has no influence on the system response. Model *4-6-11-3* has an even shorter embedment length of $0.7l_d$. For this model, several column longitudinal bars are pulled out from the shaft when the maximum drift reached for Specimen 1 has been applied. Pull-out failure of the bars causes a decrease of the load-carrying capacity with respect to the other two models, as

shown in Figure 8.30. Additional analyses not reported here have shown that for any embedment lengths longer than $0.7l_d$, pull-out failure will not occur. This indicates that $l_e = l_d + s + c$ has a good margin of safety.

The strain distributions along the column bars located at the north face of Models *4-6-11-1*, *4-6-11-2*, and *4-6-11-3* at the peak displacement of Cycle 13 are plotted in Figure 8.31a. The maximum plastic strain penetration is about 0.5 m (1.63 ft) or $14d_b$ in all the models. The distances between the bottom of the bar to the point where the bar has yielded are $50d_b$, $26d_b$, and $7d_b$ for Models *4-6-11-1*, *4-6-11-2*, and, *4-6-11-3*, respectively. With only $7d_b$ to develop the yield capacity of the bar in the last case, the pull-out failure occurring in the last model is not unexpected. Differences are observed in the bond stress distributions along these bars at the peak displacement of Cycle 13, as shown in Figure 8.31b. For the case with the shortest embedment length, the bar slips more and the bond stress is higher and more uniformly distributed along the anchorage length.

Specimen 2 had an embedment length of $l_d + s + c$ and the transverse reinforcement in its shaft was determined according to the formula of McLean and Smith (1997). A model (*4-6-14-2*) with the same embedment length but transverse reinforcement in the shaft determined with Equation 6.9 has been analyzed and compared to the model of Specimen 2 (*4-6-14-1*). With Equation 6.9, the volumetric ratio of the hoops in the lap splice region is 1.19% as compared to 1.04% provided in Specimen 2. In addition, two more models with the same embedment length but different quantities of transverse reinforcements have been analyzed. In Model *4-6-14-3*, the transverse reinforcement in the lap splice area has been determined with the general specifications for compression members in AASHTO (2010), and has a volumetric ratio of 0.74%. Model *4-6-14-4* represents Specimen 3, whose transfer reinforcement was determined with the more stringent condition, Equation 6.14, proposed to control splitting cracks in the shaft. For this specimen, the size and spacing of hoops was determined with the AASHTO LRFD Bridge Design Specifications (2010) on the confinement for

compression members, and the additional confinement required by Equation 6.14 was provided with the steel casing.

The force-displacement curves obtained for the aforementioned models, as shown in Figure 8.32, are very similar. The strain and bond stress distributions along the column bars located at the north face of these models at the maximum drift of Specimen 2 are plotted in Figure 8.33. As shown in Figure 8.33a, the plastic strain penetration increases as the transverse steel decreases. However, the difference is very small, with the maximum plastic penetration ranging from 0.64 m (2.1 ft) to 0.72 m (2.4 ft). Similarly, the peak bond resistance increases and the bond stress distribution becomes less uniform with the increase of the transverse steel, as shown in Figure 8.33b. The hoop strains in the transverse reinforcement and in the steel casing of the shafts at the peak displacement of Cycle 17 are plotted against the height in Figure 8.34. The analysis results confirm that the hoops strains increase with the decrease of the transverse reinforcement. In the case with the lowest confinement, the three upper hoops located in the upper 0.4 m (1.3 ft) of the shaft yield, while only the uppermost hoop is close to yielding when the quantities of the transverse reinforcement recommended here and by McLean and Smith (1997) are used. The model representing Specimen 3, which has the highest confinement level, does not have yielding in the hoops and steel casing. However, in the real test, the hoop strain in the steel casing near the column base slightly exceeded the yield point.

Model *4-6-14-5* replicates Specimen 2 but employs a reduced embedment length of $l_e = 0.65 l_d$. This model has bar pull-out failure exhibiting a significant load degradation under cyclic loading, as shown in Figure 8.32. Further analyses not reported here have shown that for longer embedment lengths, pull-out failure will not occur. The bond stress distribution along the column bar located at the north face of Model *4-6-14-5*, as plotted in Figure 8.33b, shows that the bond resistance has practically disappeared at the peak displacement of Cycle 17. The results plotted in Figure 8.34 show that the pull-out of the bars causes a significant increase in strain in the transverse reinforcement in the lap splice region. Therefore, wider splitting cracks can be expected. The upper hoops yield, with the top hoop experiencing a strain almost four times that experienced in Model *4-6-14-2*, which has the same quantity of transverse steel.

8.2.2 Larger-size column-shaft assemblies

Two models of a column-shaft assembly with D_c = 2438 mm (8 ft) and D_s= 3048 mm (10 ft) have been analyzed. Model *8-10-14-1* has an embedment length of $l_d + s + c$ and the transverse reinforcement in the shaft complying with Equation 6.9. The response of this model is compared to that of Model *8-10-14-2*, in which the embedment length is reduced to $l_e = 0.75 l_d$. The force-displacement curves plotted in Figure 8.35 show that Model *8-10-14-2* has a significant load degradation under cyclic loading due to bar pull-out failure. Additional analyses have shown that pull-out failure will not occur for longer embedment lengths. At a system ductility of 7, reached at the peak displacement of Cycle 17, the plastic strain penetration in Model *8-10-14-1* is 0.95 m (3.1 ft) or $22 d_b$, as shown in Figure 8.36a. This is larger than $17 d_b$ in Model *4-6-14-2*, which has the same longitudinal bar size, and has the development length and transverse reinforcement determined with the same equations but with D_c= 1219 mm (4 ft) and D_s= 1829 mm (6 ft). This difference in plastic strain penetration is caused by the more severe damage induced at the top of the shaft in Model *8-10-14-1* due to the smaller ratio of the shaft to column diameter. This increase in damage is also reflected in the bond stress distribution, which shows that the peak bond stress in Model *8-10-14-1* is at the bottom of the embedment length, as shown in Figure 8.36b. Despite the increase in damage, the embedment length in Model *8-10-14-1* is clearly sufficient to avoid the failure of the bar anchorage. Like in the other models, the pull-out of the bars in Model *8-10-14-2* causes larger strains in the transverse reinforcement in the lap splice region, as shown in Figure 8.37. This implies wider splitting cracks.

Finally, two models of a column-shaft assembly with D_c= 2438 mm (8 ft) and D_s= 3658mm (12 ft) have been analyzed with an embedment length of $l_d + s + c$ and the transverse reinforcement in the shaft complying with Equation 6.9. Models *8-12-14* and *8-12-18* have No. 14 and 18 bars, respectively, for the column longitudinal reinforcement. As shown in Figure 8.38 and Figure 8.39, these models do not show any load degradation in the force-displacement curves other than the P-delta effect. The strain distribution along the north column bar of Model *8-12-14* at the peak displacement of

Cycle 17 (a system ductility of 7), as plotted in Figure 8.40a, indicates a plastic strain penetration of 0.95 m (3.1 ft) or $22d_b$. The plastic strain penetration is the same as that in Model *8-10-14*, but in this case, more embedment length is provided to account for the larger separation between the reinforcing cages. The peak bond stress is located far from the bottom end of the bar, as shown in Figure 8.40b. For the model with larger bars, the plastic strain penetration at a system ductility of 7 is $18d_b$ (1.03 m [3.4 ft]), as shown in Figure 8.41a. The bond stress distribution, as plotted in Figure 8.41b, also shows a clear peak located far from the bottom end of the bar. Hence, these two models have a higher margin of safety against bond failure as compared to the models with D_s= 3048 mm (10 ft).

8.3 Conclusions

The ability of the FE models to simulate the bond-slip behavior in column-shaft assemblies has been validated by the results of the large-scale column-shaft tests. They have been used to study the development of column longitudinal bars in enlarged pile shafts, including the bond stress distributions along the anchorage of these bars in the four tests presented in Chapter 7. The analytical and experimental observations indicate that $l_e = D_{c,\max} + l_d$ as used in Specimen 1 is over-conservative. The analytical and experimental results for Specimens 2 through 4 show that an embedment length of $l_d + s + c$ is sufficient.

Through further FE simulations, the sufficiency of $l_d + s + c$ has been verified for larger column-shaft assemblies, and for column-shaft assemblies with different ratios of shaft to column diameter and different sizes of column longitudinal bars. Simulation results from a limited number of models have also indicated that with adequate transverse reinforcement, pull-out failures will occur only when the embedment length is equal to or shorter than $0.75l_d$. This implies that there is a good margin of safety when $l_d + s + c$ is used. Furthermore, the models have shown that the ratio of the shaft diameter to the column diameter has an influence on the performance of the shaft. A higher ratio leads to less shaft damage.

However, the finite element models in general show smaller strains in the shaft hoops near the base of the column. This could be due to the fact that the plying action of the confined concrete core of the column within the shaft is not well captured in the models.

Table 8.1: Maximum lateral load resistance

Specimen no.	Experimental results kN (kips)	FE analysis results kN (kips)	FE prediction error
1	1063 (239)	1139 (256)	7%
2	1223 (275)	1348 (303)	10%
3	1205 (271)	1365 (307)	13%
4	1023 (230)	1040 (234)	2%

Table 8.2: Maximum tensile stresses in column longitudinal reinforcement

Specimen no.	Cycle no.	Maximum tensile stress, σ_{max} MPa (ksi)	σ_{max} / f_y	σ_{max} / f_u
1	13	550 (80)	1.23	0.88
2	17	585 (85)	1.27	0.92
3	15	580 (84)	1.25	0.90
4	13	574 (83)	1.25	0.88

f_y : actual yield strength of steel.

f_u: actual tensile strength of steel.

Table 8.3: FE models of column-shaft assemblies for parametric study

Model ID	D_c mm (ft)	D_s mm (ft)	Column / shaft longitudinal reinforcement	$\rho_{v,shaft}$ [4]	Formula for l_e	l_e mm (ft)
4-6-11-1 [1]	1219 (4)	1829 (6)	18 No. 11/ 28 No. 14	0.82%	$D_{c,\max} + l_d$	2286 (7.5)
4-6-11-2				**1.07%**	$l_d + s + c$	**1422 (4.67)**
4-6-11-3				1.07%	$0.7l_d$	762 (2.5)
4-6-14-1 [2]	1219 (4)	1829 (6)	18 No. 14/ 26 No. 18	1.04%	$l_d + s + c$	1829 (6)
4-6-14-2				**1.19%**	$l_d + s + c$	**1829 (6)**
4-6-14-3				0.74%	$l_d + s + c$	1829 (6)
4-6-14-4 [3]				1.87%	$l_d + s + c$	1829 (6)
4-6-14-5				1.19%	$0.65l_d$	940 (3.1)
8-10-14-1	2438 (8)	3048 (10)	38 No. 14/ 48 No. 18	**1.58%**	$l_d + s + c$	**1829 (6)**
8-10-14-2				1.58%	$0.75l_d$	1092 (3.6)
8-12-14	2438 (8)	3658 (12)	40 No. 14/ 56 No. 18	**1.31%**	$l_d + s + c$	**2134 (7)**
8-12-18	2438 (8)	3658 (12)	34 No. 18/ 56 No. 18	**1.53%**	$l_d + s + c$	**2565 (8.4)**

[1]Test Specimen 1.
[2]Test Specimen 2.
[3]Test Specimen 3.
[4]Volumetric ratio of shaft transverse reinforcement.
Note: models employing $l_d + s + c$ and Equation 6.9 for transverse reinforcement are highlighted in bold.

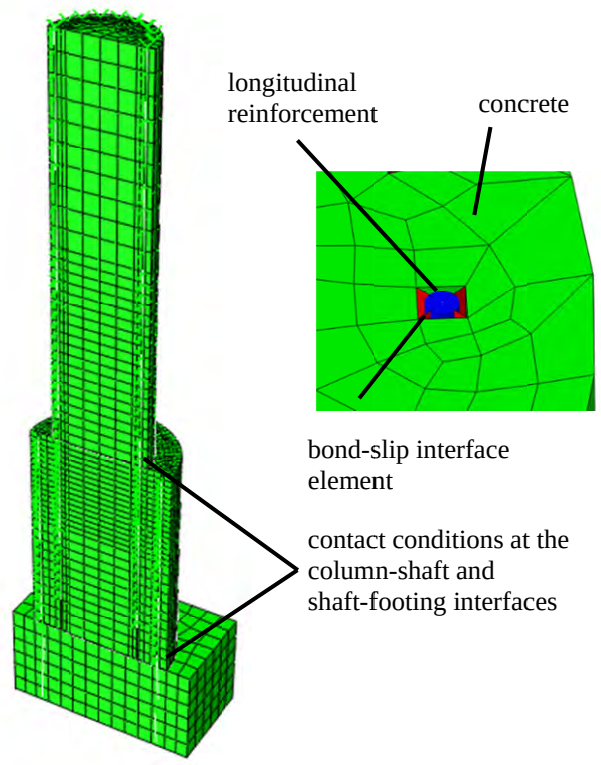

Figure 8.1: FE model of column-shaft assembly

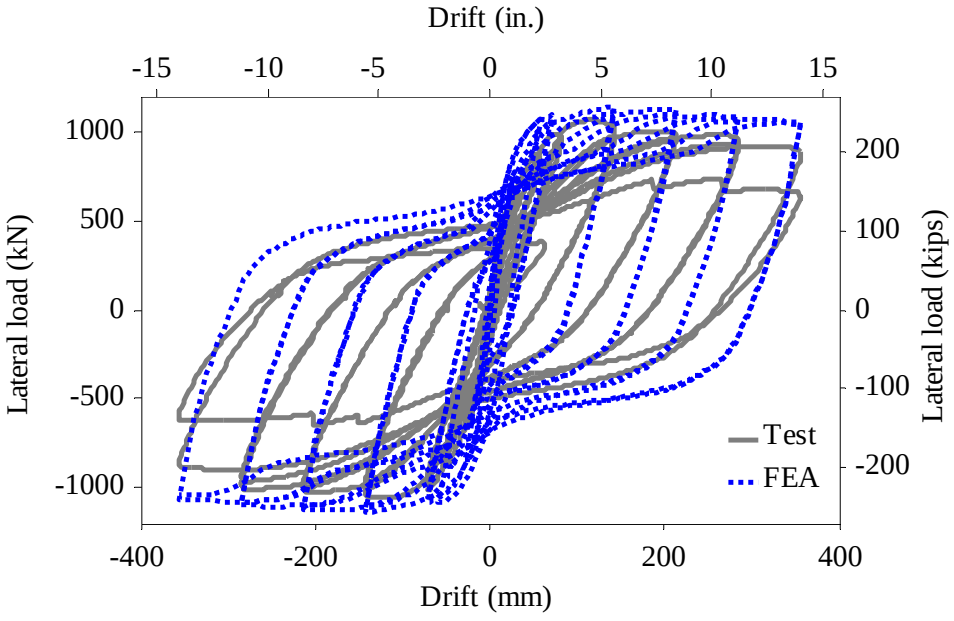

Figure 8.2: Lateral load vs. drift curves for Specimen 1

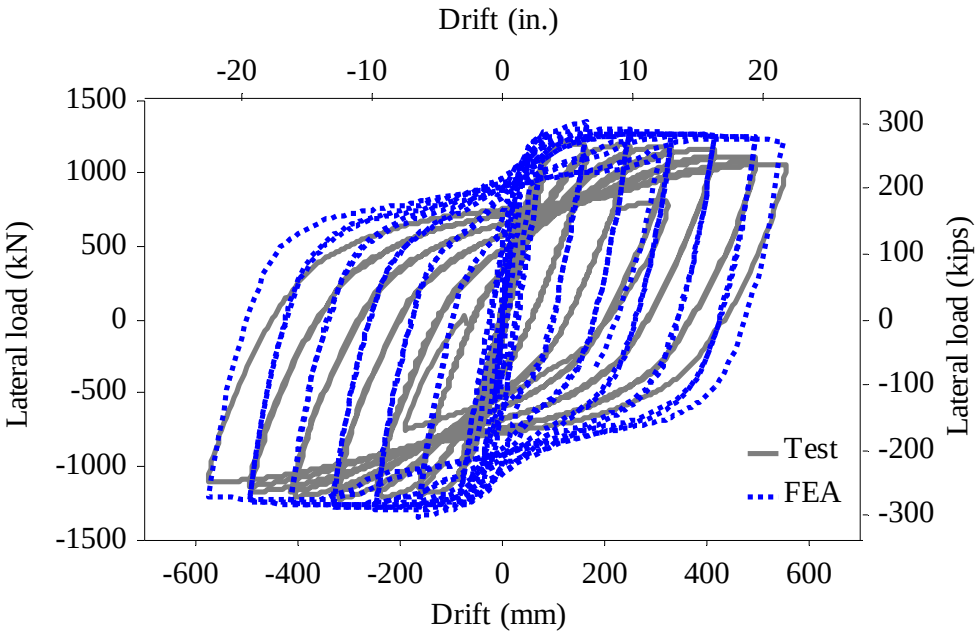

Figure 8.3: Lateral load vs. drift curves for Specimen 2

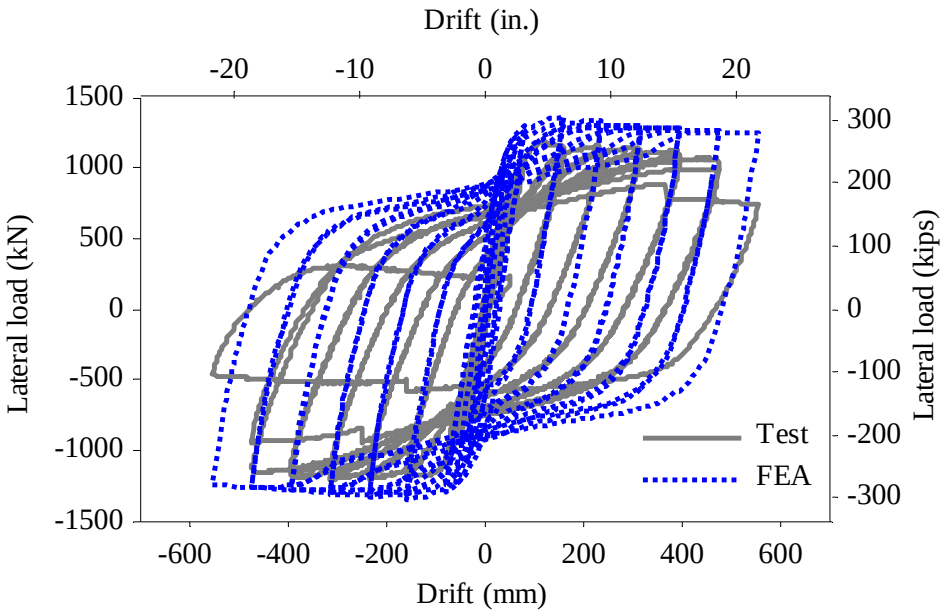

Figure 8.4: Lateral load vs. drift curves for Specimen 3

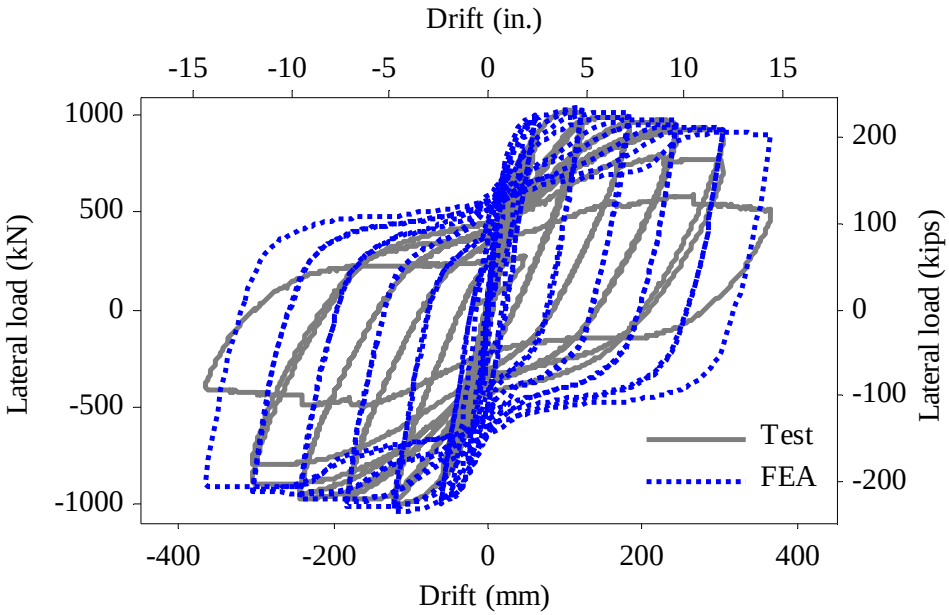

Figure 8.5: Lateral load vs. drift curves for Specimen 4

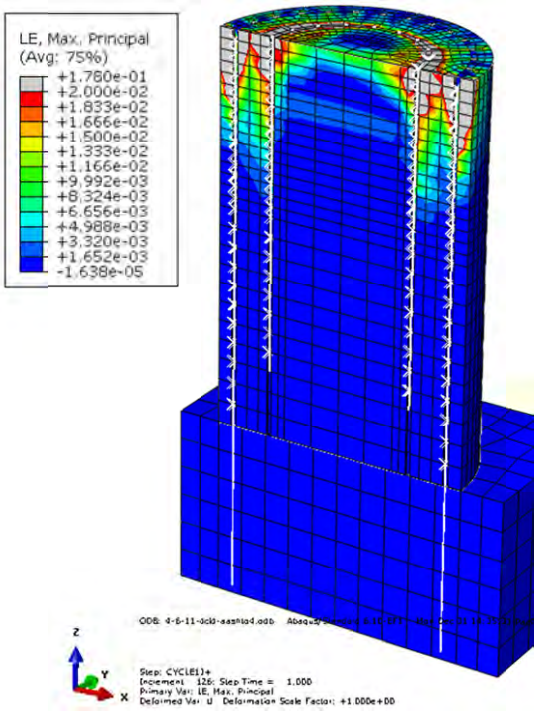

(a) Specimen 1

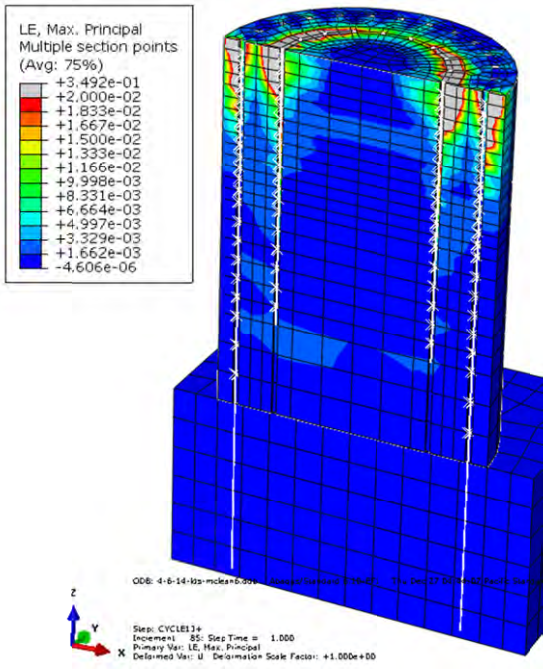

(b) Specimen 2

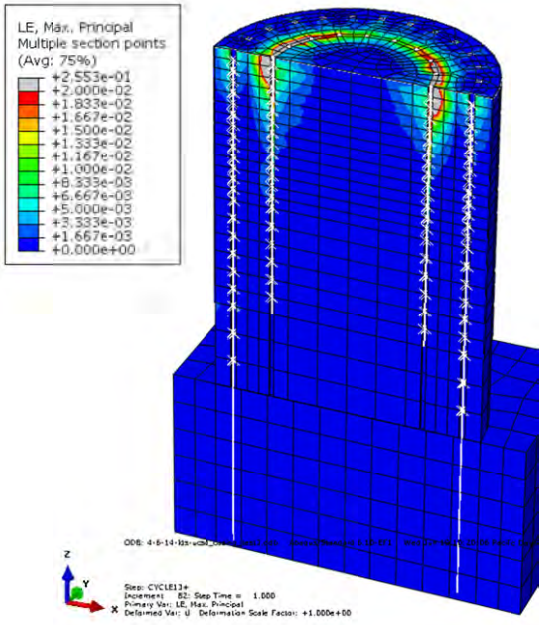

(c) Specimen 3

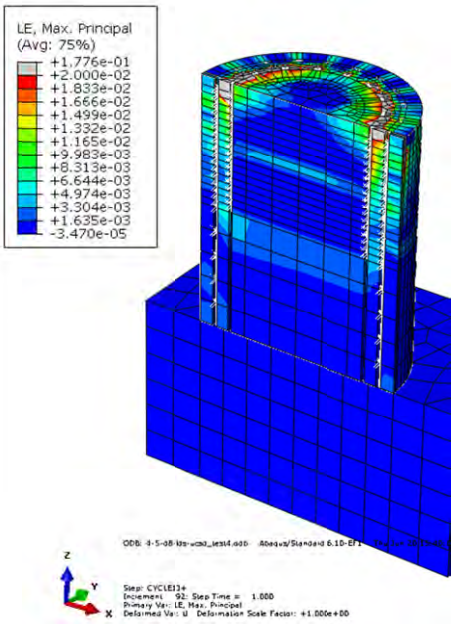

(d) Specimen 4

Figure 8.6: Maximum principal strains in shafts

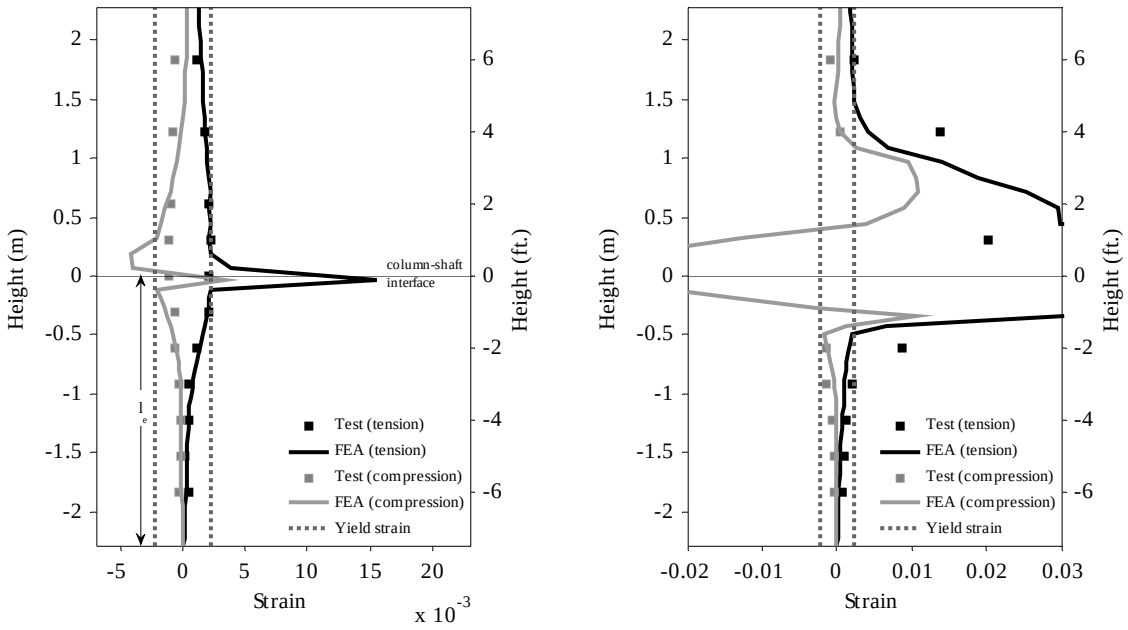

(a) Peak displacements of Cycle 4 (b) Peak displacements of Cycle 13

Figure 8.7: Strains in the column longitudinal bar at the north face of Specimen 1

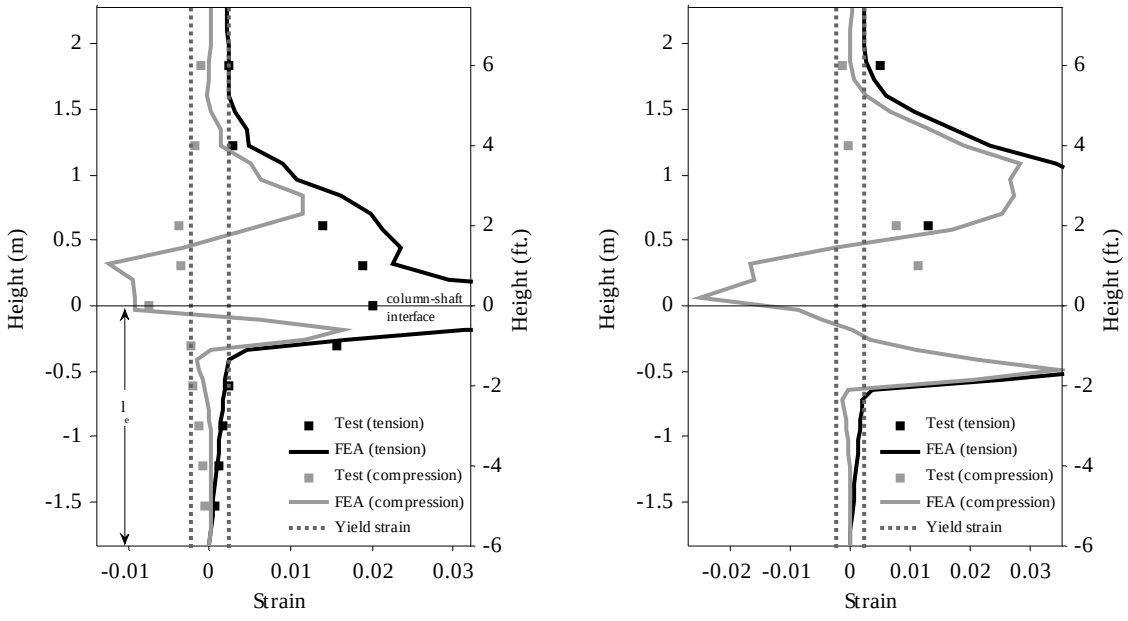

(a) Peak displacements of Cycle 9 (b) Peak displacements of Cycle 17

Figure 8.8: Strains in the column longitudinal bar at the north face of Specimen 2

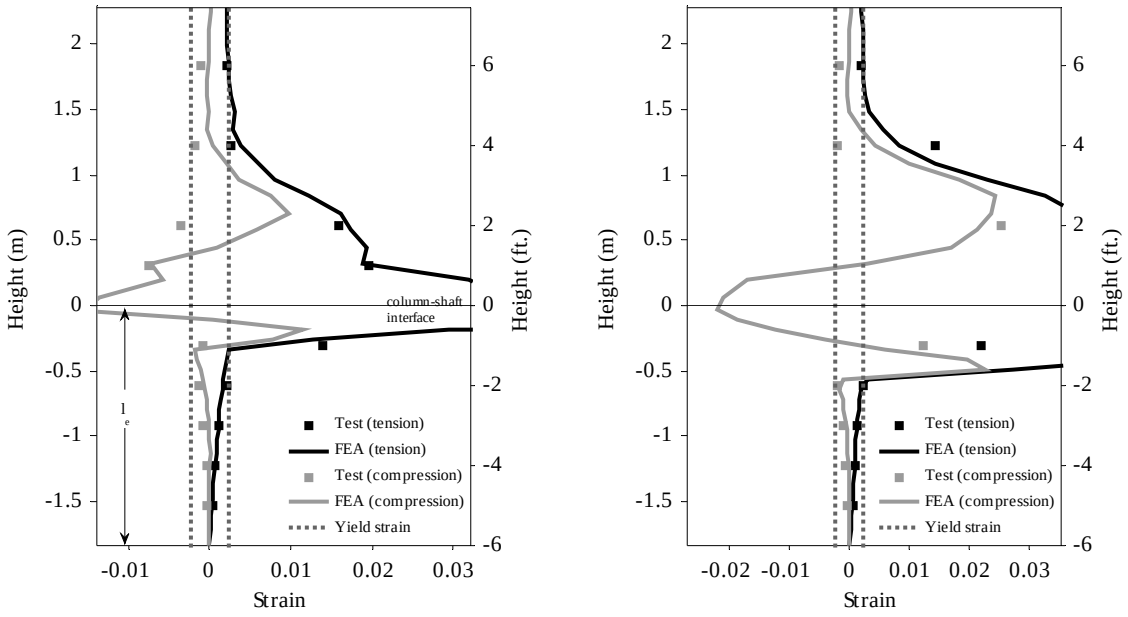

(a) Peak displacements of Cycle 9 (b) Peak displacements of Cycle 15

Figure 8.9: Strains in the column longitudinal bar at the north face of Specimen 3

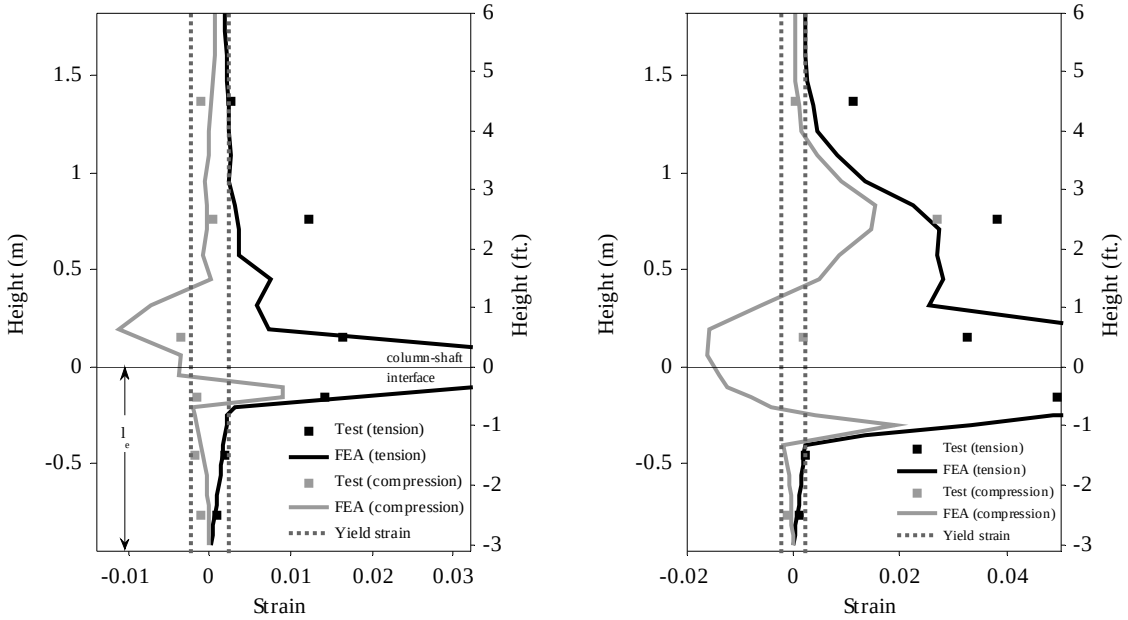

(a) Peak displacements of Cycle 7 (b) Peak displacements of Cycle 13

Figure 8.10: Strains in the column longitudinal bar at the north face of Specimen 4

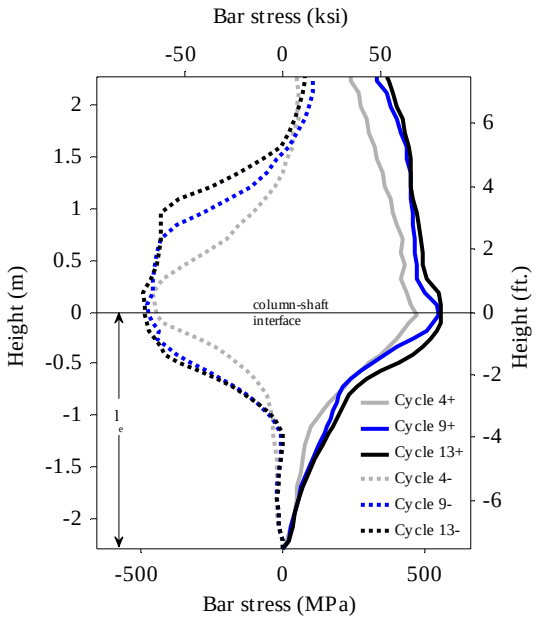

(a) Specimen 1

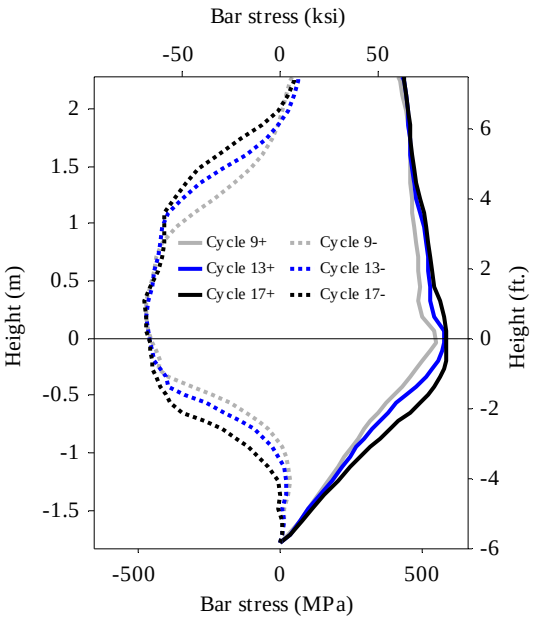

(b) Specimen 2

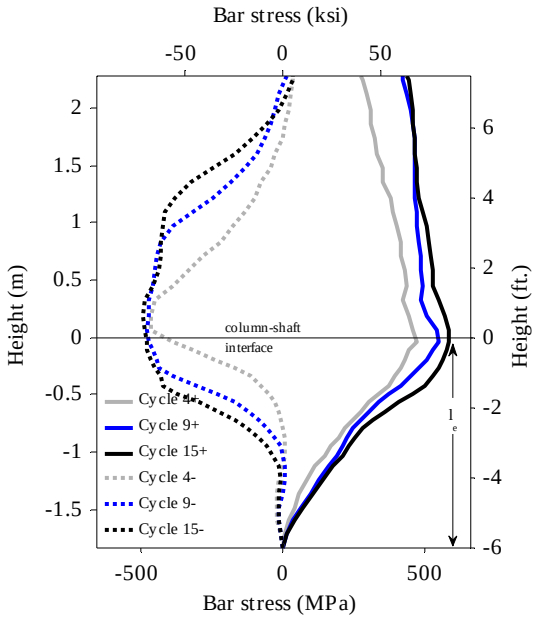

(c) Specimen 3

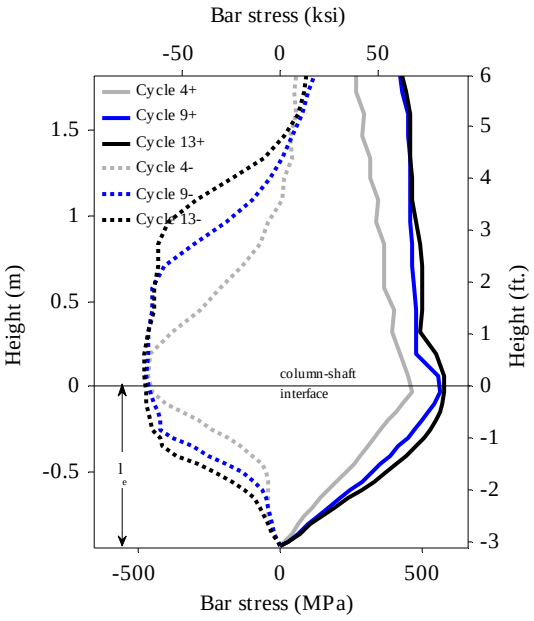

(d) Specimen 4

Figure 8.11: Axial stress variation along the column longitudinal bars at the north face of the specimens

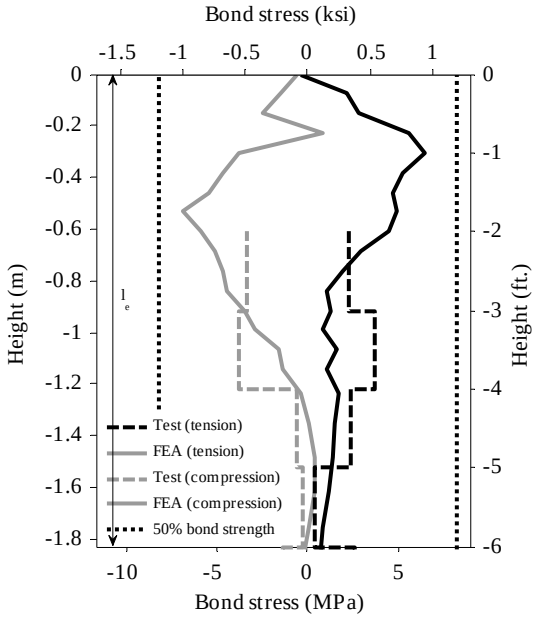

(a) Peak displacements of Cycle 9

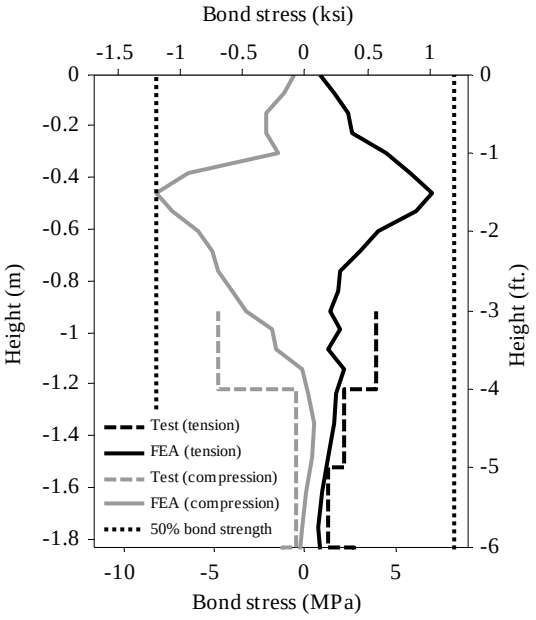

(b) Peak displacements of Cycle 13

Figure 8.12: Bond stresses along the column longitudinal bar at the north face of Specimen 1

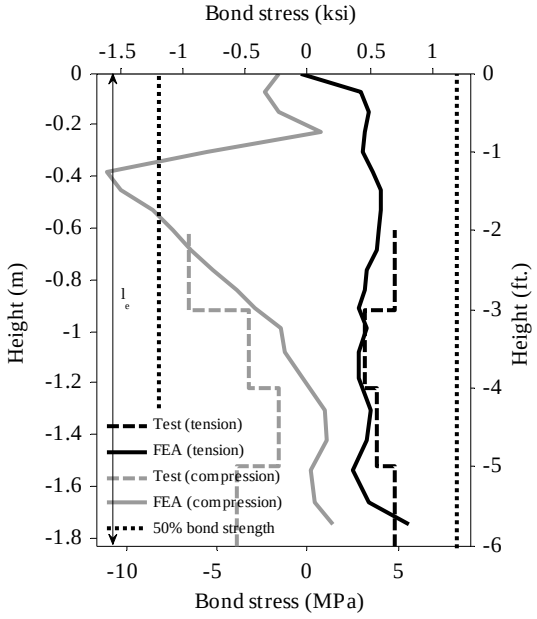

(a) Peak displacements of Cycle 9

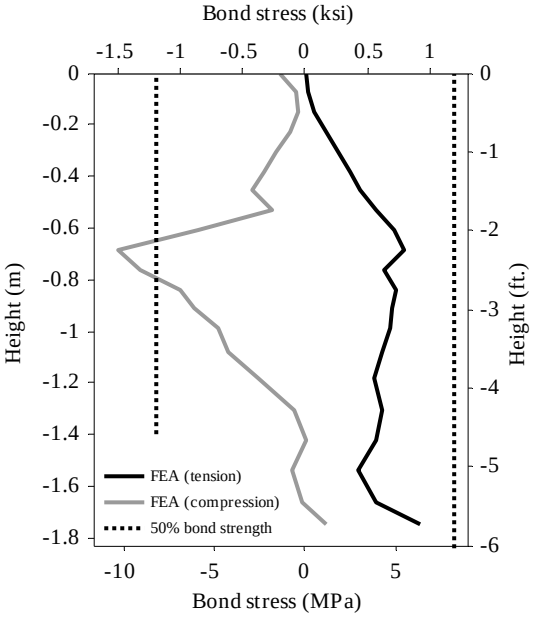

(b) Peak displacements of Cycle 17

Figure 8.13: Bond stresses along the column longitudinal bar at the north face of Specimen 2

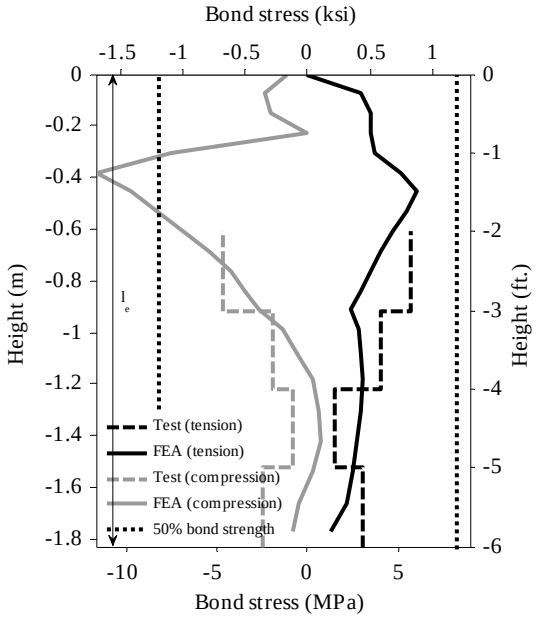

(a) Peak displacements of Cycle 9

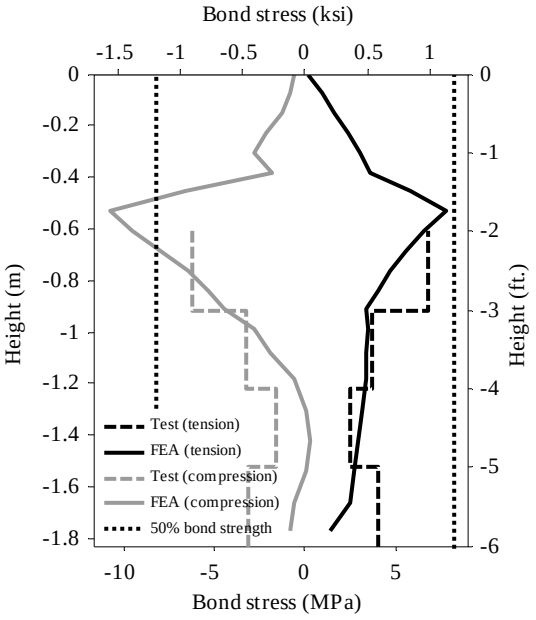

(b) Peak displacements of Cycle 15

Figure 8.14: Bond stresses along the column longitudinal bar at the north face of Specimen 3

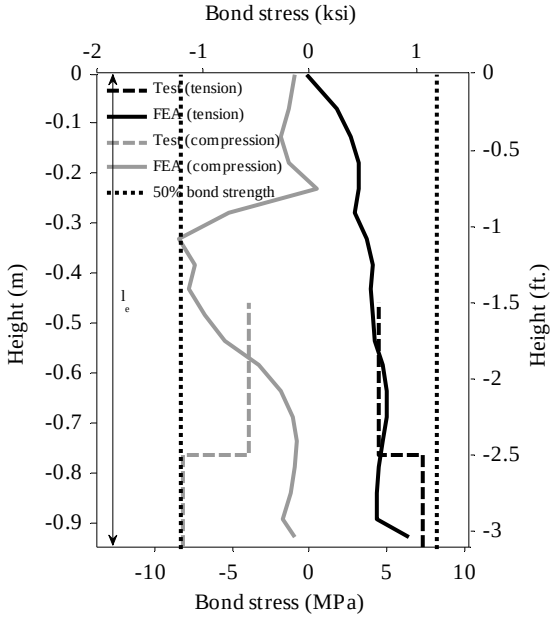

(a) Peak displacements of Cycle 9

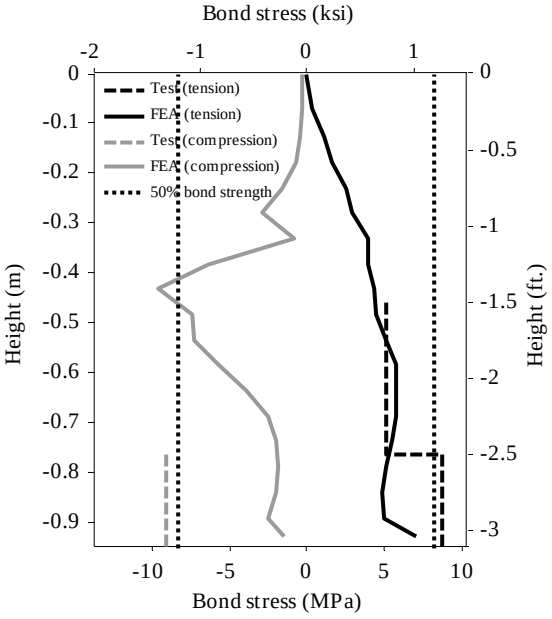

(b) Peak displacements of Cycle 13

Figure 8.15: Bond stresses along the column longitudinal bar at the north face of Specimen 4

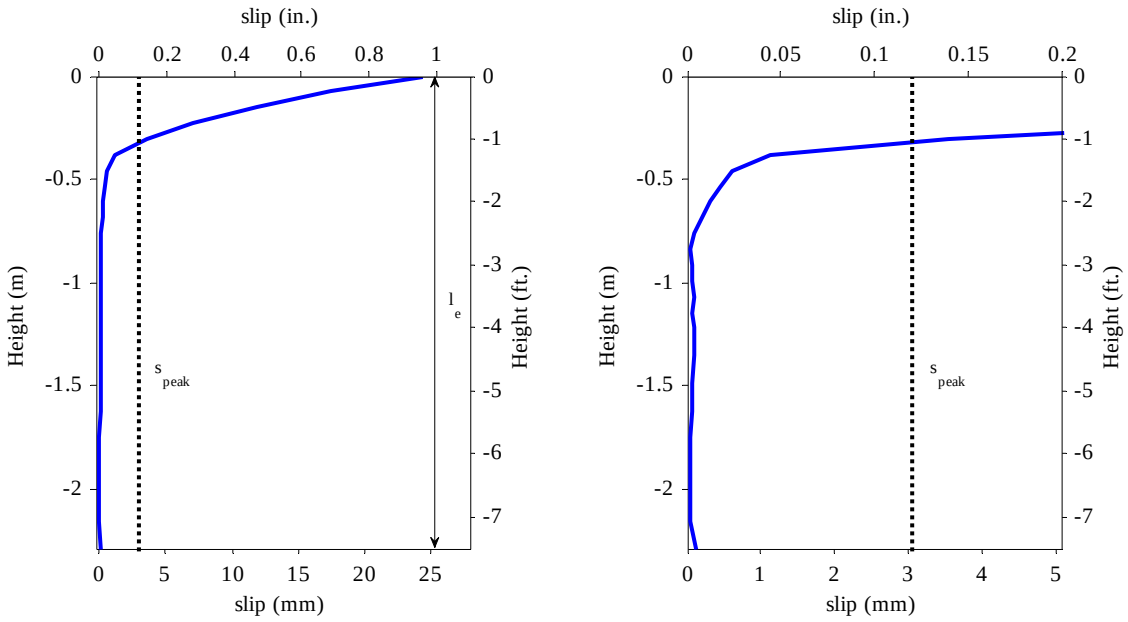

(a) Peak displacement of Cycle 13 (b) Close-up view of (a)

Figure 8.16: Bar slip along the column longitudinal bar at the north face of Specimen 1

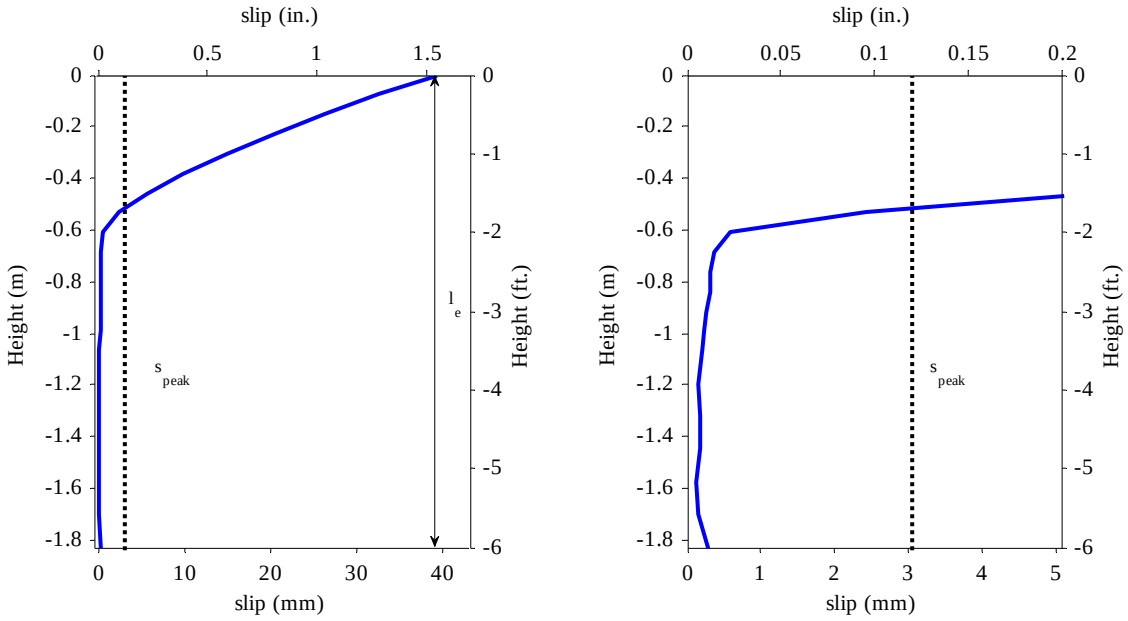

(a) Peak displacement of Cycle 17 (b) Close-up view of (a)

Figure 8.17: Bar slip along the column longitudinal bar at the north face of Specimen 2

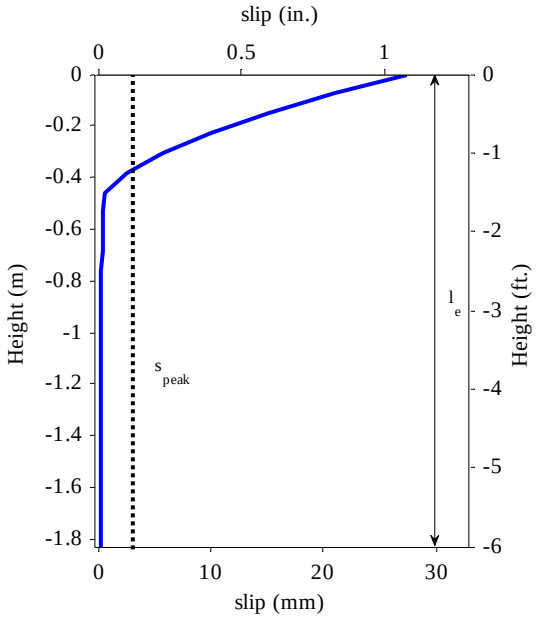

(a) Peak displacement of Cycle 15

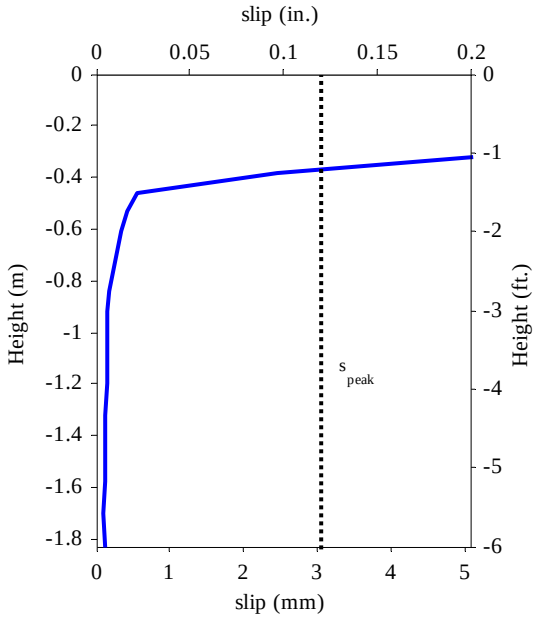

(b) Close-up view of (a)

Figure 8.18: Bar slip along the column longitudinal bar at the north face of Specimen 3

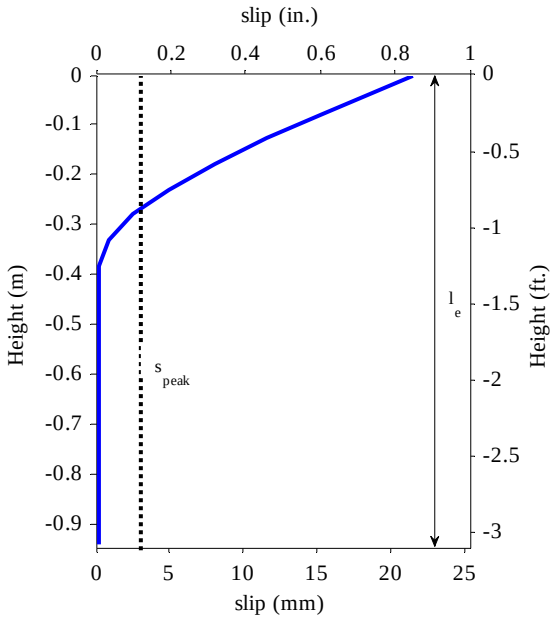

(a) Peak displacement of Cycle 13

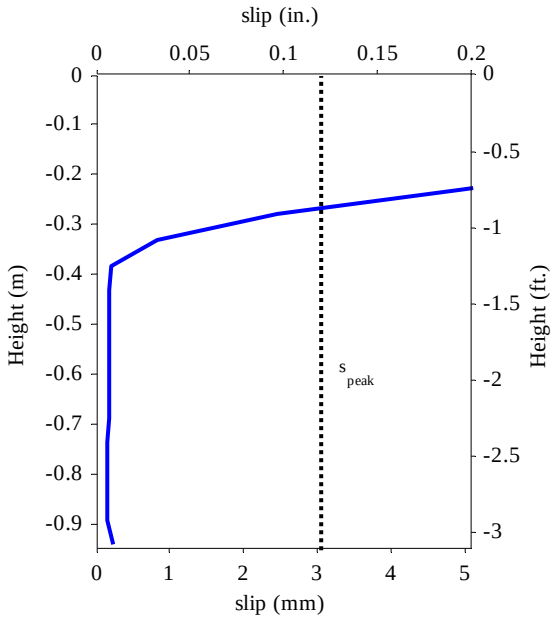

(b) Close-up view of (a)

Figure 8.19: Bar slip along the column longitudinal bar at the north face of Specimen 4

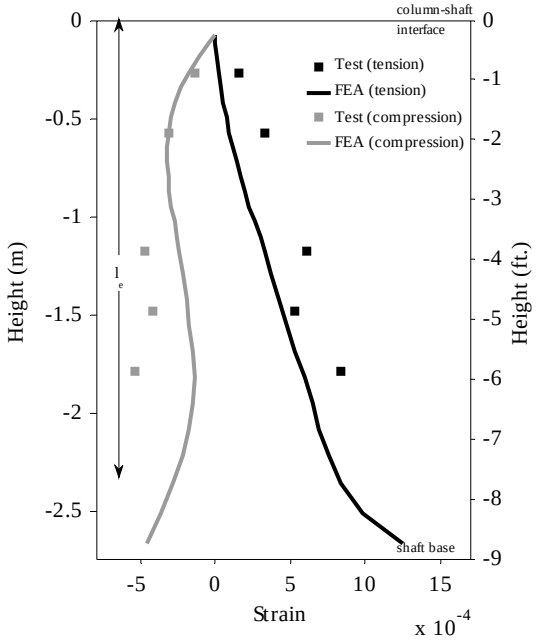

(a) Peak displacements of Cycle 4

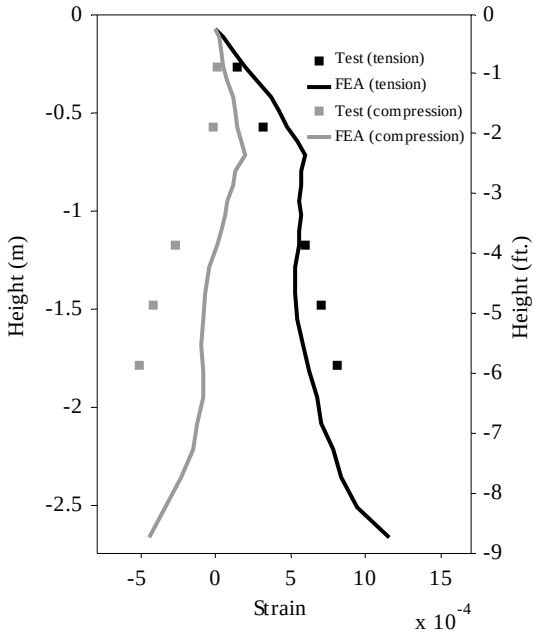

(b) Peak displacements of Cycle 13

Figure 8.20: Strains in the longitudinal shaft bar at the north face of Specimen 1

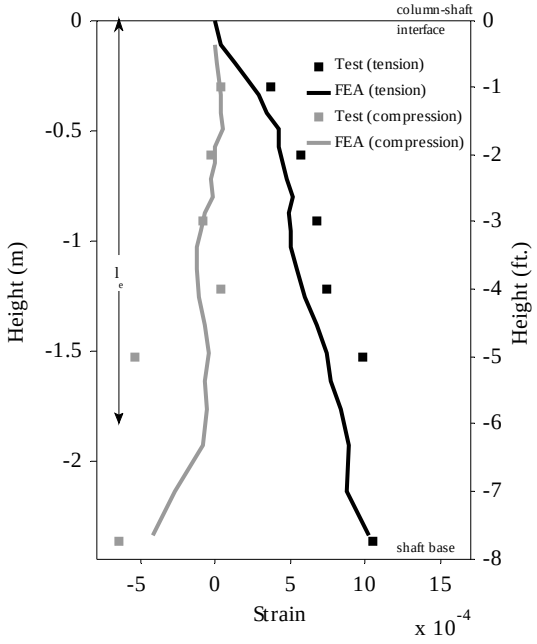

(a) Peak displacements of Cycle 9

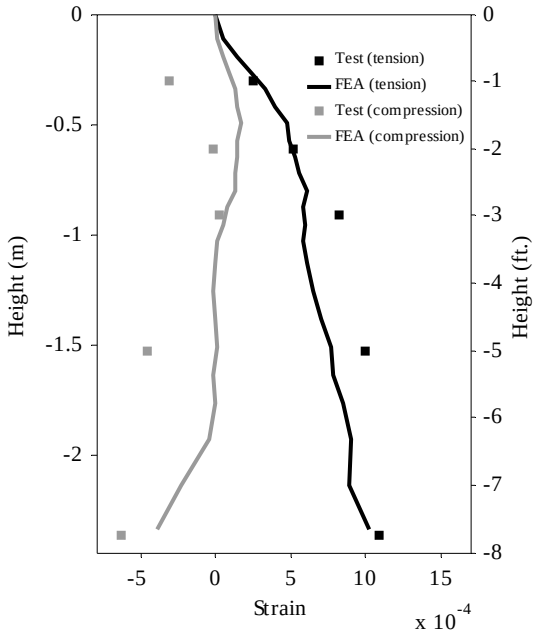

(b) Peak displacements of Cycle 17

Figure 8.21: Strains in the longitudinal shaft bar at the north face of Specimen 2

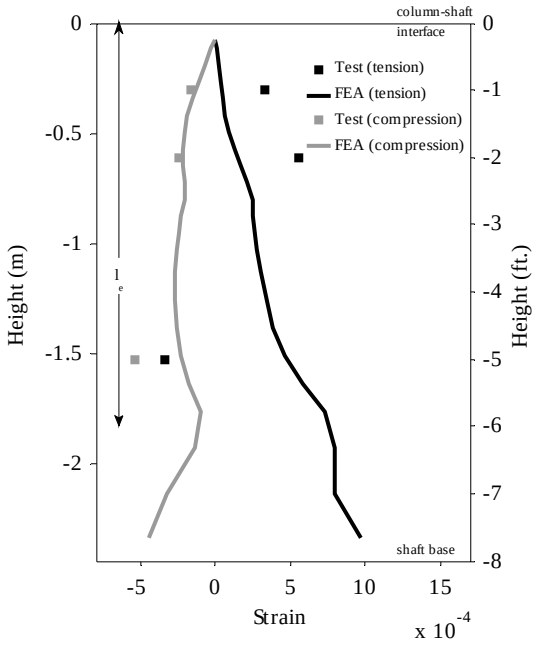

(a) Peak displacements of Cycle 9

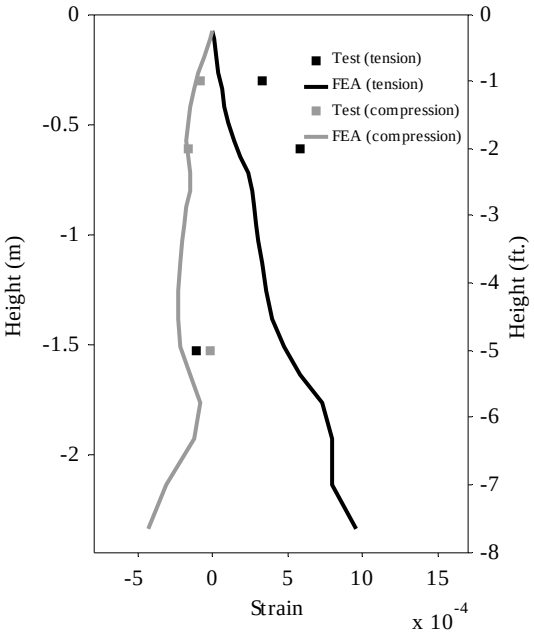

(b) Peak displacements of Cycle 15

Figure 8.22: Strains in the longitudinal shaft bar at the north face of Specimen 3

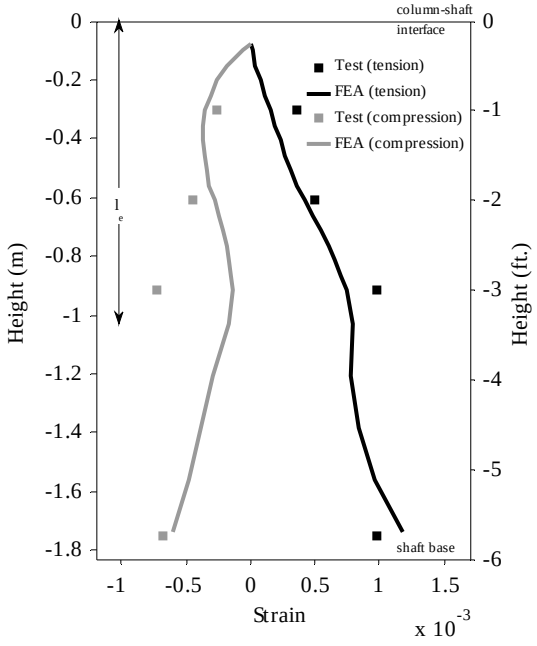

(a) Peak displacements of Cycle 4

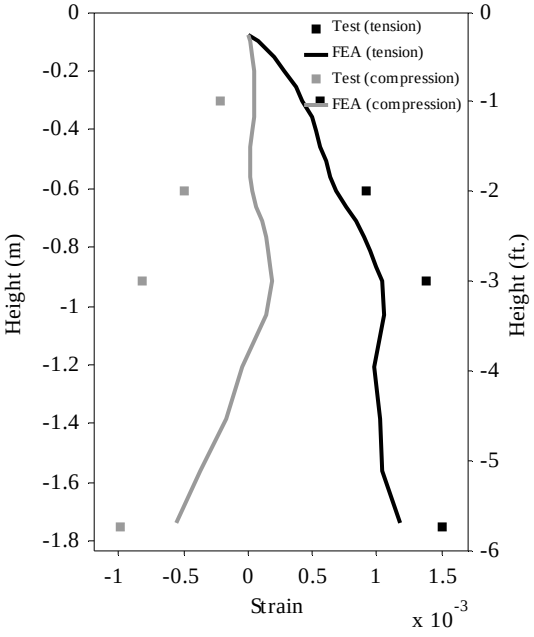

(b) Peak displacements of Cycle 13

Figure 8.23: Strains in the longitudinal shaft bar at the north face of Specimen 4

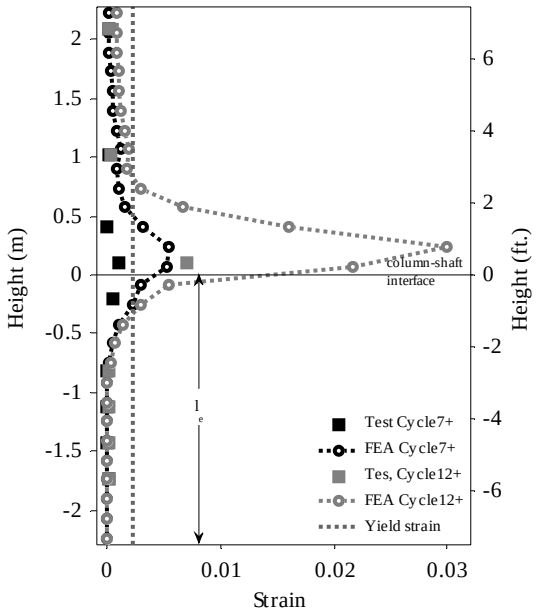

(a) South face of Specimen 1

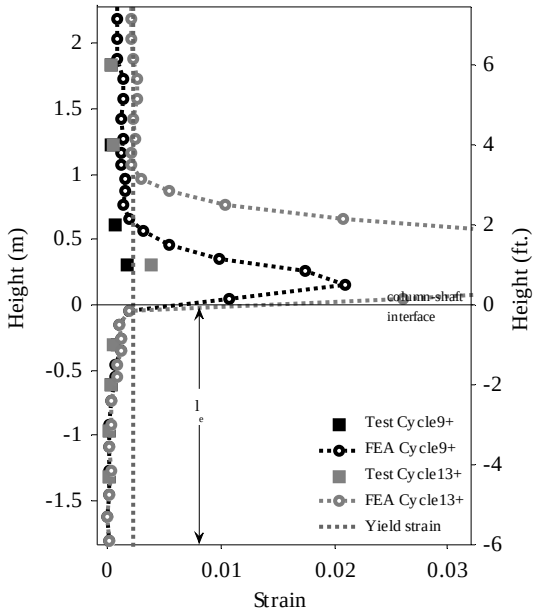

(b) South face of Specimen 2

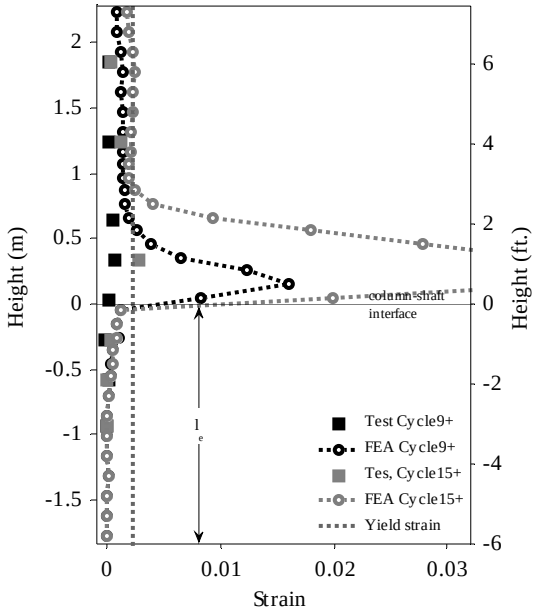

(c) South face of Specimen 3

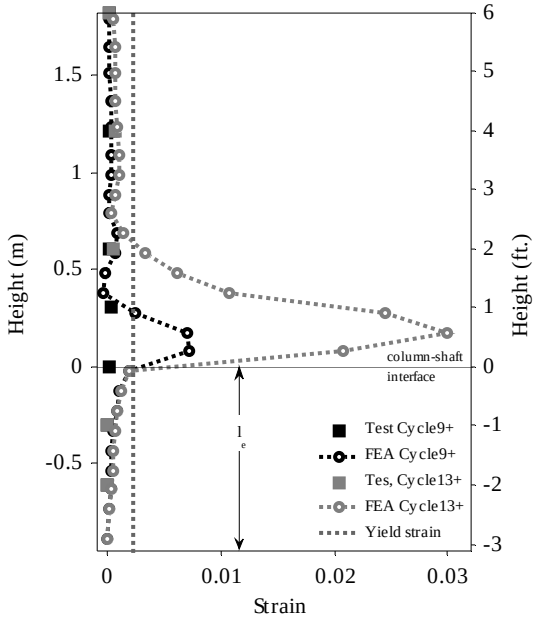

(d) South face of Specimen 4

Figure 8.24: Strains in the column hoops

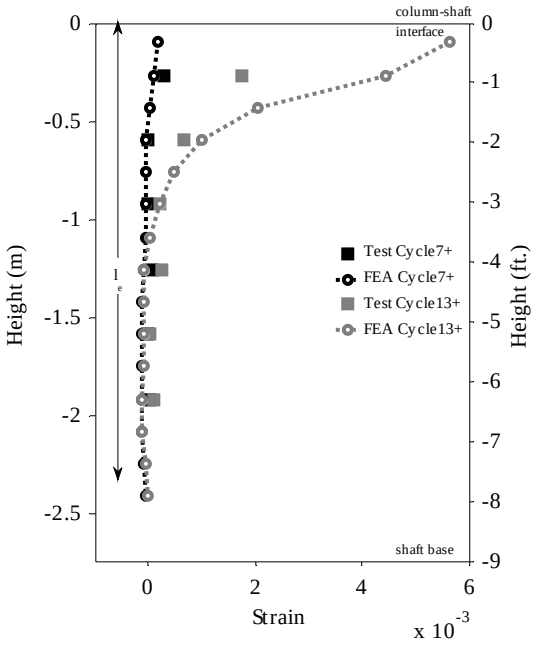

(a) Shaft hoops

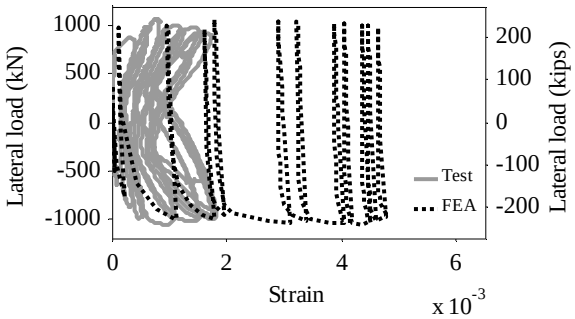

(b) Hoop at -0.3 m (-1 ft)

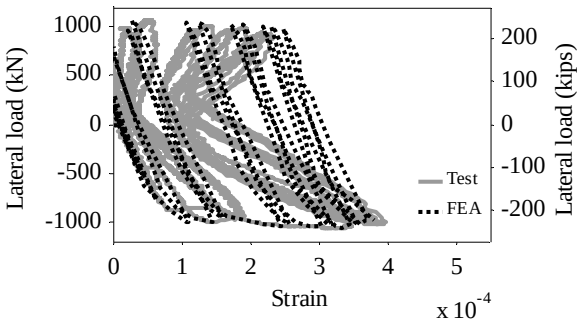

(c) Hoop at -0.91 m (-3 ft)

Figure 8.25: Strains in shaft hoops at the north face of Specimen 1

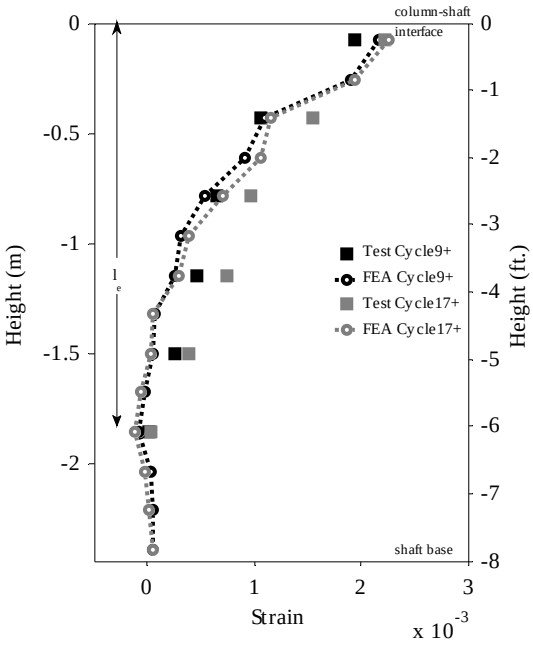

(a) Shaft hoops (north face)

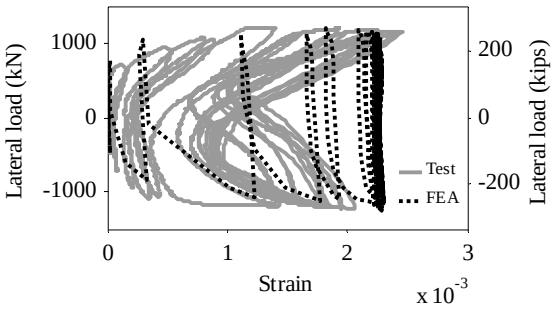

(b) Hoop at -76 mm (-3 in.) (north face)

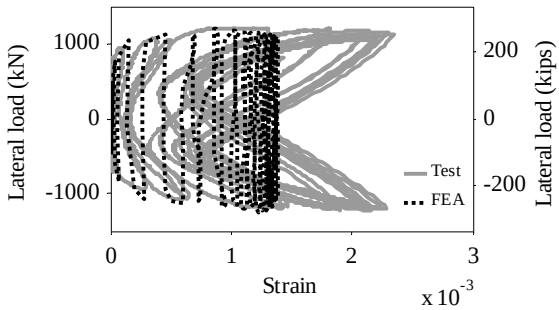

(c) Hoop at -76 mm (-3 in.) (west face)

Figure 8.26: Strains in shaft hoops in Specimen 2

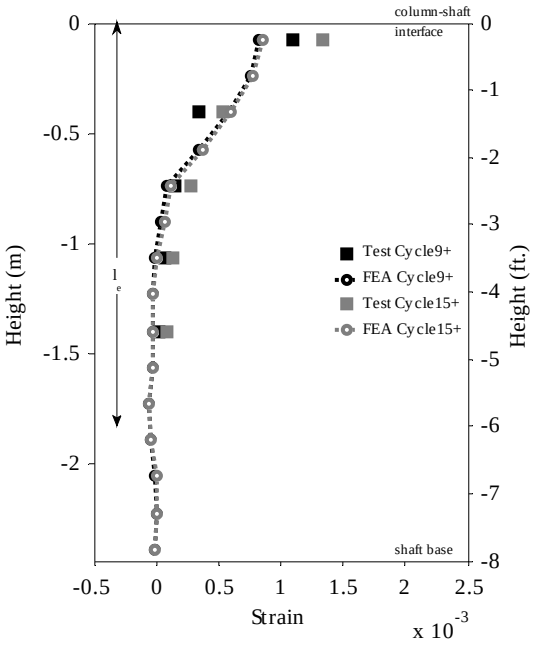

(a) Shaft hoops (north face)

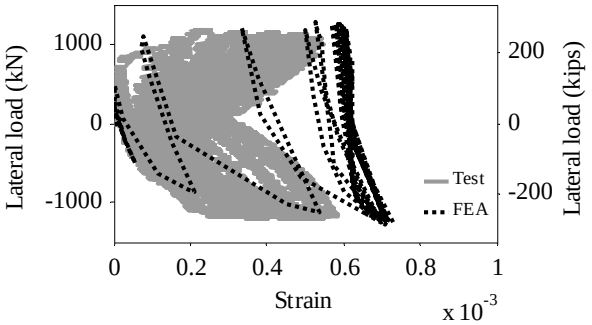

(b) Hoop at -76 mm (-3 in.) (north face)

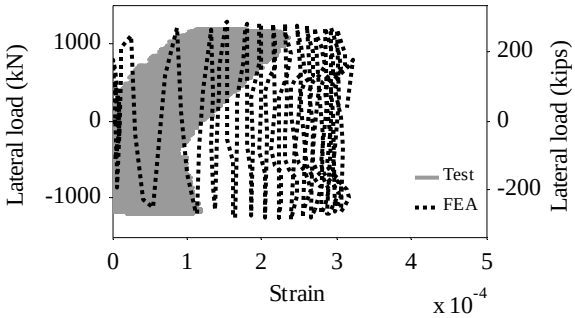

(c) Hoop at -76 mm (-3 in.) (west face)

Figure 8.27: Strains in shaft hoops in Specimen 3

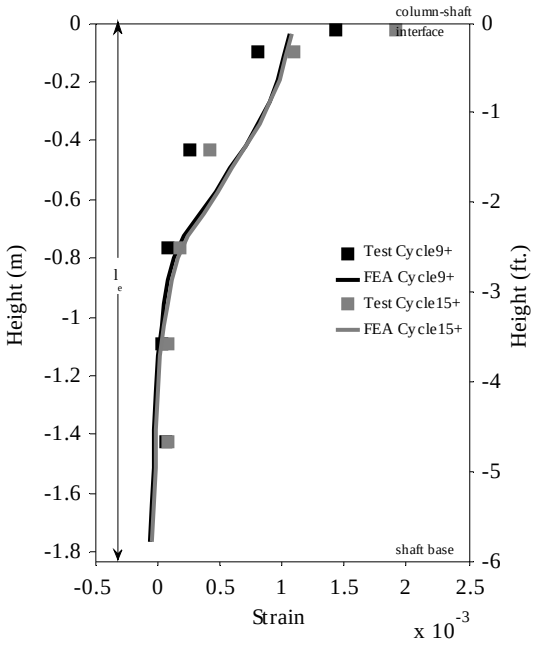

(a) Hoop strain (north face)

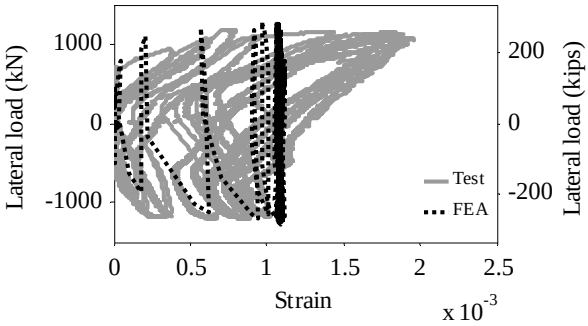

(b) Strain on the north face of hoop at -25 mm (-1 in.)

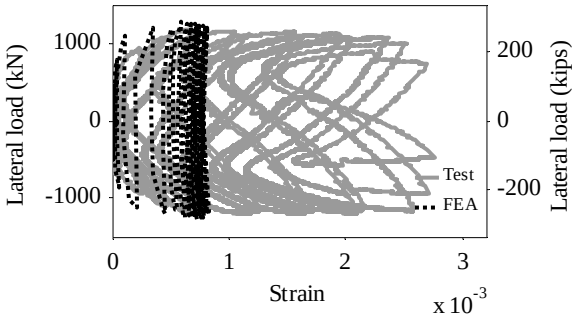

(c) Strain on the west face of hoop at -25 mm (-1 in.)

Figure 8.28: Hoop strains in steel casing in Specimen 3

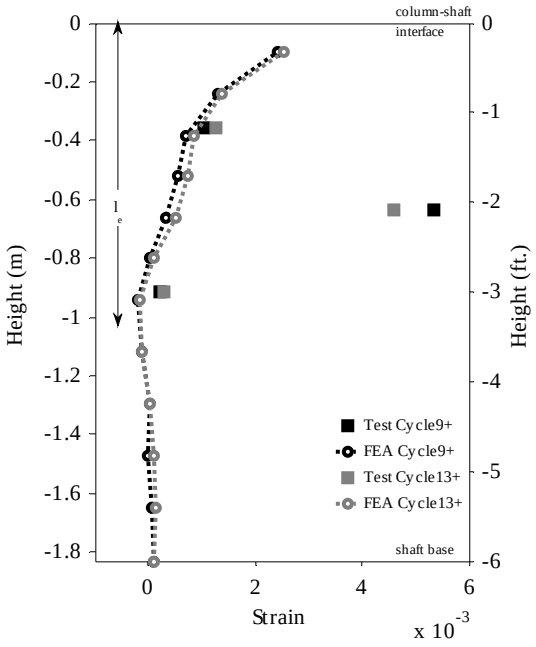

(a) Shaft hoops

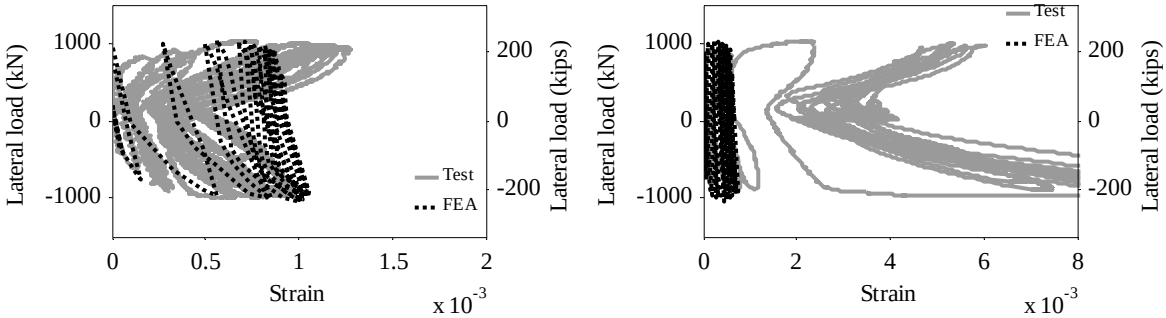

(b) Hoop at -0.36 m (-1 ft-2 in.)

(c) Hoop at -0.64 m (-2 ft-1 in.)

Figure 8.29: Strains in shaft hoops in Specimen 4 (north face)

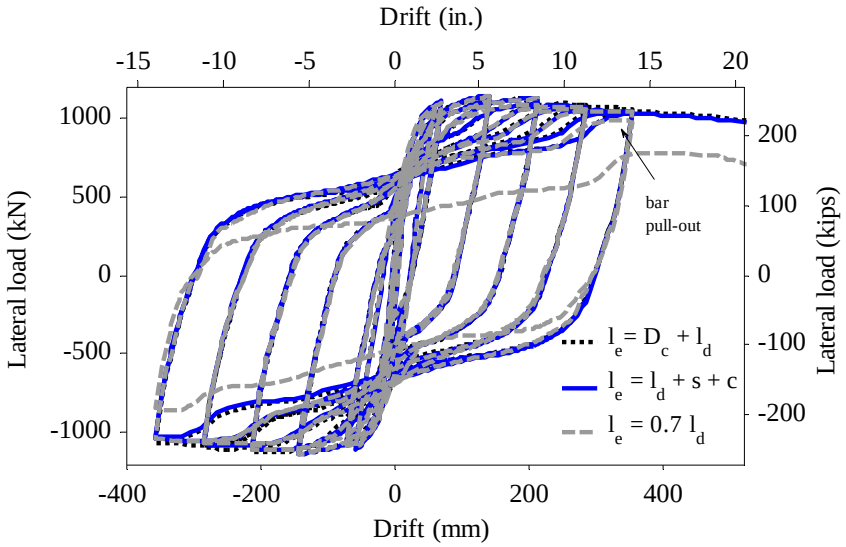

Figure 8.30: Lateral load vs. drift curves for Models *4-6-11-x*

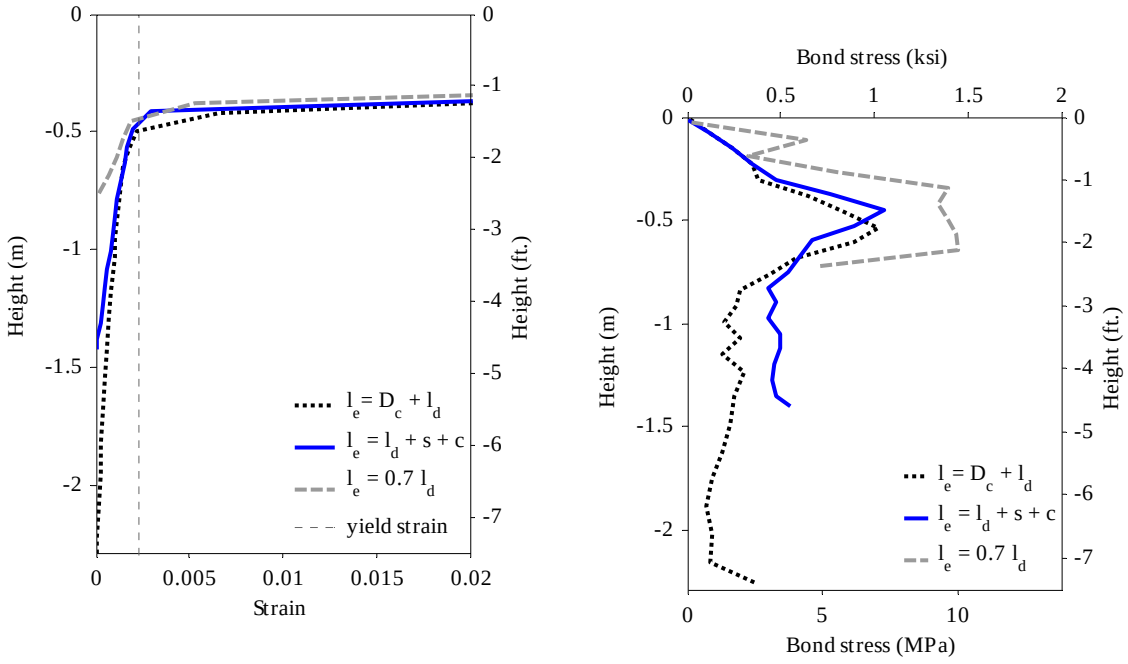

(a) Axial strain (b) Bond stress

Figure 8.31: Results for north column longitudinal bar in Models *4-6-11-x* at the peak displacement of Cycle 13

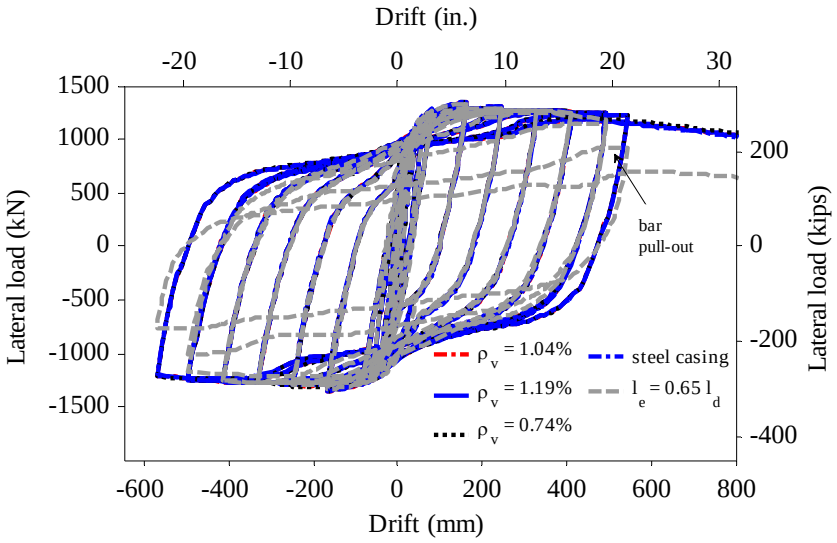

Figure 8.32: Lateral load vs. drift curves for Models *4-6-14-x*

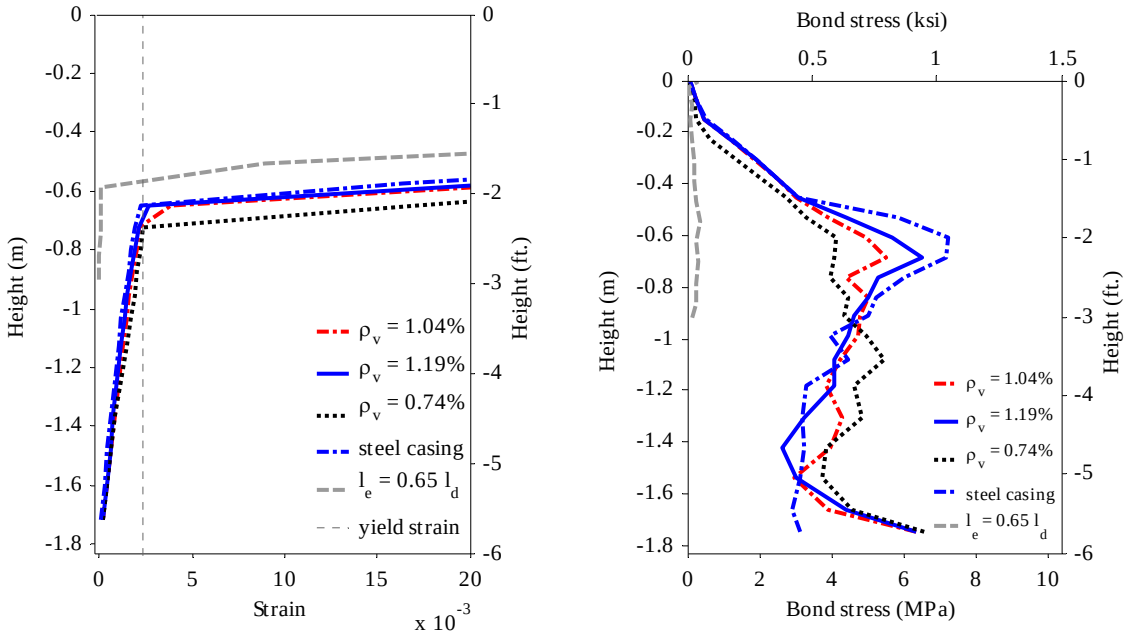

(a) Axial strain (b) Bond stress

Figure 8.33: Results for north column longitudinal bar in Models *4-6-14-x* at the peak displacement of Cycle 17

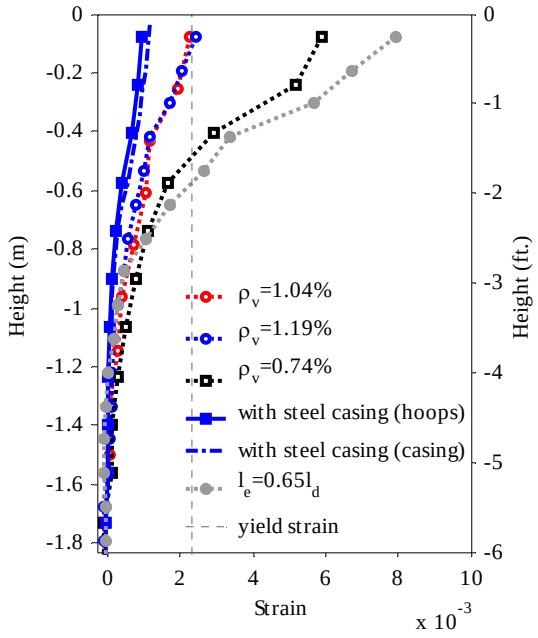

Figure 8.34: Strains in shaft hoops and casing in Models *4-6-14-x* at the peak displacement of Cycle 17

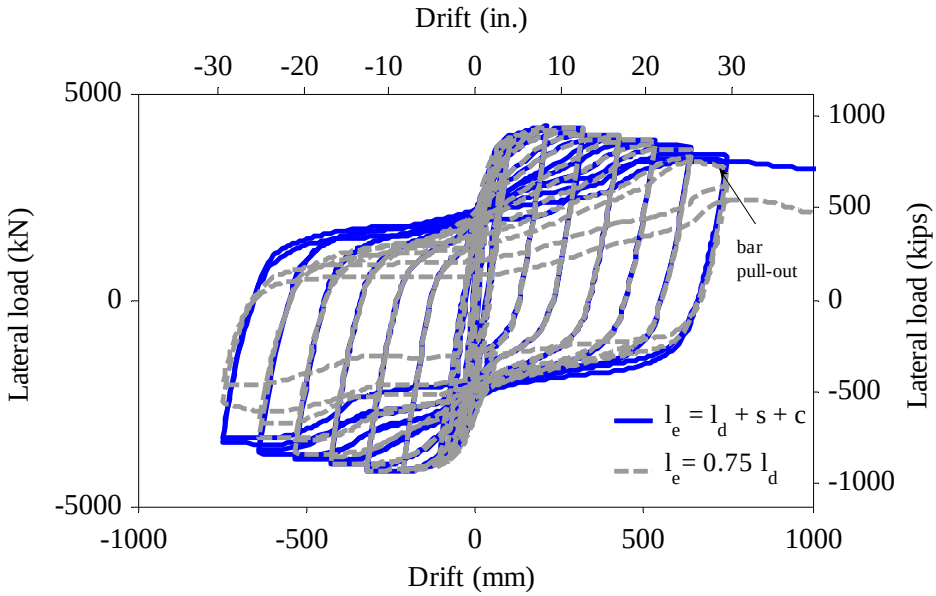

Figure 8.35: Lateral load vs. drift curves for Models *8-10-14-x*

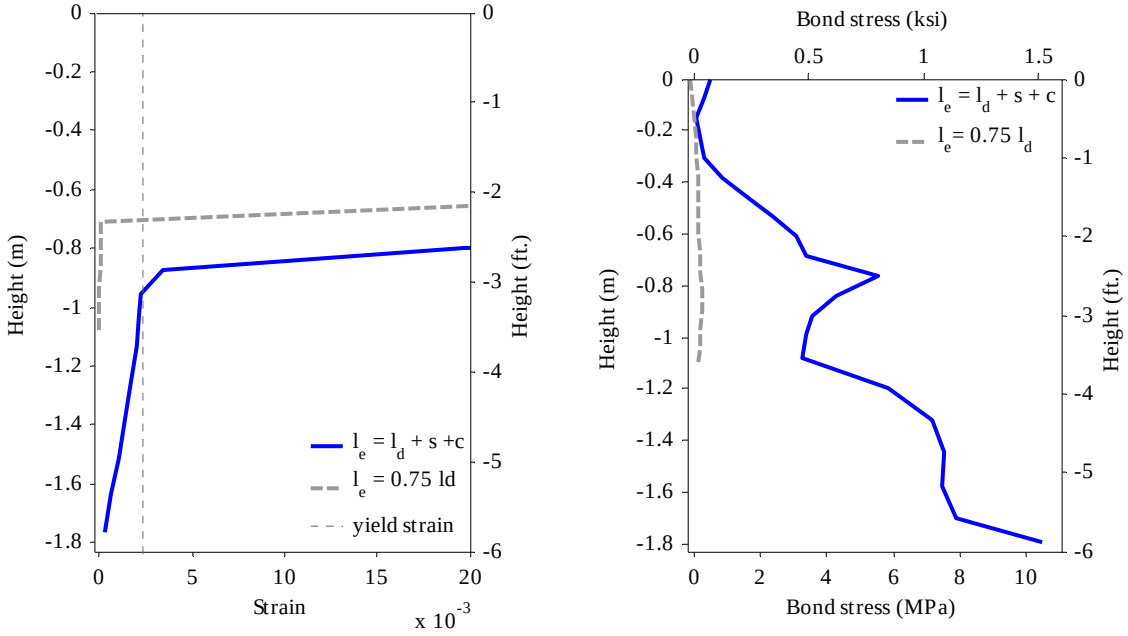

(a) Axial strain (b) Bond stress

Figure 8.36: Results for north column longitudinal bar in Models *8-10-14-x* at the peak displacement of Cycle 17

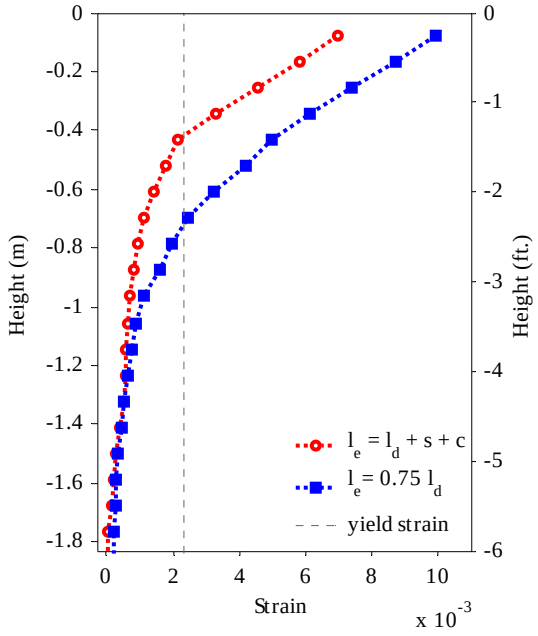

Figure 8.37: Strains in shaft hoops in Models *8-10-14-x* at the peak displacement of Cycle 17

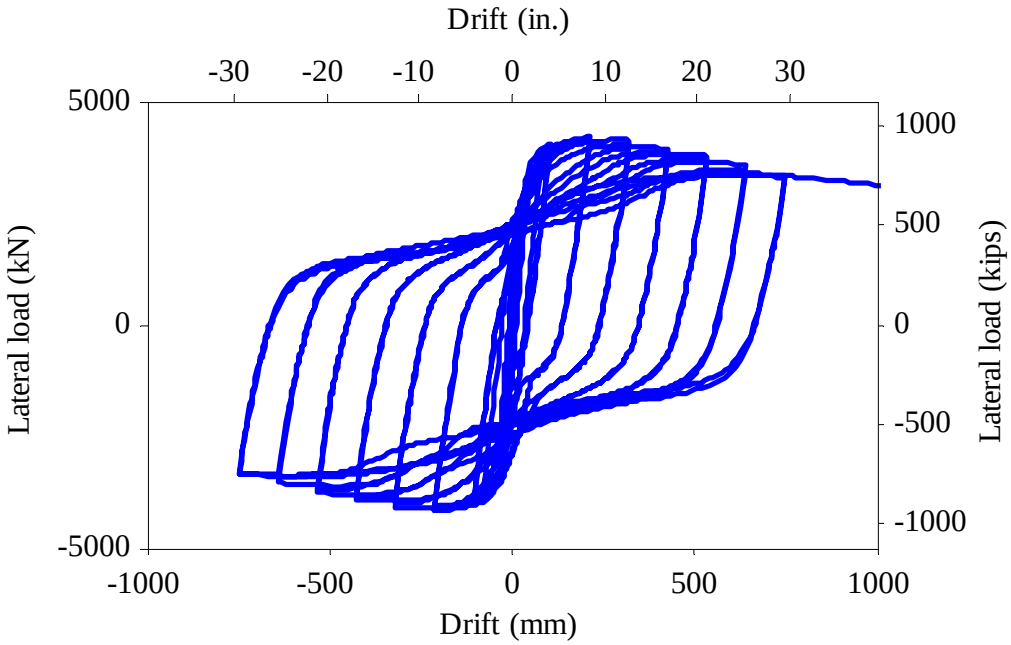

Figure 8.38: Lateral load vs. drift curve for Model *8-12-14*

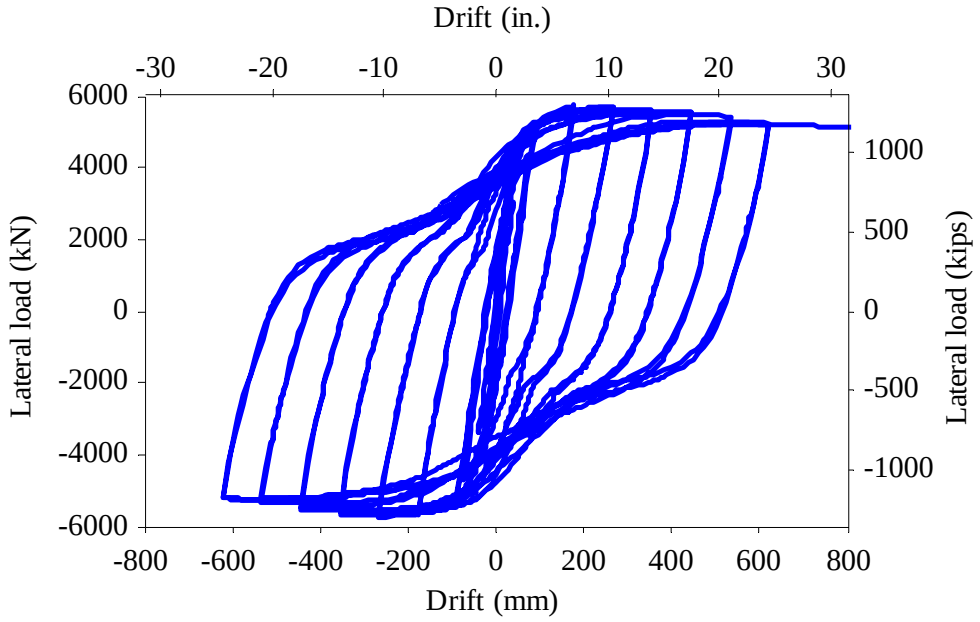

Figure 8.39: Lateral load vs. drift curve for Model *8-12-18*

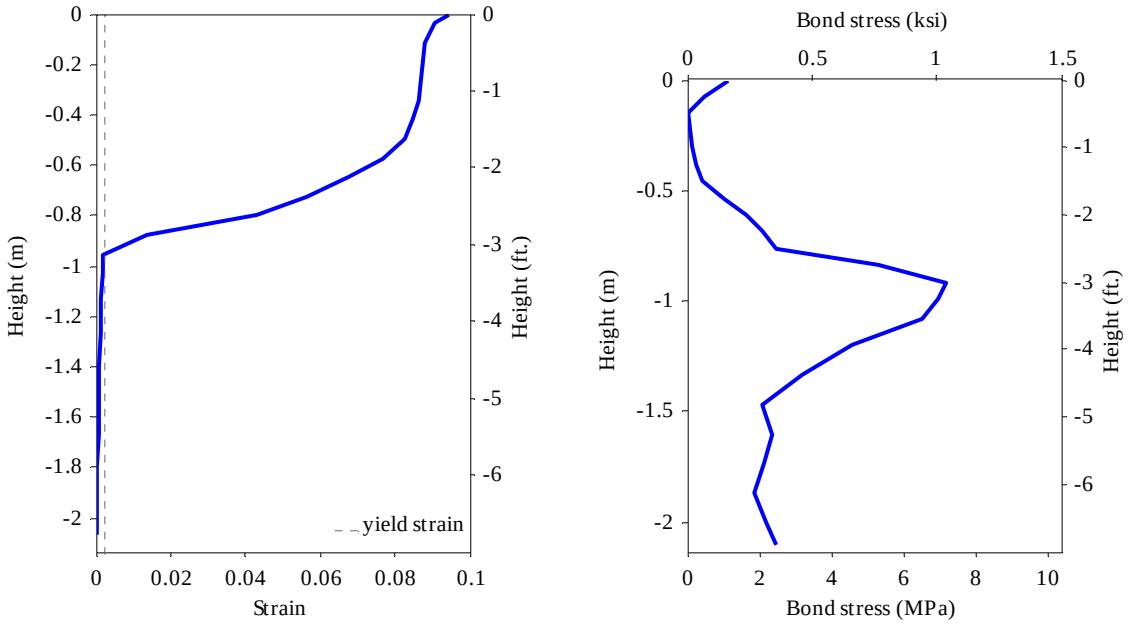

(a) Axial strain (b) Bond stress

Figure 8.40: Results for north column longitudinal bar in Model *8-12-14* at the peak displacement of Cycle 17

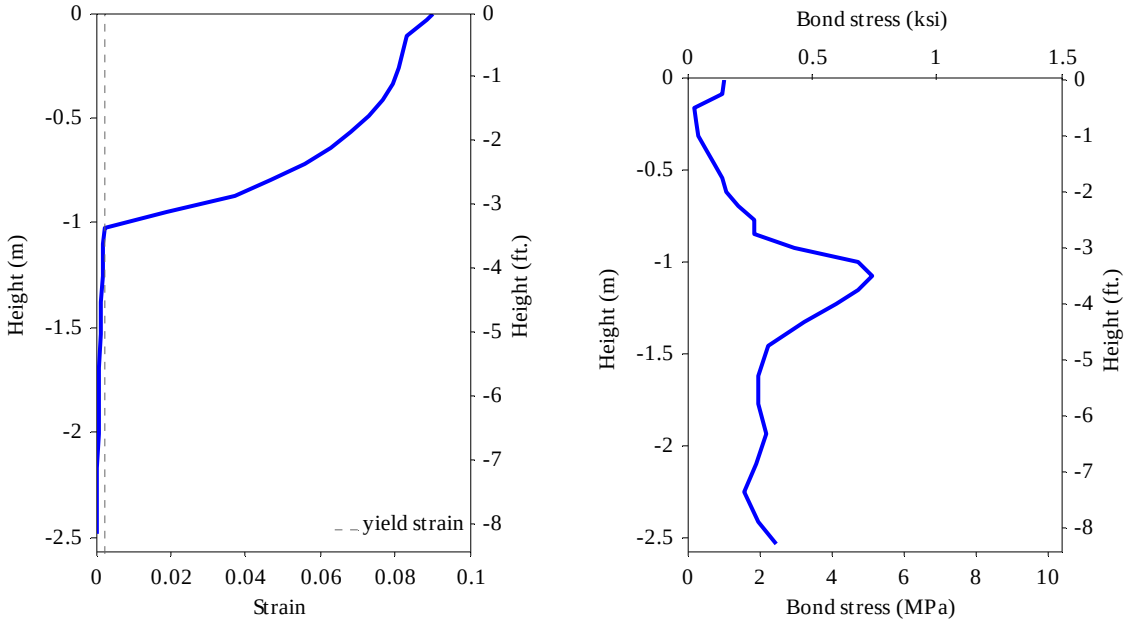

(a) Axial strain (b) Bond stress

Figure 8.41: Results for north column longitudinal bar in in Model *8-12-18* at the peak displacement of Cycle 17

CHAPTER 9

DESIGN RECOMMENDATIONS

This chapter presents new design recommendations on the minimum embedment length required for column reinforcement extended into a Type II shaft, and the transverse reinforcement required for the bar anchorage region of the shaft. These recommendations are based on the results of the experimental and analytical studies presented in the previous chapters of this report. The new recommendations are compared to those proposed by McLean and Smith (1997) and to the specifications in the Caltrans Seismic Design Criteria (Caltrans 2010).

9.1 Minimum required embedment length

Results from the four column-shaft assembly tests (presented in Chapter 7) and the numerical parametric study (in Chapter 8) have indicated that an embedment length of $l_d + s + c$ is adequate to develop the tensile strength of the longitudinal reinforcement in a bridge column, with l_d being the development length in tension according to the AASHTO LRFD Bridge Design Specifications and AASHTO LRFD Seismic Bridge Design Specifications, s the center-to-center distance between the column and shaft reinforcing cages, and c the thickness of the top concrete cover in the shaft. Nevertheless, these results do not account for the uncertainties in material properties and construction quality that could be encountered in an actual bridge. The reliability analysis presented in Chapter 5 has shown that the development length in tension, l_d, according to the AASHTO LRFD Specifications for large-diameter bars has a sufficient reliability

level to develop the yield capacity of a bar but is not sufficiently reliable to develop the tensile strength of a bar when uncertainties in material properties and construction quality are considered. In view of this, the design requirement proposed here adopts an l_d that takes into consideration of these uncertainties based on the analysis presented in Chapter 5.

However, for a column with a very large cross-section dimension, $l_d + s + c$ can result in an embedment length less than the cross-sectional dimension of the column. This may not be desirable. As shown in Figure 9.1, two types of column anchorage failure are possible in an enlarged shaft. One is the bar pull-out, and the other is the column pull-out due to concrete damage induced by a plying action when the confined core of the column rocks back and forth in the shaft. Both mechanisms could contribute to the anchorage failure of a column, as shown in Figure 1.1. The plying action introduces horizontal forces that can be relatively large near the top and bottom of the anchorage region as shown in Figure 9.1b. These horizontal forces are resisted by the surrounding concrete and the transverse reinforcement in the shaft. There is evidence that this plying action occurred in the column-shaft assembly tests, but it has not been well captured by the finite element models due to the limitations of the concrete model. In the tests, the strains in the shaft hoops near the top were much higher than those in the hoops below. In particular, the hoop strain near the top in the steel casing of Specimen 3 exceeded the yield level. This was not expected according to the design. However, the plying action in these tests did not have major detrimental effects.

The force demand on the shaft due to the plying action depends on the moment capacity of the column and the embedment length of the confined core in the shaft. The longer the embedment length is, the lower will be the force demand for a given moment from the column. By considering the fact that the moment capacity of a circular column for a given steel ratio is proportional to the cube of the column diameter and that the quantity of the transverse reinforcement in a shaft should be more or less proportional to the quantity of the longitudinal reinforcement in the column, the minimum embedment length required to resist the plying forces can be considered proportional to the column diameter. The test specimens considered in this study had embedment lengths varying

from 0.77 to 1.87 times the column diameter, and two of the columns had a longitudinal steel ratio of 2.55%, which is considered relatively high for a bridge column. Since the anchorage of these specimens performed satisfactorily in the tests, it seems appropriate to expect that an embedment length greater than one times the diameter or the larger cross-sectional dimension of the column will prevent anchorage failure due to the plying action provided that the amount of transverse reinforcement recommended in this study, as presented in the next section, is used.

Based on the above considerations, it is recommended that the minimum embedment length of column reinforcement extended into a Type II shaft be given by the following formula.

$$l_e = l_d + \frac{D_s - D_{c,\min}}{2} \tag{9.1a}$$

with

$$l_e \geq D_{c,\max} \tag{9.1b}$$

in which the term $(D_s - D_{c,\min})/2$ replaces $s + c$ for the sake of simplicity and to be applicable to non-circular columns as shown in Figure 9.2, $D_{c,\min}$ and $D_{c,\max}$ are the smaller and the larger of the cross-sectional dimensions of the column, respectively, D_s is the shaft diameter, and l_d is the development length in tension for the column longitudinal bars. Based on the reliability analysis presented in Chapter 5, the development length is to be determined by the following formula.

$$l_d = 1.4 \frac{d_b f_y}{f_c'^{3/4}} \quad \text{(in MPa)} \tag{9.2a}$$

$$l_d = 2.27 \frac{d_b f_y}{f_c'^{3/4}} \quad \text{(in ksi)} \tag{9.2b}$$

in which d_b is the diameter of the developed bars, f_y is the specified yield strength of the bars, and f_c' the specified compressive strength of the concrete in the shaft. For bundled bars, l_d shall be increased by 20 percent for a two-bar bundle and 50 percent for a three-bar bundle, according to the AASHTO LRFD Specifications. Equation 9.2 is derived from Equation 5.11, which gives the minimum embedment length required to

reliably develop the reduced ultimate tensile capacity of a bar at the flexural limit state of the column under the best confined situation considered in Section 5.11.2.1.3 of the AASHTO LRFD Specifications. As discussed in Chapter 5, the reduced ultimate tensile capacity of a bar (developed at the flexural limit state of a column) is 1.35 times the yield strength, and Equation 5.11 results in a reliability index of 1.75 considering various uncertainties. By considering the fact that the maximum center-to-center spacing of the hoops is 102 mm (4 in.) for the best confined situation and that the minimum clear spacing of reinforcement in a pile is 127 mm (5 in.) according to Section 5.13.4.5.2 of the AASHTO LRFD Specifications, the minimum length given by Equation 5.11 is divided by a modification factor of 0.75 to obtain the expression in Equation 9.2. Even though the above recommendation is based on the experimental and numerical studies conducted on large-diameter bars. It should be valid for smaller bar sizes based on the fact under well-confined situations like that in a Type II shaft, the bar size has little influence on the bond strength and cyclic bond-slip behavior.

Table 9.1 presents a comparison of the embedment lengths calculated with Equation 9.1, the formula proposed by McLean and Smith (1997), which is $1.7l_d + s$, and the specification in the Caltrans Seismic Design Criteria (2010), which are $D_{c,\max} + l_d$ and $D_{c,\max} + 2l_d$ with a staggered termination. Hence, the embedment length of the column cage in the shaft in Caltrans SDC is $D_{c,\max} + 2l_d$. In the formula proposed by McLean and Smith (1997), l_d is determined according to the AASHTO LRFD Specifications. In the Caltrans specification, l_d is determined by multiplying the basic development length l_{db} according to AASHTO (but with the expected yield strength rather than the specified) by a compounded modification factor of 0.9 for epoxy-coated bars or 0.6 for non epoxy-coated bars. Table 9.1 includes the specimens tested in this study, column-shaft systems in an actual bridge, which is the I5-I805 Connector in San Diego, and other examples. As one can observe from Table 9.1, McLean and Smith's formula leads to embedment lengths 20 to 40% shorter than those according to the Caltrans specification, while the proposed recommendation results in embedment lengths 40 to 50% shorter than the

Caltrans specification. Furthermore, it can be seen that $D_{c,\max}$ will govern the embedment length obtained with Equation 9.1 for columns with very large cross sections.

9.2 Transverse reinforcement in the bar anchorage zone of Type II shafts

According to the analytical model presented in Section 6.1.2, to ensure the development of adequate bond strength, the spacing, $s_{tr,\max}$, of the transverse reinforcement in the bar anchorage region of a shaft should be no more than that given by the following equation:

$$s_{tr,\max} = \frac{2\pi A_{tr} f_{y,tr}}{N_{col} d_{b,col} \tau_u} \tag{9.3}$$

in which A_{tr} is the cross-sectional area of a transverse reinforcing bar, $f_{y,tr}$ is the nominal yield stress of the transverse reinforcement, N_{col} is the number of longitudinal bars in the column , $d_{b,col}$ is the diameter of the longitudinal bars in the column, and τ_u is the ultimate bond strength of the column longitudinal reinforcement, which can be taken to be 16.5 MPa (2.4 ksi) for 34.5-MPa (5-ksi) concrete. For concrete strengths other than 34.5 MPa (5 ksi), τ_u can be scaled accordingly with the assumption that it is proportional to $f_c'^{3/4}$. In the case that the bar anchorage region of a shaft has a steel casing in addition to transverse reinforcement, the minimum thickness, $t_{c,\min}$, of the steel casing required to ensure an adequate anchorage capacity can be calculated as follows:

$$t_{c,\min} = \frac{1}{f_{y,c}} \left(\frac{1}{2\pi} N_{col} \tau_u d_{b,col} - \frac{A_{tr}}{s_{tr}} f_{y,tr} \right) \tag{9.4}$$

in which $f_{y,c}$ is the nominal yield strength of the casing steel, and s_{tr} is the spacing of the transverse reinforcement.

To limit the opening of radial cracks in a shaft to a nominal maximum width of $u_{cr,\max}$, the following more stringent requirement on the spacing of the transverse reinforcement should be used.

$$s_{tr,\max} = \alpha \frac{2\pi A_{tr} f_{y,tr}}{N_{col} d_{b,col} \tau_u} \tag{9.5a}$$

where

$$\alpha = \frac{u_{cr,\max} N_{sh}}{\pi D_{ext} \varepsilon_{y,tr}} \le 1 \tag{9.5b}$$

in which N_{sh} is the number of longitudinal bars in the shaft, D_{ext} is the center-to-center diameter of the shaft reinforcing cage, and $\varepsilon_{y,tr}$ is the yield strain of the transverse reinforcement. It is recommended that $u_{cr,\max}$ be 0.3 mm (0.012 in.) based on the recommendation in ACI (2001) for RC members in contact with soil under service conditions. In the case that the shaft has also a steel casing, the minimum thickness, $t_{c,\min}$, of the steel casing should be:

$$t_{c,\min} = \frac{1}{\alpha_2 f_{y,c}} \left(\frac{1}{2\pi} N_{col} \tau_u d_{b,col} - \alpha_1 \frac{A_{tr}}{s_{tr}} f_{y,tr} \right) \tag{9.6a}$$

where

$$\alpha_1 = \frac{u_{cr,\max} N_{sh}}{\pi D_{ext} \varepsilon_{y,tr}} \le 1 \tag{9.6b}$$

$$\alpha_2 = \frac{u_{cr,\max} N_{sh}}{\pi D_s \varepsilon_{y,c}} \le 1 \tag{9.6c}$$

in which $\varepsilon_{y,c}$ is the yield strain of the steel in the casing.

The proposed recommendations for the minimum transverse reinforcement are compared in Table 9.2 to that proposed by McLean and Smith (1997) and the new requirement in the AASHTO LRFD Bridge Design Specifications (2012). According to McLean and Smith, the maximum spacing of the transverse reinforcement in the lap-splice region of a shaft should be

$$s_{tr,\max} = \frac{2\pi A_{tr} f_{y,tr} l_s}{A_l f_u} \tag{9.7}$$

in which A_l and f_u are the total cross-sectional area and tensile strength of the longitudinal reinforcement, and $l_s = 1.7 l_d$. Prior to 2012, no special specification existed

in the AASHTO LRFD Bridge Design Specifications for the transverse reinforcement in the lap splice region of an enlarged pile shaft. The transverse reinforcement in the bar anchorage zone of a shaft was determined according to Section 5.7.4.6 of the AASHTO LRFD Specifications (2012) for confinement in compression members. In the 2012 Edition of the AASHTO LRFD Specifications, a new requirement has been included in Section 5.11.5.2.1 on the transverse reinforcement in the lap-splice region of an enlarged shaft. This requirement, which is a modified version of the formula proposed by McLean and Smith (1997), is given in the following equation.

$$s_{tr,\max} = \frac{2\pi A_{tr} f_{y,tr} l_s}{k A_l f_{u,\min}} \tag{9.8}$$

in which $f_{u,\min}$ is the minimum tensile strength of the column longitudinal reinforcement (for ASTM A706 steel, it is 80 ksi), and k is the ratio of the amount of column reinforcement that is in tension at the nominal moment capacity of the column to the total amount of column reinforcement. This ratio can be obtained from a moment-curvature analysis; but according to Section C5.11.5.2.1 of AASHTO, k can be assumed 0.5 for most applications. For the comparison presented in Table 9.2, l_s in Equations 9.7 and 9.8 is replaced by l_d determined by Equation 9.2 to be consistent with the new recommendation for the embedment length (presented in Equation 9.1).

As shown in Table 9.2, the minimum transverse reinforcement proposed here is 30% larger than that proposed by McLean and Smith (1997) in most of the cases. If the stringent criterion on crack width control is followed and the maximum crack width is limited to 0.3 mm (0.012 in.), then the volumetric ratio of the transverse reinforcement will increase significantly, and in some cases, it will be doubled. Table 9.2 also shows that a larger amount of transverse reinforcement is needed in the bar anchorage region than in the rest of the shaft, which is governed by the confinement requirement for compression members. However, the new formula in the AASHTO LRFD Specifications results in a significantly reduced quantity of transverse reinforcement as compared to the original proposal of McLean and Smith (1997). As shown in Table 9.2, for the column-shaft Specimen 4 tested in this study, the new AASHTO formula results in 1/3 of the

transverse reinforcement actually used in the specimen (determined with Equation 9.3). In view of the severe cracking developed in the shaft of this specimen, the significantly reduced transverse reinforcement according to the AASHTO formula will not be adequate.

Table 9.1: Comparison of embedment lengths

		Column diameter mm (ft)	Shaft diameter mm (ft)	Column longitudinal reinforcing bars	Embedment length of column reinforcing cage inside shaft mm (ft)			
					Caltrans SDC (2010)[1]		McLean and Smith	Recommended (Equation 9.1)
					$l_{e,1}$	$l_{e,2}$		
Test Specimens	1	1219 (4)	1829 (6)	18 No.11	2126 (7.0)	3033 (9.9)	2169 (7.1)	1763 (5.8)
	2 and 3	1219 (4)	1829 (6)	18 No. 14	2471 (8.1)	3723 (12.2)	2859 (9.4)	2055 (6.7)
	4	1219 (4)	1524 (5)	32 No. 8 (bundled in pairs)	2054 (6.7)	2889 (9.5)	1872 (6.1)	1394 (4.6)
I-805/I5 Connector	Bent 4	2135 (7)	3000 (9.8)	32 No. 14	3387 (11.1)	4639 (15.2)	2987 (9.8)	2177 (7.1)
	Bent 12	2440 (8)	3600 (11.8)	60 No. 14	3692 (12.1)	4944 (16.2)	3134 (10.3)	2440 (8)[4]
	Bent 13	3200[2]/2135[3] (10.5/7)	3800 (12.5)	80 No. 14	4452 (14.6)	5704 (18.7)	3387 (11.1)	3200 (10.5)[4]
Other examples		1829 (6)	2438 (8)	30 No. 14	3081 (10.1)	4333 (14.2)	2859 (9.4)	2055 (6.7)
		2743 (9)	3353 (11)	80 No. 14	3995 (13.1)	5248 (17.2)	2859 (9.4)	2743 (9)[4]
		2743 (9)	3962 (13)	80 No. 14	3995 (13.1)	5248 (17.2)	3164 (10.4)	2743 (9)[4]
		2743 (9)	3962 (13)	56 No. 18	4370 (14.3)	5996 (19.7)	3912 (12.8)	2945 (9.7)

[1] $l_{e,1} = D_{c,\max} + l_d$, $l_{e,2} = D_{c,\max} + 2l_d$

[2] Larger cross-sectional dimension of non-circular section.

[3] Smaller cross-sectional dimension of non-circular section.

[4] Controlled by column dimension (Equation 9.1b).

Table 9.2: Comparison of transverse reinforcement in pile shafts

					Volumetric ratio of shaft transverse reinforcement in anchorage region				
		Column diameter mm (ft)	Shaft diameter mm (ft)	Column longitudinal bars	AASHTO[1]	AASHTO 2012[2] (l_s=l_d)	McLean and Smith (l_s=l_d)	Proposed minimum	Proposed to control crack opening
Test Specimens	1	1219 (4)	1829 (6)	18 No.11	0.71%	0.32%	0.75%	0.98%	1.25%
	2 and 3	1219 (4)	1829 (6)	18 No. 14	0.71%	0.38%	0.90%	1.17%	1.61%
	4	1219 (4)	1524 (5)	32 No. 8 (bundled in pairs)	0.71%	0.50%	0.97%	1.51%	2.21%
I-805/I5 Connector	Bent 4	2135 (7)	3000 (9.8)	32 No. 14	0.38%	0.40%	0.94%	1.23%	2.07%
	Bent 12	2440 (8)	3600 (11.8)	60 No. 14	0.33%	0.61%	1.45%	1.90%	2.69%
	Bent 13	3200/2135 (10.5/7)	3800 (12.5)	80 No. 14	0.31%	0.77%	1.83%	2.40%	4.55%

[1]Art. 5.7.4.6 for compression members.
[2]Art. 5.11.5.2.1 for non-contact splices in oversized shafts: k = 0.5; f_{ul} = 80 ksi for ASTM A706 steel.

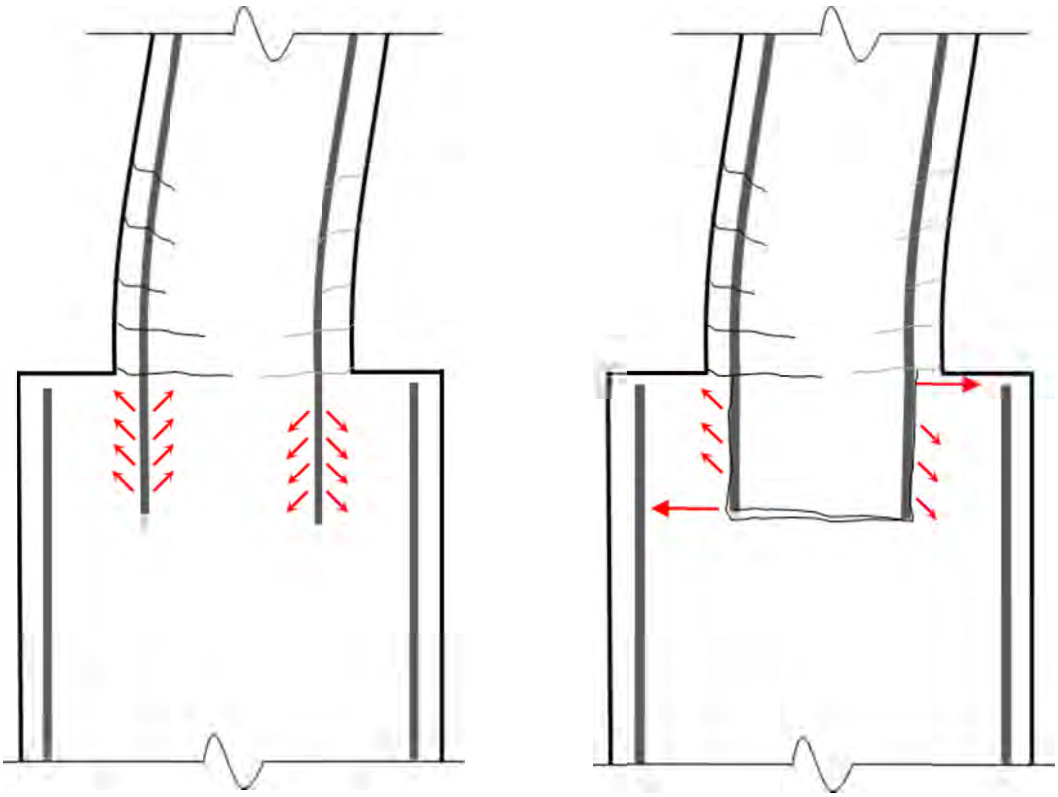

(a) Bar pull-out mode

(b) Column pull-out mode due to plying action

Figure 9.1: Behavior of column anchorage in a shaft

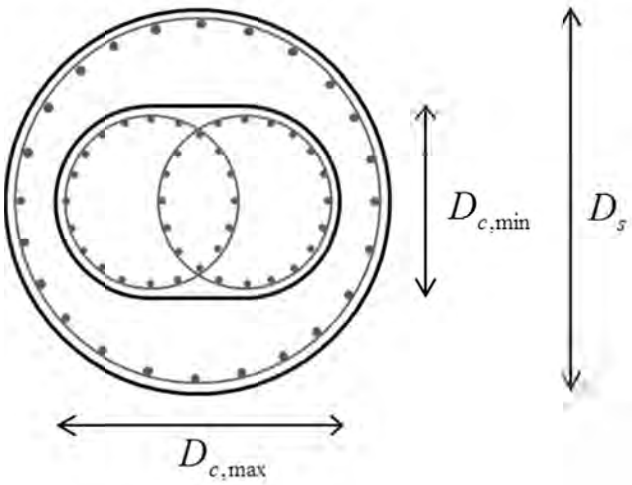

Figure 9.2: Non-circular column section

CHAPTER 10

SUMMARY AND CONCLUSIONS

10.1 Summary

The study reported here provides new data on the cyclic bond-slip behavior of large-diameter bars embedded in well-confined concrete, which were not available previously, and has resulted in improved design recommendations on the minimum embedment length required for column longitudinal reinforcement extended into enlarged (Type II) pile shafts and on the transverse reinforcement required for the bar anchorage region of a shaft.

An experimental study was carried out to obtain data on the bond strength and cyclic bond deterioration for large-diameter bars, namely, No. 11 and larger bars, which are frequently used in large bridge columns and pile shafts. A total of 22 monotonic pull-out and cyclic pull-pull tests were performed on No. 11, 14, and 18 bars embedded in cylindrical concrete specimens with the confinement condition representative of an enlarged pile shaft. Basic bond stress-vs.-slip relations for monotonic and cyclic loading were obtained, and the effect of the compressive strength of concrete and bar size on the bond strength was examined.

A new phenomenological cyclic bond stress-vs.-slip law for bars embedded in well-confined concrete has been proposed. This law has been developed based on the basic bond-slip data generated in this study and is an improvement and generalization of similar models proposed in other studies. The relation between the bond stress and slip for monotonic loading is described by a set of polynomial functions. For cyclic loading, a

similar bond stress-slip relation is used, but the bond strength is reduced at each slip reversal using two damage parameters, whose values are based on the slip history, to account for cyclic bond deterioration. The law also takes into account the reduction of the bond resistance due to the tensile yielding of a bar and the radial stress generated by bar slip in an empirical fashion. It has been calibrated with the basic bond-slip data obtained for large-diameter bars, but can be used for deformed bars of any size as validated by other test data. This law has been implemented as a constitutive model of an interface element in the finite element (FE) program ABAQUS. The new element has been used in three-dimensional FE analyses of reinforced concrete members to study their bond-slip behavior. In these analyses, a plastic-damage constitutive model for concrete and an elasto-plastic model with kinematic hardening for steel available in ABAQUS have been used.

The development of large-diameter bars in tension under a well-confined situation, like that in a bridge foundation, was studied with experimental testing and FE analyses. The bond-slip behavior and anchorage capacity for large-diameter bars with long embedment lengths were evaluated with quasi-static pull-push tests. A total of 3 specimens were tested. One had a No. 14 bar and two had a No. 18 bar embedded in a cylindrical concrete specimen that had the same diameter and confinement level as those used in the basic bond-slip tests. These tests were conducted to evaluate the adequacy of the development length requirements in the AASHTO LRFD Bridge Design Specifications (2010) under the confined level considered here. Two tests, one for each bar size, were performed with an embedment length equal to the development length required by AASHTO. A third test was conducted on a No. 18 bar with an embedment length 40% shorter than the required. This test was to confirm that this reduced length was sufficient to develop bar yielding, as predicted by a FE analysis using the proposed bond-slip element, and to provide additional data for model validation. Finite element models have been developed and validated with the experimental data, and have been used for a numerical parametric study. Based on the results of the numerical study, an empirical formula has been derived to relate the tension capacity of an anchored bar to the embedment length, compressive strength of concrete, and yield strength of steel. This

formula has been used in Monte Carlo simulations to study the reliability of the current AASHTO requirements on the development of large-diameter bars in tension considering uncertainties in material properties and construction quality.

The minimum embedment length required for column longitudinal reinforcement extended into Type II shafts was studied with large-scale tests of column-shaft assemblies and FE analyses. Four 1219-mm (4-ft) diameter columns supported on Type II shafts were tested under lateral cyclic loading. The first specimen was to assess the level of conservatism of the current Caltrans design recommendation. The embedment length was taken as $D_c + l_d$, in which D_c is the column diameter and l_d is the minimum development length required in the AASHTO LRFD Bridge Design Specifications (2010). In this test, a plastic hinge formed at the base of the column, and the specimen failed by the buckling and subsequent tensile rupture of several longitudinal bars in the plastic-hinge region. No significant damage was observed in the upper region of the shaft where the column reinforcement was anchored. A finite element analysis was performed for this test using the proposed bond-slip element to complement the experimental data. Based on the experimental and numerical results, it was determined that the minimum embedment length could be reduced to $l_d + s + c$, in which s is the distance between the column and shaft reinforcing cages and c is the thickness of the top concrete cover in the shaft. A second specimen was tested with this embedment length. The transverse reinforcement in the lap-splice region of the shaft was determined with the formula proposed by McLean and Smith (1997). This specimen behaved in a similar manner as the first one, with no indication of bar anchorage failure. A third and a fourth column-shaft assembly tests were conducted with embedment lengths of $l_d + s + c$. Specimen 3 had a steel casing, and Specimen 4 had bundled bars. These two tests were also intended to evaluate the recommendations proposed on the minimum transverse reinforcement required in the bar anchorage region of a shaft. One recommendation (which was used in Specimen 4) is on the minimum transverse reinforcement required to provide sufficient confinement to develop the necessary bond strength, and the other (which was used in Specimen 3) is more stringent and is to limit the width of splitting cracks induced by bar slip.

Finally, finite element analyses have been conducted to verify that an embedment length of $l_d + s + c$ is generally adequate for column-shaft assemblies of different dimensions and with different longitudinal reinforcement ratios and bar sizes. Based on the experimental and numerical studies, improved design recommendations have been proposed.

10.2 Conclusions

The basic bond-slip tests presented in this report have shown that the monotonic and cyclic bond stress-vs.-slip behavior of large-diameter bars, namely, No.11 and larger bars, embedded in well-confined concrete is very similar to that of No. 8 bars that were tested by Eligehausen et al. (1983). These tests have also shown a slight increase of the bond strength with the increased bar size, and that the compressive strength of concrete, f_c', has a notable effect on the bond strength. The bond strength appears to be proportional to $f_c'^{3/4}$. Other studies have indicated that the influence of the concrete strength and bar size on the bond strength depends on the level of confinement in the concrete member. However, there is a lack of comprehensive experimental data to arrive at more definitive conclusions.

The phenomenological bond-slip model proposed in this study successfully reproduces the bond-slip behavior of the large-diameter bars tested in this study as well as that of smaller bars tested by others, including the decay of bond strength under different load histories. Implemented in an interface element in ABAQUS, it provides a reliable tool to study the effect of bond slip on the behavior of reinforced concrete members and the anchorage length requirement.

The experimental and numerical investigations carried out in this study have confirmed that the development length requirements in the AASHTO LRFD Bridge Design Specifications (2010) for large-diameter bars anchored in well-confined concrete are adequate as long as there is no uncertainty in the material properties and construction quality. Tests presented in this investigation have shown that the minimum development lengths specified in AASHTO are not only sufficient to develop the tensile yielding of a

bar, but also sustain large inelastic deformation up to the ultimate strain of the steel. However, with the consideration of possible uncertainties in material properties and construction quality, the reliability analysis conducted here has shown that the AASHTO requirements have an acceptable reliability level to develop the expected yield strength of a bar but do not have the desired reliability to develop its full tensile capacity. The development length required to reliably sustain the plastic deformation and resulting strain hardening in a bar up to a level that is consistent with the Caltrans Seismic Design Criteria (SDC) has been identified.

Large-scale testing and FE analyses of column-shaft assemblies have confirmed that the minimum embedment length required by the Caltrans SDC (Caltrans 2010) for column longitudinal bars extended into an enlarged pile shaft is over-conservative. Based on these results and the aforementioned reliability analysis, improved design recommendations that can significantly shorten the required embedment length have been proposed. However, it is recommended that the embedment length be no less than the column diameter to assure a good anchorage performance under the plying action of the confined concrete core of the column. The requirements on the transverse reinforcement in the bar anchorage zone of a shaft have been developed with a simplified analytical model. They demand a significantly higher quantity of transverse reinforcement than the new formula in the AASHTO LRFD Bridge Design Specifications (2012). The experimental results have shown that the minimum transverse steel recommended in this study can provide adequate confinement to develop the necessary bond strength. However, the splitting cracks in the shaft of Specimen 4 appeared to be slightly more severe than those in the other specimens. This is probably due to the fact that the ratio of the shaft diameter to the column diameter for this specimen is smaller than that for the other three specimens. This made it less effective in resisting the plying action of the confined concrete core of the column. Based on the observations from the column-shaft assembly tests, one can expect that lowering the amount of transverse reinforcement in the shafts to the level recommended in the new AASHTO specifications could result in severe splitting cracks, which might lead to premature bond failure in the bar anchorage zone.

While the amount of transverse reinforcement recommended here is higher than that required by the current design specifications of Caltrans and AASHTO, the required embedment length is reduced by 40 to 50%. It has also been shown that the additional transverse reinforcement can be provided by an engineered steel casing, which can effectively control tensile splitting cracks induced by bar slip in a pile shaft and thus minimize the need for post-earthquake damage repair on pile shafts.

10.3 Recommendations for future research

There is a need for a comprehensive study to investigate how the bond strength varies with the bar size and the compressive strength of concrete under different levels of confinement. As previous studies have indicated, the influence of the concrete strength and bar size on the bond strength seems to depend on the level of confinement in the concrete member, but there is not sufficient data to accurately quantify this influence for different confinement levels. However, for well-confine situations, like that in a Type II shaft, the conclusions that the bar diameter has little influence on the bond strength and the bond strength is proportional to $f_c'^{3/4}$ are valid and consistent with data from other studies.

The recommendation that the embedment length of the column reinforcement extended into an enlarged shaft be no less than the column diameter is to avoid column pull-out from the shaft due to the plying action. It is based on limited experimental evidence and on engineering judgment. The plying action cannot be well captured by the finite element models presented here. Further research is recommended to better understand this mechanism.

Some shortcomings have been identified for the constitutive models available in ABAQUS for concrete and reinforcing bars. In particular, the plastic-damage constitutive model for concrete is not able to realistically simulate the closing of cracks upon unloading, and the plastic dilatation. To improve the modeling of RC members, the development of a more realistic three-dimensional constitutive model for concrete is recommended. Models capable of simulating the buckling and subsequent fracture of

reinforcing bars also need to be implemented in ABAQUS to better capture the inelastic behavior of a hinging column.

REFERENCES

Abrams, D.A., "Tests on bond between concrete and steel," *University of Illinois Bulletin*, Vol. XI, No.5, 1913.

American Association of State Highway and Transportation Officials (AASHTO), *LRFD Bridge Design Specifications*, 5th Edition, Washington DC, 2010.

American Concrete Institute (ACI), *Control of Cracking of Concrete Structure (ACI 224R-01)*, ACI Committee 224, Farmington Hills, MI, 2001.

American Concrete Institute (ACI), *Bond and Development of Straight Reinforcing Bars in Tension (ACI-408R-03)*, ACI Committee 408, Farmington Hills, MI, 2003.

American Concrete Institute (ACI), *Building Code Requirements for Structural Concrete (ACI-318-08) and Commentary*, ACI Committee 318, Farmington Hills, MI, 2008.

American Concrete Institute (ACI), *Report on Bond of Steel Reinforcing Bars Under Cyclic Loads (ACI-408R-12)*, ACI Committee 408, Farmington Hills, MI, 2012.

ASTM International, *A706/A706M-09b Standard Specification for Low-Alloy Steel Deformed and Plain Bars for Concrete Reinforcement*, West Conshohocken, PA, 2009.

Ayoub, A., "Nonlinear Analysis of Reinforced Concrete Beam–Columns with Bond-Slip Inelastic," *Journal of Engineering Mechanics*, Vol. 132, No. 11, November 2006, pp. 1177-1186.

Berry, M.P., Eberhard, M.O., *Performance Modeling Strategies for Modern Reinforced Concrete Bridge Columns*, PEER Report 2007/07, Pacific Earthquake Engineering Research Center, University of California, Berkeley, CA, 2008.

Budek, A.M., Priestley, M.J.N., Benzoni, G., "Inelastic seismic response of bridge drilled-shaft RC pile/columns," *Journal of Structural Engineering*, Vol. 24, No. 4, April 2000, pp. 510-517.

Cairns, J., Jones, K., "An evaluation of the bond-splitting action of ribbed bars," *ACI Materials Journal*, Vol. 93, No.1, January-February 1996, pp. 10-19.

California Department of Transportation (Caltrans), *Bridge Design Specifications*, Sacramento, CA, 2008.

California Department of Transportation (Caltrans), *Caltrans Seismic Design Criteria, Version 1.6*, Sacramento, CA, 2010.

Carrea, F., *Shake-Table Test on a Full-Scale Bridge Reinforced Concrete Column*, MS Thesis, Faculty of Engineering, University of Bologna, Italy, 2010.

Chai, Y.H., "Flexural strength and ductility of extended pile-shafts I: Analytical model," *Journal of Structural Engineering*, Vol. 128, No. 5, May 2002, pp. 586-594.

Chai, Y.H., Hutchinson, T., "Flexural strength and ductility of extended pile-shafts II: Experimental study," *Journal of Structural Engineering*, Vol. 128, No. 5, May 2002, pp. 595-602.

Chang, P., Dameron, R., *Finite element analysis of main column bars in column-shaft foundation connections and analysis of rebar bond*, David Evans and Associates Project No. CALT00590201.ANA, 2009.

Choi, O.C., Hadje-Ghaffari, H., Darwin, D., McCabe, S.L., *Bond of Epoxy-Coated Reinforcement to Concrete: Bar Parameters*, SM Report No. 25, University of Kansas Center for Research, Lawrence, KS, July 1990.

Choi, E., Chung, Y., Kim, Y., Kim., J., "Monotonic and cyclic bond behavior of confined concrete using NiTiNb SMA wires," *Smart Materials and Structures*, Vol. 20, No. 7, July 2011.

Ciampi, V., Eligehausen, R., Bertero, V.V., Popov, E.P., *Analytical Model for Concrete Anchorages of Reinforcing Bars under Generalized Excitations*, Report No. UCB/EERC-82/23, Earthquake Engineering Research Center, University of California, Berkeley, CA, 1982.

Clark, A.P., "Comparative Bond Efficiency of Deformed Concrete Reinforcing Bars," *ACI Journal*, Vol. 43, No. 4, December 1946, pp. 381-400.

Clark, A. P., "Bond of Concrete Reinforcing Bars," *ACI Journal*, Vol. 46, No. 3, November 1950, pp. 161-184.

Cox, J.V., Herrmann., L.R., "Development of a plasticity bond model for steel reinforcement," *Mechanics of Cohesive-Frictional Materials*, Vol. 3, No. 2, April 1998, pp. 155-180.

Cox, J.V., Herrmann., L.R., "Validation of a plasticity bond model for steel reinforcement," *Mechanics of Cohesive-Frictional Materials*, Vol. 4, No. 4, July 1999, pp. 361-389.

Daoud, A., Maurel, O., Laborderie, C., "Mesoscopic modeling of the interaction between steel reinforcement and the early-age cracking during cement hydration," *Bond in Concrete 2012*, Brescia, Italy, June 2012.

Darwin, D., Graham, E.K., "Effect of Deformation Height and Spacing on Bond Strength of Reinforcing Bars," *ACI Structural Journal*, Vol. 90, No. 6, November-December 1993, pp. 646-657.

Darwin, D., Idun, E.K., Zuo, J., Tholen, M.L., "Reliability-based strength reduction factor for bond," *ACI Structural Journal*, Vol. 95, No. 4, July-August 1998, pp. 434-442.

Eligehausen, R., Popov, E.P., Bertero, V.V., *Local Bond Stress - Slip Relationships of Deformed Bars under Generalized Excitations*, UCB/EERC- 83/23, Earthquake Engineering Research Center, University of California, Berkeley, CA, 1983.

Ellingwood, B., Galambos, T.V., MacGregor, J.G., Cornell, C.A., *Development of a Probability Based Load Criterion for American National Standard A58*, National Bureau of Standards Special Publication 577, Washington DC, 1980.

Fédération Internationale du Béton (fib), *Bond of Reinforcement in Concrete*, fib bulletin 10, Lausanne, Switzerland, 2000.

Fédération Internationale du Béton (fib), *Model Code 2010 - Final draft, Volume 1*, fib bulletin 65, Lausanne, Switzerland, 2012.

Fernandez Ruiz, M., Muttoni, A., Gambarova, P.G., "Analytical Modeling of the Pre- and Postyield Behavior of Bond in Reinforced Concrete," *ASCE Journal of Structural Engineering*, Vol. 133, No.10, October 2007, pp. 1364-1372.

Filippou, F.C., Popov, E.G., Bertero, V.V., "Modeling of R/C joints under cyclic excitations," *ASCE Journal of Structural Engineering*, Vol. 109, No.11, November 1983, pp. 2666-2684.

Gambarova, P., Rosati, G.P., Zasso, B., "Steel-to-concrete bond after concrete splitting: test results," *Materials and Structures*, Vol. 22, No. 127, January 1989, pp. 35-47.

Gambarova, P., Rosati, G.P., "Bond and splitting in reinforced concrete: test results on bar pull-out," *Materials and Structures*, Vol. 29, No. 189, June 1996, pp. 267-276.

Goto, Y., "Cracks Formed in Concrete Around Deformed Tension Bars," *ACI Journal*, Vol. 68, No. 4, April 1971, pp. 244-251.

Herrmann, L.R., Cox, J.V., *Development of a plasticity bond model for reinforced concrete*, CR 94-001, Naval Facilities Engineering Service Center, Port Hueneme, CA, 1994.

Hurblut, B.J., *Experimental and computational investigation of strain-softening in concrete*, MS Thesis, University of Colorado, Boulder, CO, 1985.

Ichinose, T., Kanayama, Y., Inoue, Y., Bolander Jr., J.E., "Size Effect on Bond Strength of Deformed Bars," *Construction and Building Materials*, Vol. 18, No. 7, September 2004, pp. 549-558.

Karthik, M.M., Mander, J.B., "Stress-block parameters for unconfined and confined concrete based on a unified stress-strain model," *ASCE Journal of Structural Engineering*, Vol. 137, No.2, February 2011, pp. 270-273.

Lee, J., Fenves, G.L., "Plastic-Damage Model for Cyclic Loading of Concrete Structures," *ASCE Journal of Engineering Mechanics*, Vol. 124, No.8, August 1998, pp. 892–900.

Lehman, D.E., Moehle, J.P., *Seismic performance of well-confined concrete bridge columns*, PEER Report 1998/01, Pacific Earthquake Engineering Research Center, University of California, Berkeley, CA, 2000.

Liu, P., Lin, H., Der Kiureghian, A., *CALREL User Manual*, UCB/SEEM-89/18, Department of Civil Engineering, University of California, Berkeley, CA, 1989.

Liu. Y., *Lateral Behavior of Reinforced Concrete Columns Supported on Type II Shafts*, MS Thesis, Department of Structural Engineering, University of California, San Diego, CA, 2012.

Lowes, L.N., Moehle, J.P., Govindjee, S., "Concrete-Steel Bond Model for Use in Finite Element Modeling of Reinforced Concrete Structures," *ACI Structural Journal*, Vol. 101, No. 4, July-August 2004, pp. 501-511.

Lubliner, J., Oliver, J., Oller, S., Oñate, E., "A Plastic-Damage Model for Concrete," *International Journal of Solids and Structures*, Vol. 25, No.3, 1989, pp. 229–326.

Lundgren, K., "Pull-out Tests of Steel-encased Specimens Subjected to Reversed Cyclic Loading," *Materials and Structures*, Vol. 33, No. 231, August-September 2000, pp. 450-456.

Lundgren, K., Magnusson, J., "Three-dimensional modeling of anchorage zones in reinforced concrete," *ASCE Journal of Engineering Mechanics*, Vol. 127, No.7, July 2001, pp. 693-699.

Lundgren, K.," Bond between ribbed bars and concrete. Part 1: Modified model," *Magazine of Concrete Research*, Vol. 57, No.7, September 2005, pp. 371-382.

Maekawa, K., Pimanmas, A., Okamura, H., *Nonlinear mechanics of reinforced concrete*, Ed. Spon Press, New York, NY, 2003.

Malvar, J., "Bond of Reinforcement under Controlled Confinement," *ACI Materials Journal*, Vol. 89, No. 6, November-December 1992, pp. 593-601.

Mander, J.B., Priestley, M.J.N., Park, R., "Observed stress-strain behavior of confined concrete," *ASCE Journal of Structural Engineering*, Vol. 114, No.8, August 1989, pp. 1827-1849.

McLean, D.I., Smith, C.L., *Noncontact lap splice in bridge column-shaft connections*, Report No. WA-RD 417.1, Washington State Transportation Center, Washington State University, WA, 1997.

Monti, G., Filippou, F.C., Spacone, E., "Finite element for anchored bars under cyclic load reversals," *ASCE Journal of Structural Engineering*, Vol. 123, No. 5, May 1997, pp. 614-623.

Monti, G., Spacone, E., "Reinforced concrete fiber beam element with bond-slip," *Journal of Structural Engineering*, Vol. 126, No. 6, June 2000, pp. 654-661.

Murcia-Delso, J., Stavridis, A., Shing, P.B., "Bond Strength and Cyclic Bond Deterioration of Large-Diameter Bars," *ACI Structural* Journal, Vol. 110, No. 4, July-August 2013, pp. 659-669.

Nowak, A.S., Szerszen, M.M., "Calibration of Design Code for Buildings (ACI 318): Part 1—Statistical Models for Resistance," *ACI Structural Journal*, Vol. 100, No. 3, May-June 2003, pp. 377-382.

Orangun, C.O., Jirsa, J.O., Breen, J.E., *The Strength of Anchored Bars: A Reevaluation of Test Data on Development Length and Splices*, Research Report No. 154-3F, Center for Highway Research, University of Texas at Austin, TX, January 1975.

Orangun, C.O., Jirsa, J.O., Breen, J.E., "Reevaluation of Test Data on Development Length and Splices," *ACI Journal*, Vol. 74, No. 3, March 1977, pp. 114-122.

Pacific Earthquake Engineering Research Center (PEER), Open System for Earthquake Engineering Simulation (OpenSees), Berkeley, CA, 2012.

Plizzari, G., Mettelli, G., *Experimental Study on the Bond Behavior of Large Bars, Technical Report*, Dept. of Civil Engineering, Architecture and Environment, University of Brescia, Italy, 2009.

Pochanart, S., Harmon, P., "Bond-Slip Model for Generalized Excitations Including Fatigue," *ACI Materials Journal*, Vol. 86, No. 5, September-October 1989, pp. 465-474.

Priestley M.J.N., Seible, F., Calvi, G.M., *Seismic Design and Retrofit of Bridges*, John Wiley &. Sons, New York, NY, 1996.

Priestley M.J.N., *Myths and Fallacies in Earthquake Engineering, Revisited*, IUSS Press, Pavia, Italy, 2003.

Raynor, D.J., *Bond Assessment of Hybrid Frame Continuity Reinforcement*, MS Thesis, University of Washington, WA, 2000.

Rehm, G., 1961, "Uber die Grunlagen des Verbundes Zwischen Stahl und Beton (On the fundamentals of steel-concrete bond)," *Deutscher Ausschuss fur Stahlbeton*, No. 1381, 1961.

Reinhardt, H.W., Blaauwendraad, J., Vos, E., "Prediction of bond between steel and concrete by numerical analysis", *Materials and Structures*, Vol. 17, No. 100, July-August 1984, pp. 311-320.

Reinhardt, H.W., "Fracture mechanics of an elastic softening material like concrete," *Heron*, Vol. 29, No.2, 1984.

Restrepo, J.I., Seible, F., Stephan, B., Schoettler, M.J., "Seismic Testing of Bridge Columns Incorporating High-Performance Materials," *ACI Structural Journal*, Vol.103, No.4, July-August 2006, pp. 496-504.

Restrepo-Posada, J.I., Park, R., Buchanan, A.H., *Seismic behaviour of connections between precast concrete members*, Research report 93-3, Department of Civil Engineering, University of Canterbury, New Zealand, April 1993.

Santos, J., Henriques, A.A., "FE modelling of bond-slip response including steel strains," *Bond in Concrete 2012*, Brescia, Italy, June 2012.

Serpieri, R., Alfano, G., "Bond-slip analysis via a thermodynamically consistent interface model combining interlocking, damage and friction", *International Journal for Numerical Methods in Engineering*, Vol. 85, No. 2, January 2011, pp. 164-186.

Shima, H., Chou, L., Okamura, H., "Bond-Slip-Strain Relationship of Deformed Bars Embedded in Massive Concrete," *Proceedings of JSCE*, Vol.6, No.387, February 1987, pp. 79-94.

Shima, H., Chou, L., Okamura, H., "Bond Characteristics in Post-Yield Range of Deformed Bars," *Proceedings of JSCE*, Vol.6, No. 387, February 1987, pp. 113-124.

Simulia, ABAQUS V. 6.10, Dassault Systemes Simulia Corp., Providence, RI, 2010.

Spacone, E., Filippou, F.C., Taucer, F.F. ''Fiber beam-column model for nonlinear analysis of R/C frames. Part I: Formulation,'' *Earthquake Engineering and Structural Dynamics*, Vol. 25, No. 7, July 1996, pp. 711–725.

Sritharan, S., Priestley, M.J.N., Seible, F., "Nonlinear Finite element analyses of concrete bridge joint systems subjected to seismic actions," *Finite Elements in Analysis and Design*, Vol. 36, No. 3-4, November 2000, pp. 215-233.

Steuck, K.P., Eberhard, M.O., Stanton, J.F., "Anchorage of Large-Diameter Reinforcing Bars in Ducts," *ACI Structural Journal*, Vol. 106, No. 4, July-August 2009, pp. 506-513.

Tepfers, R., *A Theory of Bond Applied to Overlapped Tensile Reinforcement Splices for Deformed Bar*, Publ. 73:2, Division of Concrete Structures, Chalmers University of Technology, Goteborg, Sweden, May 1973.

Tepfers R., Olsson P., "Ring Test for Evaluation of Bond Properties of Reinforcing Bars. International Conference, " *Bond in Concrete - From Research to Practice*, Riga, Latvia, October 1992.

Unanwa, C., Mahan, M., "Statistical Analysis of Concrete Compressive Strengths for California Highway Bridges," *Journal of performance of Constructed Facilities*, posted ahead of print September 22, 2012.

Viwathanatepa, S., Popov, E.P., Bertero, V.V., *Effects of Generalized Loadings on Bond of Reinforcing Bars Embedded in Confined Concrete Blocks*, Report No. UCB/EERC-79/22, Earthquake Engineering Research Center, University of California, Berkeley, CA, 1979.

Yankelevsky, D.Z., Moshe, A.A., Farhey, D.N., "Mathematical Model for Bond-Slip Behavior under Cyclic Loading," *ACI Structural Journal*, Vol. 89, No. 6, November-December 1992, pp. 692-698.

Yashinsky, M., "Earthquake Damage to Structures", *Structural Engineering Handbook*, Ed. Lian Duan, Boca Raton: CRC Press LLC, 2001.

Zhao, J., Sritharan, S., "Modeling of Strain Penetration Effects in Fiber-Based Analysis of Reinforced Concrete Structures," *ACI Structural Journal*, Vol. 104, No. 2, March-April 2007, pp. 133-141.

Zsutty, T., "Empirical Study of Bar Development Behavior," *ASCE Journal of Structural Engineering*, Vol. 111, No. 1, January 1985, pp. 205-219.

Zuo, J., Darwin, D, "Splice Strength of Conventional and High relative Rib Area Bars in Normal and High-Strength Concrete," *ACI Structural Journal*, Vol. 97, No. 4, July-August 2000, pp. 630-641.

APPENDIX A: CONSTRUCTION OF PULL-PUSH TEST SPECIMENS

The construction sequence for the pull-push specimens presented in Chapter 5 is shown in Figure A.1 through Figure A.6. These pictures correspond to the construction of Specimen 2.

Figure A.5 shows how the strain gages were attached to the central bar and the gage wires were routed. The gages were installed on the longitudinal ribs of the bars to minimize the disturbance to the bond properties. The gage wires were routed laterally inside plastic tubes placed horizontally to avoid damage as the bars slipped.

Figure A.1: Footing and cylinder cages and form for the footing

Figure A.2: Concrete pour for the footing

Figure A.3: Cylinder form

Figure A.4: Installation of the center bar

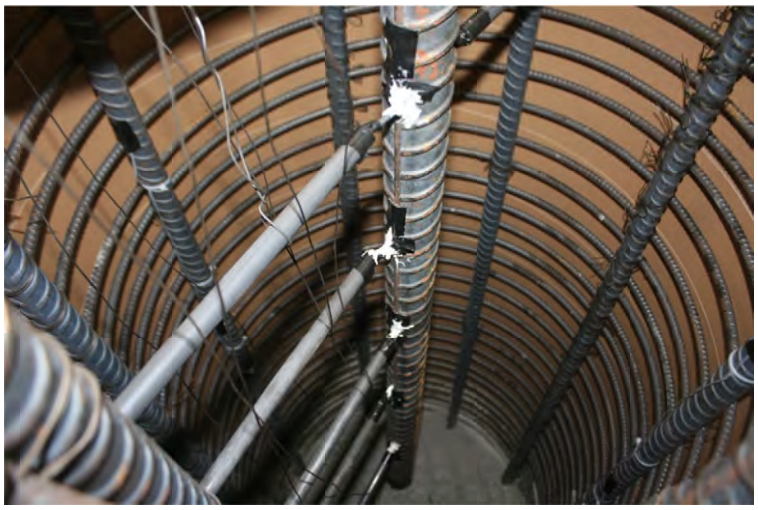

Figure A.5: Close-view of the strain gages attached to the center bar

Figure A.6: Concrete pour for the cylinder

APPENDIX B: CONSTRUCTION OF THE COLUMN-SHAFT ASSEMBLIES

This appendix contains pictures of the construction and instrumentation sequence for the column-shaft assemblies presented in Chapter 6. These pictures correspond to Specimen 1. It is the same for the other specimens.

Figure B.1: Strain gages on longitudinal reinforcing bars

Figure B.2: Strain gage on longitudinal rib of a bar

Figure B.3: Shaft cage instrumented with strain gages

Figure B.4: Column cage instrumented with strain gages

Figure B.5: Footing and shaft cages

Figure B.6: Concrete pour for the footing (Pour 1)

Figure B.7: Steel form for the shaft

Figure B.8: Construction joint at footing-shaft interface after steel brushing (same preparation for all construction joints)

Figure B.9: Concrete pour for the lower portion of the shaft (Pour 2)

Figure B.10: Pour 2 finished at the level at which the column cage would begin

Figure B.11: Installation of the column cage

Figure B.12: Concrete pour for the upper portion of the shaft in which the column cage was embedded (Pour 3)

Figure B.13: Removal of the shaft form

Figure B.14: Column form and falsework for the load stub

Figure B.15: Concrete pour for the column (Pour 4)

Figure B.16: End of Pour 4

Figure B.17: Load stub reinforcing cage

Figure B.18: Concrete pour for the load stub (Pour 5)

Figure B.19: Column-shaft assembly after removal of the form and falsework

Figure B.20: Column-shaft assembly painted white for easier crack identification

Figure B.21: Column-shaft assembly instrumented (east side)

Figure B.22: Displacement transducers at the base of the column (east side)

Figure B.23: Column-shaft assembly instrumented (west side)

Figure B.24: Post-tensioning rod to apply vertical load and trapezoid-shaped hole in the footing

Figure B.25: Setup of hydraulic jacks under the strong floor to control the load of the vertical rods

APPENDIX C: INSTRUMENTATION PLANS FOR THE COLUMN-SHAFT ASSEMBLIES

This appendix contains drawings of the instrumentation plans for the column-shaft assemblies presented in Chapter 6. The instrumentation plans include the following:

Instruments	Specimen 1	Specimen 2	Specimen 3	Specimen 4
Strain gages on column longitudinal bars	Figure C.1	Figure C.9	Figure C.18	Figure C.28 and Figure C.29
Strain gages on shaft longitudinal bars	Figure C.2	Figure C.10	Figure C.19	Figure C.30
Strain gages on column hoops	Figure C.3	Figure C.11	Figure C.20	Figure C.31
Strain gages on shaft hoops	Figure C.3	Figure C.12	Figure C.21	Figure C.32
Strain gages on steel casing	-	-	Figure C.22	-
Displacement transducers (linear potentiometers) to measure the curvature and shear deformations in the column and shaft	Figure C.4 through Figure C.6	Figure C.13 through Figure C.15	Figure C.23 through Figure C.25	Figure C.33 through Figure C.35
Displacement transducers (linear potentiometers) to measure the base rotation and slip at the interfaces	Figure C.7	Figure C.16	Figure C.26	Figure C.36
Displacement transducers (string potentiometers) to measure the lateral deflection of the specimen	Figure C.8	Figure C.17	Figure C.27	Figure C.37

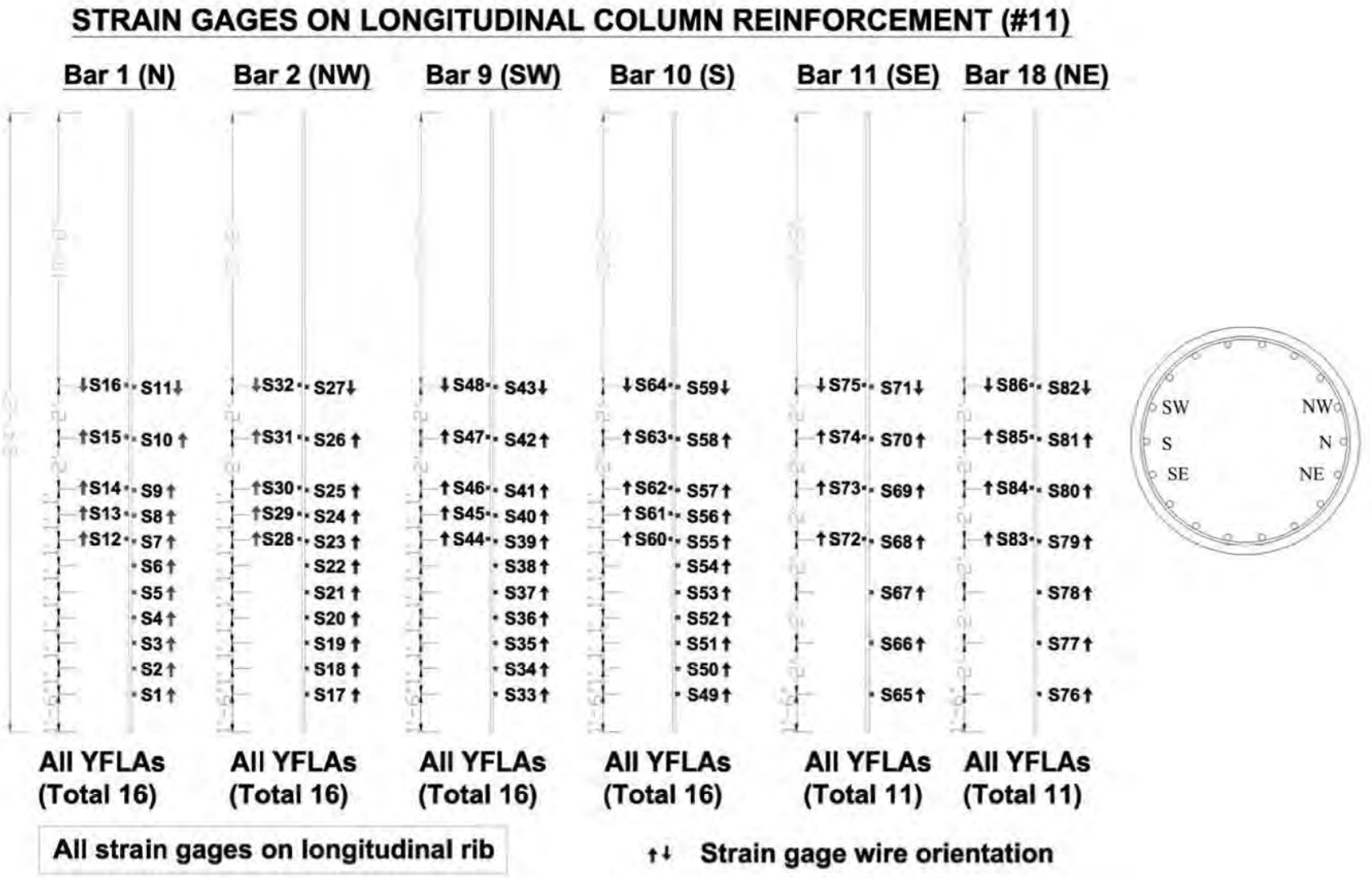

Figure C.1: Strain gages on column longitudinal bars in Specimen 1

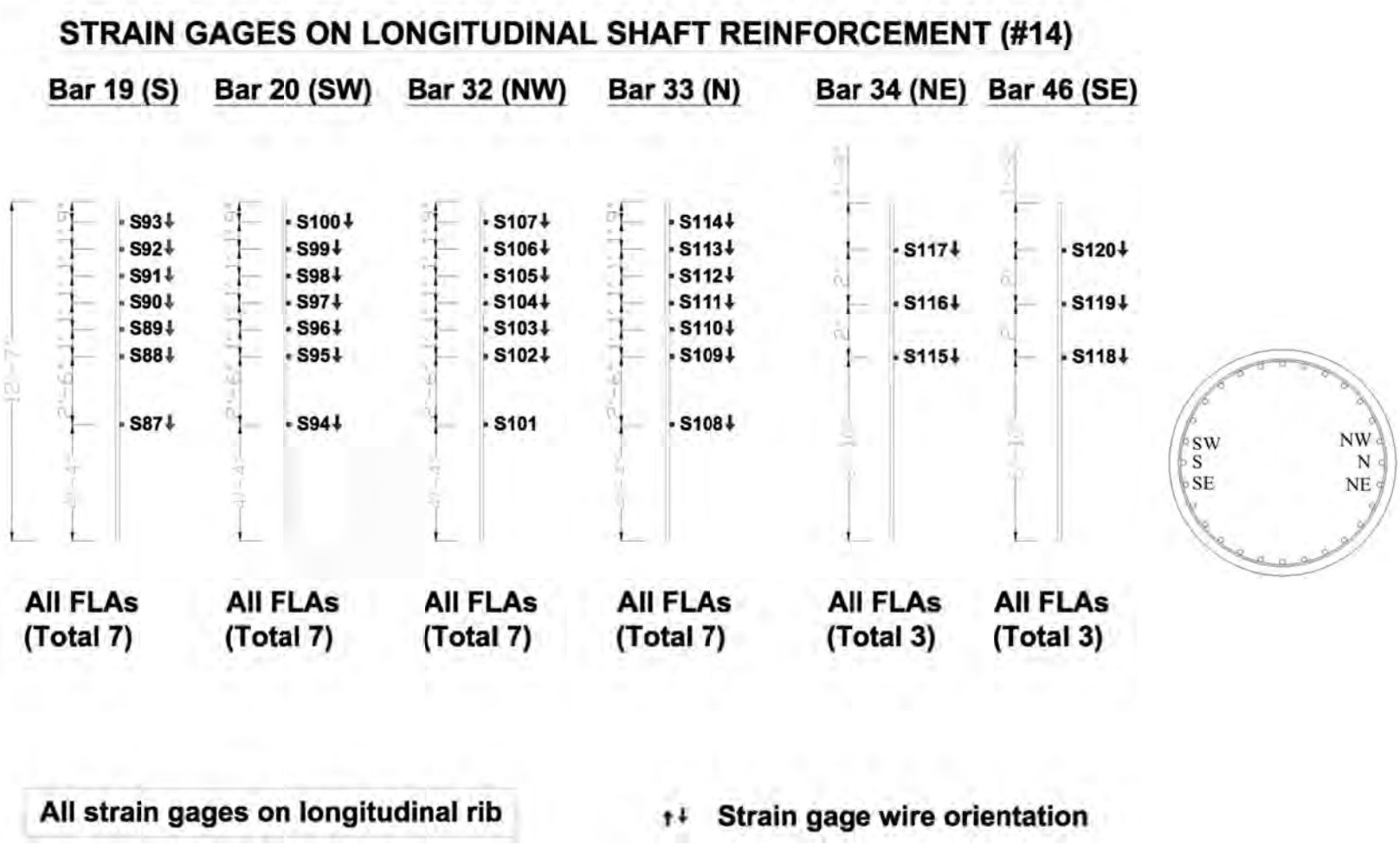

Figure C.2: Strain gages on shaft longitudinal bars in Specimen 1

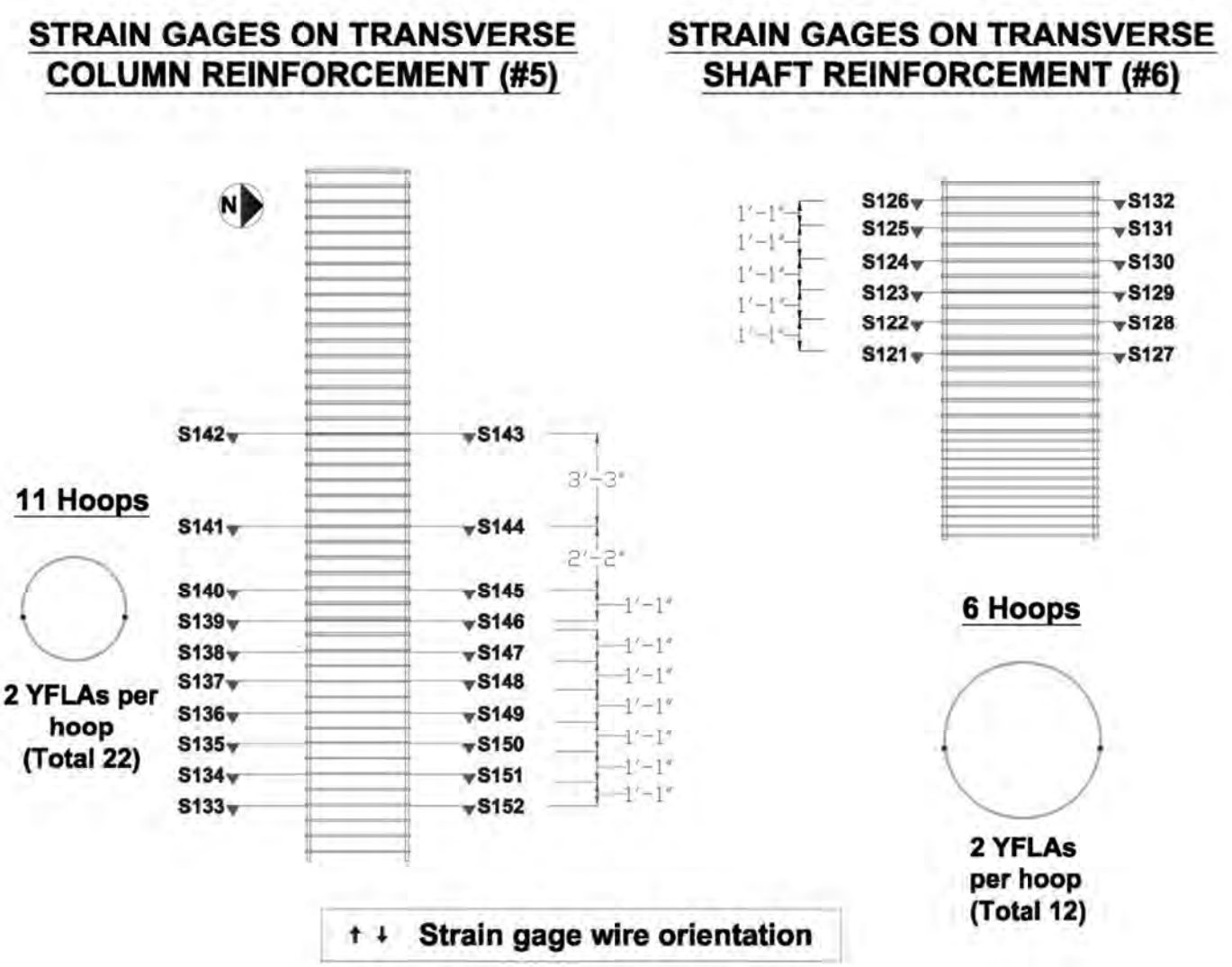

Figure C.3: Strain gages on transverse reinforcement in Specimen 1

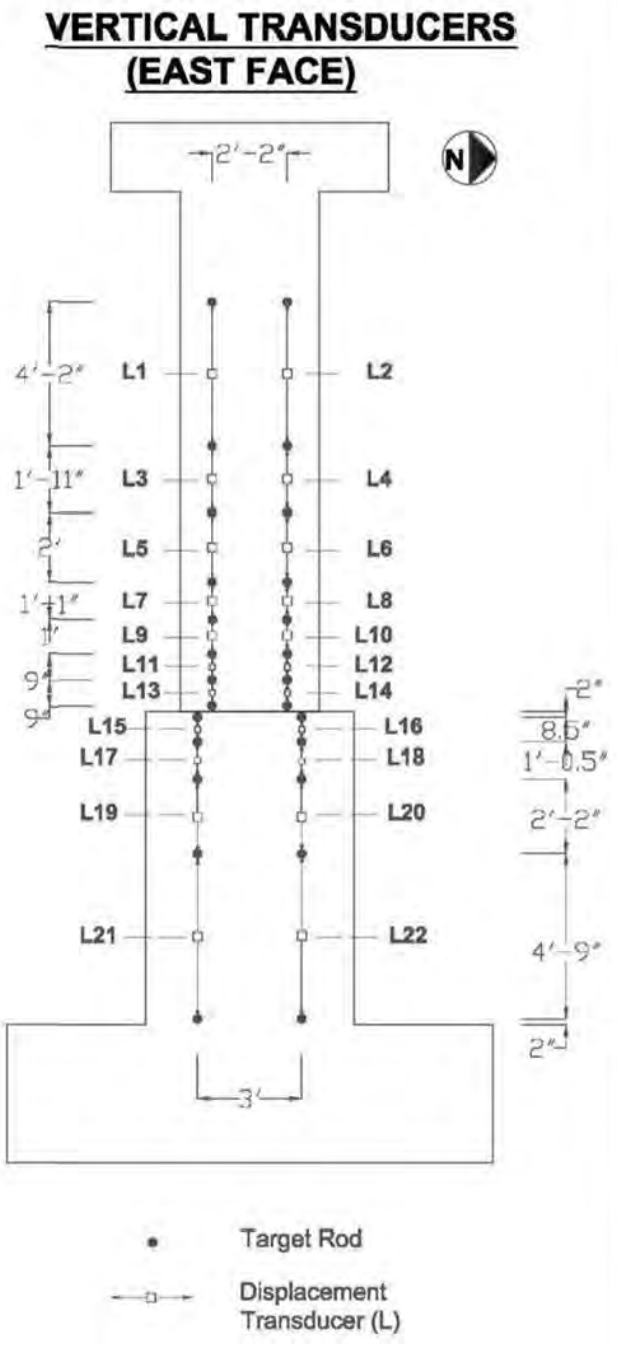

#	CENTER-TO-CENTER DISTANCE	STROKE
L1	4'-2"	2" (+1.5", -0.5")
L2	4'-2"	2" (+1.5", -0.5")
L3	1'-11"	2" (+1.5", -0.5")
L4	1'-11"	2" (+1.5", -0.5")
L5	2'	2" (+1.5", -0.5")
L6	2'	2" (+1.5", -0.5")
L7	1'-1"	2" (+1.5", -0.5")
L8	1'-1"	2" (+1.5", -0.5")
L9	1'	2" (+1.5", -0.5")
L10	1'	2" (+1.5", -0.5")
L11	9"	2" (+1.5", -0.5")
L12	9"	2" (+1.5", -0.5")
L13	9"	2" (+1.5", -0.5")
L14	9"	2" (+1.5", -0.5")
L15	~ 8 1/2"	2" (+1.5", -0.5")
L16	~ 8 1/2"	2" (+1.5", -0.5")
L17	~ 1 1/2"	2" (+1.5", -0.5")
L18	~ 1 1/2"	2" (+1.5", -0.5")
L19	~ 2'-2"	2" (+1.5", -0.5")
L20	~ 2'-2"	2" (+1.5", -0.5")
L21	~ 4'-9"	2" (+1.5", -0.5")
L22	~ 4'-9"	2" (+1.5", -0.5")

Figure C.4: Vertical displacement transducers on the east face of Specimen 1

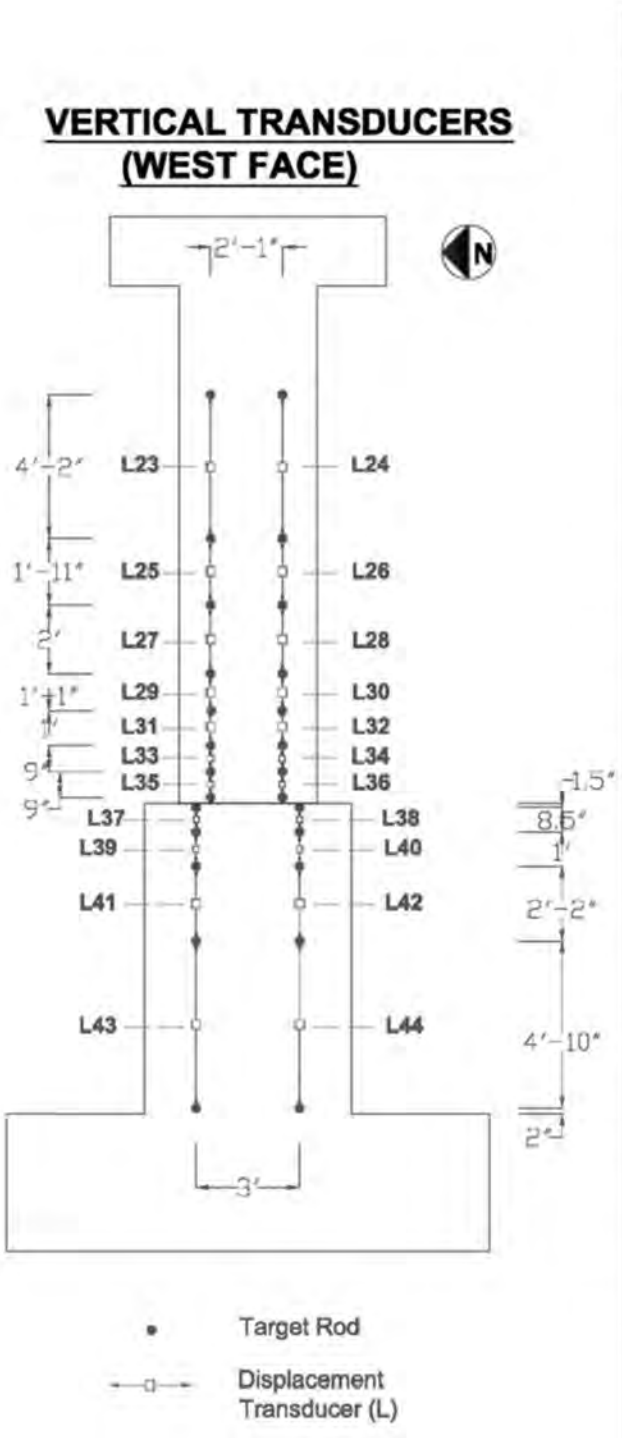

#	CENTER-TO-CENTER DISTANCE	STROKE
L23	4'-2"	2" (+1.5", -0.5")
L24	4'-2"	2" (+1.5", -0.5")
L25	1'-11"	2" (+1.5", -0.5")
L26	1'-11"	2" (+1.5", -0.5")
L27	2'	2" (+1.5", -0.5")
L28	2'	2" (+1.5", -0.5")
L29	1'-1"	2" (+1.5", -0.5")
L30	1'-1"	2" (+1.5", -0.5")
L31	1'	2" (+1.5", -0.5")
L32	1'	2" (+1.5", -0.5")
L33	9"	2" (+1.5", -0.5")
L34	9"	2" (+1.5", -0.5")
L35	9"	2" (+1.5", -0.5")
L36	9"	2" (+1.5", -0.5")
L37	~ 8.5"	2" (+1.5", -0.5")
L38	~ 8.5"	2" (+1.5", -0.5")
L39	~ 1'	2" (+1.5", -0.5")
L40	~ 1'	2" (+1.5", -0.5")
L41	~ 2'-2"	2" (+1.5", -0.5")
L42	~ 2'-2"	2" (+1.5", -0.5")
L43	~ 4'-10"	2" (+1.5", -0.5")
L44	~ 4'-10"	2" (+1.5", -0.5")

Figure C.5: Vertical displacement transducers on the west face of Specimen 1

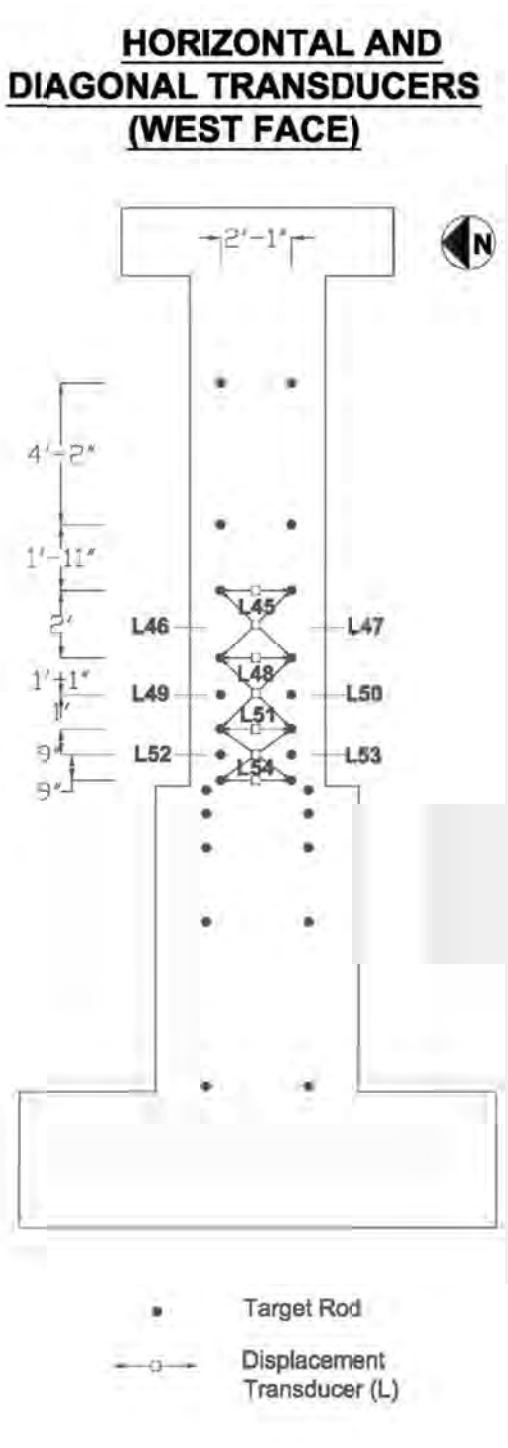

#	CENTER-TO-CENTER DISTANCE	STROKE
L45	~2'-1"	2" (+1.5", -0.5")
L46	~2'-10 1/2"	2" (+1.5", -0.5")
L47	~2'-10 1/2"	2" (+1.5", -0.5")
L48	~2'-1"	2" (+1.5", -0.5")
L49	~2'-11 1/4"	2" (+1.5", -0.5")
L50	~2'-11 1/4"	2" (+1.5", -0.5")
L51	~2'-1"	2" (+1.5", -0.5")
L52	~2'-6 3/4"	4" (+2.5", -1.5")
L53	~2'-6 3/4"	4" (+2.5", -1.5")
L54	~2'-1"	2" (+1.5", -0.5")

Figure C.6: Horizontal and diagonal displacement transducers on the west face of Specimen 1

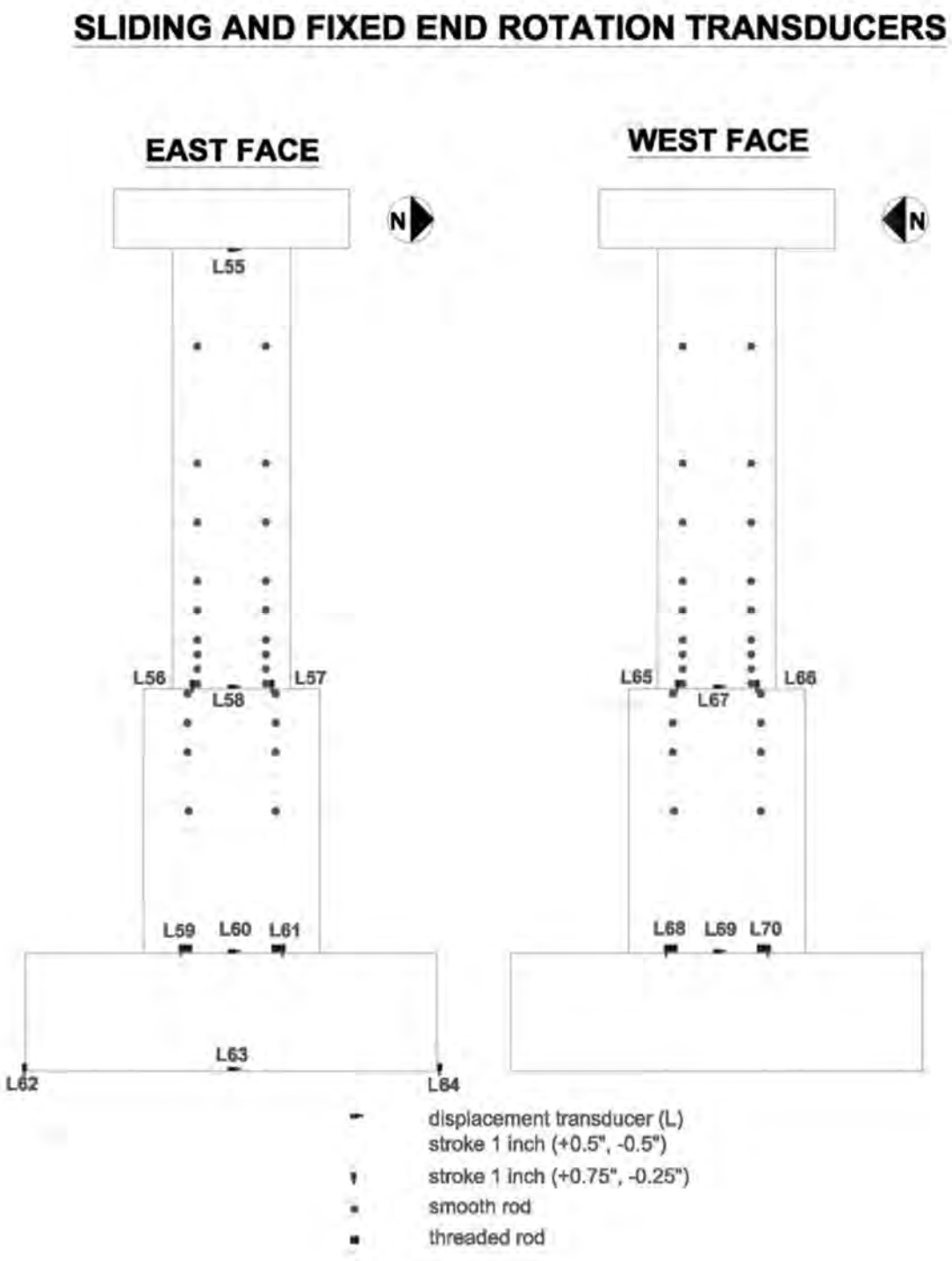

Figure C.7: Displacement transducers to measure slip and base rotation in Specimen 1

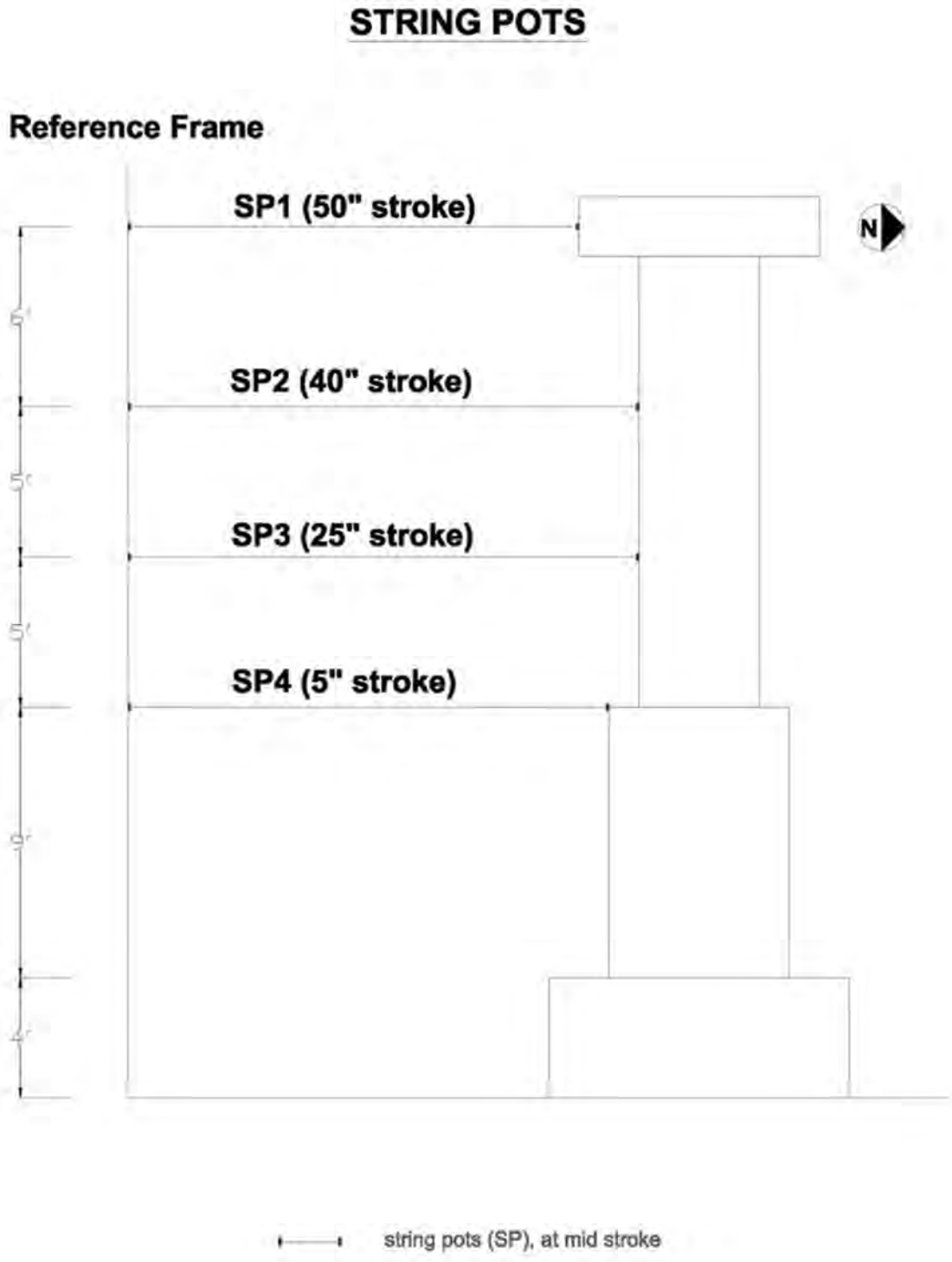

Figure C.8: String potentiometers to measure the lateral deflection of Specimen 1

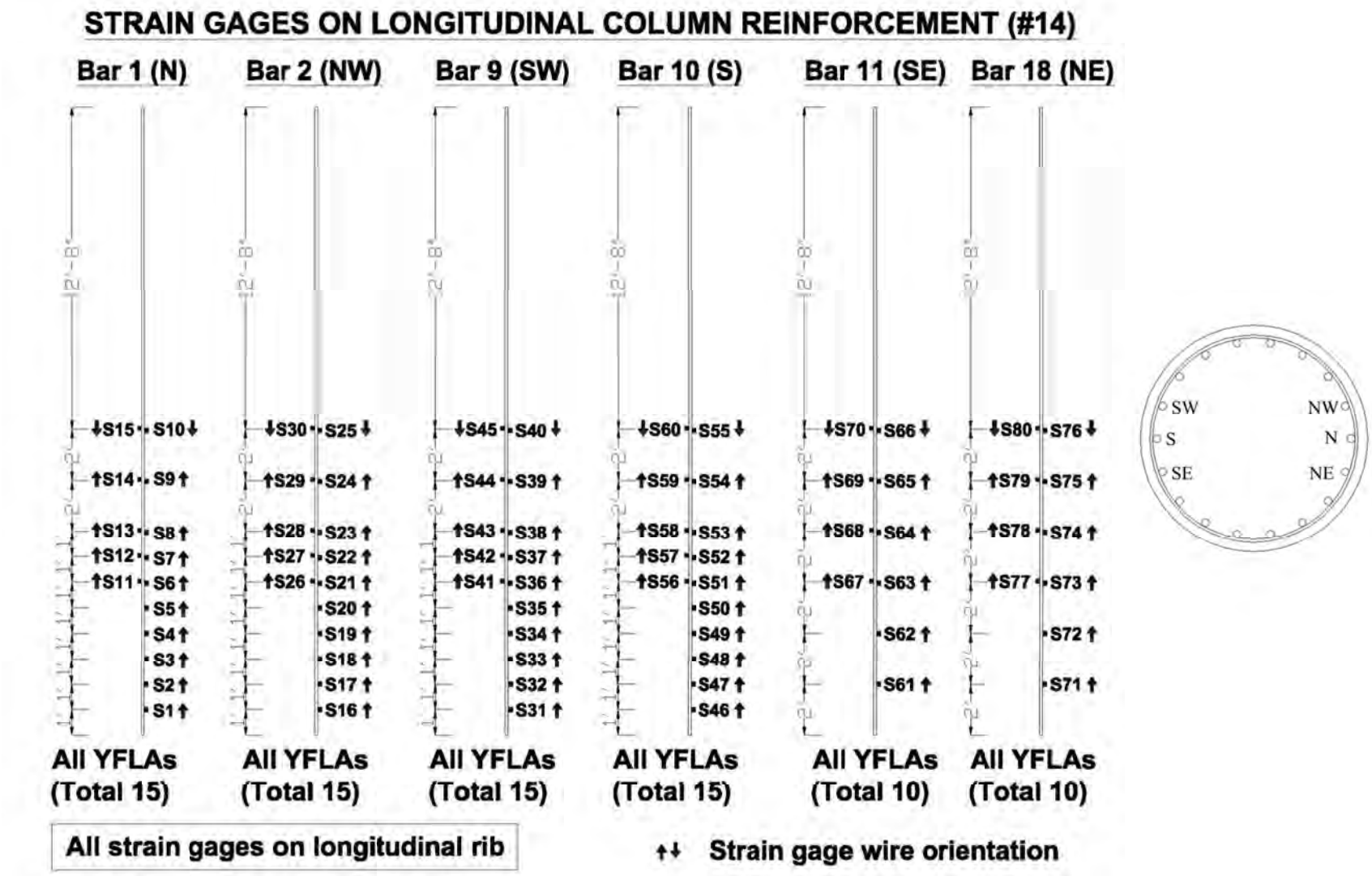

Figure C.9: Strain gages on column longitudinal bars in Specimen 2

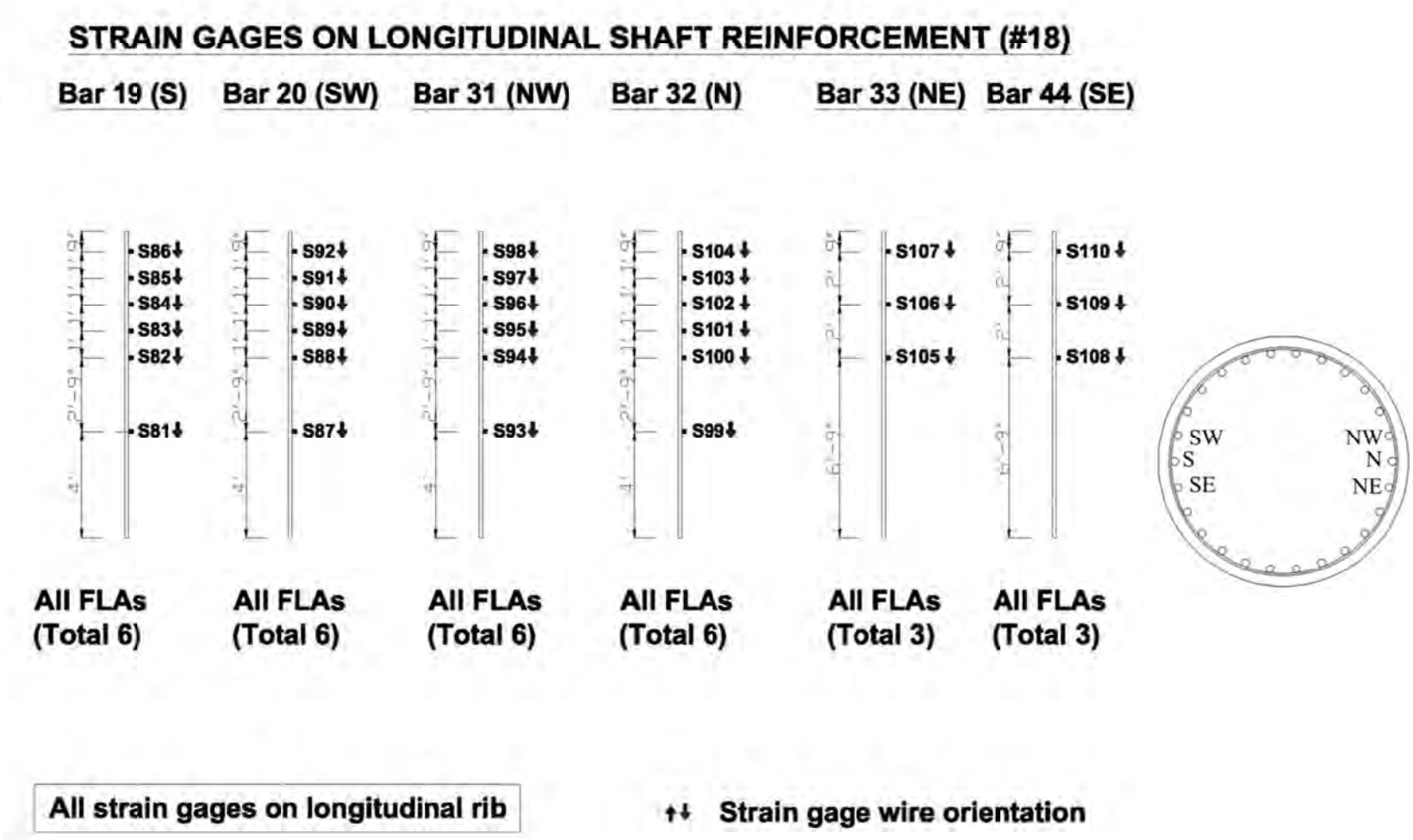

Figure C.10: Strain gages on shaft longitudinal bars in Specimen 2

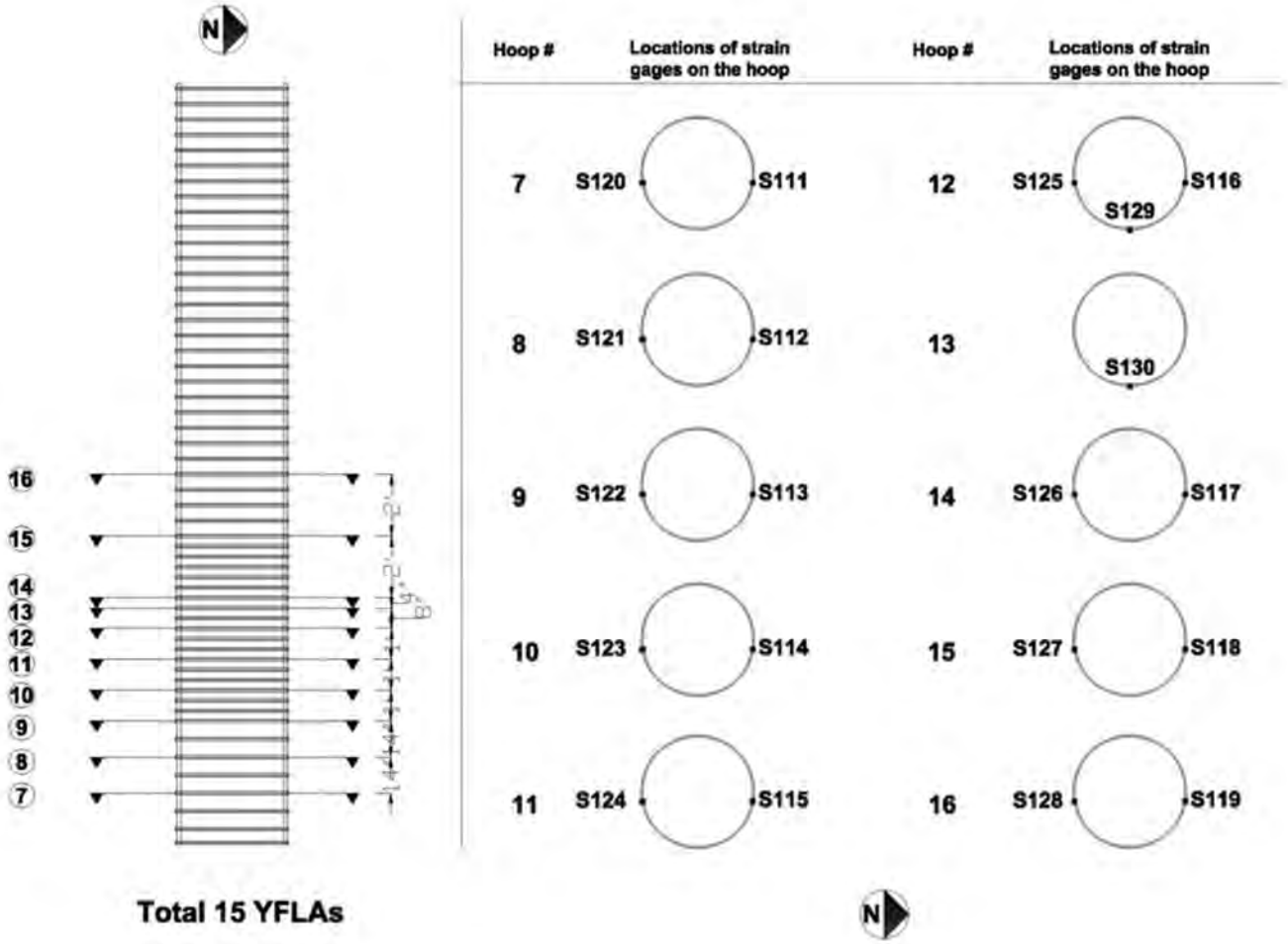

Figure C.11: Strain gages on column transverse reinforcement in Specimen 2

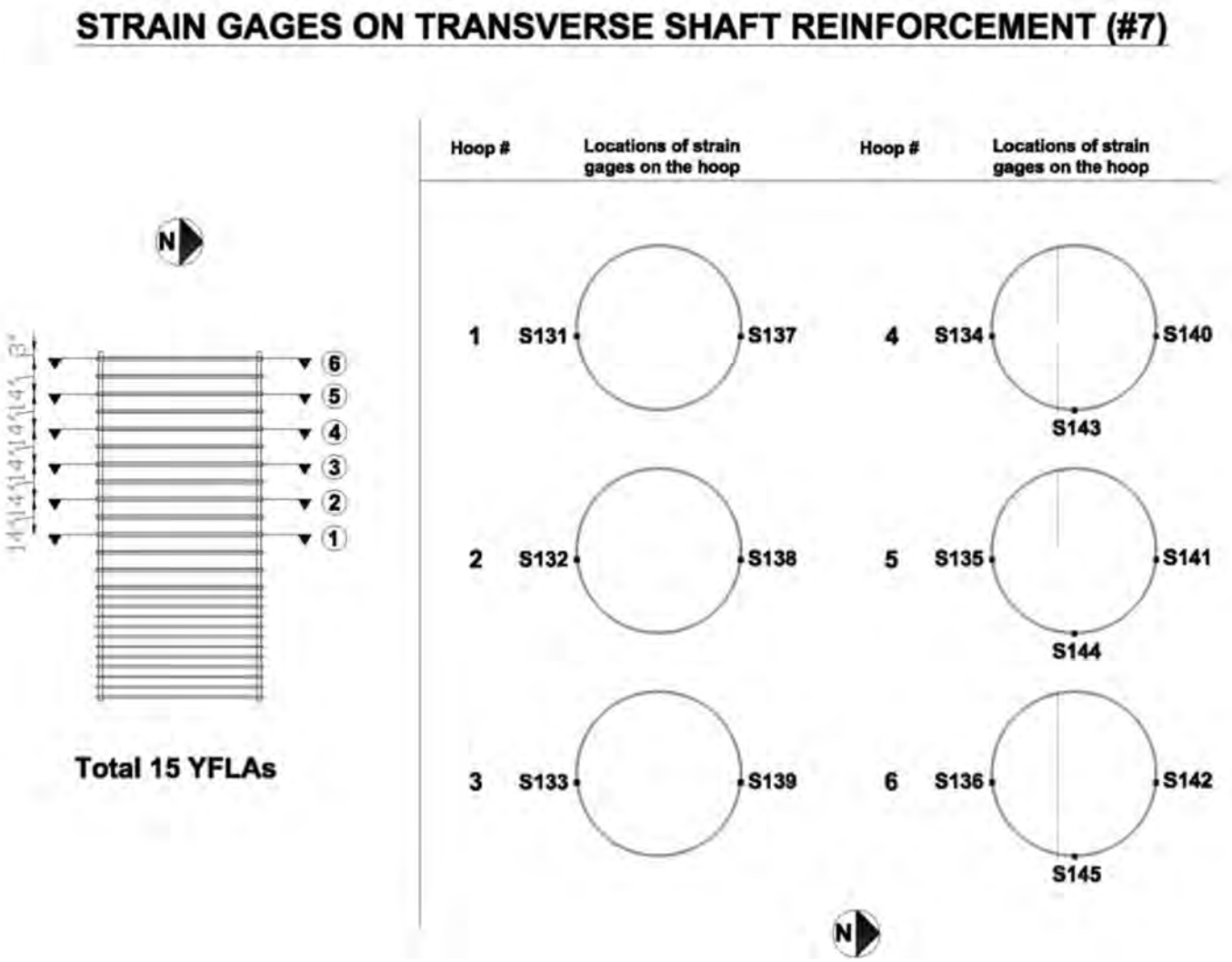

Figure C.12: Strain gages on shaft transverse reinforcement in Specimen 2

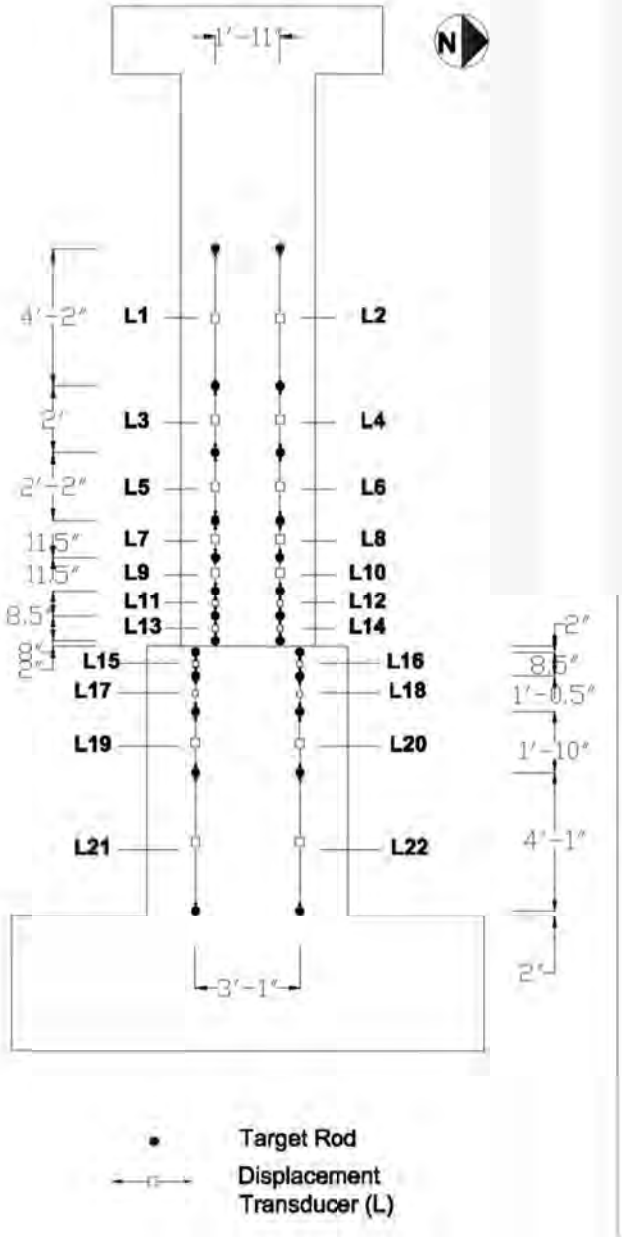

#	CENTER-TO-CENTER DISTANCE	STROKE
L1	~ 4'-2"	2" (+1.5", -0.5")
L2	~ 4'-2"	2" (+1.5", -0.5")
L3	~ 2'	2" (+1.5", -0.5")
L4	~ 2'	2" (+1.5", -0.5")
L5	~ 2'-2"	2" (+1.5", -0.5")
L6	~ 2'-2"	2" (+1.5", -0.5")
L7	~ 11 1/2"	2" (+1.5", -0.5")
L8	~ 11 1/2"	2" (+1.5", -0.5")
L9	~ 11 1/2"	2" (+1.5", -0.5")
L10	~ 11 1/2"	2" (+1.5", -0.5")
L11	~ 8 1/2"	2" (+1.5", -0.5")
L12	~ 8 1/2"	2" (+1.5", -0.5")
L13	~ 8"	2" (+1.5", -0.5")
L14	~ 8"	2" (+1.5", -0.5")
L15	~ 8 1/2"	2" (+1.5", -0.5")
L16	~ 8 1/2"	2" (+1.5", -0.5")
L17	~ 1'-1/2"	2" (+1.5", -0.5")
L18	~ 1'-1/2"	2" (+1.5", -0.5")
L19	~ 1'-10"	2" (+1.5", -0.5")
L20	~ 1'-10"	2" (+1.5", -0.5")
L21	~ 4'-1"	2" (+1.5", -0.5")
L22	~ 4'-1"	2" (+1.5", -0.5")

Figure C.13: Vertical displacement transducers on the east face of Specimen 2

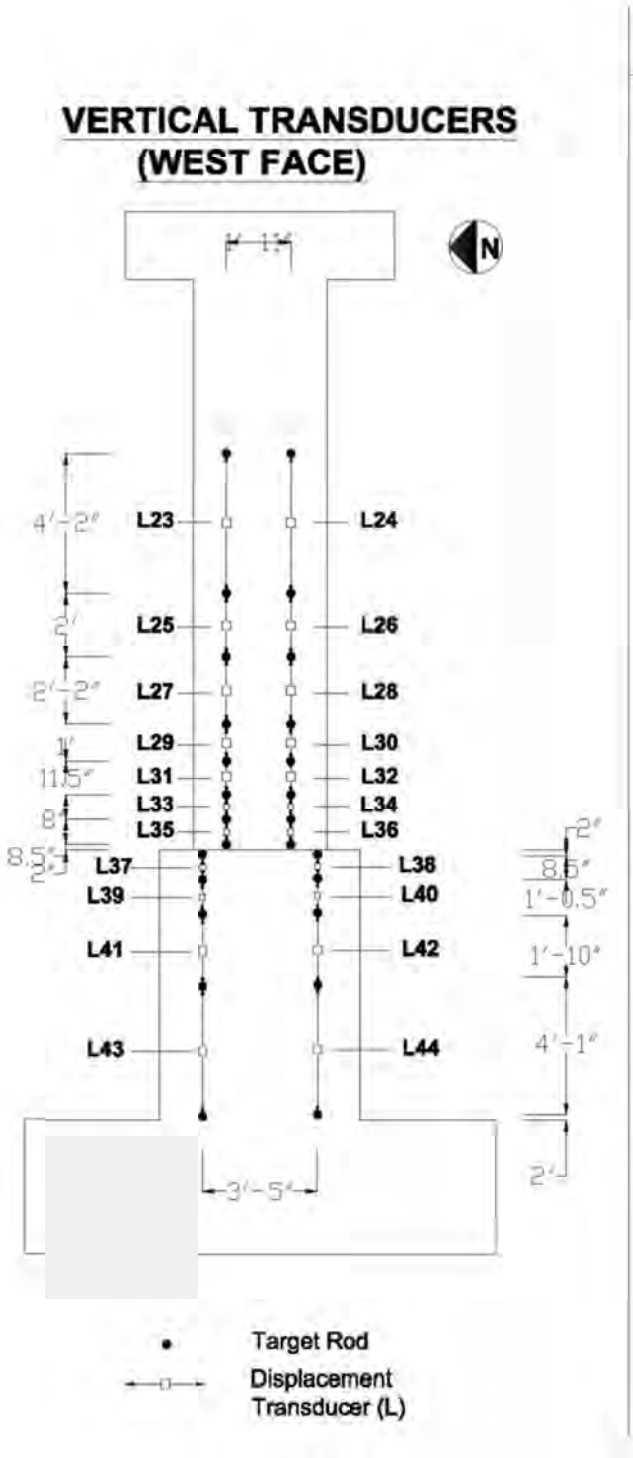

#	CENTER-TO-CENTER DISTANCE	STROKE
L23	~ 4'-2"	2" (+1.5", -0.5")
L24	~ 4'-2"	2" (+1.5", -0.5")
L25	~ 2'	2" (+1.5", -0.5")
L26	~ 2'	2" (+1.5", -0.5")
L27	~ 2'-2"	2" (+1.5", -0.5")
L28	~ 2'-2"	2" (+1.5", -0.5")
L29	~ 1'	2" (+1.5", -0.5")
L30	~ 1'	2" (+1.5", -0.5")
L31	~ 11 1/2"	2" (+1.5", -0.5")
L32	~ 11 1/2"	2" (+1.5", -0.5")
L33	~ 8"	2" (+1.5", -0.5")
L34	~ 8"	2" (+1.5", -0.5")
L35	~ 8 1/2"	2" (+1.5", -0.5")
L36	~ 8 1/2"	2" (+1.5", -0.5")
L37	~ 8 1/2"	2" (+1.5", -0.5")
L38	~ 8 1/2"	2" (+1.5", -0.5")
L39	~ 1'-1/2"	2" (+1.5", -0.5")
L40	~ 1'-1/2"	2" (+1.5", -0.5")
L41	~ 1'-10"	2" (+1.5", -0.5")
L42	~ 1'-10"	2" (+1.5", -0.5")
L43	~ 4'-1"	2" (+1.5", -0.5")
L44	~ 4'-1"	2" (+1.5", -0.5")

Figure C.14: Vertical displacement transducers on the west face of Specimen 2

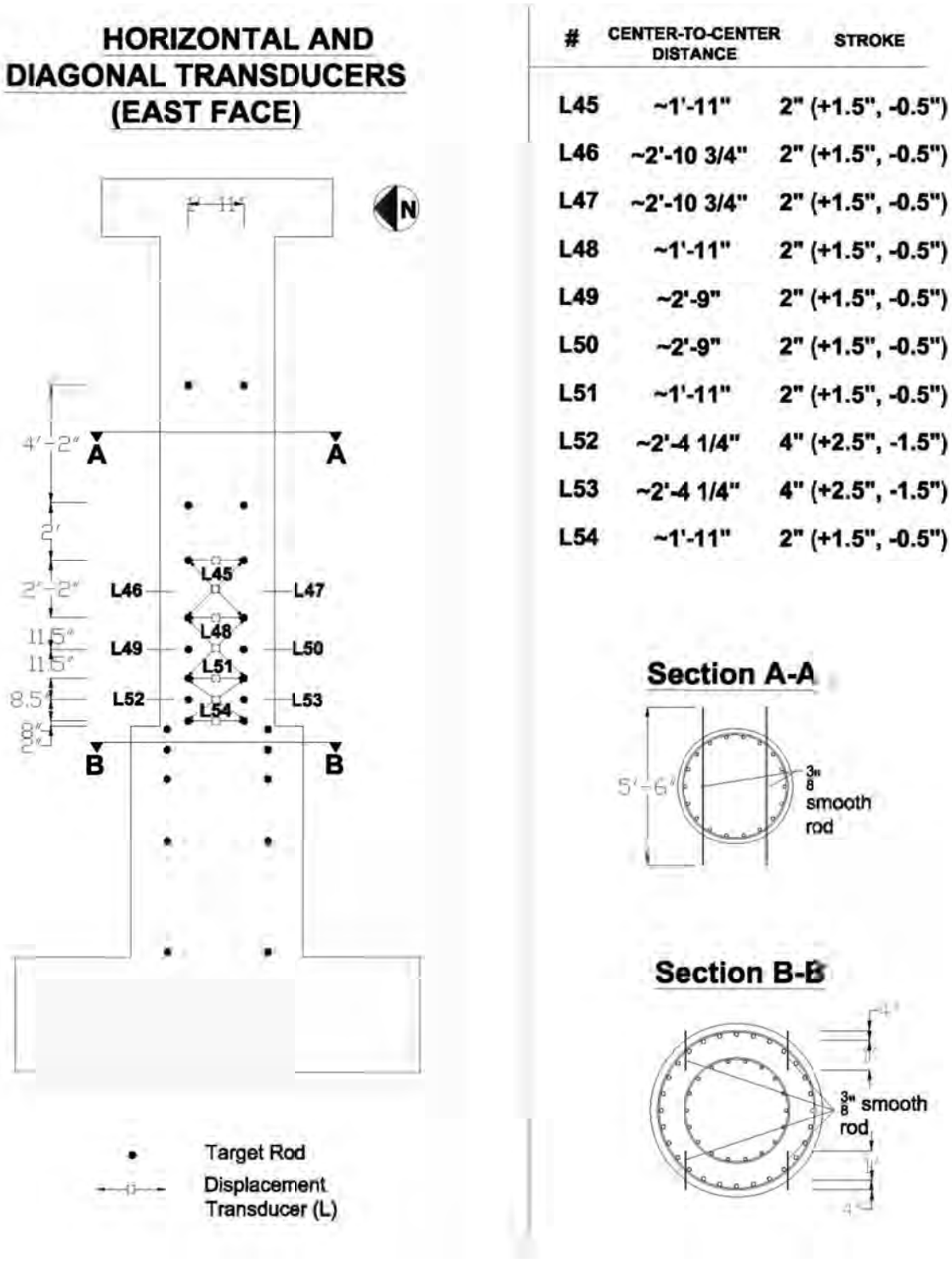

#	CENTER-TO-CENTER DISTANCE	STROKE
L45	~1'-11"	2" (+1.5", -0.5")
L46	~2'-10 3/4"	2" (+1.5", -0.5")
L47	~2'-10 3/4"	2" (+1.5", -0.5")
L48	~1'-11"	2" (+1.5", -0.5")
L49	~2'-9"	2" (+1.5", -0.5")
L50	~2'-9"	2" (+1.5", -0.5")
L51	~1'-11"	2" (+1.5", -0.5")
L52	~2'-4 1/4"	4" (+2.5", -1.5")
L53	~2'-4 1/4"	4" (+2.5", -1.5")
L54	~1'-11"	2" (+1.5", -0.5")

Figure C.15: Horizontal and diagonal displacement transducers on the east face of Specimen 2

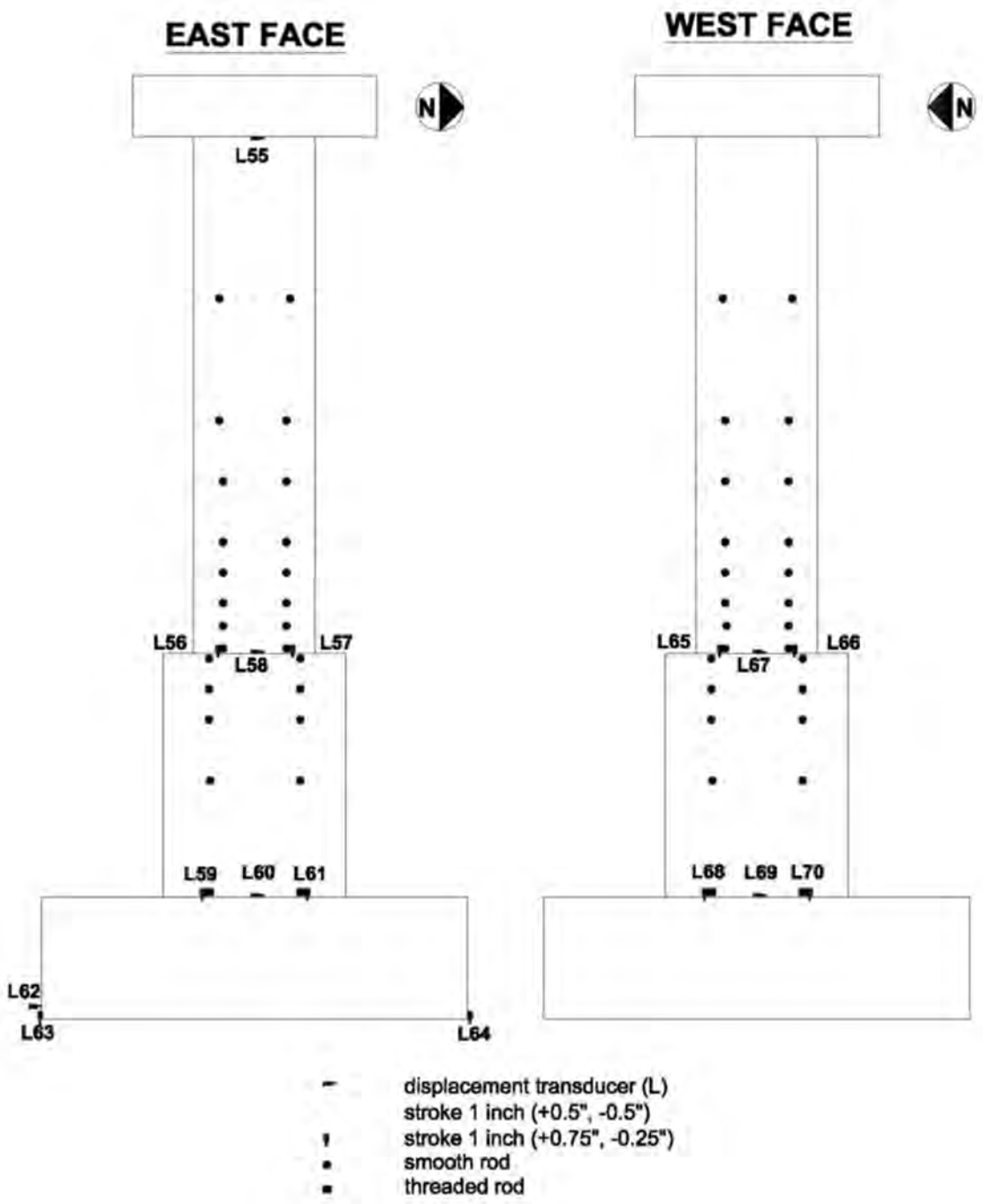

Figure C.16: Displacement transducers to measure slip and base rotation in Specimen 2

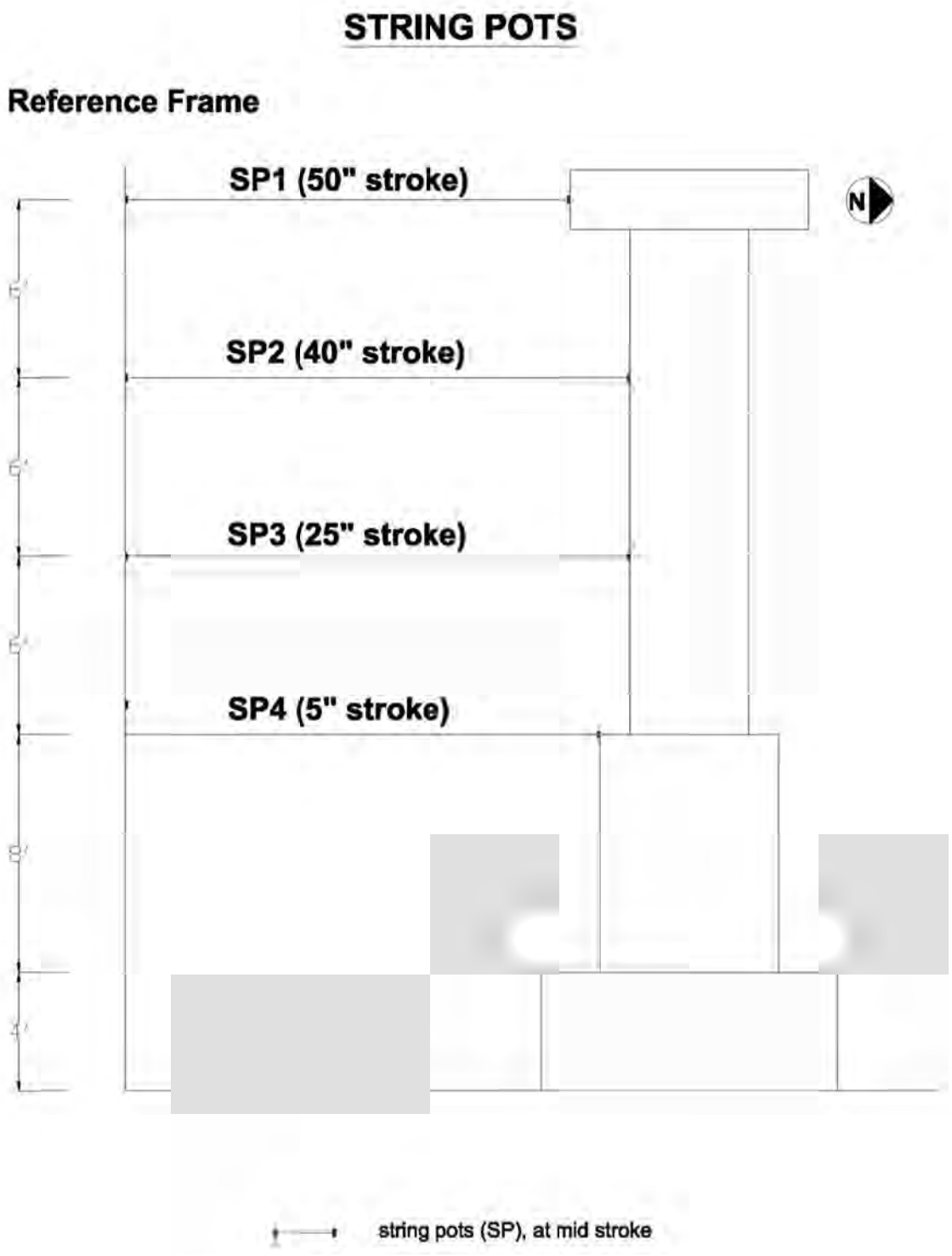

Figure C.17: String potentiometers to measure the lateral deflection of Specimen 2

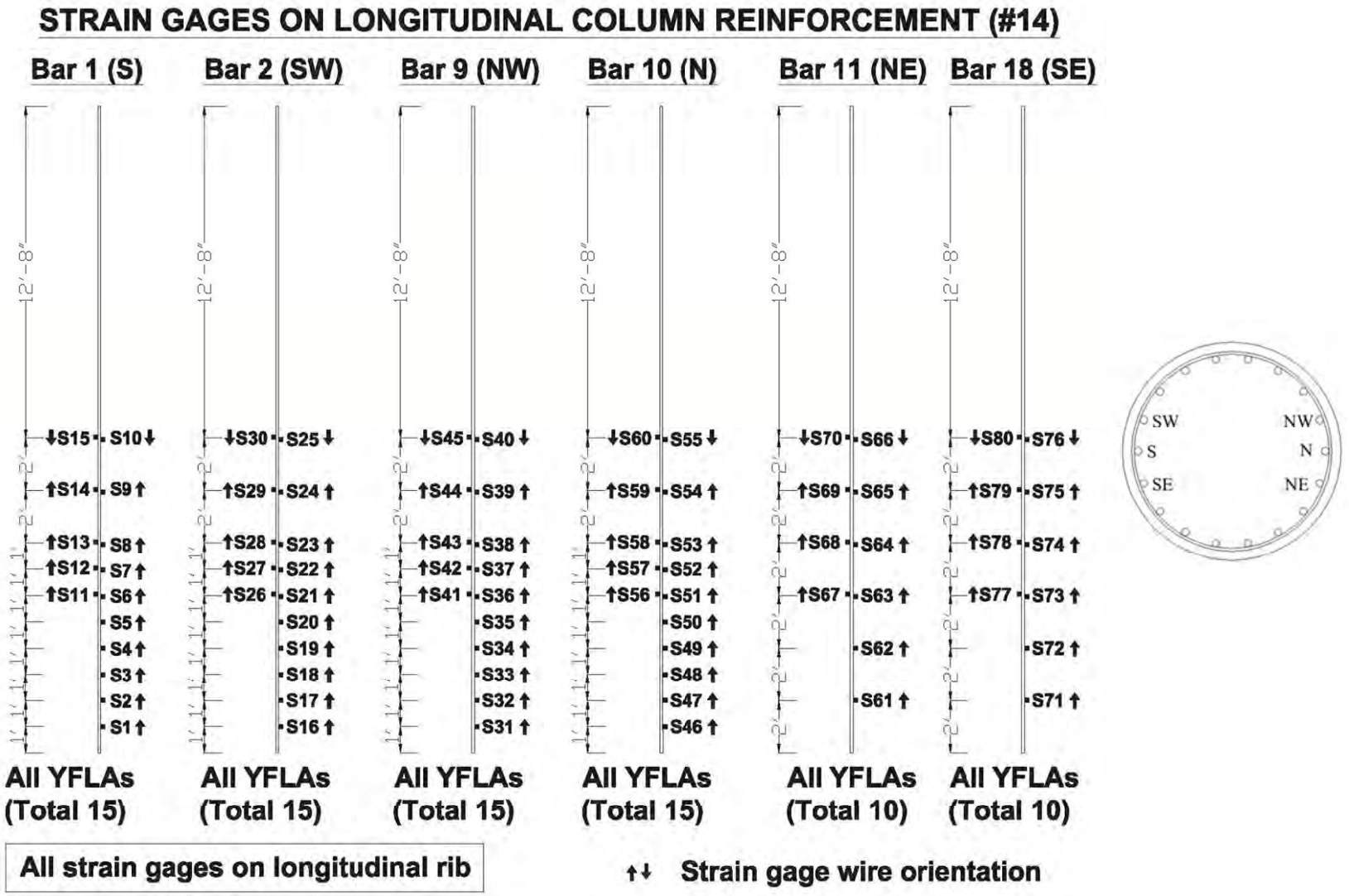

Figure C.18: Strain gages on column longitudinal bars in Specimen 3

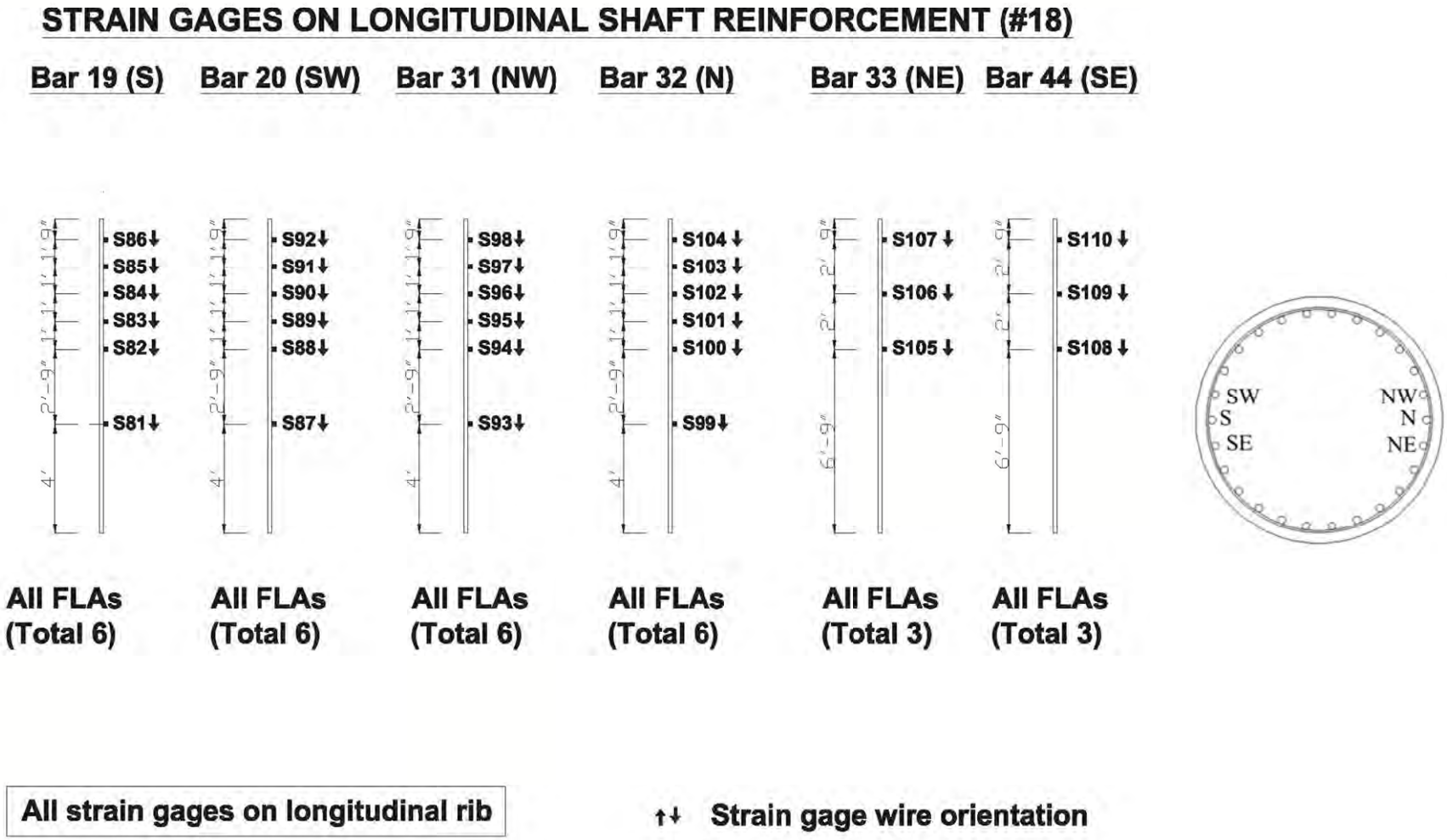

Figure C.19: Strain gages on shaft longitudinal bars in Specimen 3

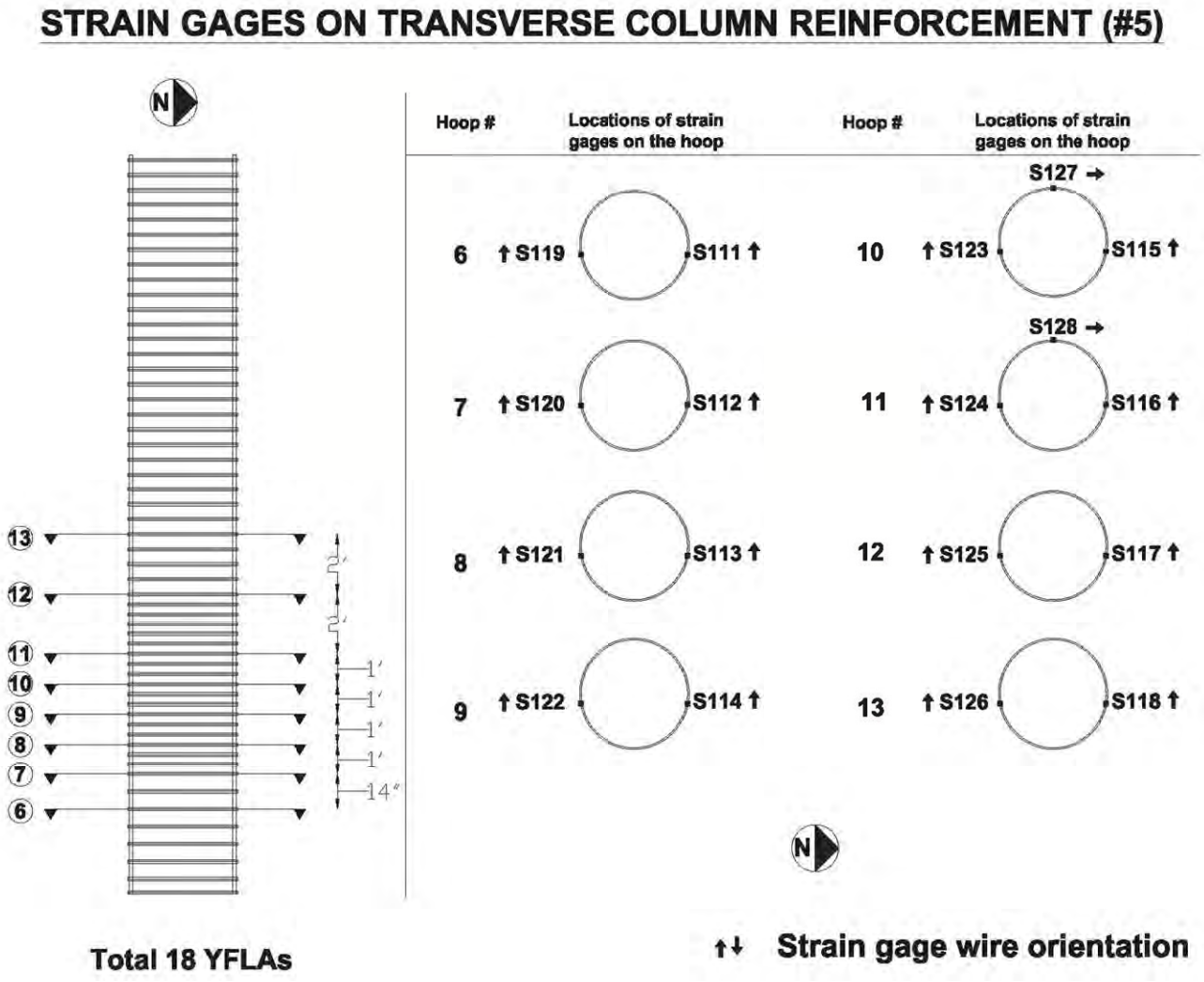

Figure C.20: Strain gages on column transverse reinforcement in Specimen 3

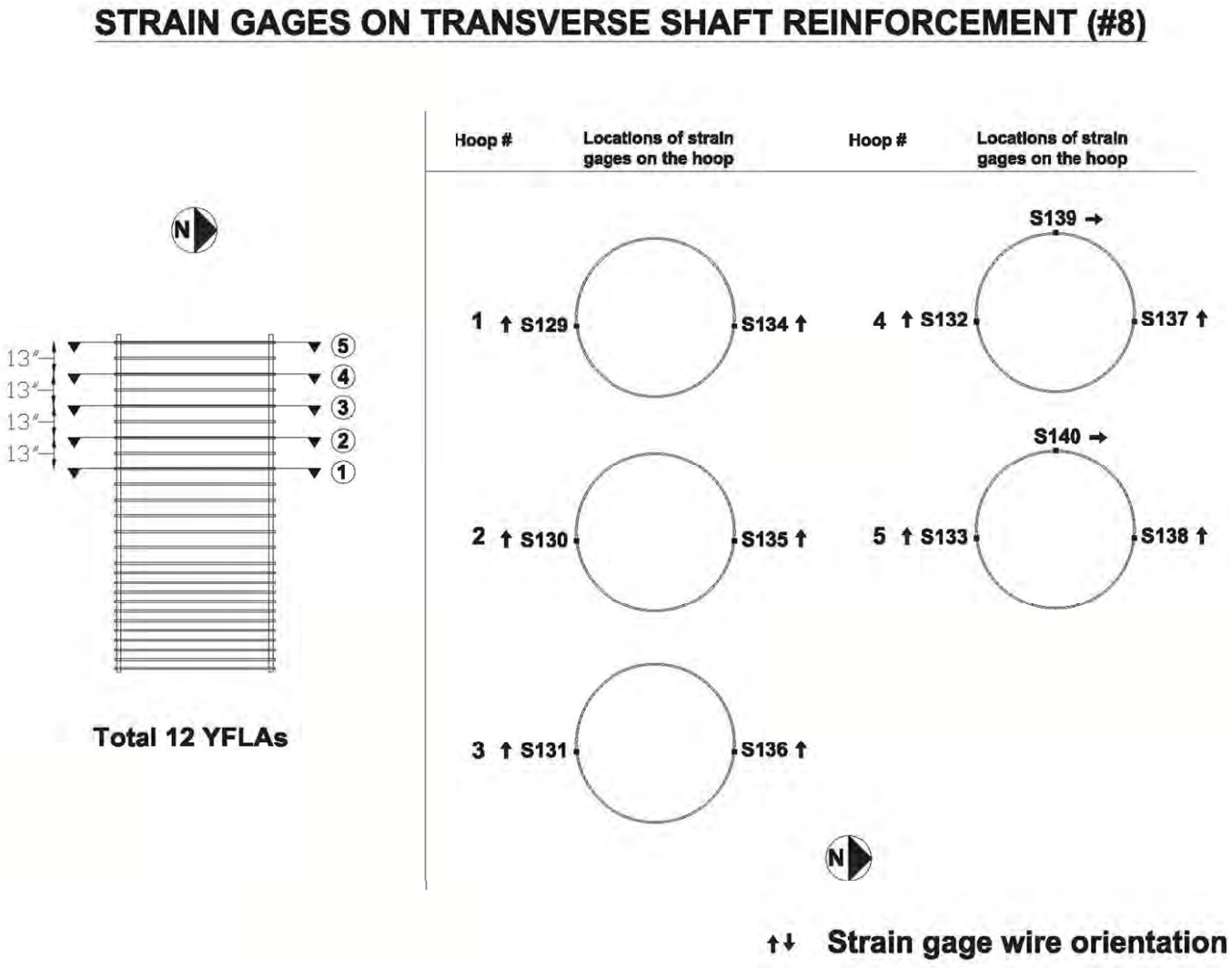

Figure C.21: Strain gages on shaft transverse reinforcement in Specimen 3

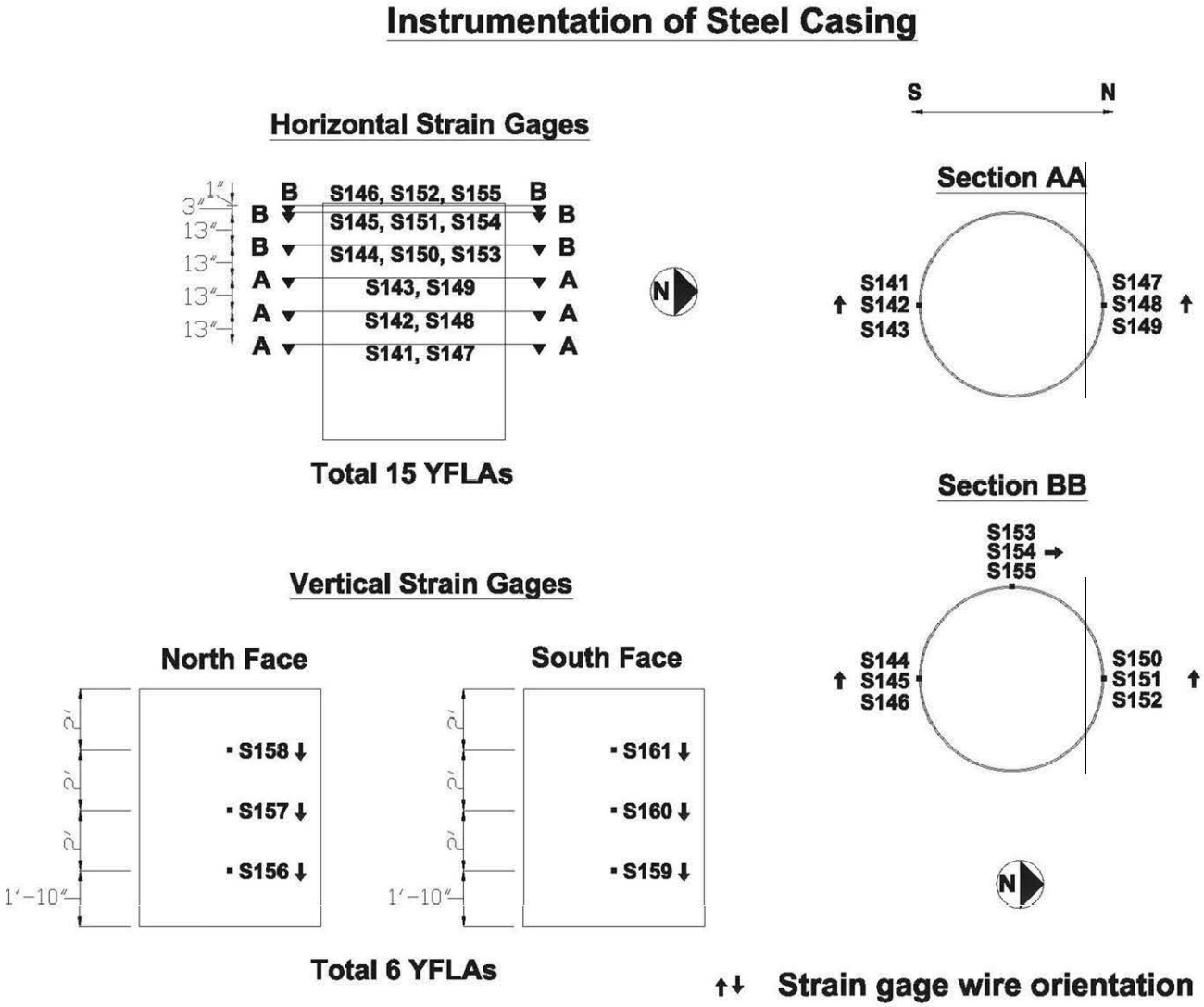

Figure C.22: Strain gages on steel casing in Specimen 3

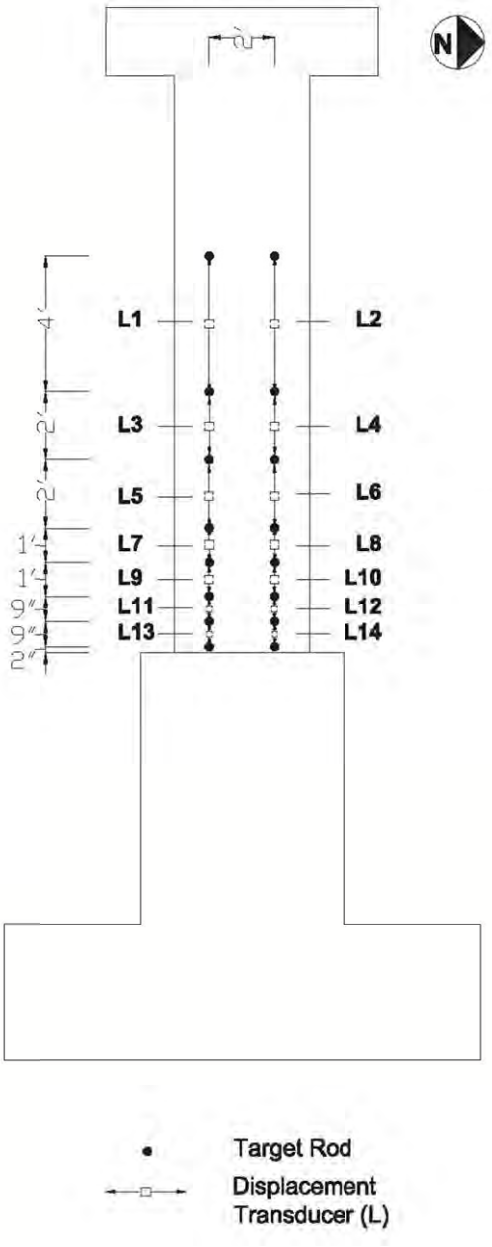

#	CENTER-TO-CENTER DISTANCE	STROKE
L1	~ 4'	2" (+1.5", -0.5")
L2	~ 4'	2" (+1.5", -0.5")
L3	~ 2'	2" (+1.5", -0.5")
L4	~ 2'	2" (+1.5", -0.5")
L5	~ 2'	2" (+1.5", -0.5")
L6	~ 2'	2" (+1.5", -0.5")
L7	~ 1'	2" (+1.5", -0.5")
L8	~ 1'	2" (+1.5", -0.5")
L9	~ 1'	2" (+1.5", -0.5")
L10	~ 1'	2" (+1.5", -0.5")
L11	~ 9"	2" (+1.5", -0.5")
L12	~ 9"	2" (+1.5", -0.5")
L13	~ 9"	2" (+1.5", -0.5")
L14	~ 9"	2" (+1.5", -0.5")

Figure C.23: Vertical displacement transducers on the east face of Specimen 3

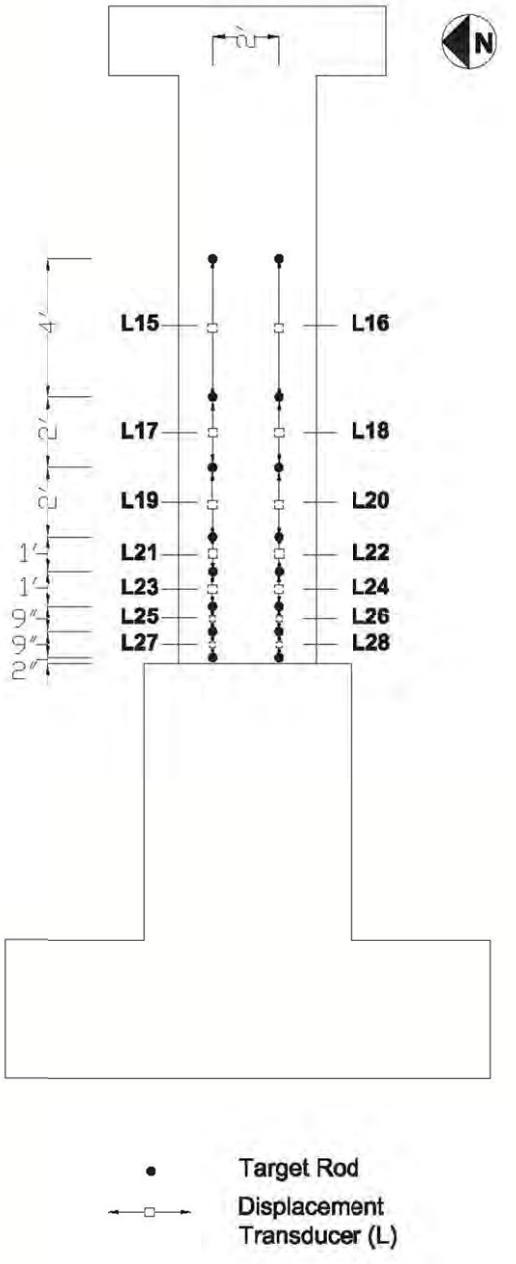

#	CENTER-TO-CENTER DISTANCE	STROKE
L15	~ 4'	2" (+1.5", -0.5")
L16	~ 4'	2" (+1.5", -0.5")
L17	~ 2'	2" (+1.5", -0.5")
L18	~ 2'	2" (+1.5", -0.5")
L19	~ 2'	2" (+1.5", -0.5")
L20	~ 2'	2" (+1.5", -0.5")
L21	~ 1'	2" (+1.5", -0.5")
L22	~ 1'	2" (+1.5", -0.5")
L23	~ 1'	2" (+1.5", -0.5")
L24	~ 1'	2" (+1.5", -0.5")
L25	~ 9"	2" (+1.5", -0.5")
L26	~ 9"	2" (+1.5", -0.5")
L27	~ 9"	2" (+1.5", -0.5")
L28	~ 9"	2" (+1.5", -0.5")

Figure C.24: Vertical displacement transducers on the west face of Specimen 3

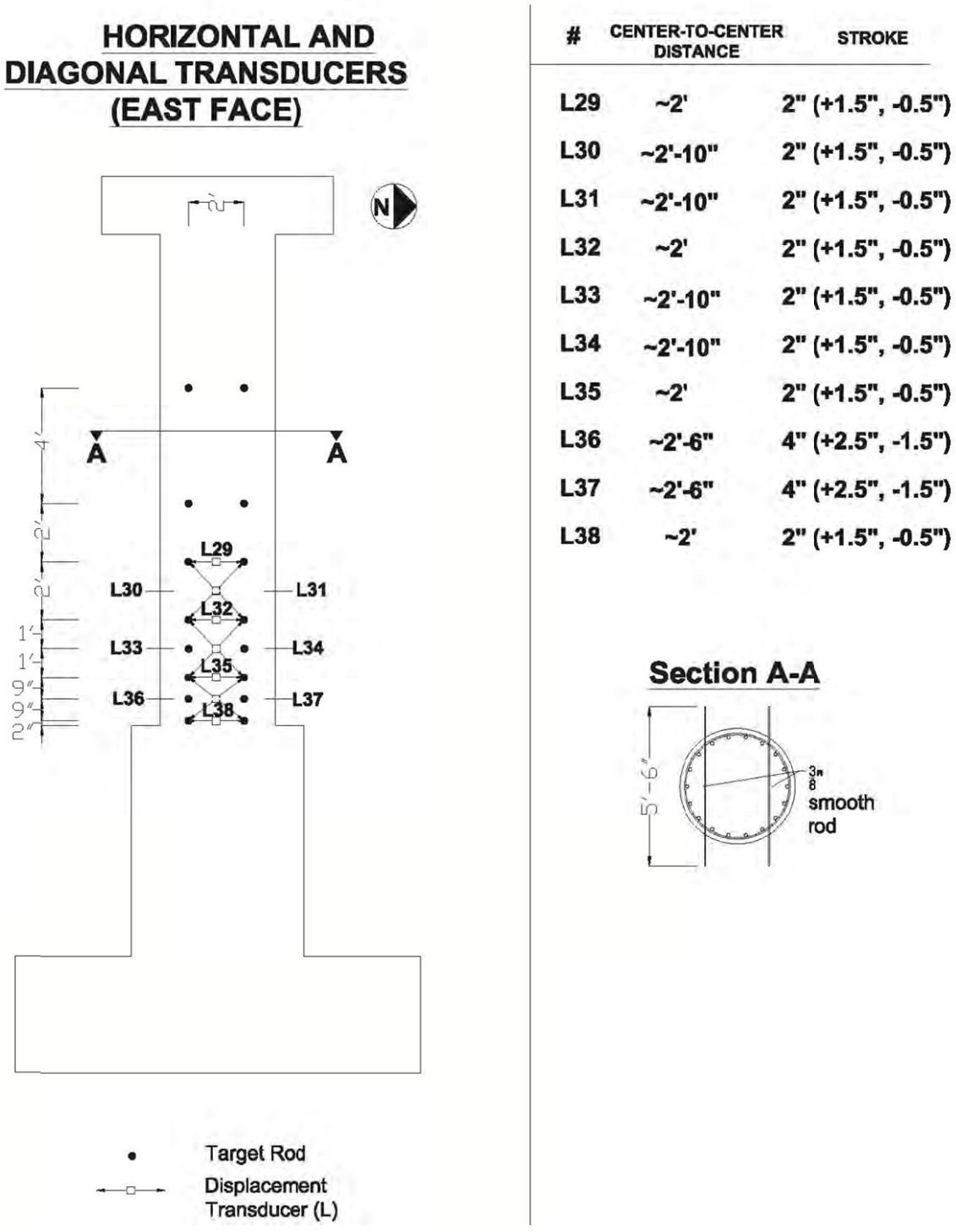

Figure C.25: Horizontal and diagonal displacement transducers on the east face of Specimen 3

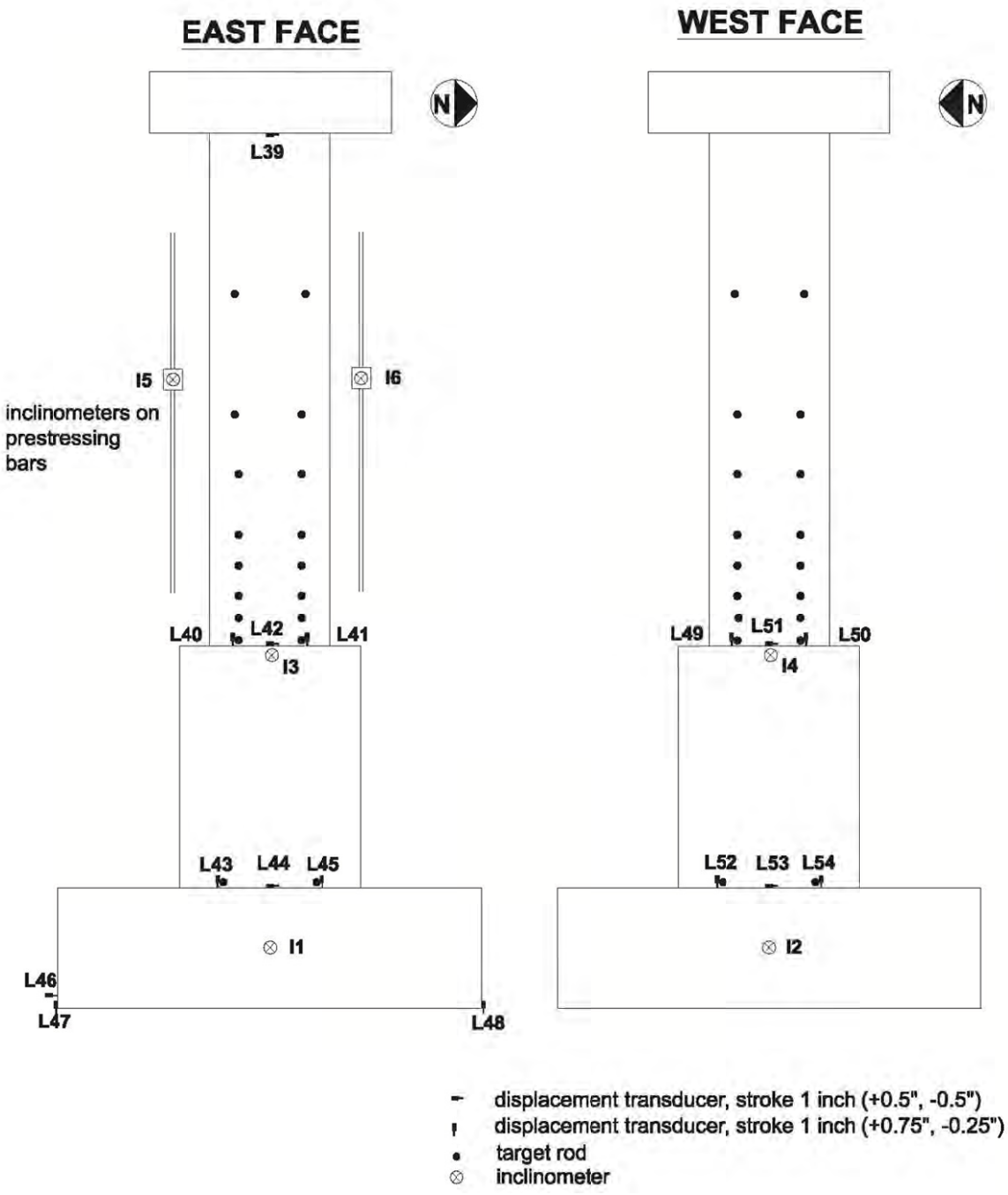

Figure C.26: Displacement transducers to measure slip and base rotation in Specimen 3

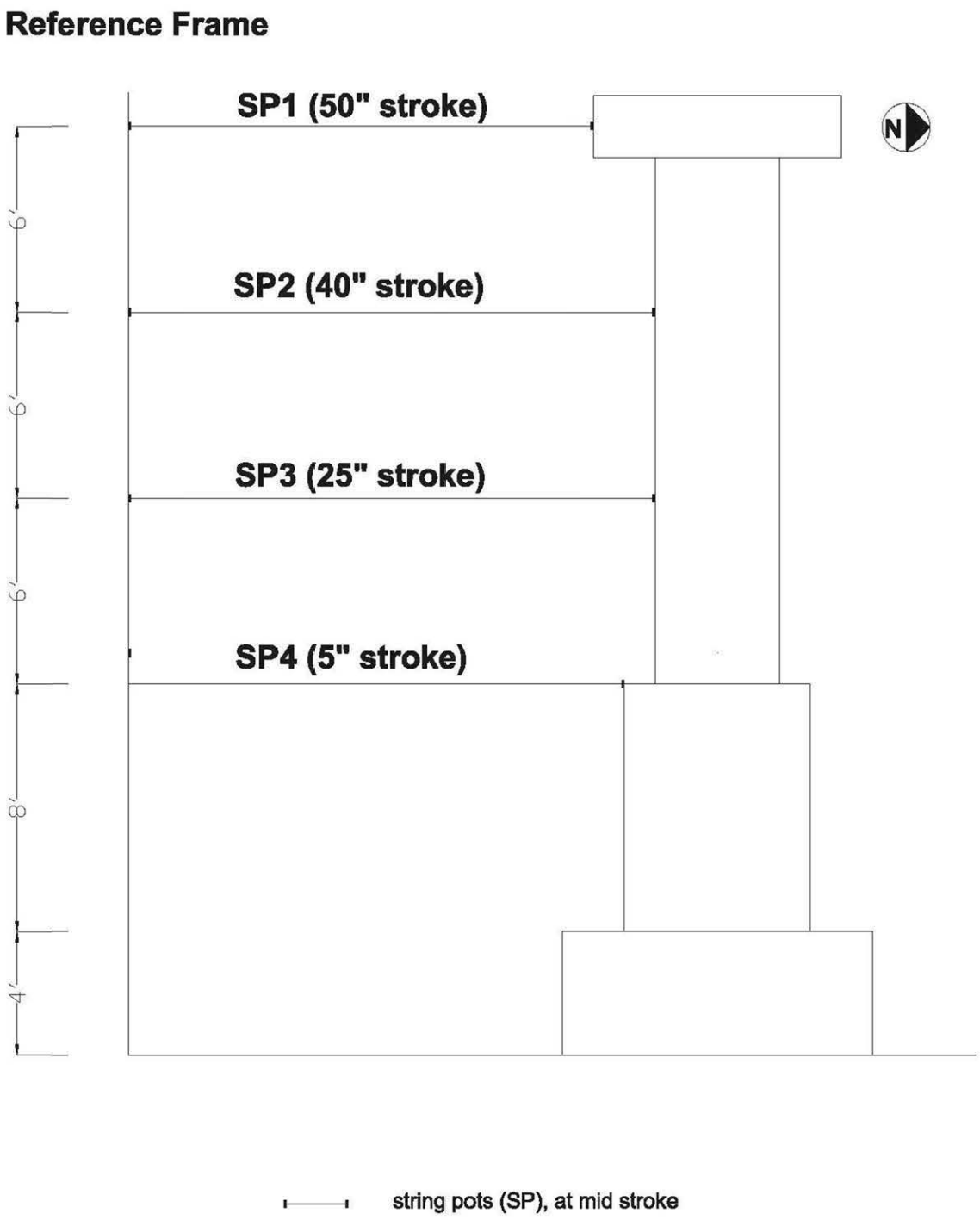

Figure C.27: String potentiometers to measure the lateral deflection of Specimen 3

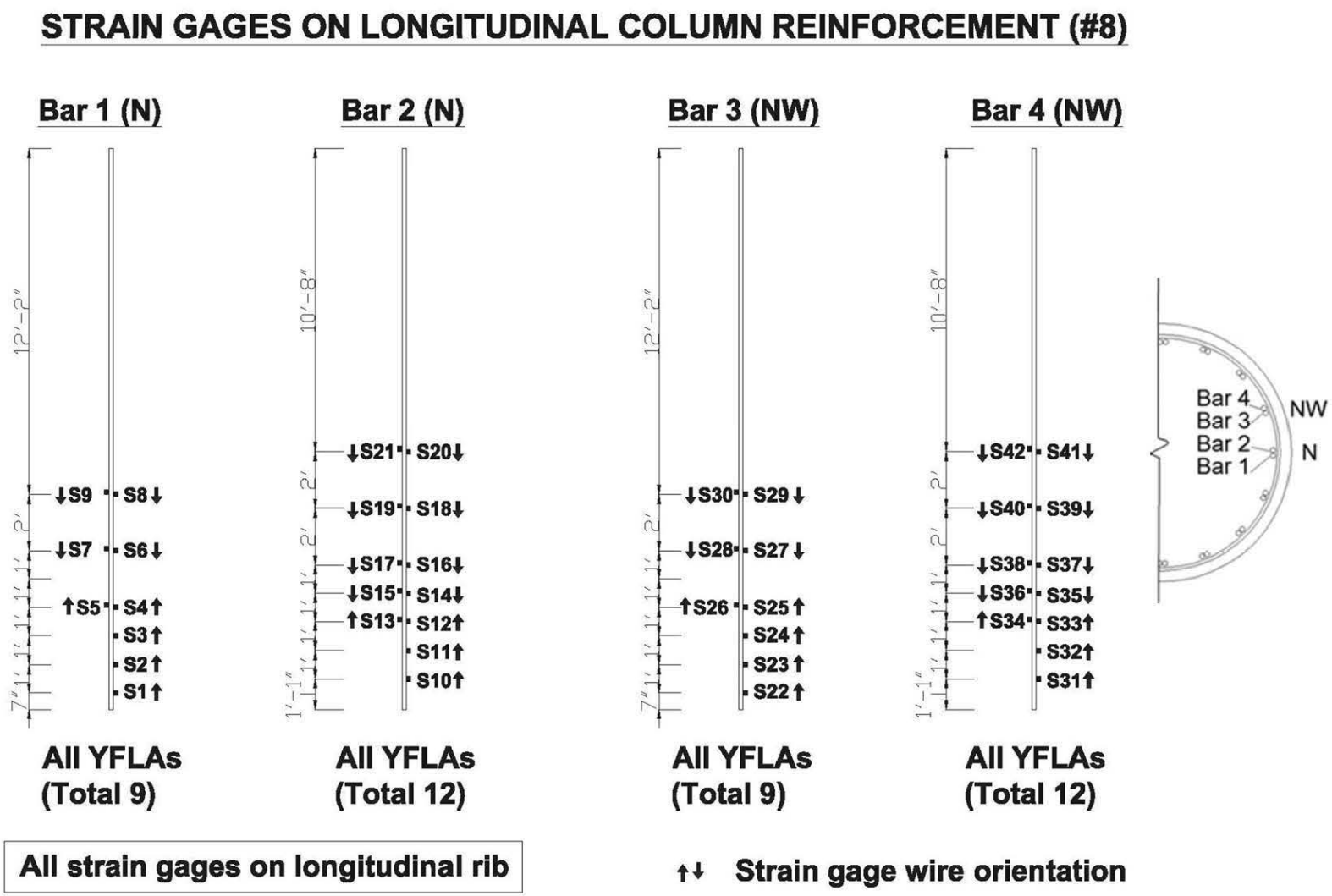

Figure C.28: Strain gages on column longitudinal bars in Specimen 4 (north face)

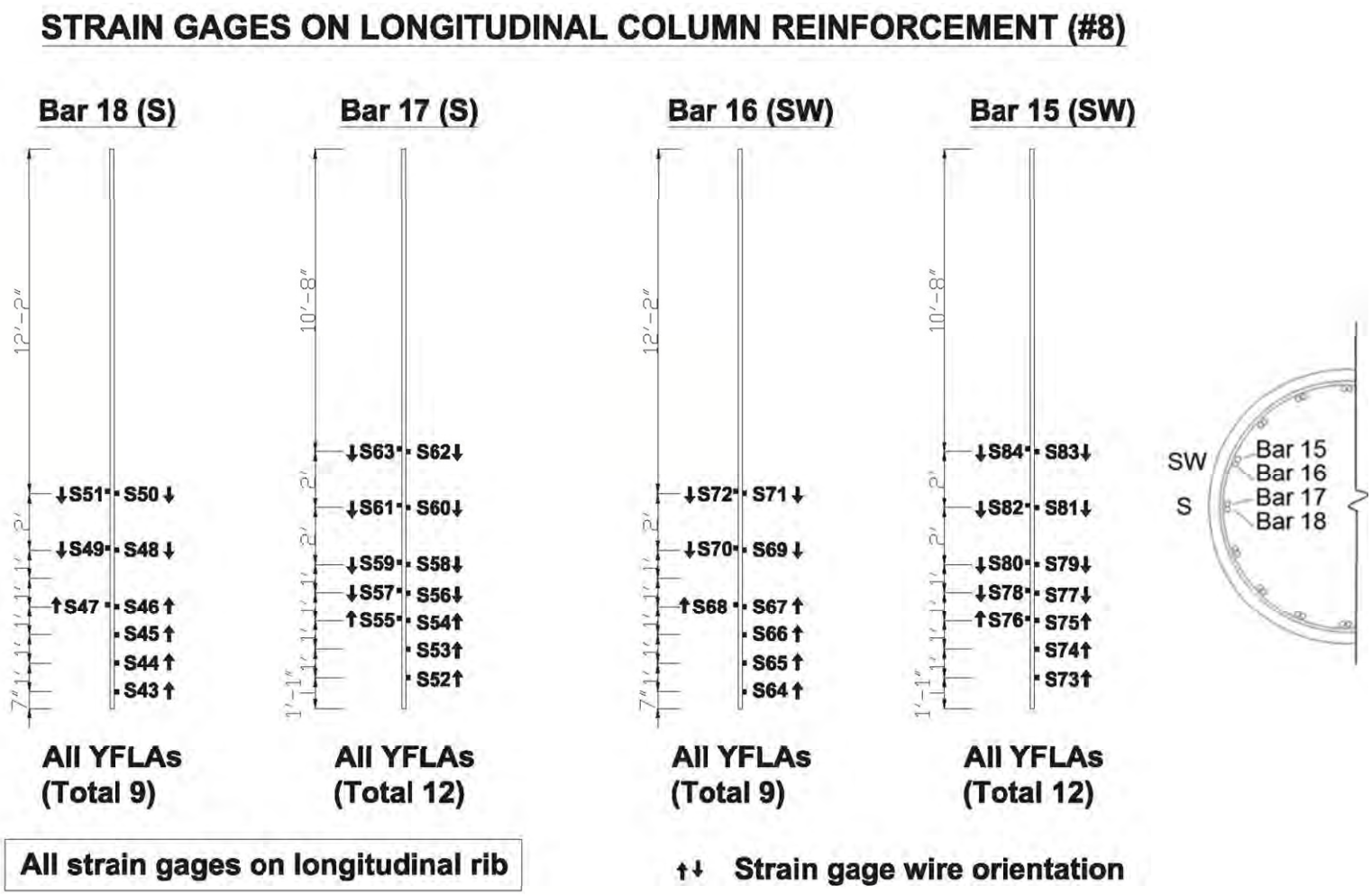

Figure C.29: Strain gages on column longitudinal bars in Specimen 4 (south face)

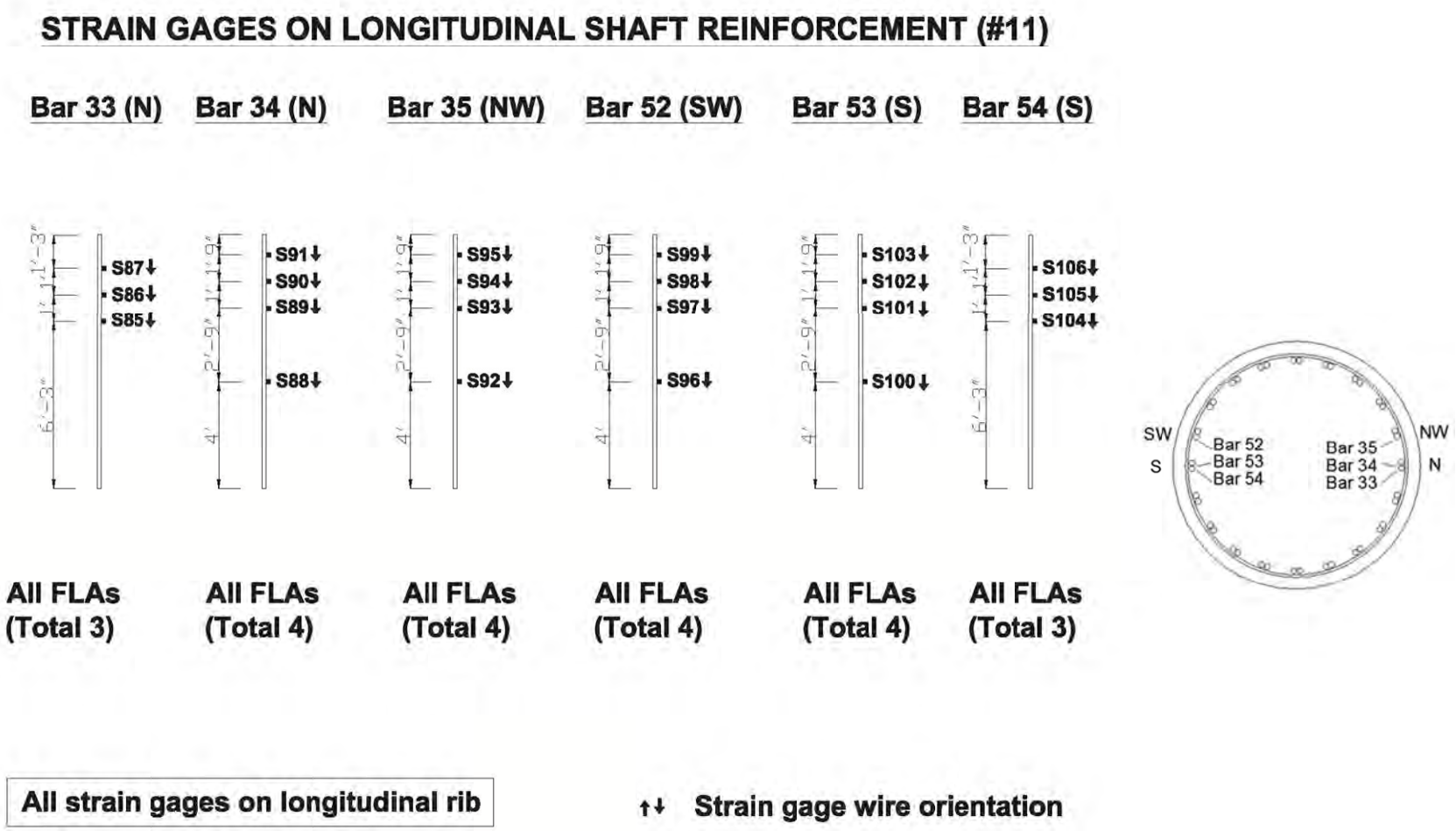

Figure C.30: Strain gages on shaft longitudinal bars in Specimen 4

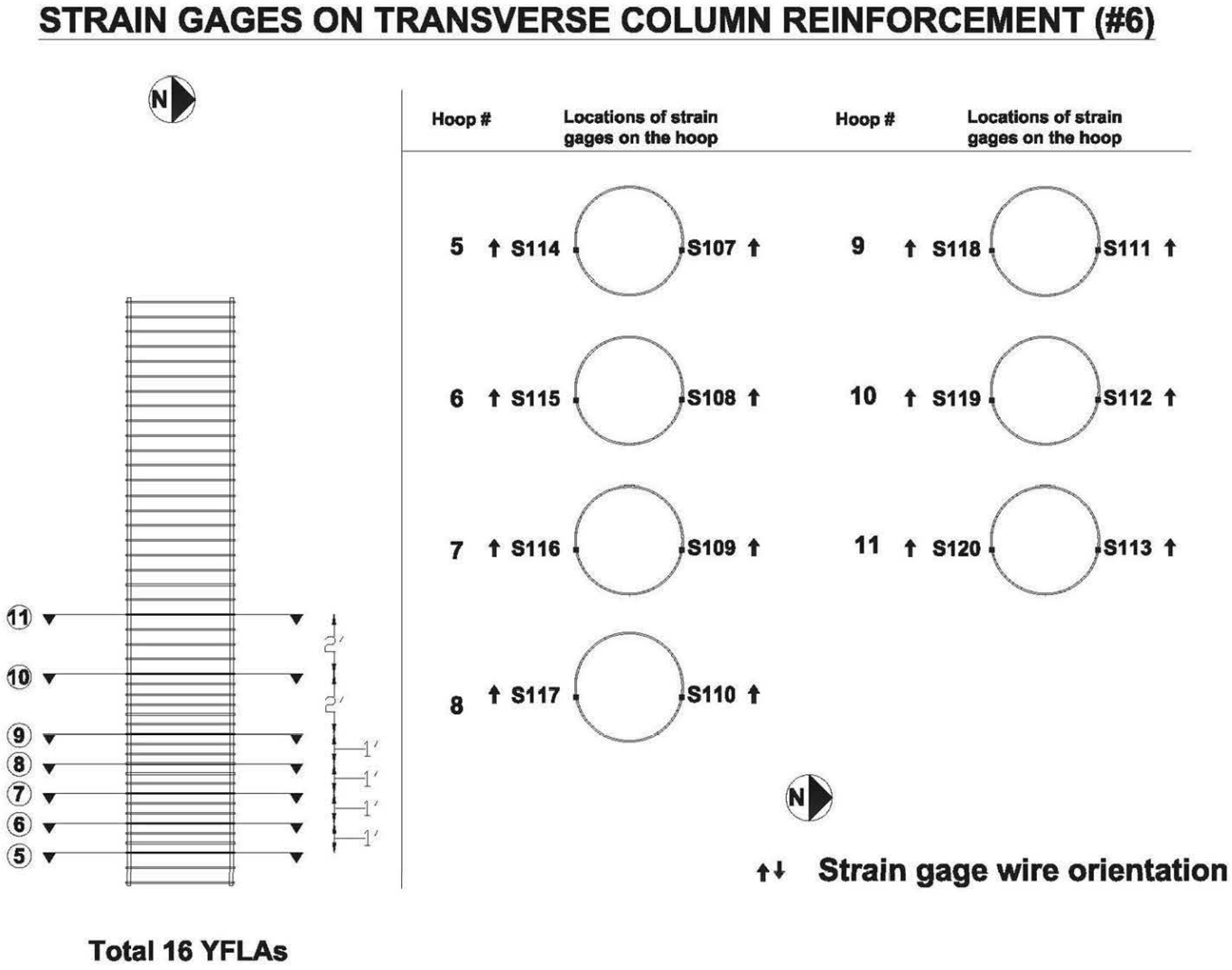

Figure C.31: Strain gages on column transverse reinforcement in Specimen 4

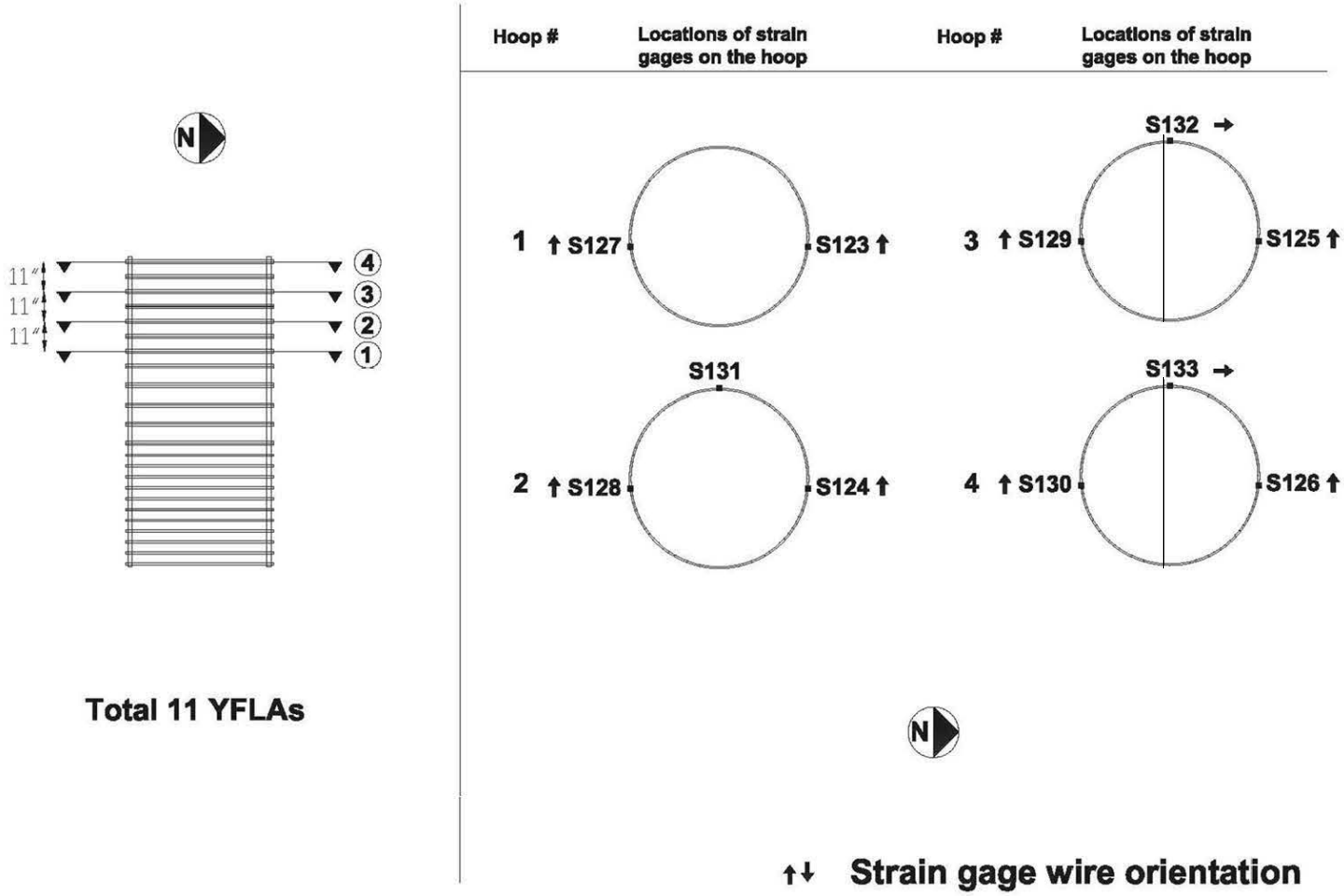

Figure C.32: Strain gages on shaft transverse reinforcement in Specimen 4

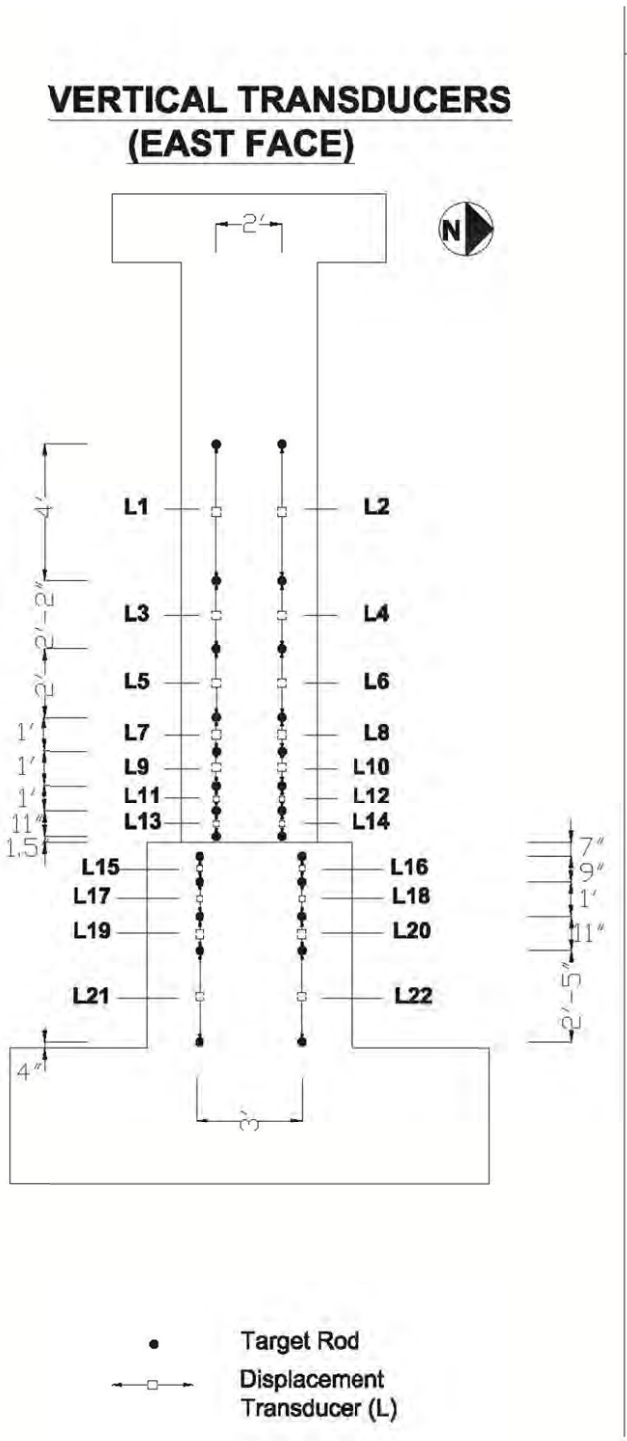

#	CENTER-TO-CENTER DISTANCE	STROKE
L1	~ 4'	2" (+1.5", -0.5")
L2	~ 4'	2" (+1.5", -0.5")
L3	~ 2'-2"	2" (+1.5", -0.5")
L4	~ 2'-2"	2" (+1.5", -0.5")
L5	~ 2'	2" (+1.5", -0.5")
L6	~ 2'	2" (+1.5", -0.5")
L7	~ 1'	2" (+1.5", -0.5")
L8	~ 1'	2" (+1.5", -0.5")
L9	~ 1'	2" (+1.5", -0.5")
L10	~ 1'	2" (+1.5", -0.5")
L11	~ 1'	2" (+1.5", -0.5")
L12	~ 1'	2" (+1.5", -0.5")
L13	~ 11"	2" (+1.5", -0.5")
L14	~ 11"	2" (+1.5", -0.5")
L15	~ 9"	2" (+1.5", -0.5")
L16	~ 9"	2" (+1.5", -0.5")
L17	~ 1'	2" (+1.5", -0.5")
L18	~ 1'	2" (+1.5", -0.5")
L19	~ 11"	2" (+1.5", -0.5")
L20	~ 11"	2" (+1.5", -0.5")
L21	~ 2'-5"	2" (+1.5", -0.5")
L22	~ 2'-5"	2" (+1.5", -0.5")

Figure C.33: Vertical displacement transducers on the east face of Specimen 4

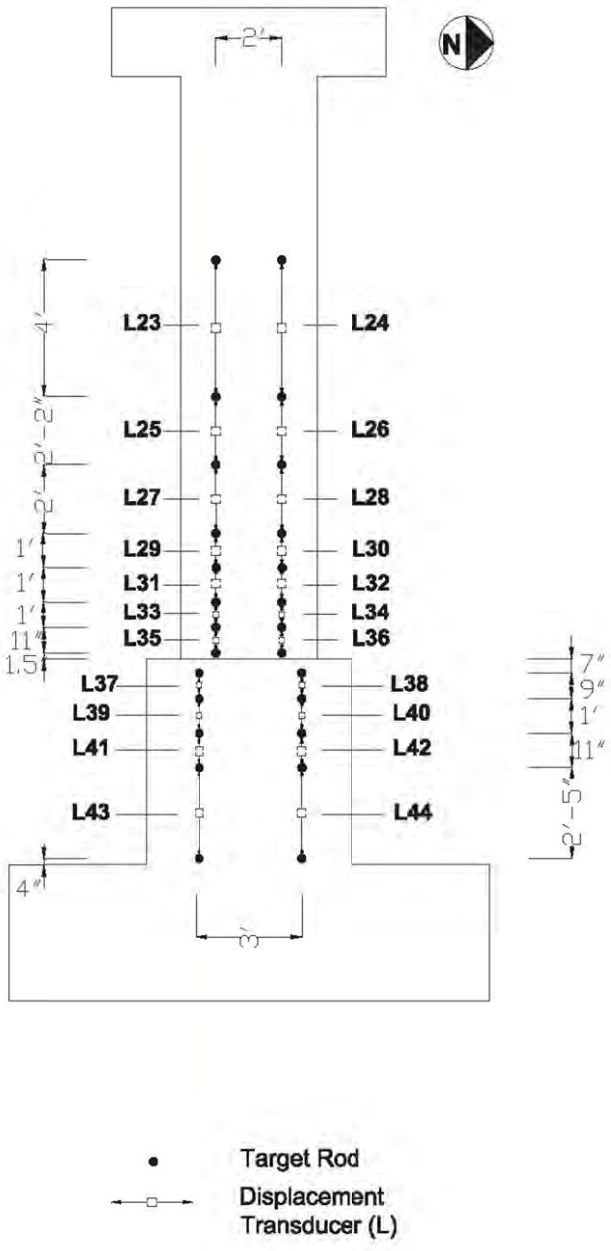

#	CENTER-TO-CENTER DISTANCE	STROKE
L23	~ 4'	2" (+1.5", -0.5")
L24	~ 4'	2" (+1.5", -0.5")
L25	~ 2'-2"	2" (+1.5", -0.5")
L26	~ 2'-2"	2" (+1.5", -0.5")
L27	~ 2'	2" (+1.5", -0.5")
L28	~ 2'	2" (+1.5", -0.5")
L29	~ 1'	2" (+1.5", -0.5")
L30	~ 1'	2" (+1.5", -0.5")
L31	~ 1'	2" (+1.5", -0.5")
L32	~ 1'	2" (+1.5", -0.5")
L33	~ 1'	2" (+1.5", -0.5")
L34	~ 1'	2" (+1.5", -0.5")
L35	~ 11"	2" (+1.5", -0.5")
L36	~ 11"	2" (+1.5", -0.5")
L37	~ 9"	2" (+1.5", -0.5")
L38	~ 9"	2" (+1.5", -0.5")
L39	~ 1'	2" (+1.5", -0.5")
L40	~ 1'	2" (+1.5", -0.5")
L41	~ 11"	2" (+1.5", -0.5")
L42	~ 11"	2" (+1.5", -0.5")
L43	~ 2'-5"	2" (+1.5", -0.5")
L44	~ 2'-5"	2" (+1.5", -0.5")

Figure C.34: Vertical displacement transducers on the west face of Specimen 4

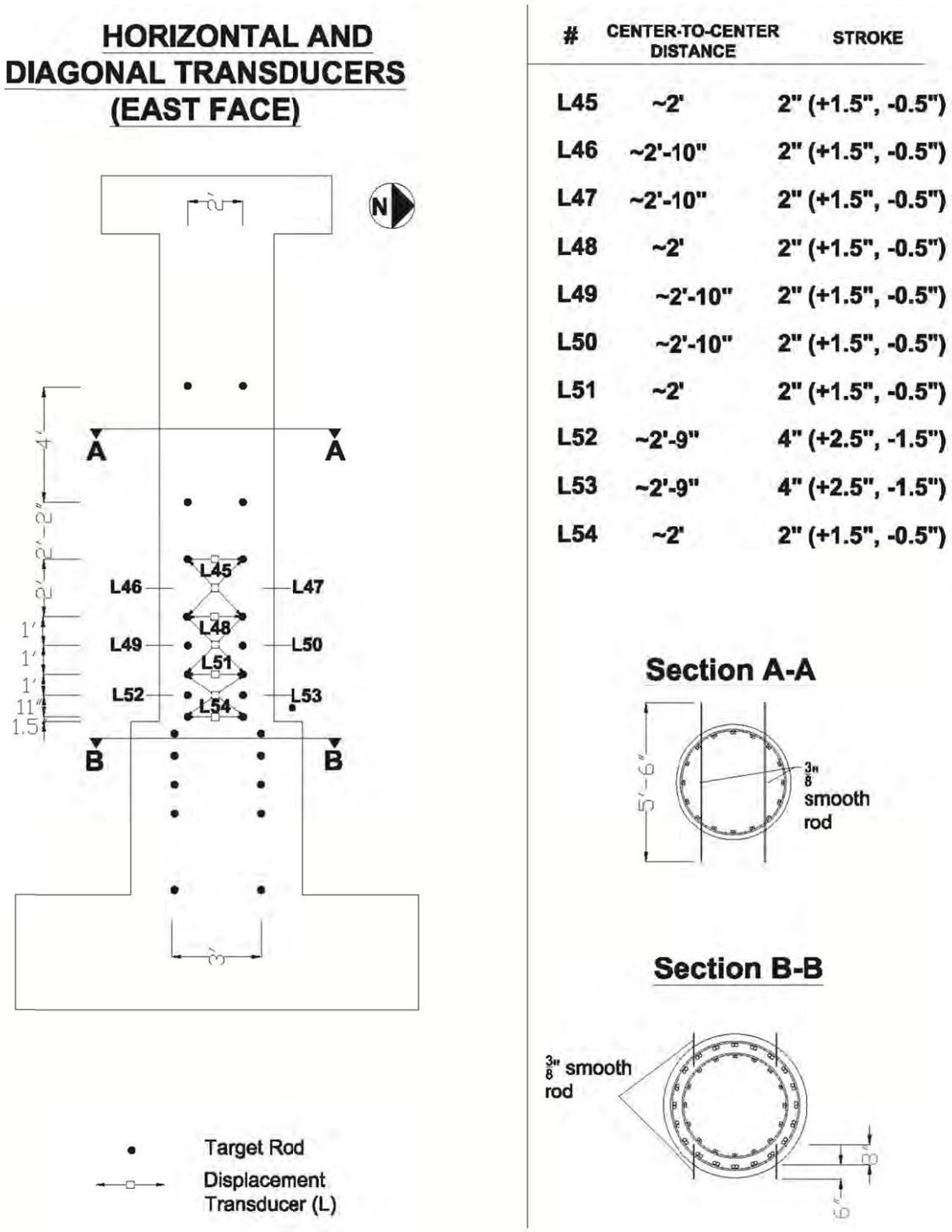

#	CENTER-TO-CENTER DISTANCE	STROKE
L45	~2'	2" (+1.5", -0.5")
L46	~2'-10"	2" (+1.5", -0.5")
L47	~2'-10"	2" (+1.5", -0.5")
L48	~2'	2" (+1.5", -0.5")
L49	~2'-10"	2" (+1.5", -0.5")
L50	~2'-10"	2" (+1.5", -0.5")
L51	~2'	2" (+1.5", -0.5")
L52	~2'-9"	4" (+2.5", -1.5")
L53	~2'-9"	4" (+2.5", -1.5")
L54	~2'	2" (+1.5", -0.5")

Figure C.35: Horizontal and diagonal displacement transducers on the east face of Specimen 4

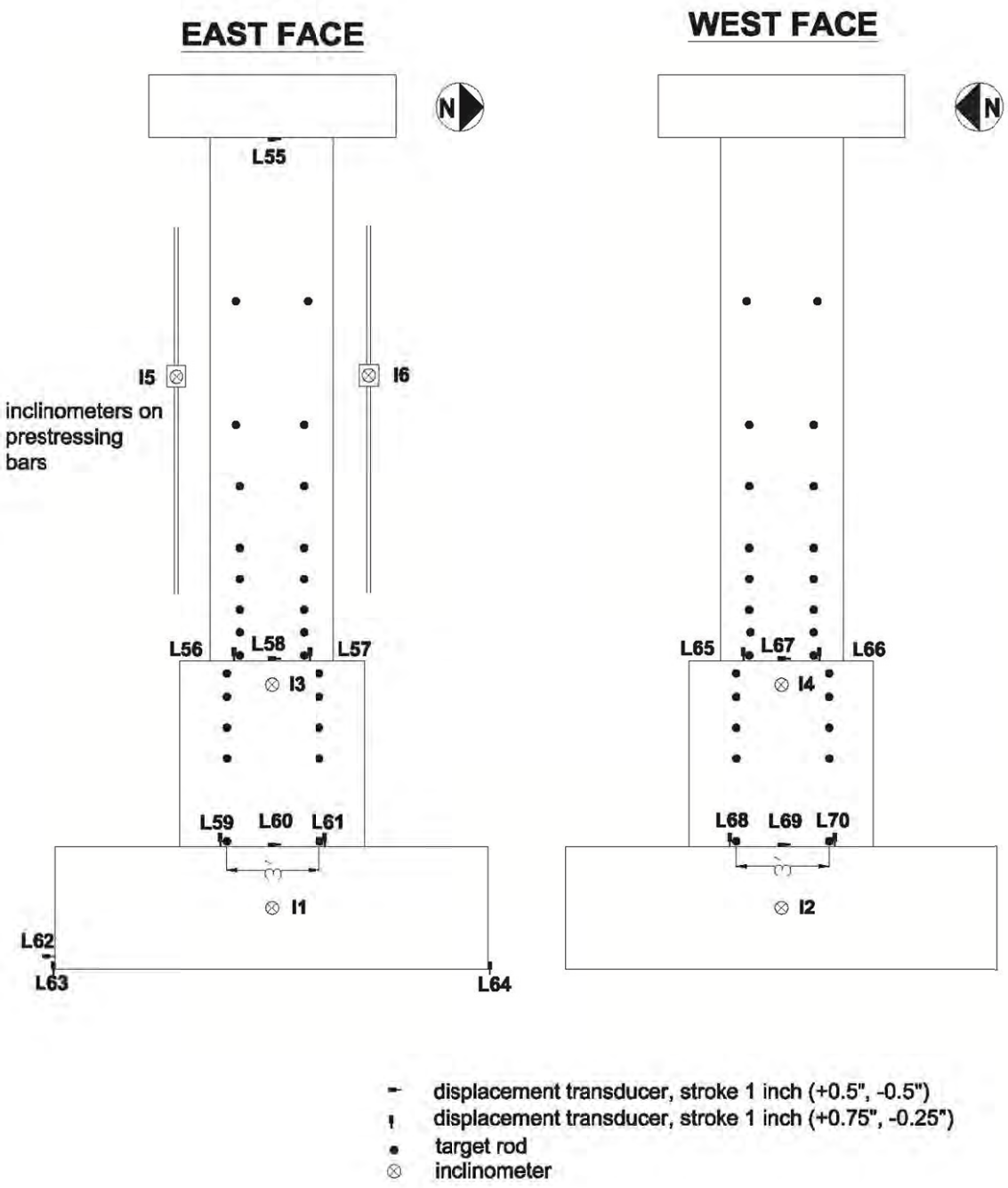

Figure C.36: Displacement transducers to measure slip and base rotation in Specimen 4

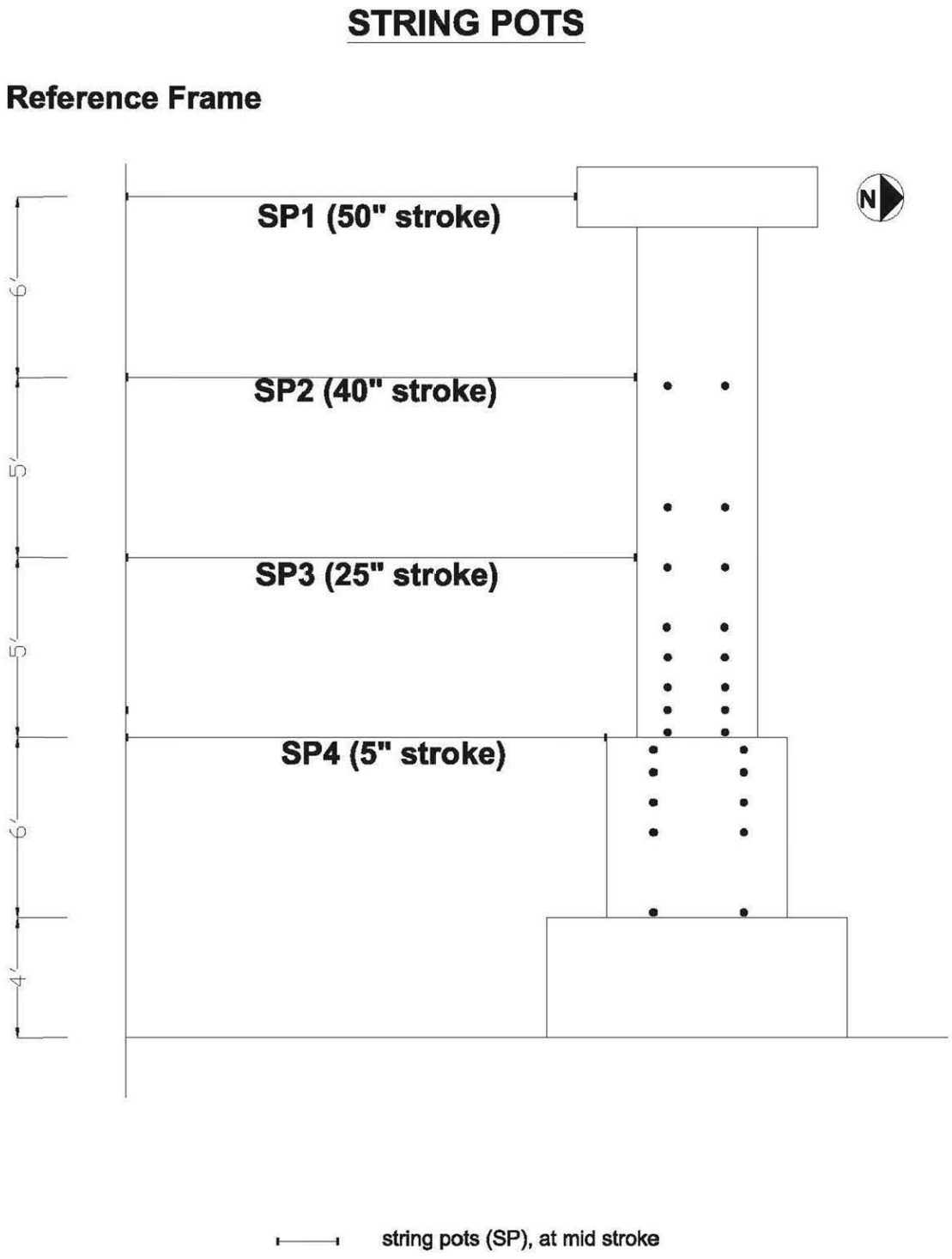

Figure C.37: String potentiometers to measure the lateral deflection of Specimen 4